

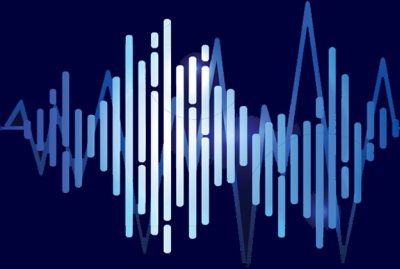


Iranian Association of Electrical
and Electronics Engineers



Shahid Chamran
University of Ahvaz

Journal of Applied Research in Electrical Engineering



Vol. 1, No. 2, Summer and Autumn 2022



PUBLISHER: SHAHID CHAMRAN UNIVERSITY OF AHVAZ

E-ISSN: 2783-2864

P-ISSN: 2717-414X



**Iranian Association of
Electrical and Electronics
Engineers**

Journal of Applied Research in Electrical Engineering

E-ISSN: 2783-2864

P-ISSN: 2717-414X



**Shahid Chamran
University of Ahvaz**

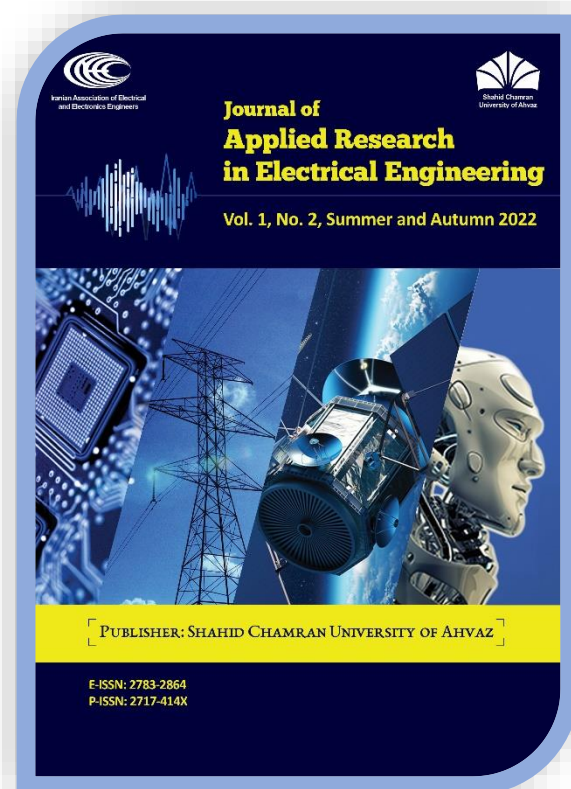
**Journal of Applied Research in Electrical Engineering (JAREE),
Volume 1, Number 2, Summer and Autumn 2022**

Publisher: Shahid Chamran University of Ahvaz, Iran

This magazine is the result of a formal partnership of **Shahid Chamran University of Ahvaz** and **Iranian Association of Electrical and Electronics Engineers**

Website: <https://jaree.scu.ac.ir>

E-mails: jaree@scu.ac.ir; jaree.scu@gmail.com



Address: Department of Electrical Engineering, Faculty of Engineering, Shahid Chamran University of Ahvaz, Golestan Street, Ahvaz, Iran

P.O. Box: 61357-85311






Tel: +986133226600-14, Ext. 5632 & 5630, +989122876375

Fax: +986133226597

Editorial Board

	Editor-in-Chief		Director-in-Charge
	<p>Prof. Mahmood Joorabian Shahid Chamran University of Ahvaz, Ahvaz, Iran <i>Power System Planning, Renewable Energy and Smart grid, FACTS Devices</i> mjoorabian@scu.ac.ir</p>		<p>Prof. Seyed Ghodratalah Seifossadat Shahid Chamran University of Ahvaz, Ahvaz, Iran <i>Power System Protection, Power Electronics, Power Quality</i> seifossadat@yahoo.com</p>
	Managing Editor		Executive Assistant
	<p>Dr. Alireza Saffarian (Associate Professor) Shahid Chamran University of Ahvaz, Ahvaz, Iran <i>Power System Protection, Power System Stability, Power Quality, Distribution Systems</i> a.saffarian@scu.ac.ir</p>		<p>Dr. Mohammad Nabipour (Assistant Professor) Shahid Chamran University of Ahvaz, Ahvaz, Iran <i>Power Electronics and Drive</i> mo.nabipour@scu.ac.ir</p>
	Associate Editor		Associate Editor
	<p>Dr. Yousef Seifi Kavian (Associate Professor) Shahid Chamran University of Ahvaz, Ahvaz, Iran <i>Electronics and Telecommunications</i> y.s.kavian@scu.ac.ir</p>		<p>Dr. Mohsen Saniei (Associate Professor) Shahid Chamran University of Ahvaz, Ahvaz, Iran <i>Power and Control</i> m.saniei@scu.ac.ir</p>
	Editorial Board		Editorial Board
	<p>Prof. Saeedallah Mortazavi Shahid Chamran University of Ahvaz, Ahvaz, Iran <i>Intelligent Control Systems, Power system Control, Automation, Fuzzy logic, Neural Networks</i> mortazavi_s@scu.ac.ir</p>		<p>Prof. Abdolnabi Kosarian Shahid Chamran University of Ahvaz, Ahvaz, Iran <i>Solid State Electronic Devices, Solar Cell Fabrication Technology</i> a.kosarian@scu.ac.ir</p>
	Editorial Board		Editorial Board
	<p>Prof. Ebrahim Farshidi Shahid Chamran University of Ahvaz, Ahvaz, Iran <i>Analog and Digital Integrated Circuits, Data Converters, Microelectronics</i> farshidi@scu.ac.ir</p>		<p>Prof. Naser Pariz Ferdowsi University of Mashhad, Mashhad, Iran <i>Nonlinear Control, Hybrid Systems, Aeronautics, Industrial Control, Applied Mathematics</i> n-pariz@um.ac.ir</p>
	Editorial Board		Editorial Board
	<p>Dr. Yousef Seifi Kavian (Associate Professor) Shahid Chamran University of Ahvaz, Ahvaz, Iran <i>Digital Circuits and Systems, Communication Networks and Distributed Systems</i> y.s.kavian@scu.ac.ir</p>		<p>Dr. Mohsen Saniei (Associate Professor) Shahid Chamran University of Ahvaz, Ahvaz, Iran <i>Power System Dynamics, High Voltage Engineering, Electricity Market, Microgrid</i> m.saniei@scu.ac.ir</p>
	Editorial Board		Editorial Board
	<p>Prof. Abbas Zarifkar Shiraz University, Shiraz, Iran <i>Optical Electronics</i> zarifkar@shirazu.ac.ir</p>		<p>Dr. Edris Pouresmaeil (Associate Professor) Aalto University, Espoo, Finland <i>Integration of renewable energies into the power grid</i> edris.pouresmaeil@aalto.fi</p>
	Editorial Board		Editorial Board
	<p>Prof. Reza Ghaderi Shahid Baheshti University, Tehran, Iran <i>Control Theory, System Identification, Control Systems, Fuzzy Engineering</i> r_ghaderisbu.ac.ir</p>		<p>Prof. Fushuan Wen Tallinn University of Technology, Tallinn, Estonia <i>Power systems and power economics</i> fushuan.wen@taltech.ee</p>
	Editorial Board		Editorial Board
	<p>Prof. Majid Sanaye-pasand University of Tehran, Tehran, Iran <i>Power Systems Protection, Digital Protective Relays, Power Systems Automation, Power System Transients</i> msanaye@ut.ac.ir</p>		<p>Prof. Zabih (Fary) Ghassemlooy North Umbria University, Newcastle upon Tyne, United Kingdom <i>Optical Communications, Visible Light, Communication Systems</i> z.ghassemlooy@northumbria.ac.uk</p>

Editorial Board (Continued)

	<p style="text-align: center;">Editorial Board</p> <p>Prof. Mahdi Tavakoli University of Alberta, Alberta, Canada <i>Robotics and Telerobotics, Haptics and Teleoperation Control, Surgical and Therapeutic Robotics, Image-Guided Surgery</i> mahdi.tavakoli@ualberta.ca</p>		<p style="text-align: center;">Editorial Board</p> <p>Prof. Mohamad Hassan Modir Shanechi Illinois Institute of Technology, Chicago, USA <i>Nonlinear and intelligent systems, Power system dynamics and security, Power system planning and maintenance scheduling</i> shanechi@iit.edu</p>
	<p style="text-align: center;">Editorial Board</p> <p>Prof. Mohammad Shahidehpour Illinois Institute of Technology, Chicago, USA <i>Power Systems, Microgrids, Power System Operation, Power System Planning</i> ms@iit.edu</p>		<p style="text-align: center;">Language Editor</p> <p>Majid Sadeghzadeh Hemayati <i>English Language Editing</i> m_s_hemayati@yahoo.com</p>
		<p style="text-align: center;">Page Designer</p> <p>Dr. Mahyar Abasi Shahid Chamran University of Ahvaz, Ahvaz, Iran mahyarabasi1368@yahoo.com</p>	

About Journal

Journal of Applied Research in Electrical Engineering (J. Appl. Res. Electr. Eng.) is a single-blind peer-reviewed, **open access** and **free of charge** international journal published by Shahid Chamran University of Ahvaz in cooperation with Iranian Association of Electrical and Electronics Engineers (IAEEE). The JAREE is a medium for global academics to exchange and spread the latest discoveries and advances in their applied research in electrical engineering. The JAREE aims at presenting important results of analytical, computational and experimental works within all specialized fields of electrical engineering (electronics, power, control and telecommunications). It welcomes high quality original research papers from contributors throughout the world. All papers are subject to a peer reviewing procedure. Submission, processing and publication of the papers in JAREE is **free of charge**.

Types of accepted papers include:

- Research articles
- Review articles
- Applied articles

Research papers are expected to present innovative solutions, novel concepts, or creative ideas that can help to address existing or emerging technical challenges in electrical engineering.

Application papers are expected to share valuable industry experiences on dealing with challenging technical issues, developing/adopting new standards, applying new technologies or solving complex problems. JAREE welcomes application papers that can have a significant impact on industry practices in the coming years.

Review papers are expected to provide insightful and expert reviews, tutorials, or study cases on an important, timely and widely-interested topic in electrical engineering.

All researchers in the fields of electrical science are invited to publish their scientific and research achievements in this journal. Interested authors can submit their manuscripts in the journal's website. More information is available in the website on how to prepare and submit the manuscripts.

Amis and Scope

The *Journal of Applied Research in Electrical Engineering* aims to provide a medium for dissemination of innovative and consequential papers that present analytical, computational and experimental works within all specialized fields of electrical engineering (electronics, power, control and telecommunications). The scope of the journal includes, but is not limited to, the following topic areas:

Electronics:

- Optical electronics, photonics and solar cells
- Integrated analog circuits and mixed signals
- Integrated radio frequency circuits
- Digital electronics (VLSI)
- Semiconductor devices
- Sensor technology

Power:

- Dynamics and stability of the power systems
- Power system protection
- Electric power quality
- Operation and planning of the power systems
- High voltage insulation technology
- Flexible AC Transmission Systems (FACTS)
- Electric power distribution systems
- Smart grids, micro-grids, renewable energies and distributed generation
- Reliability of electrical energy systems
- Energy management and electricity market
- Electric machines and transformers
- Power electronic and electric drives

Control:

- Linear and non-linear control systems
- Adaptive, optimal and stochastic control
- Fuzzy systems, neural networks and intelligent control
- Robotic and mechatronic
- Modeling, Identification and optimization of systems
- Guidance and navigation systems
- Automation, industrial control and instrumentation

Telecommunications:

- Signal and image processing
- Wireless and cellular communication systems
- Telecommunication networks
- Radar and sonar
- Information theory and coding
- Cognitive radio
- Antenna design
- Microwave devices
- Wave propagation and electromagnetic compatibility

Indexing Databases and Social Networks

Directory of Open Access Journals (DOAJ):

<https://doaj.org/toc/2783-2864>

Google Scholar:

<https://scholar.google.com/citations?user=F7KQPtYAAAAJ&hl=en&authuser=1>

Directory of Open Access Scholarly Resources (ROAD):

<https://portal.issn.org/resource/ISSN/2783-2864>

LinkedIn:

<https://www.linkedin.com/in/journal-of-applied-research-in-electrical-engineering-jaree-7540871b2/>

Academia:

<https://shahidchamranahwaz.academia.edu/JournalAppliedResearchinElectricalEngineering>

Mendeley:

<https://www.mendeley.com/profiles/journal-of-applied-res-in-electrical-engineer/>

Twitter:

https://twitter.com/jaree_scu

Facebook:

<https://www.facebook.com/jaree.scu>

Researchgate:

https://www.researchgate.net/profile/Jaree_Engineering

Telegram:

<https://t.me/jareescu>

Instagram:

<https://www.instagram.com/jaree.scu/>

Journal homepage:

<http://jaree.scu.ac.ir>

Journal emails:

jaree@scu.ac.ir, jaree.scu@gmail.com

Guide for Authors

How to submit a manuscript

For the initial submission, the authors have to just send the main manuscript file and the signed [Copyright Form](#) of the journal. While preparing manuscripts for initial submission, authors are kindly requested to follow the guidelines, described below:

- The manuscript should be written in a Microsoft Word file (.doc or .docx).
- The file should include text (preferably in 10 points, “Times New Roman” font) and all figures (figures can be placed within the text at the appropriate point or at the end of the text).
- The manuscript pages should be prepared either using a double-column single-line spacing layout or a single-column double-line spacing layout. A margin of at least 1.5 cm on each side is required.
- All papers should be composed of Title, Author Name, Affiliation, Corresponding author email, Abstract, Keywords, Body, and References.
- The manuscript should be written in good English. It should have been carefully checked for clarity, conciseness, the correctness of grammar, and typographical errors.
- The corresponding author should sign the journal copyright form on behalf of any and all co-authors and upload it to the Journal’s Submission System when submitting the manuscript. The journal copyright form can be downloaded from [here](#).
- The corresponding author can use the [JAREE Template for Cover Letter](#) as a default text for the cover letter when submitting the manuscript.
- It is recommended that the title of the paper does not contain abbreviations or formulae.
- The abbreviations used in the abstract should be introduced both in the abstract and again on first use in the body.
- References should be numbered in the order they are mentioned in the text.

Manuscript Submission

Submission to this journal proceeds totally online and you will be guided stepwise through the creation and uploading of your files. All correspondence, including notification of the Editor's decision and requests for revision, takes place by e-mail. To submit your manuscript, click on the [Submit Manuscript](#) link on the journal's homepage. Then, click on [Register](#) to create an author account. A message is sent to your email address containing your username and password. Then, login to the Journal’s Submission System at the [User's login](#) page using the username and password to submit your new manuscript. Once you have logged in, you can change your password by clicking on the My Home link at the top menu.

Copyright and Open Access License

An author submitting a paper should ensure that he or she has the right to publish the paper and that it contains nothing defamatory. The JAREE will assume that all co-authors have agreed to the submission of any paper received. The corresponding author should sign the journal copyright form on behalf of any and all co-authors and upload it to the Journal’s Submission System when submitting the manuscript.

Contents

Article Title and Authors	Page No.
RTWSM: Real-Time Ad Hoc Wireless Sensor System Monitoring of Local Air Particle Pollution Reza Ghanavati, Yousef Seifi Kavian, and Abdolnabi Kosarian	112
Reactive Power Coordination Between Solid Oxide Fuel Cell and Battery for Microgrid Frequency Control Saeed Aminzadeh, Mehrdad Tarafdar Hagh, and Heresh Seyedi	121
On the Cramer-Rao Lower Bound Based Analysis of Direct Position Determination and DOA Position Finding for Co-Channel Emitter Localization Ali Eshkevari, and Seyed Mohammad Sajad Sadough	131
Influence of Gas Insulated Switchgear Configuration Components on UHF PD Signals Reza Rostaminia, Mehdi Vakilian, and Keyvan Firuzi	139
Optimal Switch Placement in Radial Distribution Networks to Reduce Energy Loss and Improve Network Security in Khuzestan Province Conditions Ali Rouhipour, Elaheh Mashhour, and Mohsen Saniei	149
A New Approach for the Transformer Differential Protection Based on S-Transform and Fuzzy Expert System Saeid Hasheminejad	159
Investigating the Effects of Phosphorene Nanotubes (PNTs)-on-Gold Substrates on the Enhancements of the Sensitivity of SPR Biosensors Amir Davami, and Mohammad Hadi Shahrokh Abadi	169
Designing of the Controller for Shipboard Microgrid Based on Linear Matrix Inequality Farhad Amiri, and Mohammad Hassan Moradi	175
Energy Management in Distribution Systems Considering Consumer Behavior and Internet of Things Moaiad Mohseni, Mahmood Joorabian, and Afshin Lashkarara	186
Design of Tunable Low-Power Band-Stop Filter for Elimination of 50 Hz Power-Line Noise Amirreza Solaymanpour, and Shahbaz Reyhani	197
A Novel 2-D BWA-MEM FPGA Accelerator for Short-Read Mapping of the Whole Human Genome Mahdi Taheri, and Ali Mahani	203
A Fourth-order MASH DDSM for Accurate Fractional Frequency Synthesizers Seyed Ali Sadatnoori	211

Copyrights

© 2022 Licensee Shahid Chamran University of Ahvaz, Ahvaz, Iran. This article is an open-access article distributed under the terms and conditions of the Creative Commons Attribution –Non-Commercial 4.0 International (CC BY-NC 4.0) License (<http://creativecommons.org/licenses/by-nc/4.0/>).





Iranian Association of
Electrical and Electronics
Engineers

Journal of Applied Research in Electrical Engineering

E-ISSN: 2783-2864

P-ISSN: 2717-414X

Homepage: <https://jaree.scu.ac.ir/>



Research Article

RTWSM: Real-Time Ad Hoc Wireless Sensor System Monitoring of Local Air Particle Pollution

Reza Ghanavati^{ID}, Yousef Seifi Kavian^{*ID}, Abdolnabi Kosarian^{ID}

Department of Electrical Engineering, Faculty of Engineering, Shahid Chamran University of Ahvaz, Ahvaz 61357-85311, Iran

* Corresponding Author: y.s.kavian@scu.ac.ir

Abstract: The ever-increasing threat of air pollution as a serious health hazard throughout the world requires measuring prior to devising a structured solution. Air quality monitoring systems measure the amount of particulate matter such as particles and hazardous gases in the air. Information is required on the quality of air monitoring and dust detection system in order to make managerial decisions to improve environmental conditions and prevent and treat diseases caused by dust. The present study aims to develop a simple, highly sensitive, and economical monitoring system for the determination of air particulate. In this paper, we develop a real-time ad hoc wireless airborne particle monitoring system using the IEEE 802.15.4 low power sensor network technology called RTWSM, featuring a low-cost sensor node for mass production. Its dynamic features of high scalability and ad hoc architecture enable the design to provide significantly more useful information under all environments, including indoor or outdoor monitoring applications. The performance of the proposed monitoring sensor system is evaluated in environmental and industrial occupation debates to monitor the PM_{2.5} particle data. The results confirm that the proposed experimental setup works well for local air pollution monitoring and could be extended to automation industrial applications.

Keywords: Wireless sensor networks, air particle monitoring, PM 2.5, experimental setup, IEEE 802.15.4.

Article history

Received 15 April 2021; Revised 11 July 2021; Accepted 14 August 2021; Published online 14 December 2021

© 2021 Published by Shahid Chamran University of Ahvaz & Iranian Association of Electrical and Electronics Engineers (IAEEE)

How to cite this article

R. Ghanavati, Y. S. Kavian, A. Kosarian, "RTWSM: real-time ad hoc wireless sensor system monitoring of local air particle pollution," *J. Appl. Res. Electr. Eng.*, vol. 1, no. 2, pp. 112-120, 2022. DOI: [10.22055/jaree.2021.37159.1027](https://doi.org/10.22055/jaree.2021.37159.1027)



1. INTRODUCTION

Nowadays, wireless sensor networks (WSNs) and the Internet of Things (IoT) are mature enough to be employed in extreme environmental condition monitoring and controlling applications such as harsh weather condition monitoring [1-3]. The wireless sensor networks consist of some small, low-power, and low-cost sensor nodes that communicate together wirelessly to transmit the collected and processed data from the environment [4]. WSNs have ad hoc architecture with the potential of the easy deployment of hundreds to thousands of sensors to cover the monitoring areas, which makes them a suitable solution for air pollution monitoring applications in difficult-to-access environments.

According to the World Health Organization (WHO), air pollution is one of the most important human health risks that should be considered in modern smart city systems. Some of the air quality parameters that should be measured are carbon dioxide, methane, dust particles, ozone, nitrogen dioxide, sulfur dioxide, and hydrogen sulfide [5]. These items are not

concentrated in normal conditions, but in many cases, the air is out of normal conditions, and some parameters of air pollution are increased dramatically. One of these cases is dust storms in which the size of particulate matter increased heavily. The correct prediction of dust storms is difficult in many cases.

The technology of air pollution monitoring systems is not advanced and widespread enough to allow globally predicting air quality at a country level. Consequently, there is an essential need for local air quality monitoring in different places of cities such as parks, hospitals, and schools. Monitoring systems measure the concentration of air pollutants that can be analyzed and interpreted. Then, the information is used for decision-making in different applications. For example, analyzing the data from the monitoring system allows more accurate geographical assessments, such as where the air quality is better and where it is weaker or in which areas the condition is improving and where is getting worse. The information is utilized to understand how pollution increases by traffic or industrial

activities. By analyzing the relationship between meteorology and air quality, it can be predicted whether the weather conditions cause contamination [6]. Low air quality may increase short-term health problems, such as fatigue and nausea, as well as chronic respiratory disease, heart disease, and lung cancer. Governments can take advantage of the monitoring system data from WSNs to make the right planning and decisions. Also in emergency situations, they can take useful actions such as sending relief teams, and people can use the information to manage their everyday activities [7, 8].

The sensor networks have enough potentials to meet the requirements of air pollution monitoring applications. Furthermore, clustering schemes are used in sensor networks to geographically gather local data for monitoring applications [9]. This paper presents the design and implementation of WSNs for monitoring the status of air parameters.

The remainder of the paper is organized as follows: the related works are described and discussed in Section 2. The hardware architecture and designing issues are explained in Section 3. Section 4 presents the experimental results. Finally, conclusions are made in Section 5 along with suggestions for future works.

2. RELATED WORKS

This section describes the applications of WSNs for air pollution monitoring schemes. The results as to the development of a WSN to monitor air quality in smart city programs are described in [5]. It is implemented to test the system in two cities to compare the concentration of CO₂ with airborne particles. The preliminary results indicate that the developed wireless system may be used as a low-cost tool to monitor air pollution. In [6], a new type of outdoor air quality monitoring system is studied and preliminarily practiced and has proven certain feasibility and applicability. The experimental results show that the prediction model has strong applicability and high accuracy in the period prediction of pollution weather. It is established that air pollution in the city is mainly caused by the manufacturing industry. In [7], the authors focus on using WSN for air pollution mapping and tackle the optimization problem of sensor deployment using the integer linear programming model. An appropriate coverage formulation based on an interpolation formula that is adapted to the characteristics of air pollution sensing is developed. Two deployment models are derived for air pollution mapping using integer linear programming while ensuring the connectivity of the network and taking into account the sensing error of nodes. A real-time cognitive WSN system is presented in [8] for carbon dioxide monitoring in a complex indoor environment. Moreover, the system coexists with minimum interference with other systems in the monitoring area. A prototype is designed to show the enhanced real-time data transmission. Experiments are conducted to validate and support the development of the system for real-time monitoring and alerting. In [10], the paper describes the application of WSNs and IoT for monitoring the main pollutants that determine Santander City's air quality in Spain by analyzing how event-based sampling techniques can address efficient communication between nodes and a reduction in each node's power

consumption. To meet the requirements of data acquisition from mobile pollution sources and unfixed data acquisition points in an atmospheric particle monitoring system, a real-time monitoring system is designed in [11] for atmospheric particles such as PM_{2.5} based on a single-chip microcomputer, an ET-iLink open cloud platform, and an Android operating system. A distributed real-time monitoring system for atmospheric particles has been designed, implemented, and tested in [12]. The proposed system consists of a front-end data wireless acquisition network, an embedded web server system, a central server, and remote monitoring terminals. In this study, the PM_{1.0}, PM_{2.5}, and PM₁₀ particle data were successfully collected, transmitted, and checked by the monitoring system.

The primary contribution of [13] is to design a low-power ZigBee sensor network and inter-node data reception control framework to be used in real-time acquisition and communication of data concerning air pollutant levels from volatile organic compounds (VOCs). The design is based on the ATmega16 microcontroller and the Atmel RF230 ZigBee module, which are used to effectively process communication data with low power consumption. Indoor air quality and energy conservation can be achieved by integrating the VOC monitoring system proposed. A system for monitoring and forecasting urban air pollution is presented in [14]. The system uses low-cost air-quality monitoring motes that are equipped with an array of gaseous and meteorological sensors. The research in [15] focuses on a network of low-cost and autonomic wireless sensors, aiming at a finer spatiotemporal granularity of sensing. The main contribution is to design integer linear programming models that compute sensor deployments capturing both the coverage of pollution under time-varying weather conditions and the connectivity of the infrastructure. The work in [16] describes the design and evaluation of a low-cost participatory sensing system called Haze Watch that uses a combination of portable mobile sensor units, smartphones, cloud computing, and mobile apps to measure, model, and personalize air pollution information for individuals. In [17], a method is presented for data reduction through a dynamic sub-sampling of the measured variable, data fusion from several sensors for the same variable, and data scaling taking into account the ranges of the variables. The reduction of data is implemented to save energy, reduce the transmission time, keep the channel available, and save storage space. A WSN is examined in [18] for distribution in underground coal mines. During the mining operation, the dust that is created is currently measured with manual and laboratory samples. But, with the proposed system, the status of these particles is visible at any moment. A trial version of the wireless air sensor network system is presented in [19] for monitoring and predicting air quality in the 3D area. The system distributes 200 PM_{2.5} sensors in two-dimensional space and measures a PM_{2.5} parameter at different altitudes using an unmanned airplane with a similar sensor. In [20], a collaborative system is proposed that is composed of a WSN and an air robot that is used to monitor frost in vineyards. In this way, farmers can promote their farms and crops in their own style from a completely new perspective. Design and implementation of a complete WSN platform are presented in [21], which can use a wide range of IoT applications for long-term environmental monitoring. In [22], a method is proposed for gas concentration detection

based on the WSN and laser technologies. In [23], airborne particles are measured in urban environments using WSN and the frequency of their changes is analyzed. In [24], a WN is used to monitor air pollution. In [25], a WSN is implemented in a poultry farm to monitor temperature, humidity, and air quality.

3. HARDWARE ARCHITECTURE

This section introduces the structure of the implemented WSN for air pollution monitoring. The implemented network can measure airborne particles, and then each node sends the results to the sink through other relay nodes on the route to the central station. This method uses simple, small, and inexpensive nodes to implement the network. The experimental setup has two parts: measuring the particulate matter and forming the network. These two parts are introduced separately, and the hardware is examined in detail.

3.1. Sensing the Airborne Particles

The HK-A5 sensor is used to measure airborne particulates in micrograms per cubic meter and transmit it to a controller through a serial port. The PM2.5 dust sensor is a solid particulate concentration sensor that is used to obtain suspended particles in a unit volume with dimensions of 0.3 to 10 microns. Fig. 1 shows the sensor structure diagram.

The PM2.5 sensor uses the theory of laser dispersion, that is, the dispersion of laser radiation into airborne particles so that the scattered light is collected at a particular angle to obtain the dispersion intensity in comparison with the time curve. After collecting data by a microprocessor, the sensor calculates the amount of particulate matter using the relationship between time domain and frequency range by Fourier transform and then, through a series of complex algorithms. The sensor has a small fan that samples the air and measures the amount of particulate matter according to the rules of light distribution. The sensor function is such that it sends a 32-byte packet per second. The power supply required for the sensor has the following specifications. The voltage ripple should be less than 100mV. The power supply voltage stability should be 4.95 ~ 5.05V. The power supply should be more than 1W (5V, 200mA). The upper and lower electric voltage surge needs to be less than 50% of the system power supply voltage. The serial port profile is configured as follows: a port baud rate of 9600 bit/s, none parity bit, one stop bit. The packet length is fixed at 32 bytes.

3.2. Sensor Node and Protocols for Forming the Network

To measure the amount of particulate matter in the air by the WSN, IEEE802.15.4 is considered as the MAC protocol

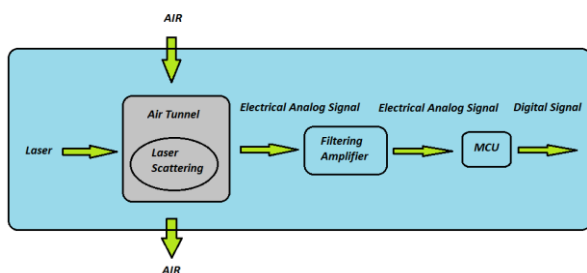


Fig. 1: The sensor structure block diagram [26].

and the sensor boards are designed to support the ZigBee protocol [27]. The IEEE 802.15.4 standard for short communications in low power sensor networks is designed to be used in the frequency bands of 868 MHz, 915 MHz, and 2.45 GHz and is supported by many scientific and commercial sensor nodes. Data transfer rates are 20, 4, and 250 kbs. The sensor boards operate at 2.4 GHz frequency and have low power consumption. The ATMEGA128L microcontroller from ATMEL Company has been used as the processing unit [28]. ATMEGA128L can be programmed by the TinyOS operating system. The sensor boards provide network and analog and digital IOs, I2C, SPI, and UART interfaces, which can be connected to external side devices and different sensor boards. The CC2420 radio is used as the transmitter/receiver in the sensor boards for wireless communication. The CC2420 radio has a data rate of 250 kbs and operates on a 2400-2485.5 MHz frequency band. Additionally, this antenna is resistant to RF interference and has an automatic data security system. The range of the radio in ideally nominative mode is suited for an open environment of 75-100 meters and in a closed environment of 20 to 30 meters. Fig. 2 shows the designed sensor board. The nesC language is used to program sensor boards. This language is, in fact, the same as language C, which has added new language features for creating and using components, as well as creating a kind of parallel processing. The codes written in nesC language are made by the TinyOS operating system and are installed on the sensor boards.

4. EXPERIMENTAL RESULTS

The results of using the WSN to measure dust and airborne particles are provided in this section. Particulate matter graphs are presented for different case studies.

4.1. The RTWSM in the Park

In this case, the real-time ad hoc wireless sensor system monitoring (RTWSM) is employed to monitor the air particulate matter in the Petrochemical Park of Mahshahr City. Nine nodes are used to cover the park area as shown in Fig. 3a. The nodes with identification numbers of 1 to 3



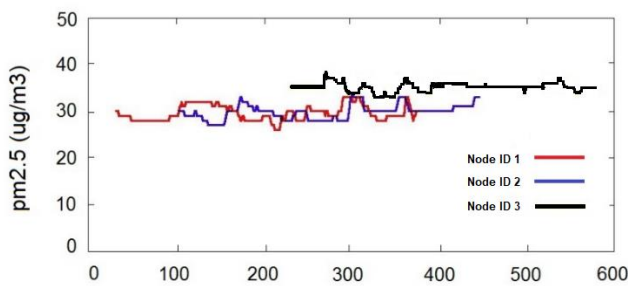
Fig. 2: The designed sensor board.



(a)



(b)



(c)

Fig. 3: The RTWSM in the park, (a) The location of the nodes in the park, (b) The location of the base station, (c) The concentration of the measured PM2.5 in the park.

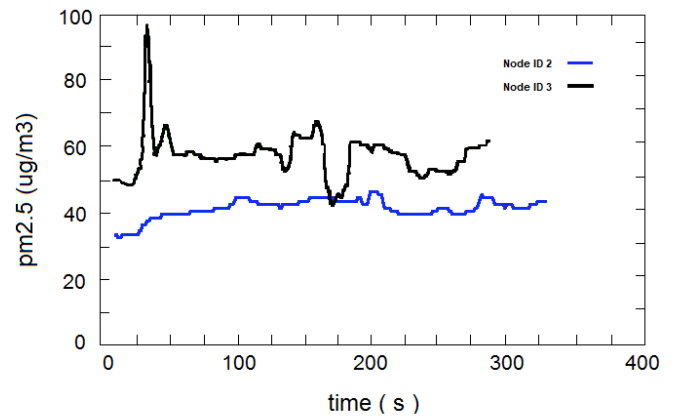
measure air particulate matter using dust sensors and nodes with numbers 4 to 8 acting as relays. Node number 500 is the central station that is connected to a laptop to capture and analyze data as shown in Fig. 3b. The results of measuring the air particulate matter by node numbers 1 to 3 are displayed in Fig. 3c. The graphs show that the airborne particle fluctuates between 25 and 40 $\mu\text{g}/\text{m}^3$.

4.2. The RTWSM in the City Center

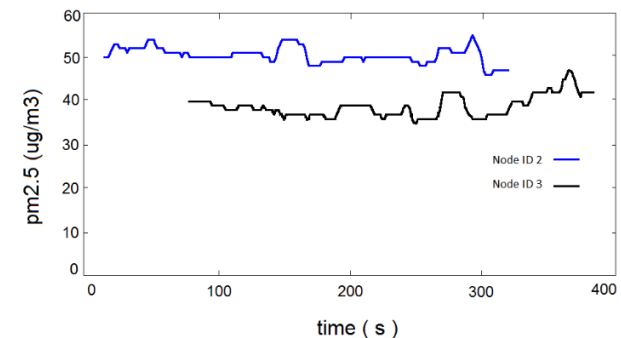
The RTWSM is used to measure particulate matter in the city center in two different places: the central square of the city and the indoor taxi and bus stations that are close to each other. The purpose of this case study is to examine the



(a)



(b)



(c)

Fig. 4: The RTWSM in the city center, (a) The RTWSM in the taxi and bus station, (b) The concentration of the measured PM2.5 in taxi and bus station, (c) The Concentration of the measured PM2.5 in the central square of the city.

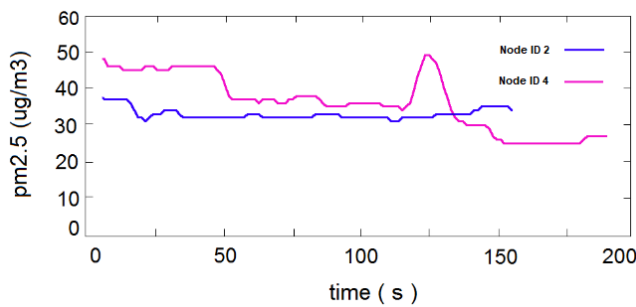
status of particulate matter in the city center, which is mainly traffic-intensive, and to investigate the effect of the indoor station on the city air pollution. However, it is important to note that the ceiling of the station has a high altitude and the air flows from four sides. Meanwhile, the weather at the time of the experiment was rainy and windy. Fig. 4a shows the taxi and bus stations in which RTWSM is installed for condition monitoring. In the network, two nodes with identification numbers 2 and 3 are used to measure the particulate matter, and a node is used as a relay to the central station. As shown in Fig. 4b, the graphs fluctuate between 40 to 60 $\mu\text{g}/\text{m}^3$ and the graphs reach the 100 $\mu\text{g}/\text{m}^3$ point when the buses get close to the sensor nodes.



(a)



(b)



(c)

Fig. 5: The RTWSM in the petrochemical desalination ponds, (a) The location of petrochemical desalination, (b) The sensor node in petrochemical desalination, (c) The concentration of the measured PM2.5 in petrochemical desalination ponds.

Fig. 4c shows the concentration of PM2.5 in the central square of the city where there is usually traffic around the square. As was mentioned above, it was rainy and winding during the experiment. Comparing Fig. 4b with Fig. 4c, it is concluded that in spite of the distance between the taxi and bus station and the central square of the city, the suspended particles in the taxi and bus station is greater than those in the central square due to being surrounded indoor.

4.3. The RTWSM for Measuring the Particulate Matter in Petrochemical Desalination Ponds (Salt Lake)

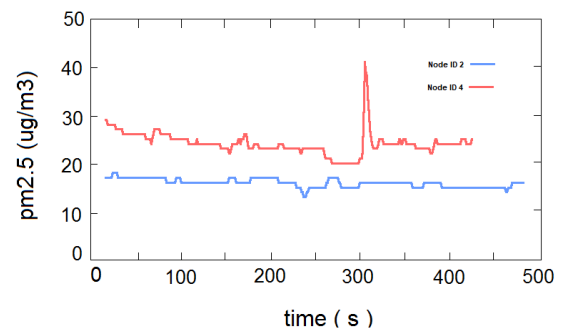
Fig. 5a shows the location of petrochemical desalination ponds between Mahshahr and Sarbandar cities. They are closer to Mahshahr. The lands around these ponds are also used as an amusement park for the public. The RTWSM was used to measure particulate matter in the area on the same day that the WSN was conducted in the central square of the city



(a)



(b)



(c)

Fig. 6: The RTWSM in the recreational sea coast port, (a) The location of the coast of the port, (b) The location of the distributed nodes, (c) The concentration of the measured PM2.5 in the coast of the port.

and the taxi and bus station. The graphs show that the difference is small, and this slight difference indicates that the particulate matter around the salt lake is lower than that in the city center. Fig. 5b shows the RTWSM wireless sensor node in the desalination ponds of Mahshahr petrochemical plants. Fig. 5c displays the particulate matter graph in these ponds.

4.4. The RTWSM for Measuring the Particulate Matter in the Recreational Sea Coast Port

The RTWSM was configured on days after rain with a clear sky and clear air. The RTWSM was employed on the same day that the sensor network was configured around petrochemicals. The airspace between this beach and the petrochemicals is about three kilometers. Fig. 6a shows the location of the distributed nodes. Fig. 6b shows the dust graphs of the two nodes that measure the dust.

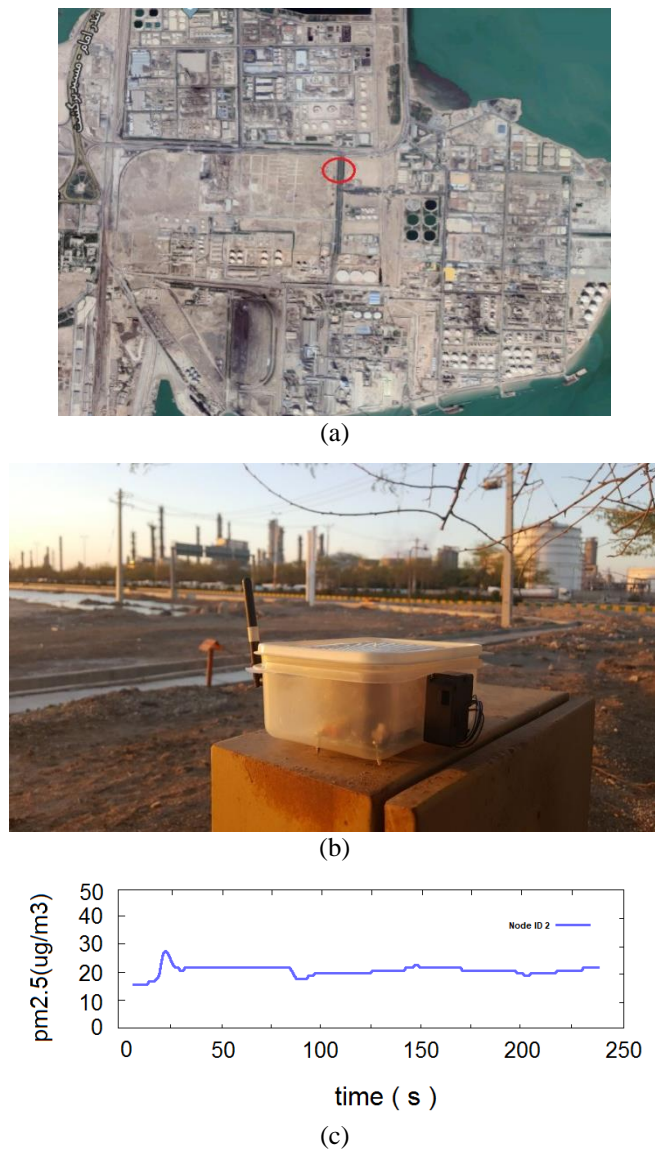


Fig. 7: The RTWSM for measuring particulate matter in the industrial petrochemical zone, (a) The location of the sensor node installed between Imam Petrochemical Complex and Razi Petrochemical Complex and the special economic zone, (b) The sensor node installed in the site, (c) The concentration of measured PM2.5 between Imam Petrochemical Complex and Razi Petrochemical Complex.

4.5. The RTWSM for Measuring the Particulate Matter in an Industrial Petrochemical Zone

Fig. 7a shows the location of the node installed between Imam Petrochemical Complex and Razi Petrochemical Complex and the special economic zone with a red mark. Fig. 7b displays the node installed on the site and Fig. 7c depicts the airborne particle graphs. This chart is for the days after rain with a clear sky and clear air.

4.6. Investigation of Particulate Matter in the Industries

Some occupations in the construction industry are examined in this section for the amount of particulate matter and the relative duration that the people involved in these occupations contact with dust and smoke – occupations like welding, carpentry, and stonework that all are linked to dirt

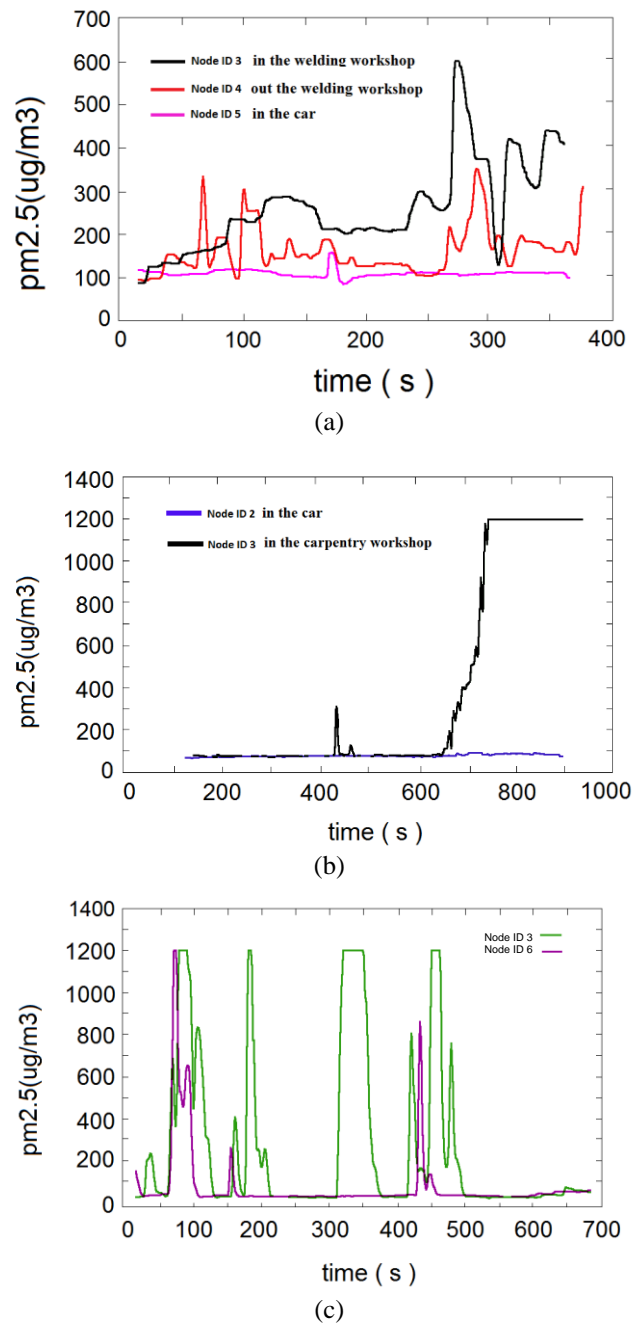


Fig. 8: The RTWSM for investigation of particulate matter in the industries, The concentration of PM2.5 at (a) the welding workshop, (b) the carpentry workshop, and (c) the stonework.

or smoke. The welding industry produces suspended particles due to the use of cutting machines. It also produces smoke due to the use of welding devices. Due to the volume of welding, smoke is produced. Fig. 8a shows dust and smoke charts in a welding workshop. As shown in Fig. 8a, in this experiment, the smoke rate reached $600 \mu\text{g}/\text{m}^3$. According to people working in the workshop, this test was not carried out at the peak of the work. In cases where more welding is performed, the smoke also increases.

Woodworking also emits particles into the air due to the use of cutting machines. The RTWSM sensor node was installed at a carpentry workshop. Fig. 8b displays dust graphs at the carpentry workshop. The graph shows that the

largest amount measured by the dust sensor is $1200 \mu\text{g}/\text{m}^3$, and this is the highest amount that this network can measure.

Comparing the charts of the welding workshop and the carpentry workshop, it is clear that the amount of dust in the carpentry is greater during cutting. But, the duration of exposure to this smoke and dust is longer in welding because the welder always has to either weld or cut, but the carpenter takes a while to work with a nail and a hammer and a glue that does not produce a lot of dust .

The WSN, in this section, was implemented along with the mosaic workers. Tessellation and stonework are jobs that at times need cutting rocks to adjust their size, and this creates intense dust and the person who makes the cuts is close to the dust and cannot get away from it at work .Now, if the cutting is done in an open space, the dust will disappear a few moments after cutting, but if the cutting is done in a closed space, this dust will last longer with the workers in this part of the construction industry. Here, we also tried to place the sensor in the same place where the person was. Fig. 8c shows the dust graphs during cutting. It is clear that in certain parts that are repeated frequently, the graphs reach their highest value, $1200 \mu\text{g}/\text{m}^3$, indicating the working time with a stone cutting machine.

4.7. Comparison of Experiments

For comparison, Table 1 presents the results of experiments in different locations where RTWSM was installed. As is evident, the measured PM2.5 varies in different places. The lowest airborne particles were measured in the industrial petrochemical area because this experiment was for the days after rain with a clear sky and clear air. The highest measured airborne particles were found in the industry.

5. CONCLUSION

An ad hoc sensor network was developed in this paper for real-time wireless monitoring of air particulate matter called RTWSM. The RTWSM was employed in dusty days, clean days, and after a foggy day in different parts of the city such as recreational and coastal parks and industrial areas including petrochemicals, as well as the building occupations that drains dust; and the related graphs were provided. The experiments show that the RTWSM, a low-cost tool for monitoring particulate matter, is scalable and can be used in the environmental debate and in the industrial occupations debate to monitor air particulate matter. Finally, it is proposed to study the application of a new platform

with a wider range for meteorological debate in future work. Furthermore, research is proposed to be conducted on preparing a network for installation in industrial environments and communicating with controllers by supporting analog 4-20 mA signals as a measure of air pollution.

ACKNOWLEDGMENT

This work was supported by Shahid Chamran University of Ahvaz under Grant Number 98/3/05/14909.

CREDIT AUTHORSHIP CONTRIBUTION STATEMENT

Reza Ghanavati: Conceptualization, Data curation, Formal analysis, Methodology, Software, Validation, Roles/Writing - original draft. **Yousef Seifi Kavian:** Conceptualization, Methodology, Project administration, Supervision, Writing - review & editing. **Abdolnabi Kosarian:** Conceptualization, Conceptualization, Conceptualization.

DECLARATION OF COMPETING INTEREST

The authors declare that they have no known competing financial interests or personal relationships that could have appeared to influence the work reported in this paper. The ethical issues; including plagiarism, informed consent, misconduct, data fabrication and/or falsification, double publication and/or submission, redundancy has been completely observed by the authors.

REFERENCES

- [1] H. Fuentes, and D. Mauricio, "Smart water consumption measurement system for houses using IoT and cloud computing," *Environmental Monitoring and Assessment*, vol. 192, no. 602, pp. 1-16, 2020.
- [2] D. R. Schoolmaster, and S. C. Piazza, "Using maintenance records from a long-term sensor monitoring network to evaluate the relationship between maintenance schedule and data quality," *Environmental Monitoring and Assessment*, vol. 192, no. 54, 2020.
- [3] H. F. Rashvand, and A. Abedi, *Wireless sensor systems for extreme environments: space, underwater, underground, and industrial*. Wiley: 2017.
- [4] H. R. Sharif and Y. S. Kavian, *Technological breakthroughs in modern wireless sensor applications*. IGI Global: 2015.
- [5] B. Guanochanga, R. Cachipuendo, W. Fuertes, DS. Benítez, T. Toulkeridis, J. Torres, and F. Meneses, "Towards a real-time air pollution monitoring systems implemented using wireless sensor networks: preliminary results," in *IEEE Colombian Conference on Communications and Computing (COLCOM)*, May 2018, pp. 1-4.
- [6] Q. Han, P. Liu, H. Zhang, and Z. Cai, "A wireless sensor network for monitoring environmental quality in the manufacturing industry," *IEEE Access*, vol. 7, pp.78108 – 78119, 2019.

Table 1: Comparison of experiments

Location of RTWSM	PM2.5 Measured ($\mu\text{g}/\text{m}^3$)
Park	between 25 and 40
City Centre	between 30 and 100
Petrochemical Desalination Ponds	between 20 and 50
Recreational Sea Coast Port	between 15 and 42
Industrial Petrochemicals Zone	between 15 and 30
Industries (welding workshop, carpentry workshop, stonework)	between 30 and 1200

- [7] A. Boubrima, W. Bechkit, and H. Abraham, "On the deployment of wireless sensor Networks for Air quality mapping: optimization models and algorithms," *IEEE/ACM Transactions on Networking*, vol.27, no. 4, pp. 1629-1642, 2019
- [8] P. Spachos, and D. Hatzinakos, "Real-time indoor carbon dioxide monitoring through cognitive wireless sensor networks," *IEEE Sensor Journal*, vol.16, no.2, pp. 506-514, 2016.
- [9] S. Siavoshi, Y. S. Kavian, M. Tarhani, and H. F. Rashvand, "Geographical multi-layered energy-efficient clustering scheme for ad hoc distributed wireless sensor networks," *IET Wireless Sensor Systems*, vol. 6, no. 1, pp. 1-9, 2016.
- [10] C. Santos, JA. Jiménez and F. Espinosa, "Effect of event-based sensing on IoT node power efficiency. case study: air quality monitoring in smart cities," *IEEE Access*, vol.7, pp. 132577-132586, 2019.
- [11] L. Bao, "Cloud connection oriented real-time monitoring system for atmospheric particles," *IET Wireless Sensor Systems*, vol.10, no.1, pp. 31-36, 2020.
- [12] L. Bao, and H. Wang, "Distributed real-time monitoring system for atmospheric particles," *IET Wireless Sensor Systems*, vol. 7, no.4, pp. 91-97, 2017.
- [13] C. Peng, K. Qian, and C. Wang, "Design and Application of a VOC Monitoring System Based on a ZigBee Wireless Sensor Network," *IEEE Sensors Journal*, vol.15, no.4, pp. 2255-2268, 2015.
- [14] K. B. Shaban, A. Kadri, and E. Rezk, "Urban Air Pollution Monitoring System with Forecasting Models," *IEEE Sensors Journal*, vol. 16, no.8, pp. 2598-2606, 2016.
- [15] A. Boubrima, W. Bechkit, and H. Rivano, "Optimal WSN deployment models for air pollution monitoring," *IEEE Transactions on Wireless Communications*, vol.16, no.5, pp. 2723 – 2735, 2017.
- [16] K. Hu, V. Sivaraman, B. G. Luxan, and A. Rahman, "Design and evaluation of a metropolitan air pollution Sensing System," *IEEE Sensors Journal*, vol. 16, no.5, pp. 1448-1459, 2016.
- [17] J. Botero-Valencia, L. Castano-Londono, D. Marquez-Viloria, and M. Rico-Garcia, "Data reduction in a low-cost environmental monitoring system based on LoRa for WSN," *IEEE Internet of Things Journal*, vol. 26, no.2, pp. 3024-3030, 2019.
- [18] O. Mahdavi-pour, et. al., "Wireless sensors for automated control of total incombustible content (TIC) of dust deposited in underground coal mines," in *2015 IEEE Sensors*, Busan, Korea (South), 2015, pp. 1-4.
- [19] Y. Yang, Z. Bai, Z. Hu, Z. Zheng, K. Bian, and L. Song, "AQNet: Fine-grained 3D spatio-temporal air quality monitoring by aerial-ground WSN," in *2018 IEEE Conference on Computer Communications Workshops (INFOCOM WKSHPS)*, Honolulu, HI, USA, 2018, pp. 1–2.
- [20] J. Valente, D. Sanz, A. Barrientos, J. D. Cerro, A. Ribeiro, and C. Rossi, "An air-ground wireless sensor network for crop monitoring," *Sensors*, vol. 11, no.6, pp. 6088-6108, 2011.
- [21] M. T. Lazarescu, "Design of a WSN platform for long-term environmental monitoring for IoT applications," *IEEE Journal on emerging and selected topics in circuits and systems*, vol.3, no.1, pp. 45-54, 2013.
- [22] T. Yefei, and L. Ruijin, "Gas concentration detection based on WSN & laser technology," in *2021 Asia-Pacific Conference on Communications Technology and Computer Science (ACCTCS)*, Shenyang, China, 2021, pp. 324-326.
- [23] G. R. Espinosa, B. Montrucchio, F. Gandino, and M. Rebaudengo, "Frequency analysis of particulate matter in urban environments under low-cost sensors," in *2021 International Conference on Computer Communication and Artificial Intelligence (CCAI)*, Guangzhou, China, 2021, pp. 97-105.
- [24] M. Godase, and M. K. Bhanarkar, "WSN node for air pollution monitoring," in *2021 6th International Conference for Convergence in Technology (I2CT)*, Maharashtra, India, 2021, pp. 1-7.
- [25] P. Jayarajan, M. Annamalai, V. A. Jannifer, and A. A. Prakash, "IOT Based Automated Poultry Farm for Layer Chicken," In *2021 7th International Conference on Advanced Computing and Communication Systems (ICACCS)*, Coimbatore, India, 2021, pp. 733-737.
- [26] <https://www.componentsmart.pl/datasheets/3f/SEN0177.pdf>, accessed 27 January 2019.
- [27] H. Hadadian, Y. S. Kavian, and A. Mahmoudi, "A Markov model for investigating the impact of IEEE802.15.4 MAC layer parameters and number of clusters on the performance of wireless sensor networks," *Wireless Networks*, vol. 25, no. 7, pp. 4415-4430, 2019.
- [28] M. Hadadian, Y. S. Kavian, and A. Mahmoudi, "On the processing architecture in wireless video sensor networks: node and network level performance evaluation," *Multimedia Tools and Applications*, vol. 78, no.17, pp. 24789-24807, 2019.

BIOGRAPHY



Reza Ghanavati was born in 1989. He received his B.Sc. degree in electronic engineering from Islamic Azad University of Mahshahr, Iran in 2011 and his M.Sc. degree in electrical engineering from Shahid Chamran University of Ahvaz, Iran in 2019. His fields of interest are the design of electronic circuits based on microcontrollers. He is the head of instrumentation in Amirkabir Petrochemical development plans.



Yousef Seifi Kavian is an Associate Professor with the Electrical Engineering Department of Shahid Chamran University of Ahvaz. Dr. Kavian's research interests include networks and embedded systems. He has published four books and 150 technical papers in journals and international conferences. He has over 20 years of industrial experience and collaborations. Dr. Kavian received his B.Sc., M.Sc., and Ph.D., all in electrical engineering, from Shahid Beheshti University, 2001, Amirkabir University, 2003, and Iran University of Science and Technology, 2008, respectively.



Abdolnabi Kosarian was born in Behbahan, Khuzestan, Iran. He received the B.Sc and M.Sc. degrees in electrical engineering from University of Tehran, Tehran, Iran, in 2003 and 2005, respectively, and the Ph.D. degree in electrical engineering from the University of Surrey, Surrey, UK, in 1998. He is presently a Professor with the Department of Electrical Engineering, Shahid Chamran University of Ahvaz, Ahvaz, Iran. His research interests include electronics, especially amorphous silicon solar cells.

Copyrights

© 2021 Licensee Shahid Chamran University of Ahvaz, Ahvaz, Iran. This article is an open-access article distributed under the terms and conditions of the Creative Commons Attribution –Noncommercial 4.0 International (CC BY-NC 4.0) License (<http://creativecommons.org/licenses/by-nc/4.0/>).





Research Article

Reactive Power Coordination Between Solid Oxide Fuel Cell and Battery for Microgrid Frequency Control

Saeed Aminzadeh^{1,2,*} , Mehrdad Tarafdar Hagh^{1,3} , and Heresh Seyedi¹ 

¹ Faculty of Electrical and Computer Engineering, University of Tabriz, 29 Bahman Blvd, Tabriz 51666-16471, Iran

² Engineering Faculty, Islamic Azad University, Ravansar, Kermanshah, Iran

³ Engineering Faculty, Near East University, 99138 Nicosia, North Cyprus, Mersin 10, Turkey

* Corresponding Author: saeed.aminzadeh1363@gmail.com

Abstract: This paper uses the coordination between the reactive power of a solid oxide fuel cell (SOFC) and a battery to control the frequency within an islanded microgrid. By this coordination, the microgrid frequency regulation becomes faster and better during contingencies. Moreover, the energy storage capacity, which is usually required for the frequency control of islanded microgrids, has significantly been reduced. Furthermore, there will be no need to consider reserve capacity in renewable sources for frequency control. Therefore, renewable energy sources can be operated at their maximum power point. Also, this paper introduces a new frequency-reactive power control concept and a related coefficient that shows the degree of dependence of the microgrid frequency on the injected reactive power changes at each bus. This coefficient determines the priority of buses for the installation of reactive power control devices to control the frequency of the microgrid. Simulation studies have been performed in the MATLAB/Simulink environment. The results show the applicability and accuracy of the proposed coefficient and demonstrate the effectiveness of the coordinated control of reactive power between the SOFC and the battery for frequency control.

Keywords: Microgrid frequency control, solid oxide fuel cell (SOFC), coordinated control of reactive power, frequency-reactive power coefficient.

Article history

Received 17 April 2021; Revised 13 August 2021; Accepted 13 August 2021; Published online 23 February 2022

© 2022 Published by Shahid Chamran University of Ahvaz & Iranian Association of Electrical and Electronics Engineers (IAEEE)

How to cite this article

S. Aminzadeh, M. T. Hagh, and H. Seyedi, "Reactive power coordination between solid oxide fuel cell and battery for microgrid frequency control," *J. Appl. Res. Electr. Eng.*, vol. 1, no. 2, pp. 121-130, 2022.

DOI:10.22055/jaree.2021.37177.1028



1. INTRODUCTION

When a microgrid is connected to the upstream grid, the imbalance between the generated power and the consumed power in the microgrid is compensated by the upstream grid. Consequently, the frequency of the microgrid is always equal to the frequency of the upstream grid. However, in the disconnected state, the microgrid loses its powerful support. As a result, a fast balance between the generated power and the consumed power in the microgrid is essential for frequency control. Previous studies in this field have proposed various solutions for frequency control, such as the application of fast-response energy storage devices like batteries, demand response programs, the concepts of virtual synchronous generator and virtual inertia creation, load shedding in emergency cases, and the operation of renewable and sustainable energy resources at points other than

maximum power points. Some relevant works are reviewed below.

References [1-2] investigated the need for energy storage devices and load shedding strategies for the frequency control and the operation of islanded microgrids. Reference [3] studied the influence of the fluctuations in wind and solar radiation on changes in the microgrid frequency. It demonstrated that the fast performance of a battery energy storage system can mitigate this effect on the dynamic operation of the microgrid. A battery energy storage system was proposed in [4-5] to support the frequency control process in a microgrid with high penetration of renewable energy resources. Reference [6] presented a new concept of the primary frequency control by integrating the superconducting magnetic energy storage (SMES) with the battery, which not only allowed performing a good frequency regulating function but also extended the battery service time.

A novel coordinated control scheme using the demand-side management was presented in [7-8] for an islanded microgrid. Reference [9] investigated the impact of load dynamics and load sharing among inverter-interfaced distributed generation units on the frequency stability and the dynamic performance of the islanded ac microgrids. Reference [10] introduced new functions for online execution, which are capable of managing microgrid storage by taking into account the electric vehicles and the load response with the purpose of frequency control. Reference [11] proposed a new load frequency control strategy for microgrids in which electric vehicles are considered. Various centralized and decentralized dynamic load response methods were presented in [12] for controlling the initial frequency in a microgrid. Reference [13] proposed a flexible and effective control scheme for determining the size and location of loads that need shedding in order to maintain frequency within permissible limits. In [14], an auxiliary frequency control loop was added to the synchronous generator excitation system present in a microgrid. Also, an excitation was employed in addition to the governor to control the frequency using the synchronous generators. Reference [15] introduced a hierarchical control structure composed of the primary, secondary, and tertiary controllers to be used in islanded microgrids. Reference [16] presented a multi-level control architecture for the autonomous operation of the islanded microgrids with power electronic interfaces. Virtual inertia control strategies that would contribute to frequency regulation in a microgrid were proposed in [17-20]. Reference [21] presented a novel frequency and voltage control method for islanded microgrids based on a distributed hybrid control. Reference [22] proposed a decentralized control method to stabilize microgrid frequency and voltage and also to distribute generation among the distributed generations. Reference [23] presented a novel control method for the load voltage and system frequency during the islanding of the microgrid for a multi-zone power system composed of several microgrids. A number of control and management strategies were presented in [24] for coordinating microgrid resources to regulate the voltage and frequency in order to operate the microgrid independently and optimally. Reference [25] utilized a novel optimal model-less controller to create a balance between the load demand and the power generation and, as a result, to control the frequency in the islanded microgrid. Reference [26] explored the development of an internal model-based controller approach for better frequency regulation in a hybrid microgrid. In [27], an innovative independent control method was proposed for accurate division of the reactive power among the scattered energy sources and also the frequency recovery of the microgrid. Reference [28] presented a control method for dg's to simultaneously distribute the active power and recover the frequency in an islanded microgrid.

This paper introduces a new frequency-reactive power (FQ) coefficient that shows the degree of dependence of the microgrid frequency on reactive power changes in each bus. The potential of controlling frequency through reactive power control can be used in islanded microgrids perfectly because

- 1) Most resources are connected to the grid through an inverter, which reduces inertia. Hence, the frequency drops faster.

- 2) The penetration level of renewable sources such as photovoltaic and wind turbines is high. These resources are exploited at the maximum power point and they cannot participate in frequency control through active power control.

- 3) The response rate of the resources that controls frequency through active power is low, such as fuel cells and micro-turbines.

- 4) Installation and maintenance costs of fast resources such as batteries are high.

- 5) Most resources are connected to the grid through an inverter, which facilitates the control of the reactive power by the inverter.

To the best knowledge of the authors, none of the research works (some of which mentioned above) have used reactive power management, which is called the channel of frequency-reactive power in this paper, to control frequency in microgrids. Indeed, all papers have used active power management like the active power generated by generators and storage devices for frequency control, which is the conventional channel of the frequency-active power for frequency control. This paper uses a new frequency control method to control the frequency of microgrids in an islanded mode. For this purpose, using the proposed coefficient, FQ, an optimum location is first indicated for the SOFC installation. Then, a coordinated reactive power management system is proposed between the SOFC and the battery. The proposed system is added to the conventional frequency control system. This proposed coordinated control system works similar to the secondary frequency control system, except that in this system the active power is transferred from the battery to other sources, but in the proposed system the reactive power is transferred from the battery to the SOFC. By doing this, the microgrid frequency drop is reduced and the frequency regulation becomes faster during contingencies. Also, the required storage capacity is significantly reduced and there would be no need to consider reserve capacity in the renewable sources for frequency control. Obviously, in any case, the voltage magnitude should remain in its acceptable standard range as suggested by the well-known curve of CBEMA (computer business equipment manufacturers association). In [29], the authors added an additional voltage control system to the conventional frequency control system to improve its performance in the islanded microgrid. The results were compared with the results of conventional control systems and their effectiveness was proven. The main focus was on the use of the potential of the battery and local control. But this paper proposes reactive power coordination between SOFC and the battery to improve the performance of the conventional frequency control system, and the results are compared with the results of the conventional frequency control system. This paper focuses on the coordination of the battery with SOFC to introduce this coordinated control system and present its advantages over the conventional control system. The paper does not concentrate on comparing this control system with the control system proposed in [29]. In their next research efforts, the authors will make a comprehensive technical and economic comparison between these two proposed methods.

The rest of the paper is organized as follows. Section 2 introduces a new frequency-reactive power (FQ) coefficient. Section 3 proposes a coordinated reactive power management system between the SOFC and the battery. Section 4 demonstrates the effectiveness of the proposed coefficient and coordinated system through various time domain simulations performed in the MATLAB/Simulink environment in a test microgrid. Finally, Section 5 presents the main contributions and conclusions of the paper.

2. PROPOSED FREQUENCY-REACTIVE POWER COEFFICIENT

A new coefficient that presents the effect of the reactive power variation of a bus on the microgrid frequency is defined in (1): “See (1)”.

where FQ_i is the frequency-reactive power coefficient of the i -th bus, f_{MG} is the microgrid frequency, P_{bat} is the total active load on the battery, $P_{load\ total}$ is the total active power load of the microgrid, $P_{load\ j}$ is the active load connected to the j -th bus, $|V_j|$ is the voltage magnitude of the j -th bus, $|V_k|$ is the voltage magnitude of the k -th bus (the battery is connected to the k -th bus), Q_{bat} is the reactive power on the battery as a result of the reactive load variation connected to the i -th bus, and Q_i is the reactive load connected to the i -th bus. In (1), the term $(\sum_{j=1}^n [(\partial P_{load\ j} / \partial |V_j|)(\partial |V_j| / \partial |V_k|)(\partial |V_k| / \partial Q_{bat})(\partial Q_{bat} / \partial Q_i)])$ represents the total network load variations due to a change in the reactive power of the i -th bus ($\partial P_{load\ total} / \partial Q_i$). Factor FQ_i indicates that if the reactive power in the i -th bus is changed to ΔQ_i , the microgrid frequency is changed to Δf_{MG} ($\Delta f_{MG} = FQ_i \times \Delta Q_i$).

This coefficient shows the degree of dependence of the microgrid frequency on the reactive power changes of the i -th bus. It is required that the coefficients $(\partial f_{MG} / \partial P_{bat})$, $(\partial P_{bat} / \partial P_{load\ total})_i$, $(\partial P_{load\ j} / \partial |V_j|)$, $(\partial |V_j| / \partial |V_k|)$, $(\partial |V_k| / \partial Q_{bat})$ and $(\partial Q_{bat} / \partial Q_i)$ be determined and substituted in (1) to obtain FQ for the i -th bus.

The VSI inverter typically interfaces between the storage devices (such as the battery) and the AC network. Using the energy stored in these devices, the VSI can have a behavior similar to the synchronous generator. Therefore, it can control the voltage magnitude and frequency in the isolated microgrid. In this case, the reference signals of the frequency and the voltage magnitude are calculated by the following equations [30]:

$$FQ_i = \partial f_{MG} / \partial Q_i = (\partial f_{MG} / \partial P_{bat}) \times (\partial P_{bat} / \partial P_{load\ total})_i \times \sum_{j=1}^n [(\partial P_{load\ j} / \partial |V_j|)(\partial |V_j| / \partial |V_k|)(\partial |V_k| / \partial Q_{bat})(\partial Q_{bat} / \partial Q_i)] \quad (1)$$

$$\frac{\partial Q_{bat}}{\partial Q_i} = \frac{1}{\left[\left(\frac{b \times Q_{0i}}{|V_{0i}|^b} \right) \left(\frac{-K_q \times |Z_{ik}|}{|Z_{kk}|} \right) \left[V_{0i} + \left(\frac{|Z_{ik}|}{|Z_{kk}|} \right) (-K_q \times Q_{Bat}) \right]^{b-1} \right]} \quad (10)$$

$$\frac{\partial P_{bat}}{\partial P_{load\ total}} = \frac{1}{\left[(-K_{pf} \times K_p) \sum_{j=1}^n \left[(P_{0\ j}) \left(\frac{|V_{0j}| + \left(\frac{|Z_{jk}|}{|Z_{kk}|} \right) (-K_q \times Q_{Bat})}{|V_{0j}|} \right)^a \right] \right]} \quad (11)$$

$$f_{MG} = f_{0\ MG} - (K_p \times P_{bat}) \quad (2)$$

$$|V_k| = |V_{0\ k}| - (K_q \times Q_{bat}) \quad (3)$$

where $f_{0\ MG}$ and $|V_{0\ k}|$ are the values of the microgrid frequency and the battery terminal voltage magnitude at the battery no-load conditions, respectively and K_q and K_p are the droop slopes of active power and reactive power, respectively. From (2) and (3), we have:

$$\partial f_{MG} / \partial P_{bat} = -K_p \quad (4)$$

$$\partial |V_k| / \partial Q_{bat} = -K_q \quad (5)$$

The exponential load model is used to illustrate the dependence of the active and reactive powers of the microgrid loads on the voltage magnitude [31]:

$$P_{load\ j} = P_{0j} (|V_j| / |V_{0j}|)^a \quad (6)$$

$$Q_{load\ j} = Q_{0j} (|V_j| / |V_{0j}|)^b \quad (7)$$

where Q_{0j} and P_{0j} are the reactive and active power consumptions of the j -th bus at voltage V_{0j} , respectively and a and b are the dependency coefficients of the active and reactive power of the load on the voltage magnitude, respectively. By rewriting (6) in terms of $|V_j|$, we have:

$$\partial P_{load\ j} / \partial |V_j| = (a \times P_{0j} / |V_{0j}|) \times (|V_j| / |V_{0j}|)^{a-1} \quad (8)$$

The voltage magnitude of each bus in the system is affected by the changes in the voltages of other buses. The following equation shows changes in the voltage magnitude of the j -th bus due to changes in the k -th bus voltage magnitude [32]:

$$\Delta |V_j| = \Delta |V_k| (|Z_{jk}| / |Z_{kk}|) \quad (9)$$

where $|Z_{jk}|$ is the magnitude of the element of the j -th row and the k -th column of the impedance matrix, $|Z_{kk}|$ is the element magnitude of the k -th row and the k -th column of the impedance matrix.

$(\partial Q_{bat} / \partial Q_i)$ is calculated by the following equation: “See (10)”. $(\partial P_{bat} / \partial P_{load\ total})$ is calculated by the following equation: “see (11)”.

where K_{pf} is the coefficient of the dependence of the reactive power consumption on the frequency variations.

An equation for calculating FQ of each bus can be obtained by replacing equations (4), (5), (8), (9), (10) and (11) in (1).

3. COORDINATION CONTROL OF REACTIVE POWER THE SOFC AND THE BATTERY

In the normal mode, a microgrid is always connected to the upstream network. In this case, the microgrid voltage magnitude and the frequency are determined by the upstream network as an infinite bus. There is a balance between the active and reactive power generation and consumption in the microgrid and any imbalance is compensated by the upstream network. Following a fault in the upstream network or a maintenance program, in the emergency mode, the microgrid can separate from the upstream grid and operate independently. At the moment of disconnection, there is a need for energy storage such as a battery to play the role of the upstream network and to compensate for the imbalance in the production and consumption of the microgrid power in the shortest possible time. In this case, the battery determines the frequency and voltage magnitude of the microgrid with respect to its active and reactive power from (2) and (3), respectively.

At the moment of disconnection, it is possible to change the voltage magnitude in its acceptable standard range (such as the well-known curve of CBEMA) by managing the reactive power of the battery. The well-known curve of the affiliated computer business equipment manufacturers association (CBEMA) that is shown in Fig. 1 can be applied to assess the voltage quality in the case of the voltage drop/rise. The CBEMA curve shows the magnitude and duration of voltage variations in the power system [33]. As such, the total active power consumption of the microgrid and the resulting active power on the battery will change. Therefore, at the critical moment of disconnection, the frequency of the microgrid can be controlled more effectively.

The SOFC reactive power control can be used to control the reactive power of the battery. In the microgrid, the SOFC is connected to the grid via power electronics interfaces. Inverter control strategies are generally divided into two types:

- 1) **PQ Inverter Control:** the inverter is used to provide a specific active and reactive power.
- 2) **Voltage source inverter control:** the inverter is controlled to supply the load with the predetermined voltage magnitude and frequency.

The SOFC inverter is in the PQ control mode, and it can be used to control the reactive power generation or consumption of the SOFC easily and quickly.

According to (2), the reactive power of the battery to generate the voltage magnitude corresponding to the CBEMA curve is calculated by the following equation:

$$Q_{CBEMA} = (|V_0| - |V_{CBEMA}|)/K_q \quad (12)$$

where $|V_{CBEMA}|$ is the voltage magnitude corresponding to the CBEMA curve and Q_{CBEMA} is the reactive power of the battery to create $|V_{CBEMA}|$. The required reactive power of the SOFC to generate reactive power Q_{CBEMA} on the battery is calculated by

$$Q_{SOFC} = Q_{battery} - Q_{0\ SOFC} - Q_{CBEMA} \quad (13)$$

where Q_{SOFC} is the reactive power of the SOFC, $Q_{battery}$ is the reactive power of the battery, and $Q_{0\ SOFC}$ is the reactive power of the SOFC before being disconnected from the upstream network. By replacing equation (12) in (13), we have:

$$Q_{SOFC} = Q_{battery} - Q_{0\ SOFC} - ((|V_0| - |V_{CBEMA}|)/K_q) \quad (14)$$

Therefore, a supplementary reactive power controller can be added to the SOFC control system according to Fig. 2. The aim of this controller is to coordinate the reactive power of the SOFC and the battery to better control the frequency of the microgrid.

By stopping the frequency changes, after a short time and as soon as the frequency is stabilized, the battery load must be removed and supplied by controllable generation sources such as fuel cells and micro turbines. The secondary frequency control system shown in Fig. 3 does just that. The micro source active power (MS) to return the frequency to the nominal value is determined.

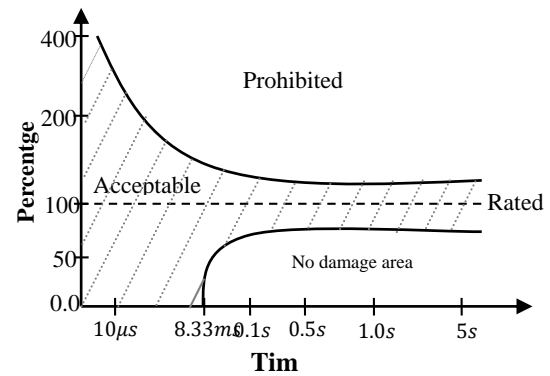


Fig. 1: The CBEMA curve.

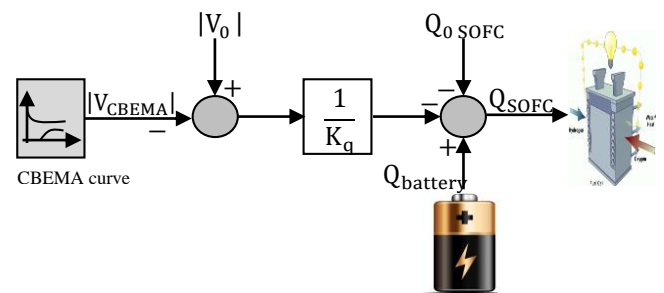


Fig. 2: The SOFC supplementary reactive power controller.

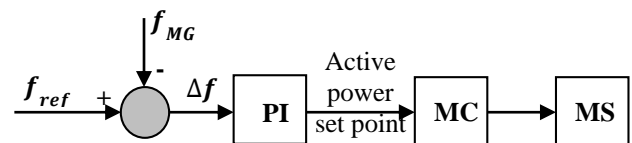


Fig. 3: The secondary frequency control system.

4. SIMULATION RESULTS

4.1. Test System

This paper uses a test system, as shown in Fig. 4, to demonstrate the effectiveness of the new coefficient and the proposed coordinated reactive power controller. This system is a low-voltage 400 V microgrid, which is simulated in the MATLAB/Simulink environment. This system is connected to an upstream medium-voltage network. The microgrid operates in normal conditions and in case of a fault in the upstream network, just after the fault, the microgrid is disconnected from the upstream network and operates independently. In this microgrid, the nominal ratings of the SOFC, the PV array, and the battery are 100kW, 10 kW, and 50 kW, respectively. The total load of the microgrid is 50 kVA, which is of constant impedance type and is distributed on buses 9 to 13. The details of active and reactive consumption of each bus are presented in Table 1. The capacitance of the lines is ignored due to their short length, and only the resistance and inductance of the lines are modeled. The length and impedance of the test microgrid lines are presented in Table 2.

4.2. The Results of The Frequency-Reactive Power Coefficient

For the test microgrid, the coefficient $(\partial Q_{bat} / \partial Q_i)$ of (10) and the coefficient $(\partial P_{bat} / \partial P_{load total})$ of (11) is calculated for all buses. The results are presented in Tables 3 and 4, respectively. Then, using (1), the coefficient FQ is calculated for all microgrid buses. The results are presented in Table 5. The parameters used to calculate these coefficients are given in Table 6. It is possible to rank the microgrid buses based on the values of this coefficient in terms of the effectiveness of reactive power injections on the frequency of the grid. This is performed for the test microgrid and the results are presented in Table 7. From the values of this table, it is concluded that buses 2 and 3 are the first priorities and buses 4 and 12 are the last priorities in the installation of reactive power control devices for frequency control. Therefore, in the test microgrid, the SOFC is installed in bus 2.

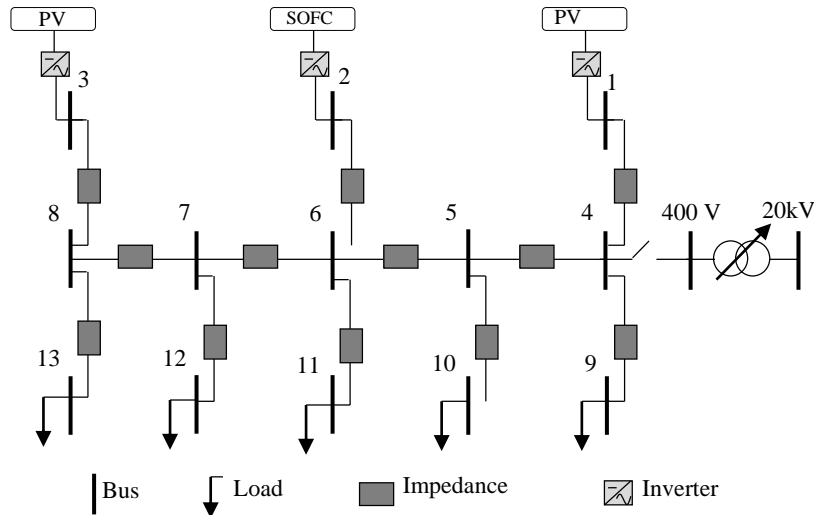


Fig. 4: The test low-voltage microgrid.

Table 1: The active (P_{Load}) and reactive (Q_{Load}) load of the i -th bus.

i	$P_{load}(kW)$	$Q_{load}(kVar)$
9	10	4
10	15	6
11	15	6
12	10	5
13	10	4

Table 2: The line length (L_{nm}) and impedance (Z_{nm})

n	m	$L_{nm}(M)$	$Z_{nm}(\Omega)$
4	1	30	$0.024 + j0.0023$
4	9	30	$0.024 + j0.0023$
4	5	100	$0.028 + j0.0083$
5	10	30	$0.024 + j0.0023$
5	6	100	$0.028 + j0.0083$
6	2	30	$0.024 + j0.0023$
6	11	30	$0.024 + j0.0023$
6	7	100	$0.028 + j0.0083$
7	12	30	$0.024 + j0.0023$
7	8	100	$0.028 + j0.0083$
8	3	30	$0.024 + j0.0023$
8	13	30	$0.024 + j0.0023$

Table 3: The values of $(\partial Q_{\text{bat}}/\partial Q_i)$ for all buses.

Bus number(i)	$\partial Q_{\text{bat}}/\partial Q_i$
1	0.8768
2	0.8769
3	0.8814
4	0.8758
5	0.8781
6	0.8755
7	0.8770
8	0.8810
9	0.8784
10	0.8761
11	0.8773
12	0.8777
13	0.879

Table 4: The values $(\partial P_{\text{bat}}/\partial P_{\text{load total}})$ for all buses.

Bus number(i)	$(\partial P_{\text{bat}}/\partial P_{\text{load total}})_i$
1	0.9411
2	0.7397
3	0.8041
4	0.9820
5	0.8483
6	1.1978
7	0.8632
8	0.9256
9	0.8832
10	0.7062
11	1.2161
12	0.8366
13	0.8674

Table 5: The values of coefficient FQ for all buses.

Bus number	FQ (Hz/MVar)
1	5.4831
2	5.2890
3	7.727
4	4.459
5	5.591
6	5.842
7	5.457
8	7.607
9	5.372
10	6.202
11	5.085
12	4.680
13	5.963

Table 6: The parameters of the test system in calculating FQ.

$$K_p = 1.2566 \times 10^{-4} \text{ Rad/(s.W)}$$

$$K_q = 3 \times 10^{-6} \text{ p.u./Var}$$

$$Q_{0 \text{ SOFC}} = 0$$

$$a=2$$

$$b=2$$

$$K_{\text{pf}} = 1.8$$

$$|V_k| = 1 \text{ p.u}$$

Table 7: The FQ values from the highest to the lowest.

Bus number	FQ (Hz/MVar)
3	7.7277
2	7.6079
10	6.2026
13	5.9639
6	5.8423
5	5.5913
1	5.4831
7	5.4578
9	5.3722
8	5.2890
11	5.0859
12	4.6807
4	4.4590

4.3. Results of the Coordinated Control of Reactive Power

It is assumed that the test microgrid is connected to the upstream network and at time $t = 10$ s, suddenly a fault occurs and the microgrid is disconnected and operates independently. In this case, three different scenarios are considered and compared:

Scenario 1: The microgrid voltage magnitude is constant and its frequency is controlled according to (1).

Scenario 2: The microgrid frequency is controlled according to (1), and its voltage magnitude is controlled according to (2) (the conventional frequency control system).

Scenario 3: In the conventional frequency control system, coordinated reactive power management between the SOFC and the battery is established for the better control of the frequency (the proposed frequency control system).

The microgrid frequency is shown in Fig. 5 for various scenarios. It is clear that the use of scenario 3 leads to a small decrease in the frequency of the network following the disconnection from the upstream network and it prevents the frequency to be out of permissible range at the initial moments and provides more time for the secondary frequency controller to return the frequency to the nominal value. It is also seen that scenario 2 outperforms scenario 1. This shows that the voltage participation in the control of the frequency is appropriate and effective.

The voltage magnitude of different buses of the microgrid under scenario 3 is shown in Fig. 6. It can be seen

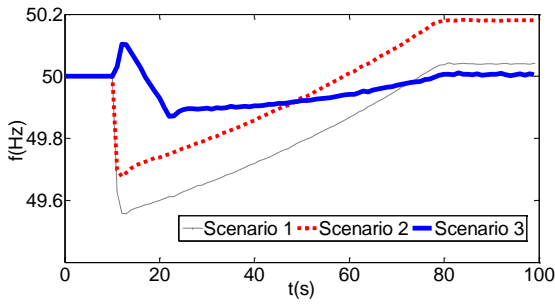


Fig. 5: Microgrid frequency under various scenarios.

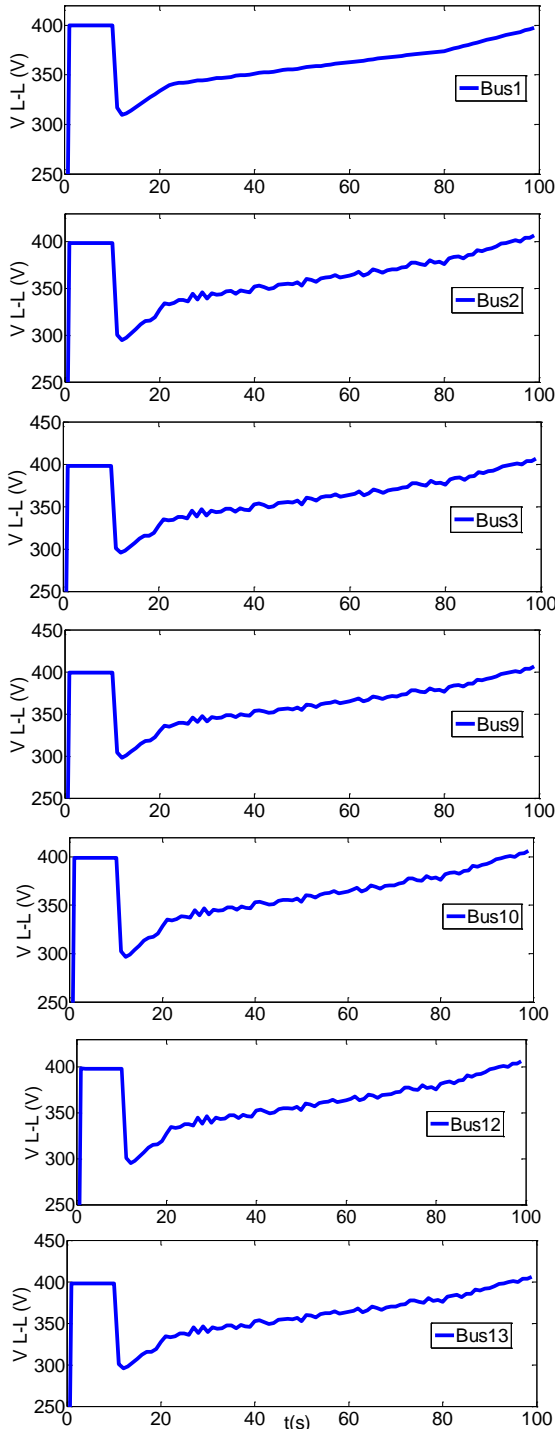


Fig. 6: Voltage magnitude of different buses under scenario 3.

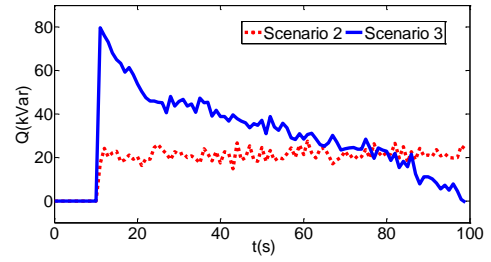


Fig. 7: The battery reactive power under various scenarios.

that the voltage magnitude of all buses, even the remote end buses, follows the CBEMA requirements. The drop in the voltage magnitude created for the specified periods of time is acceptable according to the CBEMA curve. After a short time and as soon as the frequency is stabilized, as the frequency goes toward the nominal value, the voltage tends to the nominal voltage and it returns to the nominal voltage as soon as the frequency returns to the nominal value. The voltage magnitudes of all buses are almost the same due to the small size of the microgrid.

The reactive power of the battery under scenarios 2 and 3 is shown in Fig. 7. It can be seen that in scenario 2, the reactive power of the battery is almost constant and does not participate in frequency control. While in scenario 3, it is controlled by SOFC and coordinated reactive power management. In the steady state after the fault, the reactive power of the battery is zero, and the reactive power required by the SOFC is provided.

The reactive power of the SOFC under scenarios 2 and 3 is shown in Fig. 8. The reactive power of the SOFC is assumed to be zero before disconnection. Also, in the conventional frequency control system, the SOFC does not participate in frequency control. So, as shown in Fig. 8, the reactive power of the SOFC in scenario 2 is always zero. However, in Scenario 3, the reactive power of the SOFC is not zero to participate in frequency control and it is adjusted by the coordinated control system. In the steady state after the fault, the SOFC provides all the required reactive power of the microgrid. The reactive power of the PV is assumed to be zero before and after the fault, and the PV does not participate in the reactive power control of the microgrid.

Fig. 9 presents the battery’s active power in various scenarios. In this figure, it can be seen that the active power of the battery in scenario 3 is less than that of the other scenarios. As a result, a lower capacity battery can be used in Scenario 3, and the cost of energy storage will be reduced. It is also seen that in all scenarios, with the function of the secondary frequency control system, after a period of time, the active load is transferred from the wind to the battery and the active power of the battery becomes zero. It is also seen that in all scenarios after a period of time, with the function of the secondary frequency control system, the active load is transferred from the battery to the SOFC and the active power of the battery becomes zero. Scenario 3 also performs better in this situation.

Fig. 10 depicts the SOFC active power in various scenarios. It can be seen that the SOFC active power is almost the same in all three scenarios and, after the operation of the secondary frequency control system, it rises from the initial value of 25 kW to 50 kW in the steady state.

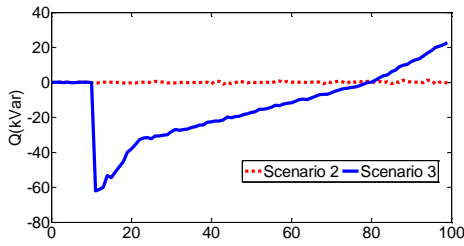


Fig. 8: The SOFC reactive power under various scenarios.

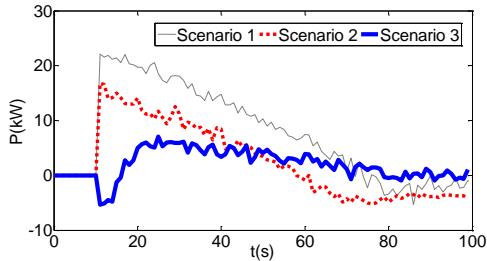


Fig. 9: The battery active power under various scenarios.

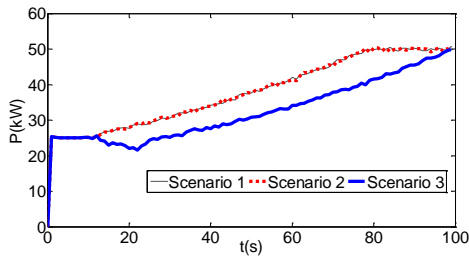


Fig. 10: The SOFC active power under various scenarios

All the entire imbalance in the active power generation and consumption is compensated by the SOFC.

The power of the PV under various scenarios is shown in Fig. 11 according to which in all three scenarios, before and after the fault, the PV active power is constant and is equal to its maximum value (10 kW). In this case, the maximum PV capacity is used, and no storage capacity is considered for frequency control.

The voltage magnitude corresponding to the CBEMA curve ($|V_{CBEMA}|$) is shown in Fig. 12. According to the curve of the CBEMA, severe voltage drop (even near zero) is allowed for a very short time.

5. CONCLUSION

This paper proposed the idea of using reactive power to control the frequency in the islanded microgrid. To indicate the amount of change in the frequency due to changes in reactive power in each bus, the frequency-reactive power coefficient (FQ) was introduced. The microgrid buses can be prioritized based on the values of this coefficient, and the appropriate location to install SOFC can be determined. The proposed coefficient is new and has not been presented in any other reference. With this coefficient, the buses can be found in which the change in their reactive power will have the greatest effect on the change in the microgrid frequency. The reactive power control sources can be installed in those buses for this purpose. Also, this paper proposed the coordinated

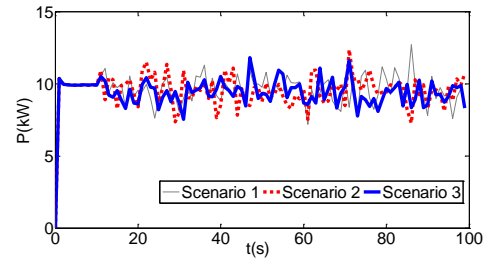


Fig. 11: The PV active power under various scenarios.

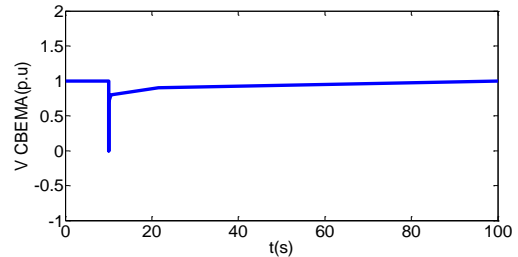


Fig. 12: The voltage magnitude corresponding to the CBEMA curve ($|V_{CBEMA}|$).

controller and the new coefficient were proven by the simulations performed in MATLAB/Simulink environment. The simulation results showed that the proposed coordinated control system outperformed the conventional frequency control system. This coordinated controller has many advantages such as reducing frequency drop at the moment of disconnection, faster frequency settling time to its nominal value, reducing the required battery capacity and the ability to operate renewable resources in maximum power point. These advantages presented and interpreted in detail in the Results section improve system stability and equipment performance and reduce costs due to more efficient use of renewable resources and the need for smaller batteries.

CREDiT AUTHORSHIP CONTRIBUTION STATEMENT

Saeed Aminzadeh: Conceptualization, Data curation, Formal analysis, Funding acquisition, Methodology, Project administration, Resources, Software, Visualization, Roles/Writing - original draft, Writing - review & editing. **Mehrdad Tarafdar Hagh:** Investigation, Supervision, Validation. **Heresh Seyedi:** Investigation, Supervision, Validation.

DECLARATION OF COMPETING INTEREST

The authors declare that they have no known competing financial interests or personal relationships that could have appeared to influence the work reported in this paper. The ethical issues; including plagiarism, informed consent, misconduct, data fabrication and/or falsification, double publication and/or submission, redundancy has been completely observed by the authors.

REFERENCES

- [1] J. Lai, X. Lu, and X. Yu, "stochastic distributed frequency and load sharing control for microgrids with communication delays," *IEEE Systems Journal*, vol. 13, no. 4, pp. 4269 - 4280, 2019.
- [2] C. Wang, S. Mei, Q. Dong, and R. Chen, "Coordinated Load Shedding Control Scheme for Recovering

- Frequency in Islanded Microgrids," *IEEE Access*, vol. 8, no. 1, pp. 215388 – 215398, 2020.
- [3] G. Delille, B. Francois, and G. Malarange, "Dynamic frequency control support by energy storage to reduce the impact of wind and solar generation on isolated power system's inertia," *IEEE Trans. Sustain. Energy*, vol. 3, no. 4, pp. 931–939, 2012.
- [4] K. W. Joung, T. Kim, and J. W. Park, "Decoupled Frequency and Voltage Control for Stand-Alone Microgrid with High Renewable Penetration," *IEEE Transactions on Industry Applications*, vol. 55, no. 1, pp. 122 - 133, 2019.
- [5] H. Zhao, M. Hong, W. Lin, and K. A. Loparo, "Voltage and Frequency Regulation of Microgrid with Battery Energy Storage Systems," *IEEE Transactions on Smart Grid*, vol. 10, no. 1, pp. 414 - 424, 2019.
- [6] J. Li, R. Xiong, Q. Yang, F. Liang, and W. Yuan, "Design/test of a hybrid energy storage system for primary frequency control using a dynamic droop method in an isolated microgrid power system," *Applied Energy*, vol. 201, 1 September, pp. 257-269, 2017.
- [7] S. Acharya, M. S. El Moursi, and A. Al-Hinai, "Coordinated Frequency Control Strategy for an Islanded Microgrid with Demand Side Management Capability," *IEEE Transactions on Energy Conversion*, vol. 33, no. 2, pp. 639 - 651, 2018.
- [8] E. Karfopoulos, L. Tena, A. Torres, P. Salas, and N. Hatziargyriou, "A multi-agent system providing demand response services from residential consumers," *Electric Power Systems Research*, vol. 120, March, pp. 163-176, 2015.
- [9] E. S. N. Raju, and P. Trapti Jain, "Impact of load dynamics and load sharing among distributed generations on stability and dynamic performance of islanded AC microgrids," *Electric Power Systems Research*, vol. 157, April, pp. 200-210, 2018.
- [10] C. Gouveia, J. Moreira, C. L. Moreira, and J. A. Peças Lopes, "Coordinating Storage and Demand Response for Microgrid Emergency Operation," *IEEE Trans. Smart Grid*, vol. 4, no. 4, pp. 1898 – 1908, 2013.
- [11] P. Jampethong and S. Khomfoi, "Coordinated Control of Electric Vehicles and Renewable Energy Sources for Frequency Regulation in Microgrids," *IEEE Access*, vol. 8, no. 1, pp. 141967 - 141976, July 2020.
- [12] A. Molina-Garcia, F. Bouffard, and D. Kirschen, "Decentralized demand-side contribution to primary frequency control," *IEEE Trans. Power Syst.*, vol. 26, no. 1, pp. 411–419, Feb. 2011.
- [13] M. Marzband, M. M. Moghaddam, M. F. Akorede, and G. Khomeyrani, "Adaptive load shedding scheme for frequency stability enhancement in microgrids," *Electric Power Systems Research*, vol.140, November, pp. 78-86, 2016.
- [14] M. Farrokhhabadi, C. A. Cañizares, and K. Bhattacharya, "Frequency Control in Isolated/Islanded Microgrids Through Voltage Regulation," *IEEE Trans. Smart Grid*, vol. 8, no. 3, pp. 1185 – 1193, 2017.
- [15] E. Rokrok, M. Shafie-khah, and J. P. S. Catalão, "Review of primary voltage and frequency control methods for inverter-based islanded microgrids with distributed generation," *Renewable and Sustainable Energy Reviews*, vol. 82, Part 3, pp. 3225-3235, February. 2018.
- [16] N. Cai and J. Mitra, "A multi-level control architecture for master-slave organized microgrids with power electronic interfaces," *Electric Power Systems Research*, vol.109, April, pp. 8-19, 2014.
- [17] K. Sh, H. Ye, W. Song, and N. Zhou, "Virtual Inertia Control Strategy in Microgrid Based on Virtual Synchronous Generator Technology," *IEEE Access*, vol. 6, May, pp. 27949 – 27957, 2018.
- [18] J. Liu, M. J. Hossain, J. Lu, F. H. M. Rafi, and H. Li, "A hybrid AC/DC microgrid control system based on a virtual synchronous generator for smooth transient performances," *Electric Power Systems Research*, vol. 162, September, pp. 169-182, 2018.
- [19] N. Sockeel, J. Gafford, B. Papari, and M. Mazzola, "Virtual Inertia Emulator-Based Model Predictive Control for Grid Frequency Regulation Considering High Penetration of Inverter-Based Energy Storage System," *IEEE Transactions on Sustainable Energy*, vol. 11, no.4, pp. 27949 – 27957, 2020.
- [20] O. Babayomi, Z. Li, and Z. Zhang, "Distributed secondary frequency and voltage control of parallel-connected vsocs in microgrids: A predictive VSG-based solution," *CPSS Transactions on Power Electronics and Applications*, vol. 5, no. 4, pp. 342 - 351, 2020.
- [21] X. Wu, C. Shen, and R. Iravani, "A Distributed, Cooperative Frequency and Voltage Control for Microgrids," *IEEE Trans. Smart Grid*, vol. 9, no. 4, pp. 2764 – 2776, 2018.
- [22] R. Jalilzadeh Hamidi, H. Livani, S. H. Hosseinian and, G. B. Gharehpetian, "Distributed cooperative control system for smart microgrids," *Electric Power Systems Research*, vol. 130, January, pp. 241-250, 2016.
- [23] T. John and S. P. Lam, "Voltage and frequency control during microgrid islanding in a multi-area multi-microgrid system," *IET Generation, Transmission & Distribution*, vol.11, no. 6, pp. 1502 – 1512, May 2017.
- [24] A. Nisar and M. S. Thomas, "Comprehensive Control for Microgrid Autonomous Operation with Demand Response," *IEEE Trans. Smart Grid*, vol. 12, no. 99, pp.1 – 9, 2016.
- [25] M.H. Khooban, "Secondary Load Frequency Control of Time-Delay Stand-Alone Microgrids With Electric Vehicles," *IEEE Trans. Industrial Electronics*, vol. 65, no. 9, pp. 7416 – 7422, Sept. 2018.
- [26] A. Jeya Veronica and N. Senthil Kumar, "Internal Model Based Load Frequency Controller Design for Hybrid Microgrid System," *Energy Procedia*, vol. 117, June, pp. 1032-1039, 2017.
- [27] M. Kosar and S. Hossein, "Decentralized Reactive Power Sharing and Frequency Restoration in Islanded Microgrid," *IEEE Trans. Power Systems*, vol. 32, no. 4, pp. 2901 – 2912, July 2017.

- [28] Y.S. Kim, E. S. Kim, and S. Moon, "Distributed Generation Control Method for Active Power Sharing and Self-Frequency Recovery in an Islanded Microgrid," *IEEE Trans. Power Systems*, vol. 32, no. 1, pp. 544 – 551, 2017.
- [29] S. Aminzadeh, M. Tarafdar Hagh, and H. Seyedi, "Reactive power management for microgrid frequency control," *International Journal of Electrical Power & Energy Systems*, Vol. 120, pp. 105959, 2020.
- [30] J. Moreira, C. L. Moreira, and J. A. Peças Lopes, "Defining control strategies for microgrids islanded operation," *IEEE Trans Power Syst*, Vol. 21, no. 2, pp. 916-924, 2006.
- [31] P. Kundur, *Power System Stability and Control*. New York, McGraw- Hill, 1994.
- [32] H. Saadat, *Power System Analysis*. New Delhi, Tata McGraw-Hill, 2002.
- [33] J. Arrillaga, N. R. Watson, and Shipu Che, *Power System Quality Assessment*. John Wiley & Sons, 2000.

BIOGRAPHY



Saeed Aminzadeh received his B.Sc. degree in electrical engineering at Shahid Beheshti University, Tehran, Iran in 2008, M.Sc. degree in electric power engineering at the Shahid Chamran University of Ahvaz, Ahvaz, Iran in 2010, and his Ph.D. degree in power engineering at the University of Tabriz, Tabriz, Iran in 2020. He has been with the Faculty of Engineering, Islamic Azad University since 2011. His current research interests include modeling, control, and optimization in microgrids.



Mehrdad Tarafdar Hagh received his B.Sc., M.Sc. (Hons.), and Ph.D. degrees in power engineering at the University of Tabriz, Tabriz, Iran in 1989, 1992, and 2000, respectively. He has been with the Faculty of Electrical and Computer Engineering, the University of Tabriz since 2000 where he is currently a professor. He has published more than 200 papers in power systems and power-electronic-related topics. His interest topics include power system operation, distributed generation, flexible ac transmission systems, and power quality.



Heresh Seyedi was born in Iran in 1979. He received his B.Sc., M.Sc., and Ph.D. degrees in electrical engineering at the University of Tehran, Tehran, Iran, in 2001, 2003, and 2008, respectively. Currently, he is with the faculty of Electrical and Computer Engineering, University of Tabriz, Tabriz, Iran. His areas of interest include digital protection of power systems and power system transients.

Copyrights

© 2022 Licensee Shahid Chamran University of Ahvaz, Ahvaz, Iran. This article is an open-access article distributed under the terms and conditions of the Creative Commons Attribution –NonCommercial 4.0 International (CC BY-NC 4.0) License (<http://creativecommons.org/licenses/by-nc/4.0/>).





Research Article

On the Cramer-Rao Lower Bound Based Analysis of Direct Position Determination and DOA Position Finding for Co-Channel Emitter Localization

Ali Eshkevari , and Seyed Mohammad Sajad Sadough* 

Faculty of Electrical Engineering, Shahid Beheshti University, Tehran 1983969411, Iran

* Corresponding Author Email: s_sadough@sbu.ac.ir

Abstract: Direct Position Determination (DPD) is known as an optimal, single-step technique for localizing co-channel signal sources since it processes the data gathered from all the array receiver elements together. In contrast, the commonly used radio location techniques include two independent stages. First, they estimate some initial parameters like direction, time, time-difference, frequency of arrival, etc., or their combination, and second, they localize signal sources using the triangulation of loci generated by the first stage. This disjoint structure leads to the sub-optimality of conventional localization algorithms. In this paper, we compare the Location root-mean-square-Error Lower Bounds (LELB) for DPD and position finding by DOA (PF-DOA) to prove the superiority of DPD over PF-DOA, which are commonly used for tactical fields or outdoor applications. Moreover, we demonstrate the advantages of DPD for indoor localization applications compared to PF-DOA techniques in terms of localization accuracy. We also introduce the single-group-array (SGA) structure for DPD in indoor applications and reveal that it outperforms both the PF-DOA and DPD with a classical multi-group-array (MGA) structure.

Keywords: Direct position determination, direction of arrival, co-channel signals, accuracy, Cramer-Rao lower bound.

Article history

Received 12 July 2021; Revised 09 September 2021; Accepted 25 September 2021; Published online 24 February 2022.

© 2022 Published by Shahid Chamran University of Ahvaz & Iranian Association of Electrical and Electronics Engineers (IAEEE)

How to cite this article

A. Eshkevari, and S. M. S. Sadough, "On the Cramer-Rao lower bound based analysis of direct position determination and DOA position finding for co-channel emitter localization," *J. Appl. Res. Electr. Eng.*, vol. 1, no. 2, pp. 131-138, 2022.

DOI: [10.22055/jaree.2021.37946.1032](https://doi.org/10.22055/jaree.2021.37946.1032)



1. INTRODUCTION

1.1. Background

During the recent decades, there has been a growing interest in the localization of co-channel signal sources by using array signal processing techniques. Civil radio frequency band monitoring, wildlife protection, seismology, sonar, and defense are some of prevalent outdoor localization applications. More recently, thanks to technical improvements, some indoor localization applications have also attracted attention, especially in the medical labs where wireless medical telemetry systems (WMTS) are an instance of non-invasive medical diagnose procedures [1].

From the estimation theory viewpoint, conventional localization techniques are sub-optimal since they have two separated stages. First, they estimate some initial parameters such as the direction of arrival (DOA), time of arrival (TOA), time-difference of arrival (TDOA), or frequency-difference of arrival (FDOA), or the received signal strength (RSS), and second, they intersect the outcome loci from the first stage to

localize the targets. As a matter of fact, the DOA-based position finding (PF-DOA) can be considered as the most commonly-used localization method.

Direct position determination (DPD) has lately been proposed as a single-step optimal technique for multiple co-channel signal localization by jointly using all data captured from sensor elements of all arrays. DPD is a statistical approach that uses a spatial-benefit function (SBF) whose peaks or extrema locate the signal transmitters. The SBF is the outcome of a mathematical solution to the localization problem, which is based on the statistical properties (normally covariance matrix) of the signals sensed on the array elements. These solutions are commonly referred to as *beamformers*. However, higher accuracy of the DPD method can be achieved at the expense of some extra hardware capabilities, such as synchronous sampling of all grouped receiver elements.

The main contribution of this paper consists of deriving Cramer-Rao lower bound (CRLB) based formulations of Location root-means-square-Error (LELB) for DPD and PF-

DOA methods in a unified framework. We also compare these bounds both analytically and numerically for outdoor and indoor applications to prove the superiority of DPD over traditional PF-DOA methods. Moreover, we propose a new structural deployment of the antenna hardware referred to as single-group-array (SGA) instead of the commonly used multi-group-array (MGA) to provide increased accuracy for DPD in indoor applications. Finally, we compare the DPD-SGA and DPD-MGA methods in both analytical and numerical ways in a WMTS lab scenario.

1.2. Literature Survey

Despite the long-time background of the PF-DOA methods, the extraction of CRLB for DOA estimation and PF-DOA is relatively recent. The CRLB for DOA estimation using vector and higher-order sensor arrays is presented in [1]. A conditional CRLB for DOA estimation and array calibration is provided in [2]. Moreover, a stochastic CRLB analysis for DOA estimation in the spherical harmonic's domain is addressed in [3]. More recently, a derivation and comparison of CRLB are presented in [4] for DOA estimators under the partial relaxation framework. Also, a CRLB analysis of data fusion for fingerprinting localization in non-line-of-sight (NLOS) environments is introduced in [5]. Moreover, a CRLB for DOA estimation exploiting multiple frequency pairs is provided in [6].

DPD was first proposed by Weiss et al. in 2004 for tactical field applications in their attempt to show that it exactly coincides with the maximum-likelihood (ML) estimation [7]. In [8] and [9], DPD is presented using different beamformers such as minimum-variance-distortionless-response (MVDR) and multiple-signal-classification (MUSIC), respectively. A comprehensive performance analysis of DPD with both MVDR and MUSIC beamformers is demonstrated in [10, 11]. Some DPD applications for wideband systems like radar and OFDM radios are provided in [12] and [13], respectively. In addition, a performance analysis of DPD using MUSIC algorithm is presented in [14]. Recently, a comparison of DPD performance using MVDR or MUSIC beamformers is demonstrated in [15]. A novel idea about applying free-space loss (FSL) in DPD problem formulation to have a more realistic path-length-dependent channel model is proposed more recently in [16]. Furthermore, a unified subspace fitting framework and its performance analysis for direct position determination in the presence of multipath propagation is addressed in [17]. In addition, a DPD method in asynchronous sensor networks is recently addressed in [18].

Table 1: Nomenclature used throughout the paper.

Symbol	Meaning
$\{\cdot\}^*$	Complex conjugate
$\{\cdot\}^T$	Transpose
$\{\cdot\}^H$	Hermitian (conjugate transpose)
\circ	Hadamard product of matrices
\otimes	Kronecker product of matrices
$\text{tr}(\cdot)$	Trace of a matrix
$\text{diag}(\cdot)$	Diagonal matrix of a vector
$\text{blkdiag}(\cdot)$	Block diagonal matrix of matrices
$\ \cdot\ $	Frobenius norm of a matrix
\mathbf{I}_N	Identity matrix of size N
\mathbf{J}_N	Exchange matrix of size N
\mathbf{U}_N	All-one matrix of size N

There are some recent works on the localization of wireless capsule endoscopy (WCE) as a commonly used indoor localization application for WMTS. Pioneering research on the accuracy of RF positioning in multi-capsule endoscopy is demonstrated in [19]. A method of DOA-based endoscopy capsule localization and orientation estimation via unscented Kalman filtering is addressed in [20]. Moreover, a positioning algorithm for WCE based on RSS is provided in [21]. A review of localization strategies for robotic endoscopic capsules is presented in [22].

1.3. Nomenclature

The conventions and notations presented in Table 1 will be used throughout the paper. Moreover, the DOA or azimuth angles are considered in navigation (clock oriented) and not in trigonometric mode.

2. PROBLEM FORMULATION

Consider M properly separated L -element receiving sensor arrays with similar *shapes* and *orientations*. We assume K sources transmitting unknown uncorrelated narrowband (NB) signals with baseband or *analytical* equivalents $s_k(t), k = 1, \dots, K$, located at enough distance from the receiving arrays satisfying far-field conditions. All transmitters and receiver sensors are assumed to be stationary during the observation period, so there is no Doppler frequency shift in the model. We aim at localizing transmitters using the sensors observed signals. The position of the k -th transmitter is denoted by the two- or three-dimensional (2D or 3D) vector \mathbf{p}_k . The NB analytical signal observed at the m -th array is given by an $L \times 1$ vector during the time interval $0 \leq t \leq T$ as

$$\mathbf{x}_m(t) = \sum_{k=1}^K \mathbf{a}_m(\mathbf{p}_k) H_m(\mathbf{p}_k) s_k(t) + \mathbf{b}_m(t), \quad (1)$$

where $\mathbf{a}_m(\mathbf{p}_k)$ is the m -th array response to a signal emitted from \mathbf{p}_k , $H_m(\mathbf{p}_k)$ is a complex scalar characterizing the channel response between \mathbf{p}_k and the (reference point of) m -th array, and $\mathbf{b}_m(t)$ denotes the zero-mean, circular complex AWGN with variance σ^2 at the m -th array receiver. The transmitters are assumed constant during a localization period, i.e., we assume M quasi-static channels. The observation time interval is $T \gg \max(\tau_m(\mathbf{p}_k))$ for the region of interest where $\tau_m(\mathbf{p}_k)$ is the propagation delay between \mathbf{p}_k and the reference point of the m -th array. Assuming enough distance between transmitters and receiver arrays, which makes the array responses only dependent on the DOA of the received signals, (1) can be expressed as

$$\mathbf{x}_m(t) = \sum_{k=1}^K \mathbf{a}_m(\phi_{mk}) H_{mk} s_k(t) + \mathbf{b}_m(t), \quad (2)$$

where ϕ_{mk} is the north-oriented polar coordinate representation of the DOA of the signal received at the m -th array from \mathbf{p}_k , and:

$$H_{mk} = H(d_{mk}, \alpha_{mk}) = \alpha_{mk} g_{mk} \frac{d_0}{d_{mk}} e^{-j2\pi \frac{d_{mk}}{\lambda}} \quad (3)$$

is the *channel response* between the m -th array and k -th transmitter with path length d_{mk} , for a carrier with wavelength λ , where α_{mk} characterizes all the stochastic

gains and attenuations through the channel path including the fading effect, d_0 is the normalizing distance to consider FSL in channel response (e.g., 10λ), and g_{mk} is the deterministic channel gain at distance d_0 from the k -th transmitter. The FSL is taken into account to produce a so-called dynamic sensor-array response (DSAR) according to [16]. The sample matrix version of (2) for N snapshots of signals is in the following form

$$\mathbf{X}_m = \mathbf{A}(\boldsymbol{\phi}_m)\mathbf{H}_m\mathbf{S} + \mathbf{B}_m, \quad (4)$$

Where:

$$\boldsymbol{\phi}_m \triangleq [\phi_{m1}, \dots, \phi_{mK}]^T, \quad (5)$$

and

$$\mathbf{H}_m \triangleq \text{diag}([H_{m1}, \dots, H_{mK}]). \quad (6)$$

To calculate the CRLB of our estimation problem, we need the sample covariance matrix of sensed signals \mathbf{X}_m [23], which is defined as

$$\mathbf{R}_m \triangleq \frac{1}{N}\mathbf{X}_m\mathbf{X}_m^H, \quad (7)$$

2.1. PF-DOA Formulation

In a PF-DOA problem of co-channel signals, the DOAs of impinging waves to each array are estimated independently and without considering other arrays. The signal received at the reference point of the m -th array can be expressed as

$$s_{mk}(t) \triangleq H_{mk} s_k(t), \quad (8)$$

so, Eq. (4) can be written as

$$\mathbf{X}_m = \mathbf{A}(\boldsymbol{\phi}_m)\mathbf{S}_m + \mathbf{B}_m, \quad (9)$$

where \mathbf{X}_m and \mathbf{B}_m are $L \times N$ matrices of the sample received signals and noise for sensor elements of the m -th array, respectively, and \mathbf{S}_m is the $K \times N$ sample matrix of the signals received at the reference point of the m -th array. The sample covariance matrix of (7) is in the form of

$$\mathbf{R}_m \triangleq \mathbf{A}(\boldsymbol{\phi}_m)\mathbf{R}_{S_m}\mathbf{A}^H(\boldsymbol{\phi}_m) + \mathbf{R}_{B_m}, \quad (10)$$

where source signals and noise sample covariance matrices are defined as

$$\mathbf{R}_{S_m} \triangleq \frac{1}{N}\mathbf{S}_m\mathbf{S}_m^H, \quad \mathbf{R}_{B_m} \triangleq \frac{1}{N}\mathbf{B}_m\mathbf{B}_m^H. \quad (11)$$

2.2. DPD Formulation

In a DPD problem of co-channel signals, the locations of signal emitters are estimated using signals sensed in all arrays together. Here, we define the pointing vector of the m -th array's reference point to position \mathbf{p}_k as

$$\tilde{\mathbf{a}}_m(\mathbf{p}_k) \triangleq \mathbf{a}(\phi_{mk})H_{mk}, \quad (12)$$

so, Eq. (4) can be written as

$$\mathbf{X}_m = \tilde{\mathbf{A}}_m(\mathbf{P})\mathbf{S} + \mathbf{B}_m, \quad (13)$$

where \mathbf{X}_m and \mathbf{B}_m are $L \times N$ matrices of the sample received signals and noise for sensor elements of the m -th array, respectively, and \mathbf{S} is the $K \times N$ sample matrix of the emitted signals. The sample covariance matrix of (7) is in the form of

$$\mathbf{R}_m \triangleq \tilde{\mathbf{A}}_m(\mathbf{P})\mathbf{R}_S\tilde{\mathbf{A}}_m^H(\mathbf{P}) + \mathbf{R}_{B_m}, \quad (14)$$

where source signals and noise sample covariance matrices are defined as

$$\mathbf{R}_S \triangleq \frac{1}{N}\mathbf{S}\mathbf{S}^H, \quad \mathbf{R}_{B_m} \triangleq \frac{1}{N}\mathbf{B}_m\mathbf{B}_m^H. \quad (15)$$

Finally, the global covariance matrix of all sensors will be

$$\mathbf{R} \triangleq \text{blkdiag}(\mathbf{R}_1, \dots, \mathbf{R}_M). \quad (16)$$

The dimensions of \mathbf{R} in (16) are $U \times U$ where $U = LM$.

3. DERIVATION OF THE CRAMER-RAO LOWER BOUND

In array processing theory, whenever a single snapshot is assumed to be a zero-mean Gaussian random variable, and when successive snapshots are supposed to be statistically independent, the (i,j) -th element of the Fisher information matrix (FIM) for any parameter estimation is defined as [23]

$$F_{ij} = -N \text{tr} \left(\frac{\partial \mathfrak{R}^{-1}}{\partial \psi_i} \frac{\partial \mathfrak{R}}{\partial \psi_j} \right) = N \text{tr} \left(\mathfrak{R}^{-1} \frac{\partial \mathfrak{R}}{\partial \psi_i} \mathfrak{R}^{-1} \frac{\partial \mathfrak{R}}{\partial \psi_j} \right), \quad (17)$$

where \mathfrak{R} is the covariance matrix for a single snapshot, N is the number of observations of array signals, and $\boldsymbol{\psi} = [\psi_i, \psi_j]$ is the vector of the estimated parameters. The CRLB states about the unbiased estimate $\hat{\boldsymbol{\psi}}$ that

$$\text{var}(\hat{\boldsymbol{\psi}}) \geq \text{tr}(\mathbf{F}^{-1}). \quad (18)$$

There are some important considerations [23].

- The physical dimension of \mathfrak{R} is *power*.
- \mathfrak{R} contains information about signal and noise powers.
- $\frac{\partial \mathfrak{R}}{\partial \psi_i}$ contains information about the array geometry.

3.1. LELB for PF-DOA

In a PF-DOA problem, the location of any arbitrary point \mathbf{p} in the monitoring area is determined by the estimation of DOAs of signals impinging each of the M array elements from that point. Then, for the m -th array, the estimation parameter is $\hat{\boldsymbol{\psi}} = [\phi_m]$, and from (17), the single-element FIM (scalar) is written as

$$F_m = N \text{tr} \left(\left[\mathbf{R}_m^{-1} \frac{\partial \mathbf{R}_m}{\partial \psi_i} \right]^2 \right). \quad (19)$$

For simplicity, we rewrite (10) for the m -th array as

$$\mathbf{R}_m \triangleq \mathbf{A}\mathbf{R}_{S_m}\mathbf{A}^H + \sigma^2\mathbf{I}_L, \quad (20)$$

where σ^2 is the noise power that is supposed to be constant for all receiver elements of the whole array.

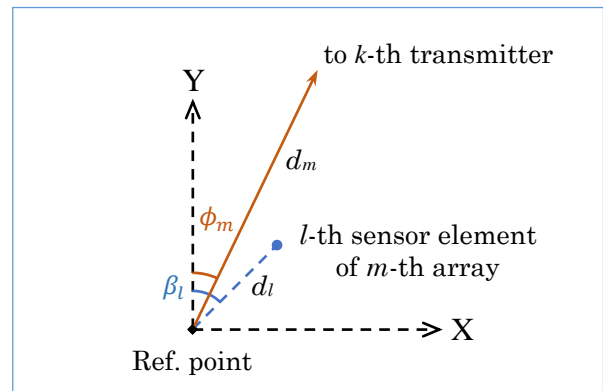


Fig. 1: Parameters definitions for m -th array properties

To achieve the matrix inversion \mathbf{R}_m^{-1} , we can use direct computations, or we can apply the matrix inversion lemma to (20) as

$$\mathbf{R}_m^{-1} = \sigma^{-2}(\mathbf{I} - \mathbf{A}(\mathbf{A}\mathbf{A}^H + \sigma^2\mathbf{R}_{Sm}^{-1})\mathbf{A}^H), \quad (21)$$

which is a proper way for a $K \times K$ diagonal matrix \mathbf{R}_{Sm} (uncorrelated source signals at the m -th array reference point) that can be simply inverted compared with direct inversion of $L \times L$ non-diagonal \mathbf{R}_m with $K < L$ and usually $K = 1$ for numerical analysis.

According to (20), we have

$$\frac{\partial \mathbf{R}_m}{\partial \phi_m} = \frac{\partial \mathbf{A}}{\partial \phi_m} \mathbf{R}_{Sm} \mathbf{A}^H + \mathbf{A} \mathbf{R}_{Sm} \frac{\partial \mathbf{A}^H}{\partial \phi_m}. \quad (22)$$

To compute the CRLB for DOA estimation of the signal emitted from the k -th transmitter, i.e., $\mathbf{p} = \mathbf{p}_k$, we notice that except for the emitter located at the point \mathbf{p}_k , other emitters are assumed to have fixed locations, so they can be ignored during the derivation procedure. We thus have

$$\frac{\partial \mathbf{A}}{\partial \phi_m} = \frac{\partial}{\partial \phi_m} [\mathbf{a}_1, \dots, \mathbf{a}_K] = \left[\mathbf{0}, \dots, \frac{\partial \mathbf{a}_k}{\partial \phi_m}, \dots, \mathbf{0} \right]. \quad (23)$$

For notation simplicity, we remove the subscript k and use $\mathbf{a} = \mathbf{a}_k$. Assuming that the signal emitted from \mathbf{p} is uncorrelated with other signals, we have

$$\frac{\partial \mathbf{R}_m}{\partial \phi_m} = \frac{\partial \mathbf{a}}{\partial \phi_m} P_m \mathbf{a}^H + \mathbf{a} P_m \frac{\partial \mathbf{a}^H}{\partial \phi_m} = P_m \frac{\partial (\mathbf{a} \mathbf{a}^H)}{\partial \phi_m}, \quad (24)$$

where P_m is the k -th diagonal element of \mathbf{R}_{Sm} representing the power received at the reference point of the m -th array from the emitter at the point \mathbf{p} . According to Fig. 1, for the l -th element of \mathbf{a} , we have

$$a_l = \exp\left(j \frac{2\pi}{\lambda} d_l \cos(\beta_l - \phi_m)\right), \quad (25)$$

$$\frac{\partial a_l}{\partial \phi_m} = j \frac{2\pi}{\lambda} d_l \sin(\beta_l - \phi_m) a_l, \quad (26)$$

where d_l and β_l are the distance and angle of the l -th element with respect to the reference point of the m -th array, respectively. Then, we have

$$\frac{\partial \mathbf{a}}{\partial \phi_m} = j \frac{2\pi}{\lambda} \text{diag}(\boldsymbol{\rho}(\phi_m)) \mathbf{a}, \quad (27)$$

$$\frac{\partial \mathbf{a}^H}{\partial \phi_m} = -j \frac{2\pi}{\lambda} \mathbf{a}^H \text{diag}(\boldsymbol{\rho}(\phi_m)), \quad (28)$$

where

$$\boldsymbol{\rho}(\phi_m) \triangleq j \frac{2\pi}{\lambda} \mathbf{d} \circ \sin(\boldsymbol{\beta} - \phi_m), \quad (29)$$

where $\mathbf{d} = [d_1, \dots, d_L]^T$ and $\boldsymbol{\beta} = [\beta_1, \dots, \beta_L]^T$. Considering (24), we have

$$\frac{\partial \mathbf{R}_m}{\partial \phi_m} = P_m \mathbf{C}_\phi \circ (\mathbf{a} \mathbf{a}^H), \quad (30)$$

where:

$$\mathbf{C}_\phi \triangleq \text{diag}(\boldsymbol{\rho}(\phi_m)) \mathbf{U}_L - \mathbf{U}_L \text{diag}(\boldsymbol{\rho}(\phi_m)). \quad (31)$$

Now, we can determine F_m , and according to CRLB about unbiased DOA estimation of $\hat{\phi}_m$, we have

$$\text{var}(\hat{\phi}_m) \geq \frac{1}{F_m}. \quad (32)$$

Finally, due to the Euclidian summability of variances, we can write the total localization variance for a PF-DOA method (like triangulation) as

$$\text{var}(\hat{\mathbf{p}}) \geq \frac{1}{M} \sum_{m=1}^M d_m^2 \text{var}(\hat{\phi}_m) = \text{LELB}_{PF-DOA}, \quad (33)$$

where d_m is the distance between the m -th array and the signal emitter at \mathbf{p} .

Moreover, considering (20), the linear signal-to-noise-ratio (SNR) at the m -th array can be expressed as

$$\text{SNR}_m = \frac{\text{tr}(\mathbf{A} \mathbf{R}_{Sm} \mathbf{A}^H)}{L \sigma^2}, \quad (34)$$

where, according to (11), \mathbf{R}_{Sm} is the covariance matrix of the signals received at the reference point of the m -th array (not at the transmitter's location).

3.2. CRLB and LELB for DPD

In a DPD problem, the location of any arbitrary point \mathbf{p} in the monitoring area is directly estimated by jointly using signal observations from M numbers of the L -sensor arrays. For notational simplicity, we rewrite (14) as

$$\mathbf{R}_m \triangleq \tilde{\mathbf{A}}_m \mathbf{R}_S \tilde{\mathbf{A}}_m^H + \sigma^2 \mathbf{I}_L, \quad (35)$$

and by considering the definition of \mathbf{R} in (16), we can write

$$\mathbf{R} \triangleq \tilde{\mathbf{A}} \mathbf{R}_S \tilde{\mathbf{A}}^H + \sigma^2 \mathbf{I}_U. \quad (36)$$

So, using (17) for estimation of $\boldsymbol{\psi} = [x, y]^T$ leads to

$$\mathbf{F}_{ij} = N \text{tr} \left(\mathbf{R}^{-1} \frac{\partial \mathbf{R}}{\partial \psi_i} \mathbf{R}^{-1} \frac{\partial \mathbf{R}}{\partial \psi_j} \right). \quad (37)$$

To compute \mathbf{R}^{-1} for an MGA structure, we consider (16) as

$$\mathbf{R}^{-1} \triangleq \text{blockdiag}(\mathbf{R}_1^{-1}, \dots, \mathbf{R}_M^{-1}), \quad (38)$$

which states that we can divide the inversion problem to M inversions of smaller dimension matrices to reduce the computational load. Moreover, we can use the matrix inversion similar to (21) for calculating \mathbf{R}^{-1} or \mathbf{R}_m^{-1} .

To calculate $\frac{\partial \mathbf{R}}{\partial \psi_i}$, we can use similar steps to (22)-(24) by which we get

$$\frac{\partial \mathbf{R}}{\partial \psi_i} = \frac{\partial \tilde{\mathbf{a}}}{\partial \psi_i} P \tilde{\mathbf{a}}^H + \tilde{\mathbf{a}} P \frac{\partial \tilde{\mathbf{a}}^H}{\partial \psi_i} = P \frac{\partial (\tilde{\mathbf{a}} \tilde{\mathbf{a}}^H)}{\partial \psi_i}, \quad (39)$$

where $\tilde{\mathbf{a}}$ is the k -th column of $\tilde{\mathbf{A}}$ with size $U \times 1$ and P is the k -th diagonal element of \mathbf{R}_S representing the emitting power of the source at \mathbf{p} . We have removed subscript k for notation simplicity. Considering (3), regarding the u -th element of $\tilde{\mathbf{a}}$, we have

$$\tilde{a}_u = \alpha_u g_u \frac{d_0}{d_u} \exp\left(-j \frac{2\pi}{\lambda} d_u\right), \quad (40)$$

$$\frac{\partial \tilde{a}_u}{\partial \psi_i} = -\left(\frac{1}{d_u} + j \frac{2\pi}{\lambda}\right) \tilde{a}_u \frac{\partial d_u}{\partial \psi_i}, \quad (41)$$

where d_u is the distance between \mathbf{p} and the u -th sensor element. Moreover, we have

$$d_u^2 = (x - x_u)^2 + (y - y_u)^2, \quad (42)$$

$$\frac{\partial d_u}{\partial x} = \frac{x - x_u}{d_u} = \sin \phi_u, \quad (43)$$

$$\frac{\partial d_u}{\partial y} = \frac{y - y_u}{d_u} = \cos \phi_u, \quad (44)$$

where ϕ_u is the direction (azimuth) of \mathbf{p} from u -th element's viewpoint. Therefore, for $\psi_i = x$, we have

$$\frac{\partial \tilde{\mathbf{a}}}{\partial x} = \text{diag}(\boldsymbol{\zeta} \circ \sin \boldsymbol{\phi}) \tilde{\mathbf{a}}, \quad (45)$$

$$\frac{\partial \tilde{\mathbf{a}}^H}{\partial x} = \tilde{\mathbf{a}}^H \text{diag}(\boldsymbol{\zeta}^* \circ \sin \boldsymbol{\phi}), \quad (46)$$

where $\boldsymbol{\zeta} = [\zeta_1, \dots, \zeta_U]^T$, $\zeta_u = -\left(\frac{1}{d_u} + j\frac{2\pi}{\lambda}\right)$, and $\boldsymbol{\phi} = [\phi_1, \dots, \phi_U]^T$. Using (39) and following similar steps for x and y , we have

$$\frac{\partial \mathbf{R}}{\partial x} = P \mathbf{C}_x \circ (\tilde{\mathbf{a}} \tilde{\mathbf{a}}^H), \quad (47)$$

$$\frac{\partial \mathbf{R}}{\partial y} = P \mathbf{C}_y \circ (\tilde{\mathbf{a}} \tilde{\mathbf{a}}^H), \quad (48)$$

where

$$\mathbf{C}_x \triangleq \text{diag}(\boldsymbol{\zeta} \circ \sin \boldsymbol{\phi}) \mathbf{W} + \mathbf{W} \text{diag}(\boldsymbol{\zeta}^* \circ \sin \boldsymbol{\phi}), \quad (49)$$

$$\mathbf{C}_y \triangleq \text{diag}(\boldsymbol{\zeta} \circ \cos \boldsymbol{\phi}) \mathbf{W} + \mathbf{W} \text{diag}(\boldsymbol{\zeta}^* \circ \cos \boldsymbol{\phi}), \quad (50)$$

where $\mathbf{W} = \mathbf{I}_M \otimes \mathbf{U}_L$.

In fact, \mathbf{W} masks any statistical dependency between signals received by different arrays in accordance with the definition of classical DPD. Finally, we can determine the elements of \mathbf{F} and then derive the CRLB. For an unbiased estimation $\hat{\mathbf{p}}$, the CRLB states that

$$\text{var}(\hat{\mathbf{p}}) \geq \text{tr}(\mathbf{F}^{-1}). \quad (51)$$

The total SNR in (36) is given by

$$\text{SNR} = \frac{\text{tr}(\tilde{\mathbf{A}} \mathbf{R}_S \tilde{\mathbf{A}}^H)}{U \sigma^2}, \quad (52)$$

and the specific SNR due to the k -th transmitter will be

$$\text{SNR}_k = \frac{\text{tr}(\tilde{\mathbf{a}}_k P_k \tilde{\mathbf{a}}_k^H)}{\sigma^2} = \frac{P_k \tilde{\mathbf{a}}_k^H \tilde{\mathbf{a}}_k}{\sigma^2}, \quad (53)$$

where P_k is the power transmitted from the k -th emitter.

Since the fading coefficients in $\tilde{\mathbf{a}}$ are considered constant during each observation interval of DPD estimation, we can average the CRLBs resulting from several observation intervals to achieve a more reliable criterion for the lower bound [24]. For an MGA structure we use LELB instead of CRLB abbreviation.

4. DPD FOR INDOOR APPLICATIONS

In addition to outdoor applications such as localization in tactical fields, there are some indoor applications that should be considered. An instance of common indoor localization applications is the medical lab of WMTS, which uses a frequency of about 1430 MHz in accordance with the Federal Communications Commission (FCC) rules [25].

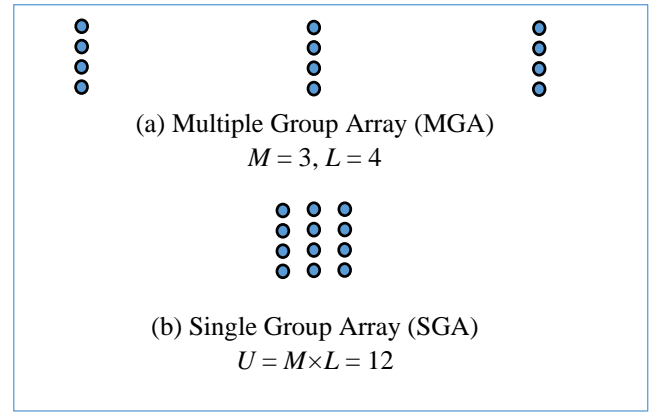


Fig. 2: Some examples of MGA and SGA structures

One essential rule in antenna array geometry is that the element spacing and the whole array dimensions should be about the carrier wavelength. This provides an opportunity for indoor applications to exploit the default localization array structure, i.e., MGA to be used as an SGA one. Fig. 2 shows the concept of MGA and SGA structures in which U is the total number of sensor elements. In DPD, the SGA structure provides more accuracy and resolution than the MGA since it takes into account the statistical dependency (covariance) between observations of all the sensor elements together, in contrast to the MGA structure that ignores any statistical dependency between the elements that belong to different groups (arrays).

For an SGA structure, (13) can be written as

$$\mathbf{X} = \tilde{\mathbf{A}}(\mathbf{P})\mathbf{S} + \mathbf{B}, \quad (54)$$

where \mathbf{X} and \mathbf{B} are $U \times N$ matrices of the sample received signals and noise for sensor elements of the whole array, respectively, and \mathbf{S} is the $K \times N$ sample matrix of the emitted signals. The sample covariance matrix of (54) is in the form of

$$\mathbf{R} \triangleq \tilde{\mathbf{A}}(\mathbf{P})\mathbf{R}_S \tilde{\mathbf{A}}^H(\mathbf{P}) + \mathbf{R}_B, \quad (55)$$

which is not a sparse matrix such as the global covariance matrix in (16) since the covariance between the observations of all U sensor elements of the SGA is taken into account. The rest of the CRLB extraction for the SGA structure is similar to the formulations presented in Subsection 3.2.

5. SIMULATIONS AND NUMERICAL ANALYSIS

This section compares the numerically determined root mean square error (RMSE) of localization and analytically derived CRLB and LELB versus SNR. Each RMSE value is obtained by 100 Monte-Carlo experiments, each including 64 samples of array observations. All values are normalized to carrier wavelength.

We first consider a tactical field map, as depicted in Fig. 3. We assume three receiving arrays ($M=3$) where each array is composed of seven sensor elements ($L=7$). All arrays are similarly deployed in the uniform circular array (UCA) or uniform linear array (ULA) structures that we refer to as UCA7 and ULA7, respectively. The element spacing is equal to about half of the wavelength of a 300 MHz carrier (0.5×1 m). We assume that the transmitter is emitting an unknown signal located at point (1500, 1500) m.

Fig. 4 and Fig. 5 show the LELB normalized to wavelength versus SNR for both PF-DOA and DPD for the case of UCA and ULA array geometries, respectively. We can observe a superior performance in terms of localization accuracy achieved by DPD over PF-DOA, especially at low SNRs, for about 2-2.5 dB and 3-4 dB for UCA and ULA geometries, respectively. We have also shown the RMSE value associated with DPD using numerical analysis.

The second performance analysis is related to a typical indoor localization problem as depicted in Fig. 6 in which both MGA and SGA structures are deployed. We assume eight receiving arrays ($M=8$) where each array is composed of five sensor elements ($L=5$). All arrays are similarly deployed in the ULA structure that we refer to as ULA5. The element spacing is equal to about three times the wavelength, which is 1430 MHz carrier (3×21 cm). We assume that one transmitter is emitting an unknown signal located at point (0, 0) m at the array center.

Fig. 7 shows the LELB normalized to wavelength versus SNR for PF-DOA and DPD with MGA structure, and CRLB for DPD with SGA structure. It can be easily seen that DPD-MGA outperforms PF-DOA by about 5 dB, and DPD-SGA outperforms DPD-MGA by about 12 dB. The normalized RMSE values of DPD-MGA and DPD-SGA are presented as well using numerical analysis.

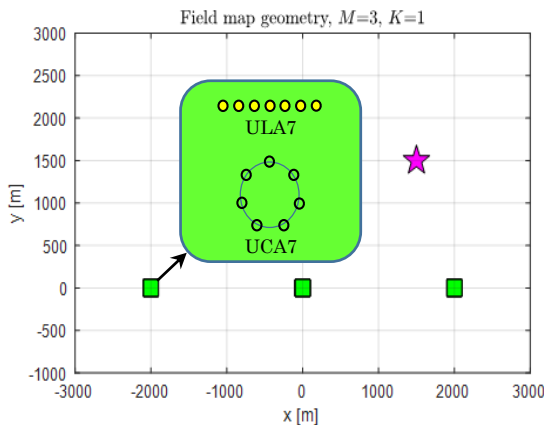


Fig. 3: The tactical field geometry considered with three 7-element ULA or UCA arrays and one transmitter.

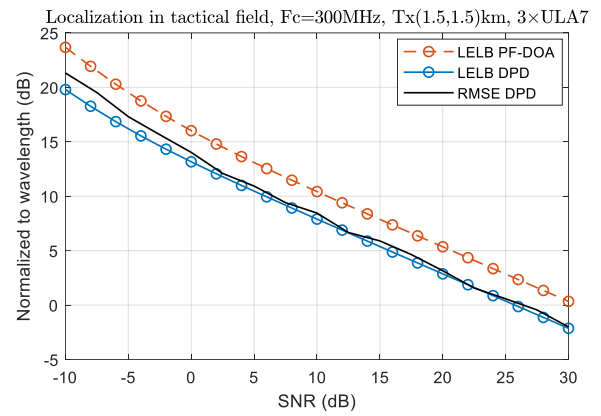


Fig. 5: The performance comparison of DPD and PF-DOA using ULA7 arrays in a typical tactical field

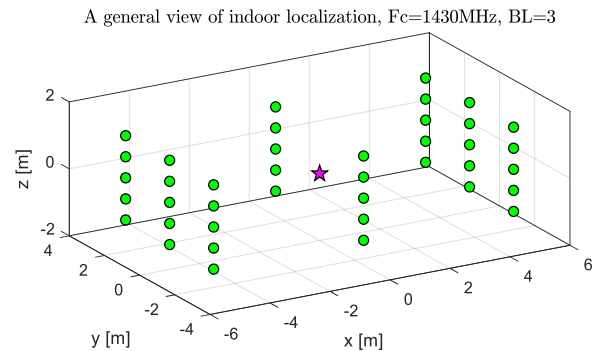


Fig. 6: A typical indoor localization application with eight 5-element ULAs as an SGA with 40 sensor elements

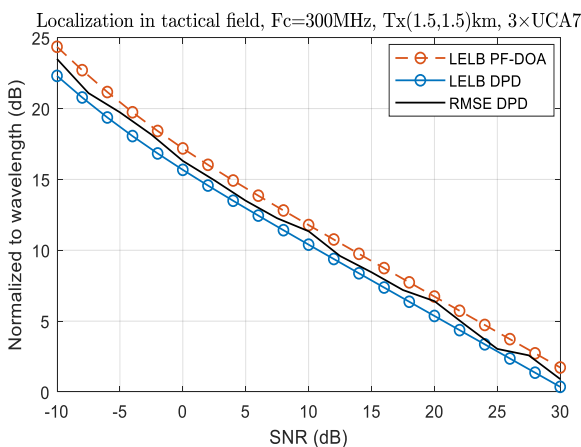


Fig. 4: The performance comparison for DPD and PF-DOA using UCA7 arrays in a typical tactical field

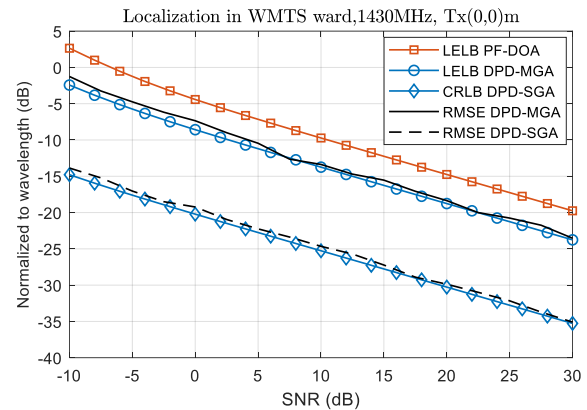


Fig. 7: The performance comparison for DPD and PF-DOA in an indoor application with the array depicted in Fig. 6 using both MGA and SGA structures

6. CONCLUSION

In this paper, we derived the formulations of CRLB and LELB for DPD and PF-DOA techniques of localization of co-channel signals for outdoor and indoor applications. By comparing the LELBs for outdoor applications, we showed that DPD can achieve localization RMSE of about 3dB lower than the PF-DOA method, which is a noticeable improvement because this means that the effective depth of the operational field has been enlarged by about 70%.

For indoor applications, we first showed that DPD with MGA structure outperforms the PD-DOA by about 5 dB. Also, we pointed out the opportunity of using an SGA

structure instead of the commonly used MGA structure and proved the superiority of using SGA over MGA by about 13dB in localization accuracy, which is a significant enhancement in accuracy for indoor localization applications.

CREDIT AUTHORSHIP CONTRIBUTION STATEMENT

Ali Eshkevari: Conceptualization, Investigation, Writing - original draft. **Seyed Mohammad Sajad Sadough:** Formal analysis, Supervision, Writing - review & editing.

DECLARATION OF COMPETING INTEREST

The authors declare that they have no known competing financial interests or personal relationships that could have appeared to influence the work reported in this paper. The ethical issues; including plagiarism, informed consent, misconduct, data fabrication and/or falsification, double publication and/or submission, redundancy has been completely observed by the authors.

REFERENCES

- [1] H. Lai and K. Bell, "Cramer-rao lower bound for DOA Estimation using vector and higher-order sensor arrays," in *Conference Record of the Forty-First Asilomar Conference on Signals, Systems and Computers*, Asilomar, 2007, pp. 1262-1266.
- [2] Z.-M. Liu, "Conditional Cramér-rao lower bounds for DOA estimation and array calibration," *IEEE Signal Processing Letters*, vol. 21, no. 3, pp. 361-364, 2014.
- [3] L. Kumar and R. M. Hegde, "Stochastic cramer-rao bound analysis for DOA estimation in spherical sarmonics somain," *IEEE Signal Processing Letters*, vol. 22, no. 8, pp. 1030-1034, 2015.
- [4] M. Trinh-Hoang, M. Viberg, and M. Pesavento, "Cramér-rao bound for DOA estimators under the partial relaxation framework: derivation and comparison," *IEEE Transactions on Signal Processing*, vol. 68, pp. 3194-3208, 2020.
- [5] J. Li, I.-T. Lu and J. Lu, "Cramer-rao lower bound analysis of data fusion for fingerprinting localization in non-line-of-sight environments," *IEEE Access*, vol. 9, pp. 18607-18624, 2021.
- [6] Y. Liang, W. Cui, and H. Wu, "Cramér-rao bound for DOA estimation exploiting multiple frequency pairs," *IEEE Signal Processing Letters*, vol. 28, pp. 1210-1214, 2021.
- [7] A. J. Weiss, "Direct position determination of narrowband radio frequency transmitters," *IEEE Signal Processing Letters*, vol. 11, no. 5, pp. 513-516, May 2004.
- [8] L. Tzafri and A. J. Weiss, "High-resolution direct position determination using MVDR," *IEEE Transactions on Wireless Communications*, vol. 15, no. 9, pp. 6449-6461, Sept 2016.
- [9] A. Amar and A. J. Weiss, "Direct position determination of multiple radio signals," *EURASIP Journal of Applied Signal Processing*, pp. 37-49, Jan. 2005.
- [10] T. Tirer and A. J. Weiss, "High resolution direct position determination of radio frequency sources," *IEEE Signal Processing Letters*, vol. 23, no. 2, pp. 192-196, Feb. 2016.
- [11] T. Tirer and A. J. Weiss, "Performance analysis of a high-resolution direct position determination method," *IEEE Transactions on Signal Processing*, vol. 65, no. 3, pp. 544-554, Feb. 2017.
- [12] A. J. Weiss, "Direct geolocation of wideband emitters based on delay," *IEEE Transactions on Signal Processing*, vol. 59, no. 6, pp. 2513-2521, 2011.
- [13] O. Bar-Shalom, "Efficient direct position determination of orthogonal frequency division multiplexing signals," *IET Radar, Sonar and Navigation*, vol. 3, no. 2, pp. 101-111, 2009.
- [14] L. Huang and L. Yilong, "Performance analysis of direct position determination for emitter source positioning," *American Journal of Signal Processing*, vol. 2, no. 3, pp. 41-45, 2012.
- [15] F. Chen and T. Zhou, "Direct position determination and effective extraction of multiple transmitters," *IET Journal of Engineering*, vol. 5, no. 21, pp. 7787-7791, 2019.
- [16] A. Eshkevari and S. M. S. Sadough, "Enhanced direct position determination using dynamic sensor array response," *IET Electronics Letters*, vol. 56, no. 7, pp. 354-357, 2020.
- [17] J. Du, H. Yu and G. Liu, "Unified subspace fitting framework and its performance analysis for direct position determination in the presence of multipath propagation," *IEEE Access*, vol. 7, pp. 6889-6914, 2019.
- [18] F. Ma, Z.-M. Liu, and F. Guo, "Direct position determination in asynchronous sensor networks," *IEEE Transactions on Vehicular Technology*, vol. 68, no. 9, pp. 8790-8803, sep, 2019.
- [19] Y. Ye, U. Khan, and K. Pahlavan, "On the accuracy of RF positioning in multi-capsule endoscopy," in *IEEE 22nd International Symposium on Personal, Indoor and Mobile Radio Communications*, Toronto, 2011, pp. 2173-2177.
- [20] S. T. Goh, S. A. Zekavat, and K. Pahlavan, "DOA-based endoscopy capsule localization and orientation estimation via unscented kalman filter," *IEEE Sensors Journal*, vol. 14, no. 11, pp. 3819-3829, 2014.
- [21] H. Wang, Y. Zhang, and G. Wang, "Positioning algorithm for wireless capsule endoscopy based on RSS," in *IEEE International Conference on Ubiquitous Wireless Broadband (ICUWB)*, Nanjing, 2016, pp. 1-3.
- [22] F. Bianchi, A. Masaracchia, and E. Shojaei, "Localization strategies for robotic endoscopic capsules: a review," *Taylor & Francis - Expert Review of Medical Devices*, vol. 16, pp. 381-403, 2019.
- [23] H. L. Van Trees, *Optimum array processing*, new york: John Wiley & Sons, Inc., 2002.
- [24] O. Bar-Shalom and A. J. Weiss, "Direct positioning of stationary targets using MIMO radar," *Elsevier Journal of Signal Processing*, vol. 91, no. 10, pp. 2345-2358, 2011.
- [25] F.C.C., "FCC Rules: Regulations for Title 47 C.F.R.," F.C.C., 2019.

BIOGRAPHY



Ali Eshkevari was born in Tehran, Iran, in 1968. He received the B.Sc. degree in electrical engineering (electronics) from the Khajeh Nasir Toosi University of Technology, Tehran, in 1991, and the M.Sc. degree in electrical engineering (telecommunication systems) from the Amirkabir

University of Technology, Tehran, in 1997. He is currently pursuing the Ph.D. degree with the Electrical Engineering Department, Shahid Beheshti University, Tehran. His Ph.D. thesis is on direct position determination of radio signals.



Seyed Mohammad Sajad Sadough was born in 1979. He received the B.Sc. degree in electrical engineering (electronic) from Shahid Beheshti University, Tehran, Iran, in 2002, and the M.Sc. and Ph.D. degrees in electrical engineering (telecommunication) from

Paris-Saclay University, Orsay, France, in 2004 and 2008,

respectively. During his Ph.D. (2004–2007), he was with the Institut Polytechnique de Paris (ENSTA), Paris, France, and Centrale Supélec—CNRS/Laboratory of Signals and Systems (LSS), Gif-sur-Yvette, France. He has been a Lecturer with the Electronics and Computer Engineering Department, ENSTA, where his research activities were focused on improved reception schemes for ultra-wideband communication systems. From December 2007 to September 2008, he was a Postdoctoral Researcher at Centrale Supélec—CNRS/LSS, where he was involved in research projects with Alcatel-Lucent on satellite mobile communication systems. In October 2008, he joined the Faculty of Electrical Engineering, Shahid Beheshti University, where he is currently an Associate Professor with the Telecommunication Department. His current research interests include optical wireless communications, signal processing for wireless communications, with particular emphasis on multicarrier and MIMO systems, joint channel estimation and decoding, iterative reception schemes, and receiver design under partial channel state.

Copyrights

© 2022 Licensee Shahid Chamran University of Ahvaz, Ahvaz, Iran. This article is an open-access article distributed under the terms and conditions of the Creative Commons Attribution –NonCommercial 4.0 International (CC BY-NC 4.0) License (<http://creativecommons.org/licenses/by-nc/4.0/>).





Iranian Association of
Electrical and Electronics
Engineers

Journal of Applied Research in Electrical Engineering

E-ISSN: 2783-2864

P-ISSN: 2717-414X

Homepage: <https://jaree.scu.ac.ir/>



Research Article

Influence of Gas Insulated Switchgear Configuration Components on UHF PD Signals

Reza Rostaminia* , Mehdi Vakilian , and Keyvan Firouzi 

Electrical Engineering Department and Centre of Excellence in Power System Management and Control,

Sharif University of Technology, Tehran 1458889694, Iran

* Corresponding Author: Reza_rostaminia@ee.sharif.edu

Abstract: Partial Discharge (PD) measurement is one of the main methods for condition monitoring of Gas Insulated Switchgears (GIS). Internal Ultra High Frequency (UHF) sensors can be applied for capturing PD propagated electromagnetic signals within the GIS. PD sensor placement inside the GIS is one of the main challenges for designing an online PD measuring system. For this aim, the impacts of different GIS components on propagated PD electromagnetic waves should be studied. In this paper, different PD sensor position angles (with respect to PD sensor) are used to investigate their sensitivity to measuring PD electromagnetic waves. Two distinguishable parameters from the calculated PD electromagnetic waves, the first rated electric field and the signal's power over the two frequency ranges (0.3-2 GHz and 0.3-3 GHz) are used to analyze and quantify the calculation results. The impacts of different enclosure diameters, different types of spacers, and various disconnecter contact gap distances (under different voltage levels) on this wave propagation are studied. Additionally, the two standard GIS busbar profiles, named L-shape and T-shape, are discussed in this paper. The results show that the attenuation degree of the measured PD EM waves is strongly influenced by the busbar dimensions and the configuration of its components. The GIS busbar designer can employ these results to select the proper PD sensors and their installation locations.

Keywords: Gas insulated switchgear, partial discharge, ultra-high frequency measurements, electric field and electromagnetic wave.

Article history

Received 13 December 2021; Revised 21 December 2021; Accepted 23 December 2021; Published online 8 March 2022.

© 2022 Published by Shahid Chamran University of Ahvaz & Iranian Association of Electrical and Electronics Engineers (IAEEE)

How to cite this article

R. Rostaminia, M. Vakilian, and K. Firouzi, "Influence of gas insulated switchgear configuration components on UHF PD signals," *J. Appl. Res. Electr. Eng.*, vol. 1, no. 2, pp. 139-148, 2022. DOI:10.22055/jaree.2021.39436.1039



1. INTRODUCTION

Ultra-High Frequency (UHF) Partial Discharge (PD) measurement is one of the most proper approaches to detecting defects within gas-insulated switchgear (GIS) in the early stages. Many studies have used this method in recent years [1-4]. In general, these research studies can be classified into the design and manufacturing of various UHF couplers and measuring systems, the PD location within GIS, and the identification of PD defect types and the degree of PD fault progress within the GIS.

One of the main challenges in using the UHF PD measurement technique in high voltage equipment is selecting a criterion for severity analysis of the measured PD. CIGRE working group D1.25 has proposed two steps for sensitivity verification of UHF PD measurement in GIS [5]. The CIGRE report aims to compare the measured PD

magnitude from the UHF method with the conventional IEC60270 method. Many items can influence the PD signal measured with the UHF method. [7] proposed a hybrid method in which UHF PD detection is used to detect the PD discharges (due to its higher sensitivity), and IEC 60270 measure is used to determine its severity. These items can be summarized as the type of defects, the location of defects in GIS enclosure, propagation parameters like reflection, refraction, attenuation, the PD sensor position within GIS enclosure which can result in various signal transmission paths based on the PD defect position, the type of sensor employed and its transfer function, and finally, the characteristics of other measurement paths from sensors to a monitoring system. Although the CIGRE publication has proposed a preliminary recommendation for sensitivity verification of UHF PD couplers in GIS, new studies are under way to develop a major solution for UHF PD

measurement. To address this concern, first, the impacts of each part of GIS on the attenuation of electromagnetic PD signals should be determined. This could also help to determine the number of PD UHF couplers and their positions within each bay of GIS. The electromagnetic waves produced by a PD in GIS coaxial structure have three different modes, namely, TEM, TE, and TM [6]. The cutoff frequency of each electromagnetic mode depends on the dimension and constructional characteristics of the enclosure and the conductors in a GIS [8]. The EM mode components propagate through straight, L-shape, and T-shape structures of GIS, which are investigated in [9-12]. In other researches, the effects of different parts of a GIS on EM wave propagation have been investigated. In [13], the effect of two kinds of spacers, bush type, and metal flange type is investigated on EM PD wave propagation within GIS. In [14], the electromagnetic wave propagation within the GIS enclosure is examined, and the effects of the insulated gas barrier on the attenuation of EM waves have been analyzed. The Finite Difference Time Domain (FDTD) method has been applied by the authors to simulate the PD electromagnetic wave behavior in a GIS straight configuration. Also, in [15], the authors have analyzed the effects of gas barrier properties, including its thickness, dielectric constant, and the spacing between adjacent bolts and the profile of its flanges on the electromagnetic PD wave leakage. In [8, 16], the authors have explored the effects of main GIS conductor discontinuity (such as the disconnectors discontinuity) on PD EM waves detected by the UHF sensors. Also, in [17] some experiments have been carried out on 66 kV and 154 kV T-shape GIS structures to investigate the PD EM wave mode of propagation through the GIS coaxial structure. In [18], the L-branch structure of 66 kV GIS has been selected to examine the attenuation implemented into PD EM waves in the TEM and TE modes.

Although extensive research has already been carried out on the effects of different parameters on PD EM wave propagation within GIS, more studies are still required on optimum placements of PD UHF sensors when using different busbar arrangements and under various voltage levels. One of the main difficulties in the evaluation of the results of PD EM wave propagation within GIS is the differences that exist among the wave shapes and amplitudes of the PD discharge pulses captured in each PD occurrence. Meanwhile, many parameters may have an impact on the measured PD EM waves, and it is very difficult to explore the exact effect of each one of them on the captured PD EM waves originated from different PD sources. Hence, to solve these problems, in this paper, a simulation model of GIS is developed in CST Microwave Studio software to study the effects of different parameters on PD EM wave behavior while a standard wave shape of PD is applied to the model. Therefore, first, the position of the UHF sensors with respect to the PD source location is determined. Then, the impacts of different enclosure sizes are investigated under various rated voltage levels of GIS. The effects of different parameters of the spacer, such as its thickness and type (i.e., in the form of barrier or support insulator), are studied. Then, the effects of disconnecting contacts (such as circuit breakers or disconnector contacts with various gap distances under different voltage levels) are analyzed. Additionally, the L-

shape and T-shape GIS and their structural impacts on the propagation of PD-based EM waves are investigated.

2. SIMULATION MODEL

2.1. Straight Structure

The CST Microwave Studio software is chosen to study PD-based EM wave propagation within the GIS model. At the first step, a straight GIS structure model is selected for the study. The impacts of the UHF sensor position with respect to the PD source position, the enclosure diameters, the spacer types, the contact thicknesses, the disconnector contact gap distance on the PD-related EM wave propagation (Fig. 1) are studied.

The length of the straight structure in this GIS sample is about 4.22 m. Its five compartments are considered to have a straight structure GIS model, while the length of each gas compartment, numbered 1 to 4, is 1 m, and the compartment number 5 is 20 cm long.

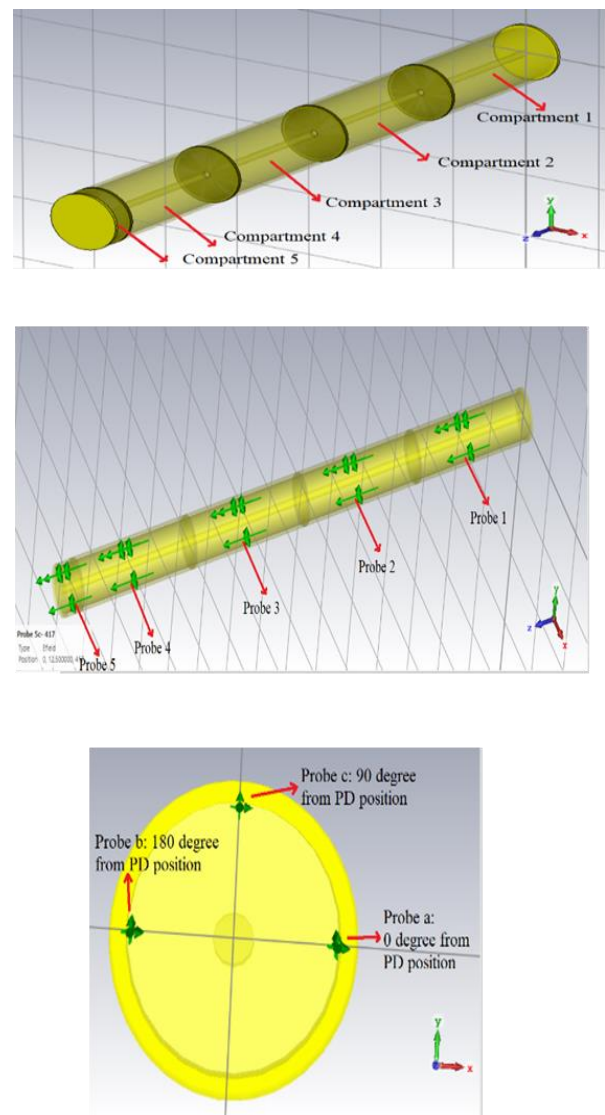


Fig. 1: Straight structure model of GIS in CST software.

The main conductor is made of aluminum. The material of the spacer insulator is epoxy resin with a thickness of 2 cm. At the two ends of the structure, two flanges with a thickness of 2 cm and the same diameter as the GIS enclosures are fitted. As it is shown in Fig. 1-c, three UHF PD probes (probe A, probe B, and probe C) are located at angles of 0° , 180° , and 90° versus the PD source (in GIS enclosure), respectively. Each probe is placed at the middle of the related compartment length while the PD source is located near the GIS main conductor along the probe-A in the middle of compartment 1.

In each compartment, there are three UHF probes located in the abovementioned direction angles with respect to the PD source. The PD current wave shape is a gaussian current pulse of 1 ns width and 15 mA amplitude representing 5 pc charge of PD (Fig. 2).

To study the difference between the effects of a barrier insulator and a support insulator on PD EM wave propagation, two types of support insulator, one with three holes and the other with four holes, are employed (Fig. 3).

Each hole has a diameter of 4 cm and is located in a symmetrical position with respect to the main conductor. To investigate the effects of the disconnecter gap distance on PD-based EM wave propagation, a gap distance is implemented along the main conductor of compartment 2 (having a straight structure) (Fig.4). The length of its gap varies from 10 cm to 30 cm.

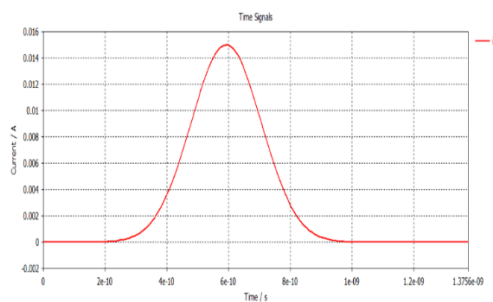


Fig. 2: The PD current gaussian wave shape.

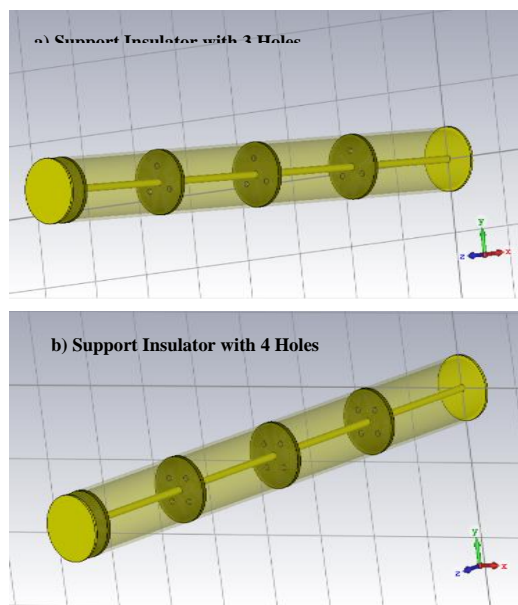


Fig. 3: Different types of support insulator as a spacer in the model, (a) with three holes, and (b) with four holes.

2.2. L-Shape Structure

Four gas compartments of the L-Shape structure are implemented to the GIS busbar in these studies. The diameter of the enclosure is 40 cm, and the length of each compartment is 1 m. In each compartment (chamber-bay), as in the straight structure model, three electric field probes are located at angles of 0° , 180° , and 90° with respect to the PD source position. The PD source is located in the middle of compartment 1, and the other dimensional parts of the model are the same as that of the straight model (Fig. 5).

2.3. T-Shape Structure

Six gas compartments are employed in the T-Shape structure model, and the length of each compartment is 1 m (Fig. 6). The PD source is placed in the middle of compartment 1. All of the other features of the model are the same as the straight structure model.

3. SIMULATION RESULTS AND DISCUSSION

The simulation results obtained from electric field probes are shown in Fig. 7 in which the time-domain and frequency-domain PD calculated signal can be seen. The time differences of signals arrival, among the different installed probes (due to their distances from the PD) can be seen.

As it is evident, a lot of distortions exist in both the time-domain and frequency-domain captured signals. These distortions are due to reflections and refractions of PD EM waves within the enclosed metal enclosure of the GIS model. The first peak value of the signal in the time domain and the power of the signal in the frequency domain are selected as criteria to analyze and compare the different measurement results of PD signals under a specific condition. The UHF range of frequency is from 300 MHz to 3 GHz. However, in most commercial UHF antennas of PD measuring systems in GIS, the signal measurement frequency is limited to 2 GHz. Accordingly, two ranges of spectrum are chosen for signal power measurement in the frequency domain. Therefore, in each scenario, the following three parameters have been compared:

- a- Emax: First peak of calculated electric field
- b- PI: the power of the signal in frequency ranges between 300 MHz to 3 GHz.
- c- PII: the power of the signal in frequency ranges between 300 MHz to 2 GHz.

As it is stated in the previous section, three probes with directions of 0° , 180° , and 90° with respect to the PD source position (probe A, probe B, and probe C, respectively) are considered. Hence, the differences between the results obtained from each one within the same compartments will be analyzed.

In Fig. 8, the electric fields calculated by these three probes are presented. The peak value of the electric field in each probe is per-united based on the value calculated by 'probe A' within compartment 1.

As it can be seen, the value of 'probe A' in compartment 1 is maximum due to the direct passage of the PD EM wave along with this probe. While 'probe B' and 'probe C' have values close to each other, which is about 0.3 with respect to the

'probe A' calculated value. Considering the values of 'Probe A' in compartments 1 to 5, it can be seen that except compartment 1, the other compartments have calculated values that are the same as each other. Also, this can be seen for 'probe B' and 'probe C' in compartments 1 to 5.

Fig. 9 depicts a comparison between the power of signals PI and PII in the two different frequency ranges. When comparing the values of these signals calculated by 'probe A', 'probe B', and 'probe C' in compartment 1, a significant reduction in signal power can be seen in 'probe A' versus the two other probes. However, the difference between powers calculated by 'probe A' and 'probe C' is more than the related difference of 'probe A' and 'probe B'. This is because of 90° direction angle of 'probe C' versus the PD source. The other important note in Fig. 9 is that the calculated values of the three probes in compartment 5 are increased versus the calculated values of the probes in the other compartments. This is due to the position of compartment 5, which is at the end of the employed GIS model. At the end of the model, the reflections of EM waves are intense, and these reflections contain a higher order of frequencies, which are more than 2 GHz. Therefore, the calculated values of probes in compartment 5, as shown in Fig. 9, are not higher than those in the other compartments. When comparing these against the results shown in Fig. 8, it can be seen that the calculated values of 'probe C' are significantly lower than the calculated values of 'probe A' and 'probe B'. Since in practice under the PD occurrence within the GIS, the position and direction angle of PD occurrence with respect to the PD sensor position within a compartment is unspecified, 'probe C' (the worst case) is selected for following the investigations.

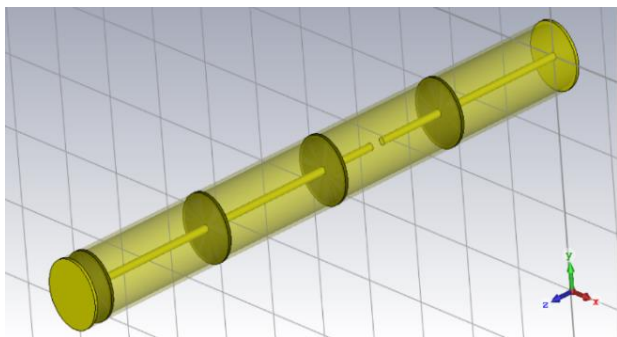


Fig. 4: The model of disconnector contacts in compartment 2 of the straight structure model.

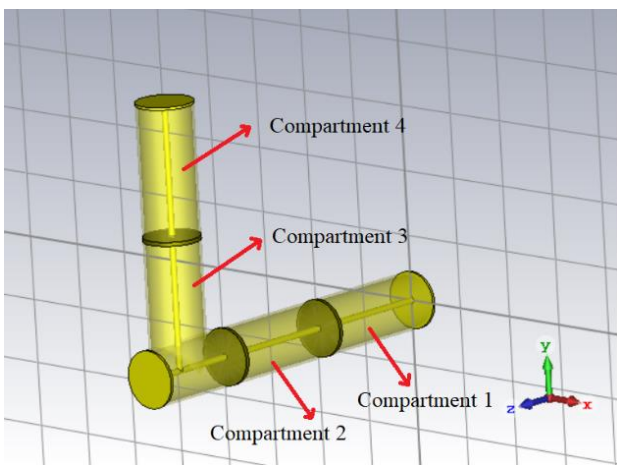


Fig. 5: The L-Shape structure of the model.

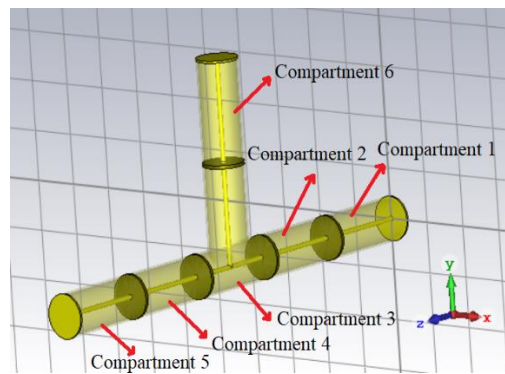
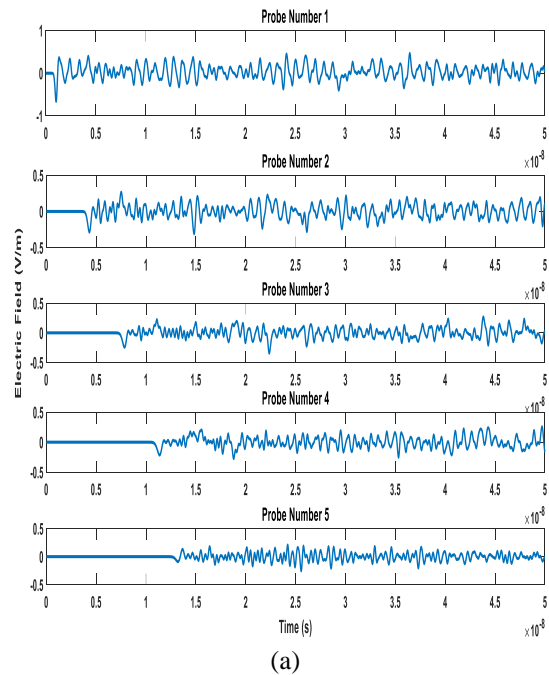
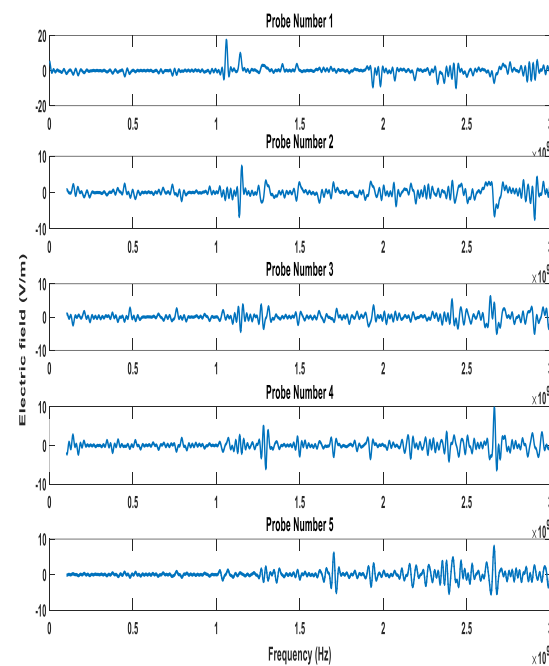


Fig. 6: The T-Shape structure of the model.



(a)



(b)

Fig. 7: Calculated PD EM wave with electric field probes: (a) Time-domain electric field, and (b) Frequency domain electric field.

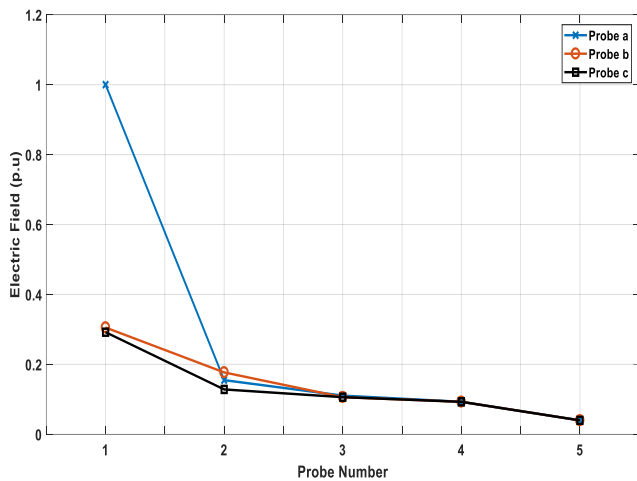


Fig. 8: Calculated electric field first peak in three sets of probe number 1.

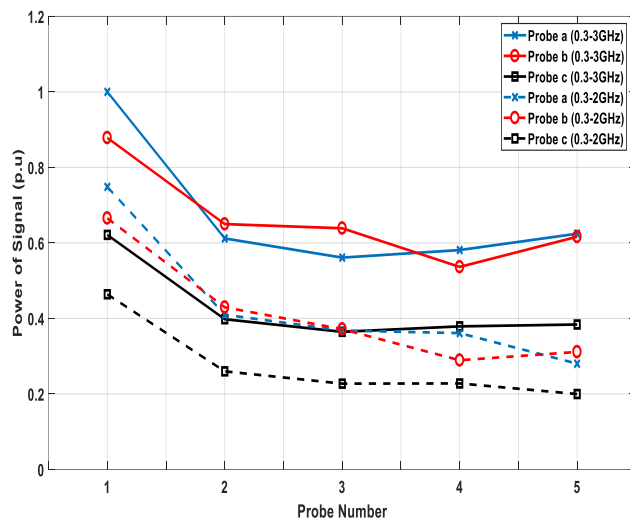


Fig. 9: The calculated signal power with frequency ranges 0.3-2 GHz and 0.3-3 GHz in three sets of probe number 1.

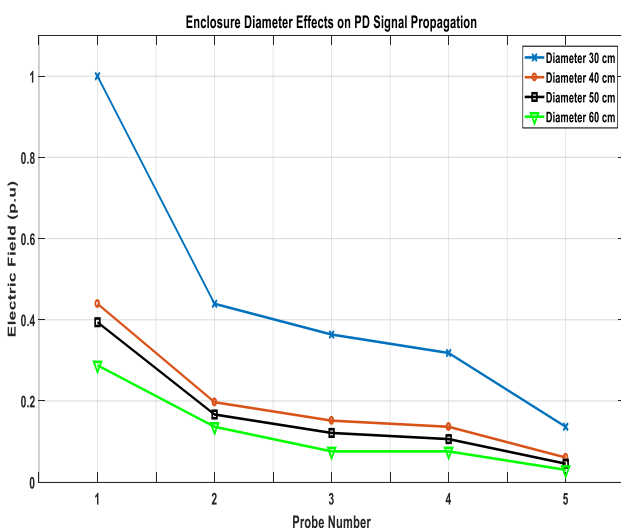


Fig. 10: The effects of different enclosure diameters on the first peak of the calculated electric field.

3.1. Effects of GIS Enclosure Diameters

Different voltage levels of GIS result in various sizes of enclosures. Multiple diameters of enclosures, i.e. 30 cm, 40 cm, 50 cm, and 60 cm, are selected to examine the effects of enclosure dimension on the propagation of PD EM wave. In this case, as the optimum design for a cylindrical GIS system, the diameter of the enclosure is considered 2.73 times the diameter of the main conductor [19]. Fig. 10 shows the electric fields calculated with 'probe C' in the five compartments (and for four diameters of the enclosure).

The electric field value for each probe is per-united based on the calculated value of 'probe C' in compartment 1 of 30 cm enclosure diameter.

As can be seen in Fig. 10, as the diameter of the enclosure increases, the calculated electric fields of each probe decrease. This is due to an increase in the distance of the PD source and the measurement probes; i.e., as the diameter of the enclosure increases, the length of the travel path for the PD-based EM wave signals will be enhanced. Although for each specific size of the enclosure, when the signal is passing compartment 1, the amplitude of the calculated PD signal decreases. There is a little difference between the calculated values located in an enclosure of 40 cm diameter with respect to a 60-cm enclosure for each probe.

Fig. 11 displays the calculated power of the signal in frequency ranges from 300 MHz to 3 GHz and from 300 MHz to 2 GHz for different enclosure diameters. The signal power calculated in an enclosure of 30 cm diameter is more than the values calculated in the enclosures of other diameters. The calculated values by each probe located inside an enclosure of 40 cm diameter is almost half of the one located inside an enclosure of 30 cm diameter. However, the calculated values of probes in enclosures of 50 cm and 60 cm diameter are almost the same.

Therefore, it can be concluded that by increasing the enclosure diameter to over 40 cm, the signal power in the frequency range from 300 MHz to 2 GHz remains unchanged, and the distance from the PD source has no significant effect on the sensitivity of the PD measurements. Meanwhile, there is a significant difference among the calculated power of the signal in different compartments in frequency ranges of 0.3-2 GHz and 0.3-3 GHz. As it can be seen in Fig. 11, the calculated power of the signal in each compartment in the frequency range of 0.3-2 GHz is almost half of the related calculated value in the frequency range of 0.3-3 GHz.

3.2. Effects of GIS Spacer

The presence of a spacer within the structure of a GIS and its effect on PD-based EM wave propagation can be studied from two points of view. In one study, the spacer thicknesses, and in the second, the type of the spacer is investigated. Different manufacturers may employ different spacer thicknesses under different operating voltage levels. To analyze the impacts of gas barrier spacer thickness, the spacer with thicknesses of 2 cm, 3 cm, 4 cm, and 5 cm are investigated. The simulation results show no significant differences between the peaks of the electric field calculated using the different probes. Fig. 12 displays the power of the signal in the frequency ranges of 300 MHz to 3 GHz and 300MHz to 2 GHz. The magnitude of wave presented in this

figure is in per-unit with reference to the 'probe C' of compartment 1, which calculated magnitude of 2 cm spacer thickness. The signal power calculated by probes, located in different compartments probe, is increased slightly as a function of the spacer thickness increment change. However, the spacer thickness affects the PD-based EM wave propagation negligibly in the frequency range of 0.3-2 GHz.

There are two types of spacers within the GIS structure: the gas barrier and the support insulator. With a gas barrier, the gas inside the two adjacent compartments cannot flow through the barrier. However, when a support insulator is employed, the gas between the two adjacent compartments can move through this insulator (Fig. 13).

A support insulator usually has three or four holes in its structure. Fig. 14 presents the signal power of PD-based EM wave propagation when different types of spacers are used. As can be seen, the signal power of UHF probes in the frequency range of 0.3-3 GHz is almost 60 percent of the power of an identical probe in the frequency range of 0.3-2 GHz. Also, in the frequency range of 0.3-3 GHz, the signal power of probe 5 is more than that of probe 4. This is due to reflections of PD-based EM waves at the end of the structure model.

However, in the frequency range of 0.3-2 GHz, the signal power decreases as one gets far away from the PD source, and the difference between the three types of the spacer is negligible. This means that the reflected wave from the end of the straight model has more components in the frequency range of 2-3 GHz. Finally, it can be concluded that each probe in the straight structure of GIS with different spacer types can cover at least 5 m for both PD localization and pattern recognition purposes.

3.3. Effects of Disconnecter

As is shown in Fig. 4, a disconnecter is considered at compartment 2 of the straight GIS model. The electric fields calculated by probes 1 to 5 are shown in Fig. 15. The distance between contacts of the conductor is varied from 10 to 30 cm. The first peak of the electric field is in per-unit of 'probe 1-C' peak. By increasing the contact distance of the disconnecter, the decrement of the electric field peak will rise. In Fig. 16, the signal power in the frequency range of 0.3-2 GHz is almost the same for different contact distances of the disconnecter. As a result, although the disconnect gap has no significant effects on PD-based EM wave signal power, it can result in a considerable reduction in the first peak of the calculated electric field. Since the PD localization within GIS is based on the time arrival difference of first electric field peaks to different sensors, this can result in errors in the estimation of the PD source position. Therefore, it is better to apply PD sensors beside each disconnecter's contacts in a GIS arrangement to ensure high accuracy in analyzing the results.

3.4. Effects of L-Shape Structure

The L-Shape structure used in this study is shown in Fig. 5. In each compartment, except for compartment 3, one set of electric field probes is located in the middle of the compartment. The positions of these electric field probes around the periphery are in direction angles of 0, 180, and 90 degrees with respect to the PD source position. In

compartment 3, two sets of electric field probes are located, one in the straight part of PD occurrence (probe 3) and the other farther after the L-shape structure (probe 4). The calculated first peak of the electric field is shown in Fig. 17. The calculated electric field peak of probe 4, in comparison to the probe 3 measurement, is significantly lower. Fig. 18 depicts the power of the signal calculated in the frequency ranges of 0.3-2 GHz and 0.3- 3GHz.

The signal power in the frequency range of 0.3-2 GHz decreases with a steady gradient. However, the signal power decrement rate, when the probe is relatively far from the PD source (i.e., in probe 4), is much higher than this decrement rate for the other probes.

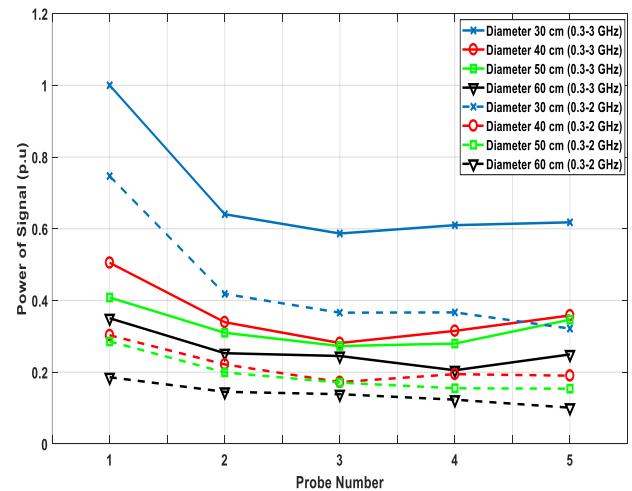


Fig. 11: The effects of different enclosure diameters on signal power in the frequency ranges of 0.3-2 GHz and 0.3-3 GHz.

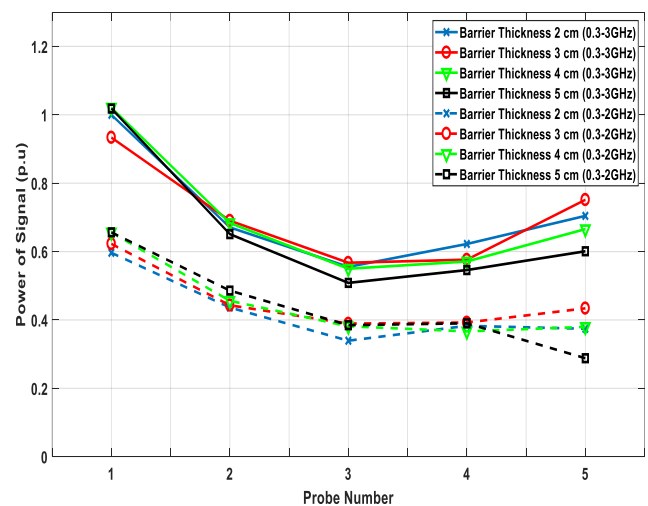


Fig. 12: The effects of barrier thickness on signal's power in the frequency range of 0.3-2 GHz and 0.3-3 GHz.

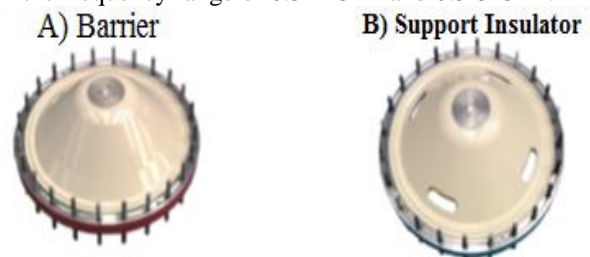


Fig. 13: Two types of spacers including (a) gas barrier, and (b) support insulator.

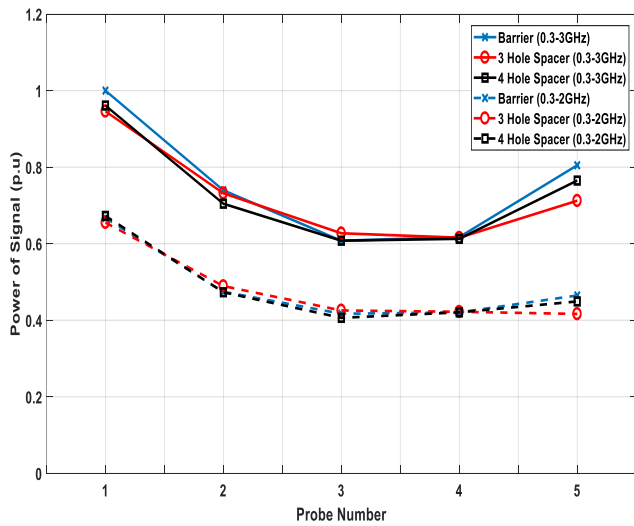


Fig. 14: The effects of spacer types on signal power in the frequency ranges of 0.3-2 GHz and 0.3-3 GHz.

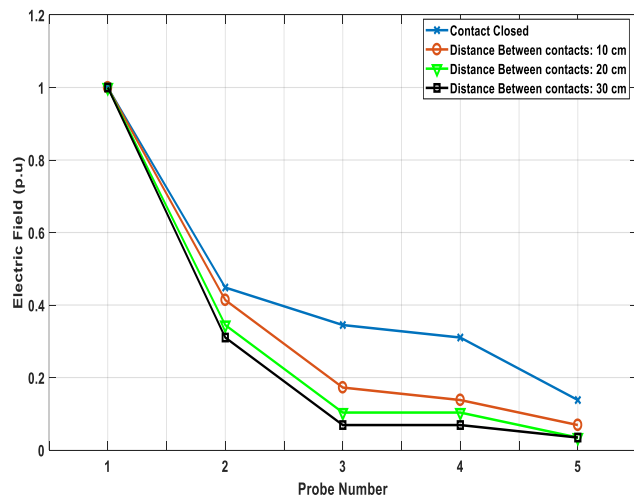


Fig. 15: The effects of disconnecter contact distance on the first peak of the calculated electric field.

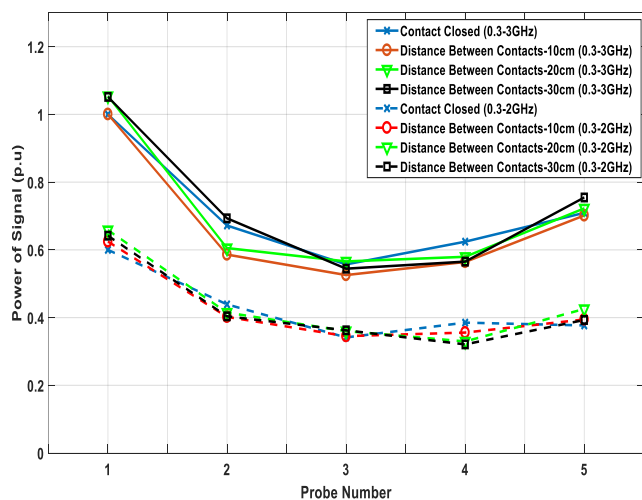


Fig. 16: The effects of disconnecter contact distance on signal power in the frequency ranges of 0.3-2 GHz and 0.3-3 GHz.

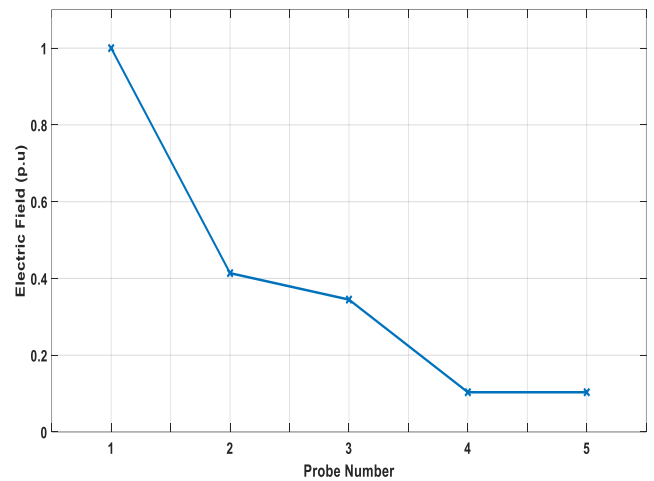


Fig. 17: The effects of L-shape structure on the first peak of the calculated electric field.

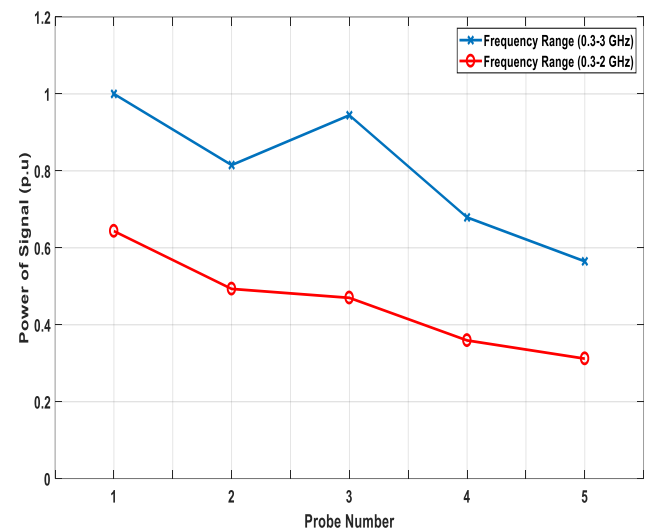


Fig. 18: The effects of L-shape structure on signal power in the frequency ranges of 0.3-2 GHz and 0.3-3 GHz.

Therefore, it can be concluded that the high-frequency components of the signal cannot pass through the L-shape structure section of the GIS. However, the decrement of the signal's power in a frequency range of 0.3-3 GHz is not related to the L-Shape structure, and it is the result of getting far from the PD source. As a result, although the signal power in these frequency ranges is almost steady for different probes in the L-shape structure, the calculated first peak of the electric field experiences a significant reduction after passing through L-shape part of the structure. This can have some effects on analyzing the calculated results, especially when PD is localized. Hence, it is better to have PD sensors in both L-shaped sections of the GIS structure.

3.5. Effects of T-Shape Structure

Fig. 6 shows the T-shape structure, which is employed to study PD-based EM wave propagation. In each compartment, except for compartment 3, one set of electric field measuring probes are applied just in the middle of the compartment. The position of the electric field probes is in direction angles 0, 180, and 90 degrees based on the PD source position. In compartment 3, like the L-shape structure, two sets of electric field probes are considered – one set in a straight direction

(probe 3) and the other in the T-branch indirect line (probe 6) with PD source. The probes marked number 7 are placed in compartment 6. In Fig. 19, the first peak of the electric field calculated on the capture of the PD-based EM wave is shown. By comparing the results of probes 4 and 6, the decrement of the signal peak in the T-branch section is shown to be more than that in the straight section. As a function of the distance increment of the UHF probe from the PD source position, the electric field peak is decreased. Fig. 20 shows the variations of power of the signal in the frequency ranges of 0.3-2 GHz and 0.3-3 GHz. As can be seen, the PD-based EM waves after passing through the T-branch section of the structure lose the high and low frequency of their powers. However, the power decrement in the frequency range of 0.3-3 GHz is more than the power decrement in the frequency range of 0.3-2 GHz. The reason is that when the PD-based EM waves are crossing a GIS T-structure, only the TEM mode of those signals will pass through while most of the TE mode of signals will be lost. As can be seen, the power of the signal in probe 7 is less than half of the power calculated by probe 1 in the frequency range of 0.3-2 GHz. Therefore,

when passing through the T-branch GIS structure, PD EM waves can lose both their signal power and their calculated first electric field. However, in the straight branch of the T-shape structure, there are no significant changes in the signal power, while a 50% decrement is seen in the first peak of the calculated electric field. Accordingly, for both PD localization and distinguishing defect type purposes, a PD sensor should be located in the T-branch of the GIS structure.

4. SUMMARY AND CONCLUSION

The GIS busbar components and structure have impacts on the calculated values of PD EM waves and the signals captured by UHF sensors. Accordingly, this paper examines the impact of the position and direction angle of PD sensors versus different PD sources on the calculated signals. It is shown that the PD sensors having a direction angle of 90 degrees versus the PD source have the lowest sensitivity regarding the PD signal measurements. Also, the following five conclusions have been investigated and verified:

1- It is shown using the calculation results that as the enclosure diameter is increased, the size of the first peak of the PD signal (electric field) is reduced. However, the signal power in the frequency range of 0.3-2 GHz encounters a small change when the enclosure diameter is increased.

2- It is also shown using the calculation results that the spacer thickness has a small impact on the size of the first peak of the electric field and the signal power in the frequency range of 0.3-2 GHz. Also, it is shown that the spacer type (i.e. a gas barrier or support insulator with three or four holes) has small effects on the EM-related PD calculated signal. Therefore, each probe in the straight structure section of GIS (with different spacer types) can cover at least a distance of 5 m for both PD localization and pattern recognition purposes.

3- The variations in the size of a disconnector gap distance (at different operating voltage levels of a GIS) affect the PD-based EM wave propagation process. As its contacts gap increases, the size of the first peak in its electric field reduces. However, the signal power in the frequency range of 0.3-2 GHz is much less influenced by contact gap distances.

Hence, for PD localization purposes, it is better to apply a PD sensor after each disconnector contact in the GIS arrangements.

4- The L-shape structure of GIS can result in a significant reduction in the calculated first peak of the PD signal electric field. However, the reduction in the gradient of its signal power in the frequency range of 0.3-3 GHz is increased while the gradient of power decrease in the frequency range of 0.3-2 GHz is constant. This means that the high-frequency TE modes of a signal cannot pass through the L-shape structure. Therefore, it is better to locate PD sensors on both sides of a GIS L-shape structure to identify the PD defects type and to localize the PD source.

5- A GIS busbar of the T-shape structure attenuates the EM PD wave propagation. The PD signal's first peak, when passed through a T-branch structure, is compared against the signal's peak in a straight branch. It is shown that in the former case, the signal is significantly reduced. Additionally, the signal's power reduction gradient in a T-branch is more than the one (at the same compartment) in a straight branch. This reduction is about half of the signal power reduction when passing through a T-branch structure. Hence, it is essential to locate a PD sensor in the T-branch of a GIS structure to localize the PD source and to identify the type of PD.

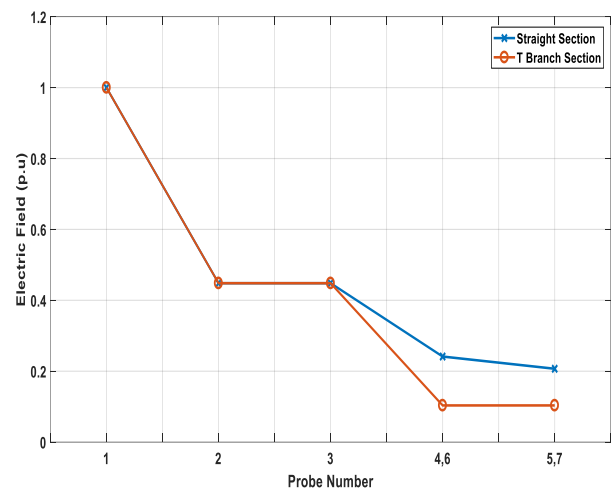


Fig. 19: The effects of T-shape structure on the first peak of the calculated electric field.

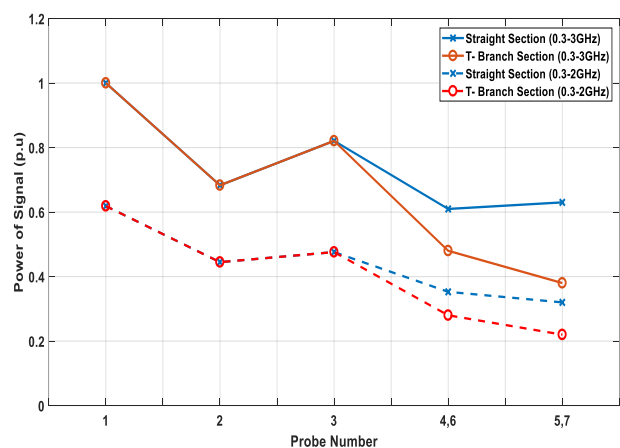


Fig. 20: The effects of T-shape structure on signal power in the frequency ranges of 0.3-2 GHz and 0.3-3 GHz.

CREDIT AUTHORSHIP CONTRIBUTION STATEMENT

Reza Rostaminia: Conceptualization, Data curation, Formal analysis, Investigation, Methodology, Project administration, Resources, Software, Supervision, Validation, Visualization, Roles/Writing - original draft, Writing - review & editing. **Mehdi Vakilian:** Investigation, Supervision, Validation, Visualization, Writing - review & editing. **Keyvan Firouzi:** Data curation, Supervision, Validation, Visualization, Writing - review & editing.

DECLARATION OF COMPETING INTEREST

The authors declare that they have no known competing financial interests or personal relationships that could have appeared to influence the work reported in this paper. The ethical issues; including plagiarism, informed consent, misconduct, data fabrication and/or falsification, double publication and/or submission, redundancy has been completely observed by the authors.

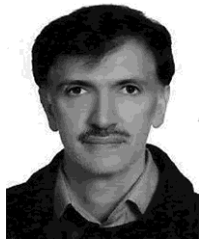
REFERENCES

- [1] X. Li, X. Wang, D. Xie, X. Wang, A. Yang, and M. Rong, "Time-frequency analysis of PD-induced UHF signal in GIS and feature extraction using invariant moments," *IET Science, Measurement & Technology*, vol.12, no. 2, pp. 169-175, 2018.
- [2] F. Bin, F. Wang, Q. Sun, S. Lin, Y. Xie, and M. Fan, "Internal UHF antenna for partial discharge detection in GIS," *IET Microwaves, Antennas & Propagation*, vol. 12, no. 14, pp. 2184-2190, 2018.
- [3] X. Li, X. Wang, A. Yang, M. Rong, "Partial discharge source localization in GIS based on image edge detection and support vector machine," *IEEE Transactions on Power Delivery*, vol. 34, no. 4, pp. 1795-1802, 2019.
- [4] C. Zachariades, R. Shuttleworth, R. Giussani, and T. Loh, "A Wideband spiral UHF coupler with tuning nodules for partial discharge detection," *IEEE Transactions on Power Delivery*, vol. 34, no. 4, pp. 1300-1308, 2019.
- [5] CIGRE, *UHF Partial Discharge Detection System for GIS: Application Guide for Sensitivity Verification*, pp. 1-35, 1995.
- [6] K. Firuzi, M. Vakilian, B. T. Phung and T. R. Blackburn, "A hybrid transformer PD monitoring method using simultaneous IEC 60270 and RF data," *IEEE Transactions on Power Delivery*, vol. 34, no. 4, pp. 1374 - 1382, 2019.
- [7] H. Muto, M. Doi, H. Fujii, and M. Kamei, "Resonance characteristics and identification of modes of electromagnetic waves excited by partial discharges in GIS," *Electrical Engineering in Japan*, vol. 131, no. 2, pp. 1-11, 2000.
- [8] M. Shi, X. Han, X. Zhang, Z. Zhang, and J. Li, "Effect of disconnecter and high-voltage conductor on propagation characteristics of PD-induced UHF signals," *IET High Volt*, vol. 3, no. 3, pp. 187-192, 2018.
- [9] S. Okabe et al., "Simulation of propagation characteristics of higher order mode electromagnetic waves in GIS," *IEEE Transactions on Dielectrics and Electrical Insulation*, vol. 13, pp. 855-861, 2006.
- [10] M. Yoshimura, H. Muto, C. Nishida, M. Kamei, S. Okabe, and S. Kaneko, "Propagation properties of electromagnetic wave through T-branch and obliquely angled tank," *IEEE Transactions on Dielectrics and Electrical Insulation*, vol. 14, pp. 328-333, 2007.
- [11] S. Okabe, S. Kaneko, M. Yoshimura, H. Muto, C. Nishida, and M. Kamei, "Partial discharge diagnosis method using electromagnetic wave mode transformation in gas insulated switchgear," *IEEE Transactions on Dielectrics and Electrical Insulation*, vol. 14, no. 3, pp. 702-709, 2007.
- [12] S. Kaneko, S. Okabe, M. Yoshimura, H. Muto, C. Nishida, and M. Kamei, "Partial discharge diagnosis method using electromagnetic wave mode transformation in actual GIS structure," *IEEE Transactions on Dielectrics and Electrical Insulation*, vol. 15, no. 5, pp. 1329-1339, 2008.
- [13] M. Hikita, S. Ohtsuka, G. Ueta, S. Okabe, T. Hoshino, and S. Maruyama, "Influence of Insulating Spacer Type on Propagation Properties of PD-induced Electromagnetic Wave in GIS," *IEEE Transactions on Dielectrics and Electrical Insulation*, vol. 17, no. 5, pp. 1643-1648, 2010.
- [14] T. Hoshino, Sh. Maruyama, and T. Sakakibara, "Simulation of propagating electromagnetic wave due to partial discharge in GIS using FDTD," *IEEE Transaction on Power Delivery*, vol. 24, no. 1, pp. 153-159, 2009.
- [15] S. Kaneko, S. Okabe, H. Muto, M. Yoshimura, C. Nishida, and M. Kamei, "Electromagnetic wave radiated from an insulating spacer in gas insulated switchgear with partial discharge detection," *IEEE Transactions on Dielectrics and Electrical Insulation*, vol. 16, no. 1, pp. 60-68, 2009.
- [16] M. Hikita, S. Ohtsuka, S. Okabe, J. Wada, T. Hoshino, and S. Maruyama, "Influence of disconnecting part on propagation properties of PD induced electromagnetic wave in model GIS," *IEEE Transactions on Dielectrics and Electrical Insulation*, vol. 17, no. 6, pp. 1731-1737, 2010.
- [17] M. Hikita, S. Ohtsuka, T. Hoshino, S. Maruyama, G. Ueta and S. Okabe, "Propagation properties of PD-induced electromagnetic wave in GIS model tank with T branch structure," *IEEE Transactions on Dielectrics and Electrical Insulation*, vol. 18, no. 1, pp. 256-263, 2011.
- [18] M. Hikita, S. Ohtsuka, J. Wada, S. Okabe, T. Hoshino, and S. Maruyama, "Propagation properties of PD-induced electromagnetic wave in 66 kV GIS model tank with L branch structure," *IEEE Transactions on Dielectrics and Electrical Insulation*, vol. 18, no. 5, pp. 1678-1685, 2011.
- [19] H. Koch, *Gas-insulated transmission lines*. John Wiley & Sons, 2012.

BIOGRAPHY



Reza Rostaminia received the B.Sc. degree in Electrical and Electronics Engineering from Babol Noshirvani University of Technology, Babol, Iran in 2007, The M.Sc. degree in Electrical Power Engineering from Khaje Nasir Toosi University of Technology (KNTU), Tehran, Iran in 2011 and the Ph.D. degree in Electric Power Engineering (High Voltage Engineering) from Shahid Chamran University of Ahwaz, Ahwaz, Iran in 2017. He was a post-doctoral researcher at the same university from 2019 to 2020. From 2015 to 2018, he was a sabbatical study in Electric Power Engineering (High Voltage Engineering) from Sharif University of Technology, Tehran, Iran in 2021. He joined the Parsian Substation Development Company, Tehran, Iran, where he is currently Technical Head of HV Substation Equipment Department. His research interest is High Voltage Engineering, Dielectrics and Insulation, Partial Discharge, Condition Monitoring and Diagnosis of High Voltage Equipment, High Voltage Substation Design and Earthing design.



Mehdi Vakilian (M'88–SM'15) received the B.Sc. degree in electrical engineering and the M.Sc. degree in electric power engineering from the Sharif University of Technology, Tehran, Iran, in 1978 and 1986, respectively, and the Ph.D. degree in electric power engineering from Rensselaer Polytechnic Institute, Troy, NY, USA, in 1993. From 1981 to 1983, he was with Iran Generation and

Transmission Company, and then with the Iranian Ministry of Energy from 1984 to 1985. Since 1986, he has been with the Faculty of the Department of Electrical Engineering, Sharif University of Technology. During 2001–2003, and 2014–2018 he was the Chairman of the department. During 2003 to 2004, and part of 2007, he was on leave of study at the School of Electrical Engineering and Telecommunications, University of New South Wales, Sydney, Australia. His research interests include transient modeling of power system equipment, especially power transformers, optimum design of high-voltage equipment insulation, monitoring of power system equipment and their insulations, especially with partial discharge measurement, power system transients, and distribution system studies.



Keyvan Firuzi received the B.Sc. degree in Electrical and Electronics Engineering from University of Tabriz, Tabriz, Iran in 2012, The M.Sc. degree in Electrical Power Engineering and the Ph.D. degree in Electric Power Engineering (High Voltage Engineering) from Sharif University of Technology, Tehran, Iran in 2014 and 2019 respectively. He was a post-doctoral researcher at the same university from 2019 to 2020. From 2015 to 2018, he was a Research Scientist with Niroo Research Institution (NRI). In 2021, he joined the Electrical and Electronics Engineering Department at METU, where he is currently working as an Assistant Professor. His research interest is High Voltage Engineering, Dielectrics and Insulation, Partial Discharge, Condition Monitoring and Diagnosis of High Voltage Equipment, Signal Processing, and Machine Learning.

Copyrights

© 2022 Licensee Shahid Chamran University of Ahwaz, Ahwaz, Iran. This article is an open-access article distributed under the terms and conditions of the Creative Commons Attribution–NonCommercial 4.0 International (CC BY-NC 4.0) License (<http://creativecommons.org/licenses/by-nc/4.0/>).





Iranian Association of
Electrical and Electronics
Engineers

Journal of Applied Research in Electrical Engineering

E-ISSN: 2783-2864

P-ISSN: 2717-414X

Homepage: <https://jaree.scu.ac.ir/>



Research Article

Optimal Switch Placement in Radial Distribution Networks to Reduce Energy Loss and Improve Network Security in Khuzestan Province Conditions

Ali Rouhipour , Elaheh Mashhour* , and Mohsen Saniei

Department of Electrical Engineering, Faculty of Engineering, Shahid Chamran University of Ahvaz, Ahvaz 6135785311, Iran

* Corresponding Author: e.mashhour@scu.ac.ir

Abstract: This paper develops a new model for the optimal placement of switches (both manual and automatic ones) in distribution networks to simultaneously reduce energy loss and improve network security. Expected energy not supplied (EENS) is assumed as the security index, and a method is developed for more exact calculation of this index regarding drastic climatic changes along with global warming and the resultant effects on both power consumption patterns and power network occurrence. The objective function of the problem is minimizing investment and maintenance costs, the cost of energy loss, and EENS cost. The suggested model can locate optimal places for installing the switches and their seasonal closed and open states so that the total costs can be minimized. The model is implemented on two test networks and evaluated under different scenarios. According to the results, despite the higher costs of automatic switches, the application of automatic switches is more economical in low-security networks for improving network security.

Keywords: Sectionalizing switch, tie switch, expected energy not supplied, seasonal network configuration, energy loss, investment cost.

Article history

Received 21 August 2021; Revised 28 December 2021; Accepted 31 December 2021; Published online 8 March 2022.

© 2022 Published by Shahid Chamran University of Ahvaz & Iranian Association of Electrical and Electronics Engineers (IAEEE)

How to cite this article

A. Rouhipour, E. Mashhour, and M. Saniei, "Optimal switch placement in radial distribution networks to reduce energy loss and improve network security in Khuzestan province conditions," *J. Appl. Res. Electr. Eng.*, vol. 1, no. 2, pp. 149-158, 2022. DOI: [10.22055/jaree.2021.38321.1034](https://doi.org/10.22055/jaree.2021.38321.1034)



1. INTRODUCTION

Distribution network loss and security have always attracted the attention of distribution network operators. In some countries including Iran, the power industry is controlled with a wholesale competition model. In this model, distribution companies purchase the power required for consumers and network losses at an hourly price from a wholesale power market while receiving money only for energy delivered to the end-users at a regulatory price. Therefore, power loss reduction and security improvement of these networks are viable solutions for decreasing the costs of power purchase and increasing the revenue of distribution companies by the continuous sale of power to subscribers.

A review of the literature shows that reducing distribution network losses and increasing network security have always been the focus of scholarly attention. Methods proposed for reducing network losses include reactive power resources management [1], optimal conductor selection [2, 3], network reconfiguration (to reduce power or energy losses) [4, 5], or a combination of these methods [6]. In some cases,

network reconfiguration has been proposed to reduce the loss and improve the security of the distribution network [7]. The solutions proposed for improving network security can be classified into three general classes. The first class, which involves a very limited number of works, seeks to improve network security through improving the security of different system components [8]. The second class contains studies that rely on other feed resources, such as distributed generations (DGs) [9]. The third class subsuming many works focuses on sectionalizing the placement of switches to improve distribution network security [10-15]. In [10], an optimal sectionalizing switch placement problem in distribution networks is formulated to minimize the sum of investment cost, customer outage cost, and switch installation and maintenance cost. Then, it is solved using the Simulated Annealing (SA) algorithm. In [11], sectionalizing switch placement is done for manual and automatic switches in a distribution network to minimize the sum of investment cost and customer interruption cost using the immune algorithm. In [12], the problem of finding optimal number and places of sectionalizing switches is formulated to minimize the switch

purchasing and maintenance costs and customer interruption cost, and the problem is then solved by a fuzzy optimization method. In [13], the problem of finding optimal number and places of automatic switches in distribution networks is modelled and solved to minimize the sum of customer interruption cost, investment cost, and maintenance cost in the form of a mixed-integer linear optimization problem. In [14], a method is presented for determining the optimal combination of sectionalizing and tie switches for the optimal design of the distribution automation system so as to minimize the losses and keep 100% of the reliability of service restoration. Moreover, an algorithm is provided to determine the optimal switch placement based on the pre-determined number for each kind of switch. In [15], the differential search algorithm is used to determine the optimal placement and number of remote-control switches in a radial distribution network so that the cost of expected energy not supplied and investment cost can be minimized. In [16], a model is developed for the optimal simultaneous allocation of fault indicators and sectionalizing switches in a complex distribution network based on reliability and cost-benefit analyses. The objective function is minimizing the sum of investment cost, maintenance cost, and customer interruption cost. In [17], a risk-based two-stage mixed-integer linear programming model is presented for the optimal placement of sectionalizing switches in active distribution networks considering the island mode operation of distributed energy resources.

Note that the third solution for reducing losses (i.e., network reconfiguration) and the third solution for improving network security (i.e., sectionalizing switch placement) are interrelated. In other words, optimal network reconfiguration to minimize energy losses is affected by the placement of the switches. Besides, network security depends not only on the place of the switches but also on the network configuration in normal conditions. Therefore, sectionalizing switch placement with the mere aim of improving network security and then using these switches in the reconfiguration process to reduce network loss is not necessarily the cost-effective and optimal solution. So, it is essential to pay attention to both roles of switches during the normal functioning of the network and during outages after a fault. In this regard, the drastic changes in climate and increased temperature of the earth and the resultant effects on power consumption patterns and power network occurrences should be taken into account. This increase in the earth's temperature is notable in some areas of the world such as parts of the Middle East. For example, in June and July of 2017, some parts of the Middle East experienced their maximum temperature compared to their previous patterns in a relatively long period of 4 weeks. In this context, on June 29th, 2017, Ahvaz city, the capital of Khuzestan province in Iran, was the warmest city in the world with a temperature of 54.29°C [18]. The air temperature rises and subsequently the feeling temperature rise increase the use of the cooling electric devices, such as split air conditioners, which, in turn, affects the consumers' load patterns in the warm season of the year. In Iran, for example, although the demand-side management policies have been encouraged, the daily time of the load peak, which used to occur at night in the summertime, has changed to the afternoon (i.e., the hours of the maximum daily air temperature) since 2011.

Furthermore, since 2011, the annual load peak, which belongs to the summer season, has experienced an average growth of 4.61% per year [19].

These changes in the consumption patterns have caused the load curves in warm and cold durations (seasons) to be significantly different in terms of both the shape and peak of the consumption. Therefore, optimal network configurations in the normal state of the network operation are different in warm and cold periods.

Moreover, in recent years, the volume of the atmospheric pollutants emitted from hydrocarbon sources and the dust hazes in the Middle East (owing to the water elimination policies and droughts) have increased. The frequent resting of these pollutants on the insulators of power distribution and transmission lines leads to insolation breakage of the insulators and consequently increases the line outage rate during the dense fogs or intermittent rains in cold seasons. For example, in spite of all preventive measures already taken, the rate of outages caused by dust hazes and air pollutant concentrations in the cold season is still notable in the southwest of Iran. As a result, the reasons behind fault occurrences and distribution of the number and time of interruptions in two warm and cold seasons are different. Evidently, using an average annual load, and indexes such as the number of annual feeder section interruptions and their average annual repair time as the basis for calculating the average out-of-service time of the load points and hence for the annual expected energy not supplied (as network security index) reduces the precision of calculations.

To solve the above-mentioned concerns in the operation of distribution networks in the south of Iran, a new and applied model is proposed here for optimal placement of switches in distribution networks in that the seasonal variations in load patterns that necessitate changes in network configurations are considered. Moreover, it simultaneously takes into account the considerations of both normal and post-fault conditions. In other words, the presented model takes account of the roles of switches in normal conditions and upon fault and outage occurrences and also determines the optimal seasonal configuration of the network. The objective function is to minimize the total costs of the network including the investment cost, maintenance cost, energy loss cost, and the cost of annual expected energy not supplied (as the network security index). For a more precise calculation of this index, the indices for the number of the feeder sections' interruptions and their average time of repair have been defined here seasonally rather than annually. By expanding the existing relations, the index for the annual expected energy not supplied has thus been calculated based on the aforesaid seasonal values and the average of the seasonal consumption of the loads. The suggested model can optimally determine the switch placement and seasonal configurations of the network in such a way that the total costs of the network are minimized. The remainder of the paper is organized as follows. Section II redefines the annual expected energy not supplied index for real networks considering climatic changes. Section III represents the formulation of the proposed model. Implementation results of the model on test networks are given in Section IV. Section V provides conclusions.

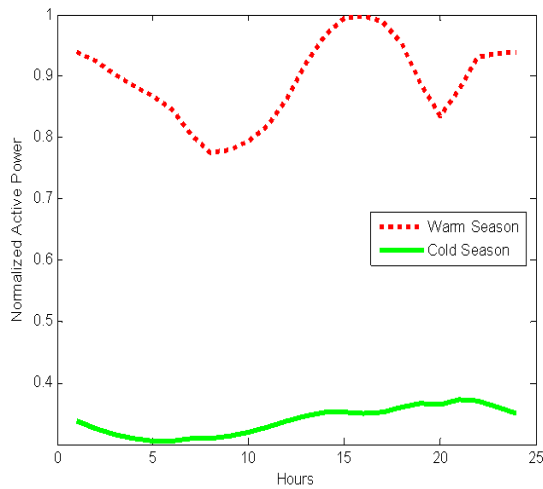


Fig. 1: The load curve of a sample feeder in Khuzestan province for two cold and warm seasons (normalized).

2. REDEFINITION OF ANNUAL EXPECTED ENERGY NOT SUPPLIED WITH RESPECT TO THE CHANGES IN CLIMATE

One geographical region that has negatively been affected by climatic changes, the rise of air temperature, and increased concentration of air pollutants (such as hydrocarbon pollutants and hazes from the droughts) is Khuzestan province, southwest of Iran. The power distribution network of Khuzestan is a network with a low annual load factor (about 50%). The load factor in the 8-month period of the warm season is around 70% and the load factor in the 4-month period of the cold season is about 25%. Moreover, the load peak of the warm season is about 3-4 times greater than that of the cold season (see Fig. 1), which can be attributed to the wide application of the split air conditioners in the warm season. This significant difference in the amounts of consumption and load behavior in warm and cold seasons besides the climatic conditions of the region would affect system operation, which entails avoiding the integrated view of the whole year in the system operation and instead the features of each season should be considered. One important problem in the operation of such systems is dissimilar reasons for faults and accordingly, for the number of interruptions and the time of repair and restoration of the system in cold and warm seasons, meaning that the distribution of the number and time of interruptions in these seasons are different. One index for estimating network security is expected energy not supplied generally defined in the literature as follows [10]:

$$EENS = \sum_{i=1}^{N_{lp}} L_{av,i} \times U_{lp,i} \quad (1)$$

$$U_{lp,i} = \sum_{j=1}^n \lambda_j \times r_j \quad (2)$$

where $EENS$ is expected energy not supplied in a year (in kWh), $L_{av,i}$ denotes annual average load at load point i (kW), $U_{lp,i}$ is the annual average time of interruption for load point i (minute), λ_j is the number of failures of section j of the feeder which is placed between substation and load point i in

a year, r_j is the average repair time of section j of the feeder that is placed between substation and load point i in a year (minute), N_{lp} is the number of load points, and n denotes the number of feeder sections between substation and load point i .

As is seen, this index is affected by the average annual consumption and the average annual interruption time. Concerning the nonhomogeneous distribution of the number and time of interruptions and different consumption levels in cold and warm seasons, (1) and (2) are not precise enough to be utilized for calculating expected energy not supplied index in the studied distribution networks that are situated in warm and polluted areas. Therefore, indexes λ_j and r_j , based on which the average time of out-of-service for load points is computed (see (2)), need to be defined and calculated separately for warm and cold durations. Note that the method for seasonal calculation of these indexes is similar to their annual calculations considering seasonal information. However, such calculations are beyond the scope of the present study. In this work, having the said indexes as seasonal, the expected energy not supplied is calculated seasonally and annual expected energy not supplied is obtained from the sum of the expected energy not supplied indexes of the two seasons:

$$EENS_k = \sum_{i=1}^{N_{lp}} L_{av,i,k} \times U_{lp,i,k} \quad (3)$$

$$U_{lp,i,k} = \sum_{j=1}^n \lambda_{j,k} \times r_{j,k} \quad (4)$$

$$EENS = \sum_k^K EENS_k \quad (5)$$

where $EENS_k$ denotes the expected energy not supplied in season k (kWh), $L_{av,i,k}$ is the seasonal average load at load point i (kW), $U_{lp,i,k}$ refers to the seasonal average time of interruption for load point i (minute), $\lambda_{j,k}$ is the number of failures of section j of the feeder that is placed between substation and load point i in season k , $r_{j,k}$ denotes the average repair time of section j of the feeder that is placed between substation and load point i in season k (minute), and k is an index for time durations of a year, $k \in \{1: \text{warm}, 2: \text{cold}\}$.

To confirm this, a real case is exemplified. The annual number of interruptions of a sample feeder section of a feeder in the distribution network of Ahvaz in 2015 was 21 (with 6 and 15 for warm and cold seasons, respectively). Besides, the average interruption time per year was 34.17 minutes where 9.6 and 44 minutes were observed for warm and cold seasons, respectively. The same was also true for most of the other feeder sections. Moreover, the average consumptions in the warm season, cold season, and total year for most of the load points were significantly different (e.g., 75.44 kW, 24.29 kW, and 37.43 kW, respectively for a sample load point). The annual expected energy not supplied of the abovementioned sample network is calculated using (1) as to be 69.68 MWh. Moreover, the expected energy not supplied in the cold season and that in the warm season is calculated using (2) at 7.419 and 26.68 MWh, respectively. Accordingly, the annual expected energy not supplied from (5) is 34.099, which is

different from the value obtained from (1). Besides, based on the real information from the record system of the network events, the real value of the energy not supplied for this network is equal to 34.55 MWh. This finding well corroborates the authenticity of our suggested modified model for the calculation of the expected energy not supplied.

3. PROBLEM FORMULATION

3.1. Objective Function

The objective function of the presented model has three components, as follows:

3.1.1. The first component– minimization of energy loss cost for normal conditions of the network

This study considers energy loss corresponding to Joule loss affected by network configuration and consumption pattern of loads in cold and warm seasons. Generally, the energy loss cost for season k is calculated as follows:

$$Loss - Cost_k = N_k \times \sum_{t=1}^{24} \rho_{t,k} \times Loss_{t,k} \quad (6)$$

where $Loss_{t,k}$ is power loss at hour t for a typical day of season k (warm or cold) in the first year of the project which can be obtained from load flow calculations considering the network configuration and load patterns of different consumers, N_k is the number of days of season k , and $\rho_{t,k}$ denotes the price of the energy market at hour t of the day corresponding to season k (\$/kWh). Note that the costs of the first year are calculable based on the existing load and market prices. However, for the next years, both the amount of loss (influenced by load growth) and energy prices (influenced by economic factors) change. Since Joule loss is proportional to the second power of load current, having the annual load growth rate, network losses in the project lifetime can be estimated. Also, by applying interest and inflation rates to the unit price of energy in the first year, costs of energy loss for the project lifetime can be calculated. Hence, the first component of the objective function is:

$$OF_1 = \sum_{y=1}^T \sum_{k=1}^K Loss - Cost_k \times PW^{(y-1)} \cdot (1 + 0.01 \times Lg_k)^{2(y-1)} \quad (7)$$

$$PW = \frac{1 + Infr}{1 + Intr} \quad (8)$$

where T is the lifetime of the project, Lg_k denotes the percentage of load growth corresponding to season k , $Infr$ is the inflation rate and $Intr$ is the interest rate.

Note that practically in each season, the annual growth rate of the base load and that of the load peak are not similar. Although this point can be entered into problem formulation, it is here disregarded for the simplicity of calculations while keeping the problem generality.

3.1.2. The second component– minimization of cost of expected energy not supplied (CEENS)

Expected energy not supplied is an energy amount that could have been consumed by users if no fault had occurred in the system but has become inaccessible after the fault occurrence. Note that when a fault occurs, a number of loads

are restored by the switching process and some other ones remain without electricity until the complete removal of the fault. Therefore, by expanding (3) and considering the cost of load interruptions, the cost of expected energy not supplied (CEENS) for the first year of the project is:

$$CEENS = \sum_{k=1}^K \left(\sum_{i=1}^{N_{s,k}} L_{av,i,k} \times U_{lp,i,k} \times CE_{i,k} + \sum_{i=1}^{N_{n,k}} L_{av,i,k} \times U_{lp,i,k} \times CE_{i,k} \right) \quad (9)$$

where $N_{s,k}$ is the number of restored load points after a fault (based on network configuration in season k), $N_{n,k}$ is the number of unrestored load points after a fault (based on network configuration in season k), and $CE_{i,k}$ is the cost of energy not supplied at load point i based on the tariff of season k (\$/kWh).

The first term in (9) shows the load points restored by switching after the fault occurrence. The second sentence is related to the loads remaining without electricity during the faulty section repair. Obviously, in the first term, the average interruption time equals the average restoration time, and in the second term, the average interruption time equals the average repair time. Applying the annual load growth and interest and inflation rates to the first year costs, the net present value of CEENS of the project lifetime is calculated. So, the second component of the objective function is expressed by (10):

$$OF_2 = \sum_{y=1}^T CEENS \times PW^{(y-1)} \cdot (1 + 0.01Lg_k)^{(y-1)} \quad (10)$$

3.1.3. The third component–minimization of investment and maintenance costs

This has three parts. The first part is related to the cost of establishing any new switch including the cost of purchase and installation of switches. The second part is due to the cost of moving the existing switches to new positions, and the third one is related to maintenance costs. Purchase, installation, and replacement costs are for the first year, but maintenance costs are for the project lifetime. So, the third component of the objective function is:

$$O.F_3 = (NS_{new} \cdot C_{new}) + (NS_{plc} \cdot C_{plc}) + \sum_{y=1}^T (N_{total} \cdot C_{maint} \cdot PW^{y-1}) \quad (11)$$

$$N_{total} = NS_{new} + N_c + N_{tie} \quad (12)$$

where NS_{new} is the number of new switches, C_{new} is the cost of purchase and installation of new switches (\$), NS_{plc} denotes the number of existing switches that are placed in new positions, C_{plc} is the cost of replacement of existing switches in the new position (\$), N_c is the number of sectionalizing (normally closed) switches in the original network, N_{tie} denotes the number of tie-switches (normally open switches) in the original network, and C_{maint} denotes the maintenance cost of a switch (\$).

3.1.4. General objective function of the problem

Since each component of the objective function considers the net present value of the related costs for the whole project lifetime, all three components are of the same

economic value. Therefore, the general objective function of the problem is defined by (13) and minimized in the trend of problem-solving.

$$O.F = O.F_1 + O.F_2 + O.F_3 \quad (13)$$

3.2. Constraints

1. Maximum number of purchased switches:

This constraint is considered with respect to the budget limitations of the distribution company:

$$NS_{new} \leq N_{sw,max} \quad (14)$$

where $N_{sw,max}$ is maximum number of new switches which can be purchased.

2. Power capacity of lines:

$$S_{ij}(t) = \left(\sum_{j=1}^{N_{node}} |Y_{ij}V_iV_j| < (\theta_{ij} + \delta_j(t) - \delta_i(t)) \right)^* \quad (15)$$

$$|S_{ij}(t)| \leq S_{ij,max} \quad \forall i, j = 1: N_{node}, i \neq j \quad (16)$$

$$\forall t = 1: 24$$

where $S_{ij}(t)$ is the apparent power passing through the line connected between node i and node j , $Y_{ij} = |Y_{ij}| < \theta_{ij}$ is component (i, j) of nodal admittance matrix, $V_i(t) = |V_i(t)| < \delta_i(t)$ denotes the voltage of node i , N_{node} is the number of nodes, and $S_{ij,max}$ is the capacity of the line connected between node i and node j .

3. Voltage limits of buses:

$$V_{i,min} \leq |V_i(t)| \leq V_{i,max} \quad \forall t = 1: 24 \quad (17)$$

4. Keeping radial structure and feeding all loads:

This constraint is necessary for the feasibility of the proposed configurations for cold and warm seasons. According to graph theory, for a radial network, the number of graph branches equals the number of nodes minus 1. Also, there exists one and only one path between every two nodes of a continuous graph corresponding to a radial network. Therefore, this constraint is formulated as:

$$N_{br} = N_{node} - 1 \quad (18)$$

$$Np_{ij} = 1 \quad \forall i, j = 1: N_{node}, i \neq j \quad (19)$$

where N_{br} denotes the number of branches and Np_{ij} is the number of paths between node i and node j .

3.3. Solving the Problem

The presented optimization model is a mixed-integer nonlinear programming problem. Among the existing algorithms for optimization problems, the evolutionary algorithms (EA) simulate natural evolution principles to find optimal solutions. These algorithms are population-based and free-derivative that easily model the constraints. Although they do not determine the condition for reaching absolute optimum, they take advantage of some operators that reduce their chance of involving in local optimum, so they have a good chance for reaching the optimal solution. Due to its wide applicability, straightforwardness, and versatility, the genetic algorithm is one of the best evolutionary algorithms [20, 21]. Here, the optimization problem is solved by a genetic algorithm.

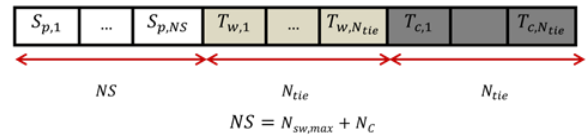


Fig. 2: The chromosome structure.

Each chromosome comprises the selected places of sectionalizing switches and places of tie-switches (normally open) in warm- and cold-season configurations. A typical chromosome structure is given in Fig. 2. Each gene actually shows the number of network branches on which the switch is installed. In the chromosome shown in Fig. 2, $S_{p,i}$ shows the location of the sectionalizers. Also, $T_{w,i}$ and $T_{c,i}$ show the location of tie-switches in warm and cold seasons, respectively. The number of nonzero values in the first part of each chromosome (white-color part) represents the total number of the sectionalizers in the structure. By comparing the number and place of all the switches (sectionalizers and tie-switches) in each chromosome to the number and place of the existing switches in the original configuration, the number of new switches purchased (NS_{new}) and the number of the existing switches in the present structure that must be replaced (NS_{plc}) are determined. From the second (light grey) and the third (dark grey) parts of each chromosome, the configurations of warm and cold seasons are obtained, respectively. By the method in [4], the constraint of keeping radial structure and feeding all loads is checked. If this constraint is violated in a given chromosome, a very large value is assigned as the objective function to this chromosome and the next chromosome is examined. If this constraint is satisfied, the objective function is calculated. Recall that the first and second components of the objective function depend on the proposed configurations for the two seasons. In this respect, for each proposed configuration of the warm and cold seasons, 24 load flow programs are run and the first component is calculated using (7). For load flow calculations, the backward-forward algorithm is used as in [22]. Other problem constraints are checked based on the load flow results and for each constraint violation, a penalty is applied. The imposed penalty is a variable value as a function of the distance of the violated constraint from the feasible area. Next, for each infeasible chromosome, a coefficient of the penalty values is subtracted from the value of the objective function of the worst feasible chromosome in the present population. The obtained value is assumed to be the objective function of the infeasible chromosome. By doing so, the infeasible chromosomes that do not violate the constraint of keeping radial structure and feeding all loads are not discarded and their information can be used for the algorithm search procedure. In the reproduction process, the roulette-wheel selection is used for a new generation. Using a test and set method, a two-point crossover with a rate of 0.8 is selected. Besides, the mutation rate is determined using a test and set of 0.05. If the objective function does not improve after a certain number of consecutive iterations, the algorithm will stop. In this work, these iterations are determined for each network by the test and set method. The general problem-solving algorithm is shown in Fig. 3.

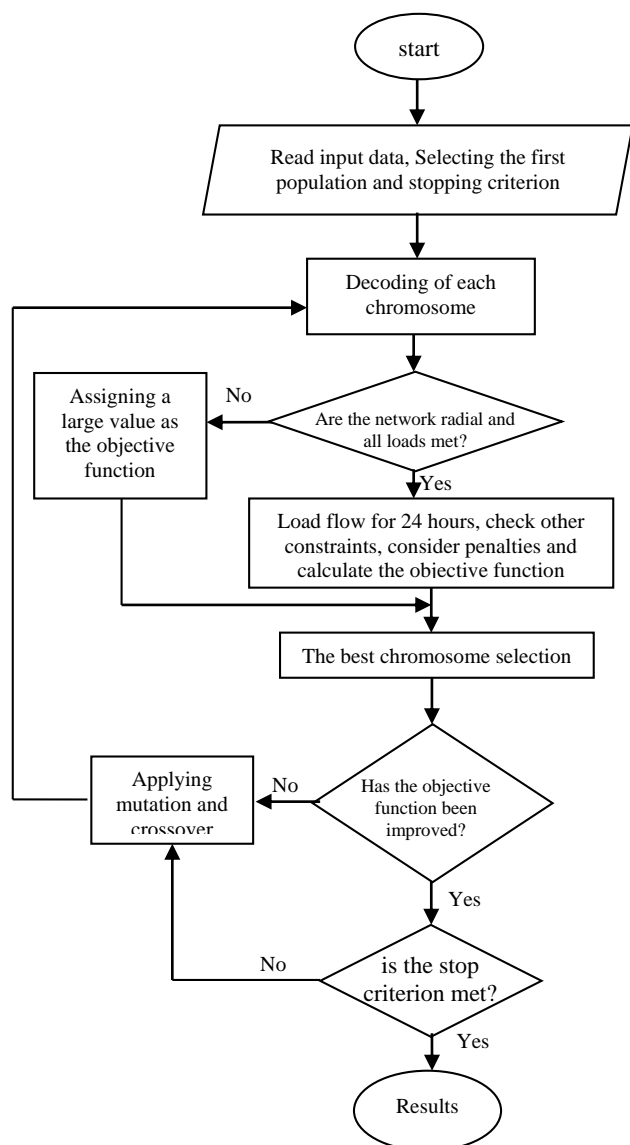


Fig. 3: The solving algorithm.

4. NUMERICAL RESULTS

4.1. Assumptions

The project lifetime is 5 years, the inflation rate is 11%, and the interest rate is 15%. The costs of purchase and installation of any new automatic and manual switches are US\$ 5000 and 3000, respectively. The cost of replacing any existing switch and its installation in a new place is 0.1 of the purchase and installation cost of a new switch. The cost of annual maintenance for any switch is 0.02 of its purchase and installation cost. The annual load growth rates in warm and cold seasons are 3% and 0.5%, respectively. The cost of expected energy not supplied for different types of users is calculated as the average tariffs of the Power Ministry of Iran for different types of subscribers in warm regions and is assumed to be 0.03 US\$/kWh. Energy market prices are similar to the energy market prices in Iran. Service restoration times for automatic and manual switches are 1 minute and 30 minutes, respectively.

4.2. Test Systems

To evaluate the proposed model, two test systems are used. The first one is a 33-bus system with characteristics in [4]. To have a real network's conditions, the system is modified and three types of loads as residential, commercial, and administrative and teaching centres are considered. Fig. 4 shows the single-line diagram of the modified 33-bus system. The load pattern for different consumers of this system is presumed to be similar to the load behavior of the consumers in Khuzestan, Iran [4]. Also, the distribution of the number and the time of interruptions in cold and warm seasons are assumed to be similar to the ruling conditions in studied real networks. Since the present study has introduced a novel model, the validity of the results cannot be investigated through the literature. Therefore, the validity of the suggested model is confirmed by analyzing the results obtained for different scenarios of the 33-bus system. The second test system has two 33-kV feeders from the power distribution network of Ahvaz city, the center of Khuzestan, with 332 buses to show the efficiency of the proposed model in real systems. This system has three normally closed switches and two normally open switches with residential and commercial subscribers. The details of this system are available in [23].

4.3. Results for Modified 33-Bus Test System

Section I of Table 1 shows the original system conditions, i.e., the location of the switches, normally open switches, the cost of seasonal energy loss, and the cost of seasonal expected energy not supplied considering the load and prices in the first year. The maximum number of new switches is assumed to be four and sectionalizing switch placement results for this system are given under five scenarios in section II of Table 1.

Scenario 1: All switches are assumed to be manual and the switch placement is intended to minimize energy not supplied and investment and maintenance costs. After that, optimal seasonal configuration for minimizing energy loss cost is attained by reconfiguration. Two new switches are purchased and four of the existing switches are replaced. The normally open switches in the cold season are 7, 33, 34, 35, and 37. Also, the normally open switches in the warm season are 14, 27, 33, 35, and 36. The comparison of the results with the original network conditions shows that in the first year, energy loss costs in the cold and warm seasons have been reduced from US\$ 803.2 and 15021 to US\$ 670 and 11941 (16.58% and 20.5%), respectively, and total year decrease is 20.3%. Also, the costs of expected energy not supplied in the cold and warm seasons have been reduced from US\$ 818 and 3088.5 to US\$ 813.9 and 2707.6 (5% and 12.33%), respectively, and the total annual reduction is 9.8%. Besides, the total cost in the project lifetime is US\$ 89425.

Scenario 2: All switches are assumed to be manual and the switch placement is done by the proposed model. In the first year of the project, energy loss costs in the cold and warm seasons have been reduced by 20.56% and 22.1%, respectively and by 22% in the total year. Expected energy

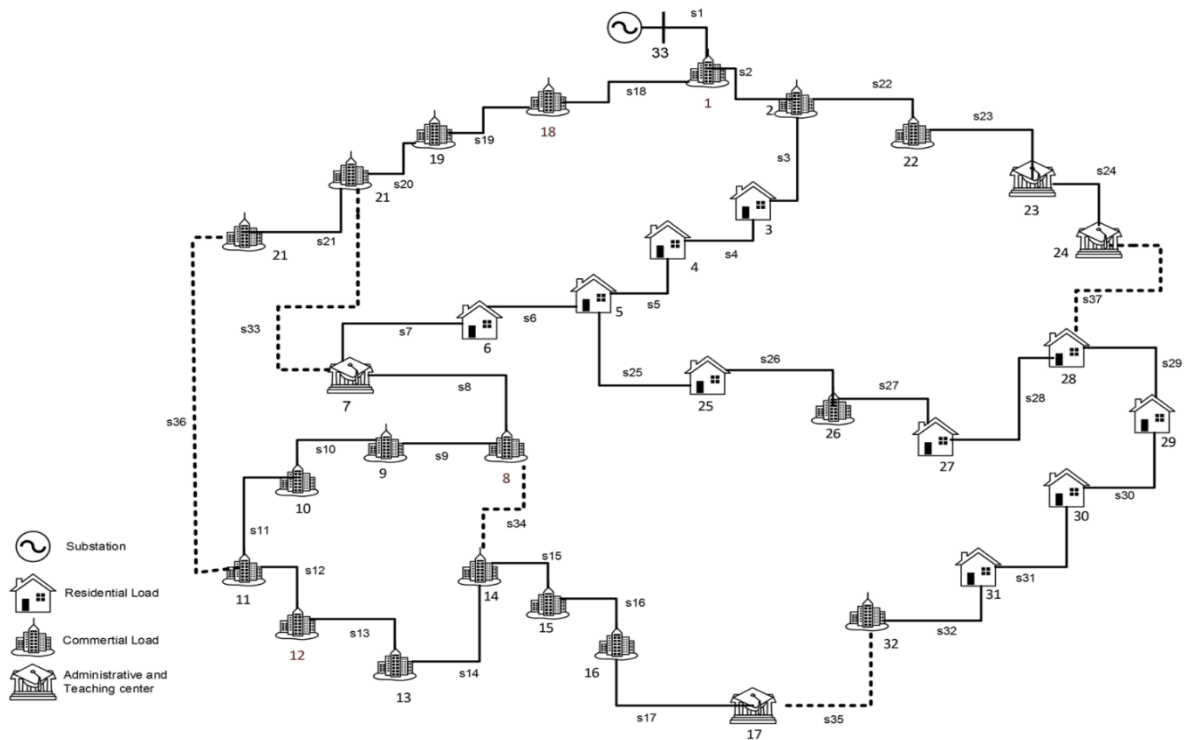


Fig. 4: The modified 33-bus test network.

Table 1: The results of sectionalizing switch placement for modified 33-bus test system.

Part 1: Initial condition							
Switches Position	Tie-Switches	Cost of Energy Loss (\$)		Cost of EENS (\$)			
		Cold Season	Warm Season	When all switches are manual		When all switches are automatic	
				Cold Season	Warm Season	Cold Season	Warm Season
9-14-33-34-35-36-37	33-34-35-36-37	803.2	15021	818	3088.5	738	2596
Part 2: Optimization Results							
		Scenario No.					
		1	2	3	4	5	
Number of New Switches		2	2	2	2	2	
Number of Replaced Switches		4	3	3	3	3	
Tie-Switches		Cold Season 7-33-34-35-37	Warm Season 7-9-14-32-37	7-9-14-32-37	7-9-14-32-37	7-9-14-32-37	
		Warm Season 14-27-33-35-36	7-33-34-35-37	9-33-34-35-37	7-33-34-35-37	7-33-34-35-37	
First Year	Cost of Energy Loss (\$)	Cold Season	670	638	638	638	638
		Warm Season	11941	11700	11761	11700	11700
	Cost of EENS (\$)	Cold Season	813.9	795.5	654	1591.2	1262
		Warm Season	2707.6	2831	1800	5583	3788
Lifetime of Project	Total Cost of Energy Loss (\$)		63491	62128	62440	62128	62128
	Total Cost of EENS (\$)		16604	17110	11553	33844	23564
	Total Investment Cost		9329	8729	15048	8729	14548
	Total Cost (\$)		89425	87969	89043	104701	100240

not supplied costs in the cold and warm seasons have been reduced by 2.75% and 8.33%, respectively and by 7.16% in the total year. The total cost in the project lifetime equals US\$ 87969. As is seen, the cost of energy not supplied in

scenario 1 is low, compared to scenario 2, since switch placement in scenario 1 is focused on minimizing energy not supplied and investment and maintenance costs, and thus the places determined for installing the switches are optimal only from the said aspects. So, the application of these switches for

finding optimal seasonal configuration to minimize energy loss cost cannot necessarily yield the best response. However, in scenario 2, switch placement is done by focusing on minimizing energy not supplied and energy loss costs besides investment and maintenance costs. As observed, in this scenario, reductions in the costs of energy loss in the cold and warm seasons and in the total year are more than the reductions in scenario 1. Although in scenario 2, the reduction in the cost of energy not supplied is smaller than this reduction in scenario 1, the total costs of scenario 2 in the project lifetime have been reduced by 1.6%, compared to scenario 1. This result supports the proposed model in the present study.

Scenario 3: All switches are assumed to be automatic and switch placement is conducted by our model. Two new switches are purchased and three of the existing switches are replaced. Here, the normally open switches of the cold season are similar to that of scenario 2. The normally open switches in the warm seasons are 9, 33, 34, 35, and 37. In the first year, energy loss costs in the cold and warm seasons are US\$ 638 and 11761 and the expected energy not supplied costs are US\$ 654 and 1800, respectively. In the cold seasons of the first year, the energy loss costs are similar to those in scenarios 2 and 3 due to similar configurations of cold seasons. However, due to different configurations of the warm seasons, the energy loss cost in the warm season of the first year in scenario 3 shows a 61-dollar (0.52%) increase compared to scenario 2, and in annual bases, a 0.49% increase is seen. Besides, due to the very short restoration time with automatic switches compared to manual ones, the costs of expected energy not supplied for the cold and warm seasons in the first year in scenario 3 have had US\$ 141.5 (17.78%) and US\$ 1031 (36%) reductions, respectively, compared to scenario 2. Nonetheless, due to the higher investment costs in automatic switches, the total cost of scenario 3 is 1.2% greater than that of scenario 2. In a network with a low level of security, the decrease in the cost of expected energy not supplied due to automatic switches is expected to go beyond the increase in the original investment costs for these switches. This is shown in scenarios 4 and 5.

Scenario 4: In this scenario, the number of occurrences and the repair time for each feeder section are assumed to be double and manual switch placement is done by the proposed model.

Scenario 5: This scenario is similar to scenario 4, except that the switches are here automatic.

In scenario 4, the costs of energy not supplied in the cold and warm seasons in the first year are US\$ 1591.2 and 5583, respectively. In scenario 5, they are US\$ 1262 and 3788, showing 20.68% and 32% reductions compared to scenario 4. In scenario 5, a 4.2% decrease in total cost in the project lifetime is observed compared to scenario 4. As it is seen, despite the higher investment cost of automatic switches, in the low-security networks, they can be more economic for improving network security.

4.4. Results for the Real System

The costs of energy loss and expected energy not supplied per year (considering the load and prices in the first year) are US\$ 28850 and 4189.9, respectively. The maximum number of new automatic switches is assumed to be two and

switch placement is done by the proposed model. No new switch is purchased and four of the existing ones are replaced. Therefore, the existing switches are not in proper places in the original network structure, and replacement of these switches can reduce the costs of energy loss and energy not supplied without installing new switches and spending investment costs. Due to these replacements and network reconfigurations, the costs of energy loss and energy not supplied in the first year decrease to US\$ 24330.9 and 3331.1 (i.e., 15.56% and 20.5% reductions), respectively, and the total cost in the whole project lifetime equals US\$ 142882.4. The detail of the results is provided in [23].

5. CONCLUSIONS

This study introduces a novel and applied model for switch placement in radial distribution networks in which both roles of switches in normal operating conditions and in the presence of fault are taken into consideration. Moreover, the conditions of Khuzestan's distribution networks in both warm and cold seasons are incorporated in the model. The objective function is to minimize investment and maintenance costs, the cost of energy loss, and the cost of expected energy not supplied. The cost of energy loss in each season is calculated based on the network configuration of the normal condition in that season. The expected energy not supplied is also calculated seasonally and the annual expected energy not supplied is obtained by the sum of expected energy not supplied in the cold and warm seasons. This model can determine optimal places for installing sectionalizing switches and optimal network's configurations for minimizing the total costs. The model is confirmed through a 33-bus network under the first and the second scenarios. The total costs of scenario 2, which is corresponding to the presented model, are decreased by 1.6% compared to scenario 1, which is like the common cases in previous papers. The comparison of scenarios 2, 3, 4, and 5 shows that in low-security networks, the application of automatic switches for improving network security can be more economic. The results of implementation on a real network in Ahvaz show that the existing switches in the original network structure are not properly positioned and the costs of energy loss and energy not supplied significantly decrease by replacing these switches and without purchasing new ones.

CREDIT AUTHORSHIP CONTRIBUTION STATEMENT

Ali Rouhipour: Data curation, Methodology, Resources, Roles/Writing - original draft. **Elaheh Mashhour:** Project administration, Supervision, Validation. **Mohsen Saniei:** Validation, Writing - review & editing.

DECLARATION OF COMPETING INTEREST

The authors declare that they have no known competing financial interests or personal relationships that could have appeared to influence the work reported in this paper. The ethical issues; including plagiarism, informed consent, misconduct, data fabrication and/or falsification, double publication and/or submission, redundancy has been completely observed by the authors.

REFERENCES

- [1] A.A. El-Fergany, "Optimal capacitor allocations using evolutionary algorithms," *IET Gen. Trans. & Dist.*, vol. 7, no. 6, pp. 593-601, 2013.
- [2] Z. Wang, H. Liu, D. C. Yu, X. Wang, and H. Song "A practical approach to the conductor size selection in planning radial distribution systems," *IEEE Trans. Power Del.*, vol. 15, no. 1, pp. 350-354, 2000.
- [3] J. F. Franco, M. J. Rider, M. Lavorato, and R. Romero "Optimal conductor size selection and reconductoring in radial distribution systems using a mixed-integer LP approach," *IEEE Trans. Power Del.*, vol. 28, no. 1, pp. 10-20, 2013.
- [4] S. H. Alemohammad, E. Mashhour, and M. Saniei, "A market-based method for reconfiguration of distribution network," *Electr. Power Syst. Res.*, vol. 125, pp. 15-22, 2015.
- [5] A.Y. Abdelaziz, F.M. Mohamed, S.F. Mekhamer, and M.A.L. Badr, "Distribution system reconfiguration using a modified tabu search algorithm," *Electr. Power Syst. Res.*, vol. 80, no. 8, pp. 943-953, 2010.
- [6] V. Farahani, B. Vahidi, and H. A. Abyaneh, "Reconfiguration and capacitor placement simultaneously for energy loss reduction based on an improved reconfiguration method," *IEEE Trans. Power Syst.*, vol. 27, no. 2, pp. 587-595, 2012.
- [7] B. Amanulla, S. Chakrabarti, and S. N. Singh, "Reconfiguration of power distribution systems considering reliability and power loss," *IEEE Trans. Power Del.*, vol. 27, no. 2, pp. 918-926, 2012.
- [8] G. A. Hamoud and L. Lee, "Criticality assessment of distribution feeder sections," *IEEE Trans. Power Syst.*, vol. 27, no. 1, pp. 298-304, 2012.
- [9] N. Khalesi, N. Rezaei, and M. Haghifam, "DG allocation with application of dynamic programming for loss reduction and reliability improvement," *Journal of Electrical Power & Energy Syst.*, vol. 33, no. 2, pp. 288-290, 2011.
- [10] R. Billinton and S. Jonnavithula, "Optimal switching device placement in radial distribution systems," *IEEE Trans. Power Del.*, vol. 11, no. 3, pp. 1646-1651, 1996.
- [11] C.-S. Chen, C.-H. Lin, H.-J. Chuang, C.-S. Li, M.-Y. Huang, and C.-W. Huangl, "Optimal placement of line switches for distribution automation systems using immune algorithm," *IEEE Trans. Power Syst.*, vol. 21, no. 3, pp. 1209-1217, 2006.
- [12] I. Goroohi Sardou, M. Banejad, R. Hooshmand, and A. Dastfan, "Modified shuffled frog leaping algorithm for optimal switch placement in distribution automation system using a multi-objective fuzzy approach," *IET Gen. Trans. Dist.*, vol. 6, no. 6, pp. 493-502, 2012.
- [13] A.A. Jahromi, M.F. Firuzabad, M. Parvania, and M. Mosleh, "Optimized sectionalizing switch placement strategy in distribution systems," *IEEE Trans. Power Del.*, vol. 27, no. 1, pp. 362-370, 2012.
- [14] S. I. Lim, T. S. Sidhu, M. S. Choi, S. J. Lee, and B. N. Ha, "A optimal composition and placement of automatic switches in DAS," *IEEE Trans. Power Del.*, vol. 28, no. 3, pp.1474-1483, 2013.
- [15] S. Ray, A. Bhattacharya, and S. Bhattacharjee, "Optimal placement of switches in a radial distribution network for reliability improvement," *International Journal of Electrical Power & Energy Sys.*, vol. 76, no. 6, pp. 53-68, 2016.
- [16] L. Wang, J. Lin, G. Liu, G. Wang, Q. Zhong, and Y. Zhao, "An MIP-based model for the deployment of fault indicators and sectionalizing switches in distribution networks," *Electr. Power Syst. Res.*, vol. 179, 106076, 2020.
- [17] M. Moradijoz, S. Moradijoz, M. Parsa Moghaddam, and M.-R. Haghifam, "Flexibility enhancement in active distribution networks through a risk-based optimal placement of sectionalizing switches," *Reliability Engineering & System Safety*, Vol. 201, 106985, 2020.
- [18] AccuWeather, (June 29, 2017). [Online]. Available: <https://www.accuweather.com/en/ir/ahvaz/210047/month/210047?monyr=6/01/2017>
- [19] "Monthly information of simultaneous load peak of the whole network," *Tavanir specialized parent company, Deputy of Research and Human Resources, Office of Information Technology, Communication and Statistics*, 2016.
- [20] K. Deb, "Multiobjective optimization using evolutionary algorithms," *Wiley, Chichester*, 2002.
- [21] M. Gen and R. Cheng, "Genetic algorithm and engineering optimization," *John Wiley & Sons*, 2000.
- [22] S.M. Moghaddas-Tafreshi and E. Mashhour, "Distributed generation modeling for power flow studies and a three-phase unbalanced power flow solution for radial distribution systems considering distributed generation," *Electr. Power Syst. Res.*, vol. 79, no. 4, pp. 680-686, 2009.
- [23] E. Mashhour, " Optimal placement of line switches for pilot feeders of Ahvaz distribution network to improve the security indices," *Research Project Report, Shahid Chamran University of Ahvaz*, June 2016.

BIOGRAPHY

Ali Rouhipour was born in Behbahan, Khuzestan, Iran in 1992. He received the B.Sc. and M.Sc. degrees in Electrical Power Engineering from Shahid Chamran University of Ahvaz, Ahvaz, Iran in 2014 and 2016 respectively. His interest topics include reliability, rearrangement and restructuring of power networks.





Elaheh Mashhour (M'08) was born in Tehran, Iran, in 1974. She received the Ph.D. degree in Electrical Engineering from K. N. Toosi University of Technology, Tehran, Iran, in 2010. She worked in Khuzestan Electric Power Distribution Company for 15 years as the manager of network and load control

office, the manager of power market office and head of DG participation unit. From 2011, she has been an Assistant Professor and a Faculty Member with the Electrical Engineering Department, Shahid Chamran University of Ahvaz, Ahvaz, Iran. Her research interests are distribution system automation and planning, power market, network resiliency and deep learning.



Mohsen Saniei was born in Dezful, Iran, 1966. He received B.Sc. in Electrical Power Engineering from Ferdowsi University of Mashhad, in 1989, and received M.Sc. in Electrical Power Engineering from Tarbiat Modarres University, in 1992. He completed his Ph.D. in Electrical Engineering from

Strathclyde University, Glasgow, UK, in 2004. His interest is in power system dynamics, microgrid and power system operation.

Copyrights

© 2022 Licensee Shahid Chamran University of Ahvaz, Ahvaz, Iran. This article is an open-access article distributed under the terms and conditions of the Creative Commons Attribution –NonCommercial 4.0 International (CC BY-NC 4.0) License (<http://creativecommons.org/licenses/by-nc/4.0/>).





Iranian Association of
Electrical and Electronics
Engineers

Journal of Applied Research in Electrical Engineering

E-ISSN: 2783-2864

P-ISSN: 2717-414X

Homepage: <https://jaree.scu.ac.ir/>



Research Article

A New Approach for the Transformer Differential Protection Based on S-Transform and Fuzzy Expert System

Saeid Hasheminejad*

Department of Electrical and Computer Engineering, Graduate University of Advanced Technology, Kerman, Iran.

*Corresponding Author: SaeidHasheminejad@yahoo.com

Abstract: This paper presents a novel method to discriminate between the magnetizing inrush and external and internal fault currents in power transformers. Fault type identification and faulted phase selection are also possible by the proposed algorithm. The proposed method has two main parts. First, by means of S-transform, which is the most accurate method in the field of signal processing, some useful features are extracted from the input signal. Then, the extracted features are converted to some numerical indices. In the second part, an effective decision maker is needed to classify the input signal. One of the best methods, which have been used for decision-making applications is fuzzy logic. So, the numerical indices are used as inputs for the fuzzy system. The output of the fuzzy system not only can reveal whether the input signal is the magnetizing inrush, external or internal fault, but it can also identify the fault type when there is an internal fault. Finally, the faulted phases can be identified with a supplemental algorithm. To generate the test signals, a three-phase transformer is modeled in PSCAD/EMTDC. Testing the proposed algorithm by different simulated data shows the robustness of the proposed method in the transformer differential protection.

Keywords: Transformer differential protection, inrush current, internal fault, S-transform, fuzzy expert system.

Article history

Received 01 September 2021; Revised 31 December 2021; Accepted 31 December 2021 Published online 9 March 2022.

© 2022 Published by Shahid Chamran University of Ahvaz & Iranian Association of Electrical and Electronics Engineers (IAEEE)

How to cite this article

S. Hasheminejad, "A new approach for the transformer differential protection based on S-transform and fuzzy expert system," *J. Appl. Res. Electr. Eng.*, vol. 1, no. 2, pp. 159-168, 2022. DOI: [10.22055/jaree.2021.38432.1035](https://doi.org/10.22055/jaree.2021.38432.1035)



1. INTRODUCTION

Power transformers are considered as one of the most important components of a power system. The protection of different components of a power system is also a critical issue. Therefore, fast and reliable protection of the power transformers is an important problem that needs to be addressed properly. The accurate protection of these transformers can decrease possible damages and increase the reliability of the power supply. There are some special operating conditions that can lead to the reduction of the protection accuracy [1]. It can be said that there are some disturbances, such as magnetizing inrush, internal fault, external fault, and ultra-saturation, which can affect the performance of a power transformer [2-3]. The protection scheme for a transformer must be reliable (no missing operation), secure (no false tripping), fast (short fault clearing time), and stable [4].

When an internal fault occurs, the protection relay should be able to trip the transformer from the network to limit the internal damage caused by the fault to the transformer. Differential relaying plays the main role in the electrical protection of a power transformer. When there is an internal fault, a differential current flow through the relay whose amplitude is much higher than the differential current amplitude in the normal operating condition. This quantity can be used as a discriminative feature to understand a fault condition. But, in some situations, differential current can have a high value, and relay should not perform. In fact, when a transformer is energized, a magnetizing inrush current will flow through the transformer and cause the differential current to have a high value. It is a transient current that does not damage the transformer, so there is no need to trip the transformer. The same condition occurs when the transformer is energized in parallel with an already operating transformer [5] or when the transformer recovers from an external fault. The external fault can also make the amplitude of the

differential current much higher than its usual value but it should not make the differential relay trip the transformer.

Taking all the above into consideration, it can be understood that a protective scheme must be able to distinguish internal faults from inrush currents and external faults. Magnetizing inrush currents have a high level of the second harmonic component that was traditionally a discriminative feature to distinguish the magnetizing inrush currents from the internal faults [6], [7]. Methods that are based on the second harmonic component are no longer applicable in the transformer differential protection because there are some contents of the second harmonic component, while CT saturates. Moreover, there can be a low level of the second harmonic component in the magnetizing inrush currents due to the modern core material of the power transformer [8], [9]. There are other methods that are based on the waveform identification. In these methods, some features are extracted from the signal waveform and according to these features, it is decided if the waveform is an internal fault or a magnetizing inrush current [10].

Various methods have recently been presented to solve this problem. Some have used artificial neural networks and genetic algorithms to identify the inrush current [11, 12], which are system-dependent and impose a high computational burden. Others have used wavelet transform (WT) for this purpose [13-14]. WT can be affected by the high-frequency noise, which is a considerable drawback [15]. Other drawback of utilizing WT is the dependability of its accuracy on the choice of the mother wavelet, which can only be derived by trial and error. In [16], an algorithm that is based on the wave shape properties of the transformer average differential power during inrush and internal faults is used to discriminate between these two events. A method based on the Clarke transform with fuzzy sets is presented in [17], and methods based on the wavelet packet transform are presented in [18] and [19] to be used for the differential protection of the power transformers. A Kalman-filter-based algorithm is presented in [20] for the same purpose.

Another phenomenon that leads to an over-current in the transformer differential relays is the external fault, which has not been considered in the above-reviewed papers. Since the external faults are not related to any faults in the transformer, the differential relay should not operate in this situation. This paper presents an effective method based on the S-transform and fuzzy system. The proposed method can discriminate between the internal faults, external faults, and inrush currents. This method is based on the characteristics derived from the wave shapes of these three signal types. S-transform is a convertible time-frequency analyzing technique and has not only the useful characteristics of both Fourier transform (FT) and wavelet transform (WT) but also characteristics superior to both previous time-frequency analyzing techniques. FT cannot extract non-stationary features of the signals, so it is not possible to use it to analyze the transient signals such as the magnetizing inrush currents. As mentioned before, high-frequency noise and the choice of the mother wavelet affect the accuracy of WT. S-transform can extract both the time and frequency properties of the signals. As a result, it can be used to extract transient information of the signals. This method is immune to noise and there is no need for any mother wavelet or things like that [21].

After the feature extraction, an effective classifier is needed to classify the input signals. In this paper, a fuzzy system is used to classify the input signals to reveal if there is an internal fault, an external fault, or a magnetizing inrush. In addition, when there is an internal fault, the proposed method can extract the fault type, whether there is a single-phase, double-phase, double-phase-to-ground, three-phase, or three-phase-to-ground fault. The phases that have encountered a fault will be revealed then.

2. POWER TRANSFORMER SPECIFICATIONS

For the simulation purpose, a three-phase transformer is simulated in PSCAD/EMTDC software. Different signals are extracted from the simulated transformer.

2.1. Magnetic Core Saturation

The magnetic core saturation is simulated by compensating for the current source across the winding wound closest to the core [22]. The simulation model is shown in Fig. 1.

In Fig. 1, $I_s(t)$ is the magnetizing current that is related to the flux linkage through the $\lambda-I$ characteristic and can be derived from the voltage and current measurements during the no-load test. In the case of having a high value for the linkage flux, the slope of this curve tends toward the saturated core inductance of the transformer winding. This characteristic is calculated by means of the PSCAD/EMTDC platform based on the magnetizing current at the rated voltage, the air core saturated reactance of the winding and the position of the knee point.

2.2. Remanence

When a transformer works in its normal operation, the flux linkages corresponding to the three phases have the same magnitude with 120° phase deviation. In the case of de-energizing the transformer, the linkage flux will freeze at the flux remanence point. The degree of the magnetizing inrush current during energization is a direct function of the remanence that exists in the leg of the transformer core. So, it is necessary to simulate the residual flux of the core. Residual flux can be simulated by inserting a controlled DC current source in parallel to each low-voltage transformer winding [23].

2.3. Inrush Current

The existence of the inrush current in a power transformer has different reasons. It is mostly the result of the transformer energization. Recovering the transformer from an external fault and energizing the transformer in parallel to an already operated transformer are other reasons for the existence of an

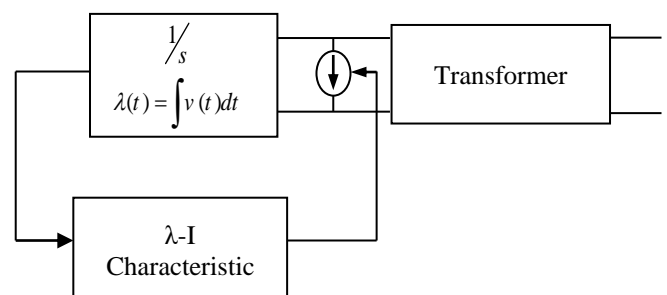


Fig. 1: Modeling the magnetic core saturation.

inrush current for the existence of an inrush current in a power transformer. Inrush currents are transient currents that flow through the transformer windings for several cycles and their initial amplitude is much higher than the transformer's nominal current. A magnetizing inrush current has the following features:

- It consists of the DC offset and odd and even harmonics (especially the second harmonic component).
- There are uni-polar or bi-polar pulses along with low current value intervals.
- The ratio of the second harmonic component to the first one has a relatively high value.

There are time intervals between pulses with very low current values [24].

2.4. Internal Fault

Internal faults are the other reason for having high amplitude differential currents in the transformer windings. The common features of the internal fault currents are as follows:

- There is a DC offset in some of the internal fault currents.
- In the first moments after the fault inception, the slope of the internal fault current is higher than that of the inrush current.
- If there is no harmonic in the system, the internal fault has a sinusoidal trend.

The following items have a considerable effect on the internal fault current specifications:

- Fault type (single-phase-to-ground (SLG), double-phase-to-ground (DLG), double-phase (LL) and three-phase (3PH)).
- Load condition
- The phase voltage at the instant of the fault inception
- The impedance of the fault.

2.5. External fault

Sometimes when an external fault occurs, a relatively high magnitude current flows through the differential relay. For example, in the case of the CT saturation, external faults lead to the high amplitude differential currents. The fault type, fault inception angle, fault impedance and the transformer core remanence flux are some of the main parameters that affect the external fault specifications.

3. S TRANSFORM

The S transform (ST), introduced by Stockwell [25], can be considered the "phase correction" of the continuous wavelet transform (CWT). The CWT of the function $h(t)$ is defined by:

$$W(\tau, d) = \int_{-\infty}^{\infty} h(t) \cdot w(d, t - \tau) dt \quad (1)$$

The ST is a CWT with a specific mother wavelet multiplied by a phase-corrected factor:

$$s(\tau, f) = e^{j2\pi f \tau} \cdot W(d, \tau) \quad (2)$$

where the mother wavelet $w(f, t)$ is defined as:

$$w(f, t) = \frac{|f|}{\sqrt{2\pi}} e^{-\frac{t^2 f^2}{2}} \cdot e^{-j2\pi f t} \quad (3)$$

In (1), parameter d is the inverse of the frequency and f is the frequency. Finally, the ST equation can be written as follows:

$$S(\tau, f) = \frac{|f|}{\sqrt{2\pi}} \int_{-\infty}^{\infty} h(t) e^{-\frac{(t-\tau)^2 f^2}{2}} e^{-j2\pi f t} dt \quad (4)$$

The ST can also be written as an operation on the Fourier spectrum $H(f)$ of $h(t)$:

$$S(\tau, f) = \int_{-\infty}^{\infty} H(\alpha + f) e^{-\frac{2\pi^2 \alpha^2}{f^2}} e^{j2\pi \alpha \tau} d\alpha \quad (5)$$

Since ST is a representation of the local spectra, Fourier or time average spectrum can be directly calculated by averaging the local spectrum as:

$$H(f) = \int_{-\infty}^{\infty} S(f, \tau) d\tau \quad (6)$$

$$h(t) = \int_{-\infty}^{\infty} \left\{ \int_{-\infty}^{\infty} S(f, \tau) d\tau \right\} e^{j2\pi f t} df \quad (7)$$

The power disturbance signal $h(t)$ can be defined in a discrete form as $h(kT)$, $k=0, 1, \dots, N-1$, where T is the sampling time interval and N is the total sampling number. The discrete Fourier transform can be calculated as:

$$H\left[\frac{n}{NT}\right] = \frac{1}{N} \sum_{k=1}^{N-1} h(kT) e^{-j\frac{2\pi nk}{N}} \quad (8)$$

$$n = 0, 1, 2, \dots, N-1$$

Using (5), the ST of a discrete time series $h(kT)$ is given by (let $\tau \rightarrow kT$ and $f \rightarrow n/NT$)

$$S\left[kT, \frac{n}{kT}\right] = \sum_{m=0}^{n-1} H\left[\frac{m+n}{NT}\right] e^{-\frac{2\pi^2 m^2}{n^2}} \cdot e^{j\frac{2\pi mk}{N}} \quad 1 \quad n \neq 0 \quad (9)$$

$$k, m = 0, 1, 2, \dots, N-1 \quad n = 1, 2, \dots, N-1$$

$$S[kT, 0] = \frac{1}{N} \times \sum_{m=0}^{N-1} h\left(\frac{m}{NT}\right) \quad n = 0 \quad (10)$$

So, the ST matrix $S [kT, n/NT]$ is used to analyze the power system signals in which the rows are frequencies and the columns are the time values. Each column displays the ST magnitude with all frequencies at the same time and each row displays the ST magnitude with the time varying from 0 to $N-1$ in the same frequency where $n=0, 1, \dots, \frac{N}{2}-1$. In this paper, the ST amplitude (STA) matrix is:

$$A(kT, f) = \left| S\left[kT, \frac{n}{NT}\right] \right| \quad (11)$$

Apart from having the ST amplitude matrix, considering the ST phase matrix (STP) is also profitable to analyze the power quality disturbances in a three-phase manner.

$$P(kT, f) = \arctan \left(\frac{\text{Im} S\left(\left[kT, \frac{n}{NT}\right]\right)}{\text{Re} S\left(\left[kT, \frac{n}{NT}\right]\right)} \right) \quad (12)$$

4. POWER TRANSFORMER DIFFERENTIAL PROTECTION

The algorithm, proposed in this paper, consists of two different steps. In the first step, some features are extracted from the relay signal using a proper time-frequency analyzing technique. In the second step, the relay signal should be classified using a proper classifier according to the features extracted in the previous step.

4.1. Feature Extraction

One of the best methods, which is used for this purpose, is the ST. This technique can be used to extract all frequency, time, and transient features of the signal. Besides, this technique is immune to noise and its output is easy to analyze. The ST output is a complex matrix. If we calculate the absolute value of each component of this matrix, according to (11), we would have an STA matrix that is used for feature extraction. Fig. 2(a) shows the normal signal without any disturbances and Figs. 2(b) and 2(c) are the time-frequency amplitude curves generated from its STA matrix. Here, the sampling frequency is 10 kHz and the signal's main frequency is 50Hz. Fig. 2(b) is called the maximum amplitude curve (MAC), which indicates the frequency components of the input signal. It is extracted from each column of the STA matrix. Fig. 2(c) is called the standard deviation curve (SDC). To explain this curve, the STA matrix should be explained more precisely. When the input signal has n samples, the STA matrix will have $n/2$ rows and n columns. Each row shows the input signal amplitude deviations versus time, and each column shows the frequency components of the input signal in each time sample. When the input signal has a fixed amplitude, the values in each row of the STA matrix will remain approximately constant. Therefore, the standard deviation of the values of each row is near zero. But, when there is a transient signal added to the main signal, the standard deviation of the respective row (respective frequency which is the frequency of the transient signal) will have a nonzero value. In this paper, we use this curve to detect the fault-generated transient components.

Figs. 3-12 present the sampling signals of the internal fault, inrush current and external fault along with their related three-phase MACs and SDCs. To generate MACs and SDCs, one cycle of each of the three phases is recorded and then ST is applied to the recorded signals. The differential currents are extracted from a Y/ Δ , 50Hz, 500 MVA, and 400/230 kV three-phase transformer, which is modeled in PSCAD/EMTDC. Fig. 3 shows the three-phase differential currents related to a Bg fault with 10 Ohms fault resistance and the fault inception angle of 90 degrees. It is worth mentioning that each of Figs. 4, 6, 8, 10, and 12 contains the MACs and SDCs of all the three phases. In fact, samples 1 to 100 are related to phase A, samples 101 to 200 are related to phase B, and samples 201 to 300 are related to phase C.

In Fig. 4, it is expected that the region related to phase B has a peak in both MAC and SDC. For example, in Fig. 4(a), the region related to phase B is between samples 100 and 200. A peak at the beginning of the phase B region shows that there is a peak in the fundamental frequency in the MAC of phase B. Fig. 5 shows an ACg fault with zero Ohms resistance with the fault inception angle of 45 degrees. Note that this angle is

the angle of phase A voltage at the fault inception time.

Fig. 7 shows the three-phase currents for a three-phase fault with 5 Ohms resistance with the fault inception angle of 30 degrees.

Fig. 9 shows the three-phase current signals for an inrush situation. Here, the source impedance is 10 Ohms and the voltage angle of phase A is 90 degrees at the switching inception time.

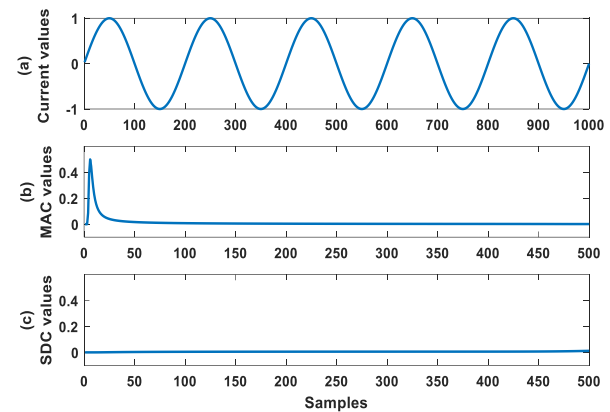


Fig. 2: Normal signal and the related curves extracted by S-transform, (a): Normal signal, (b) MAC values, (c) SDC values.

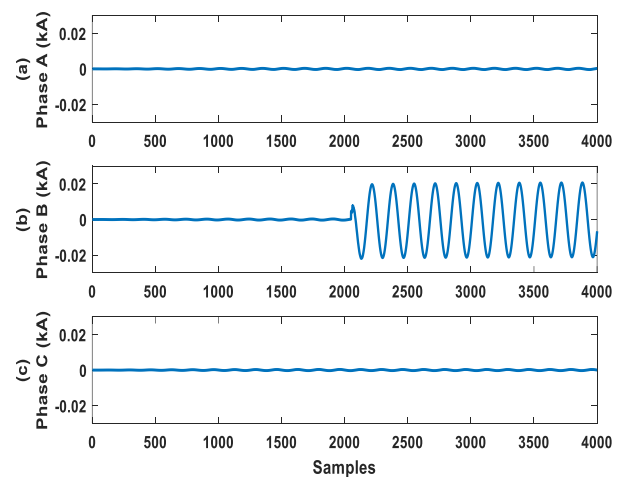


Fig. 3: Differential currents related to a Bg fault, (a) Phase A, (b) Phase B, (c) Phase C.

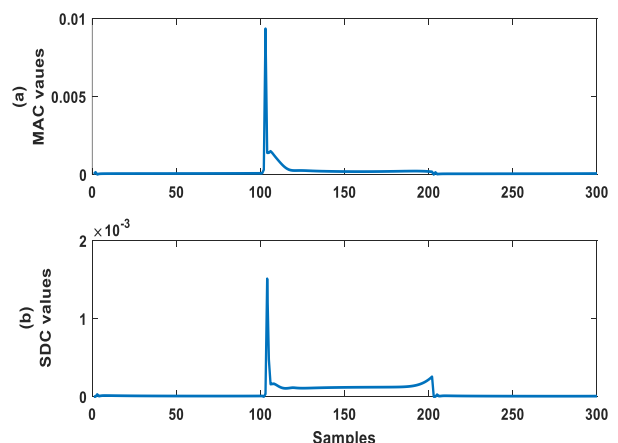


Fig. 4: ST outputs for the three phases for a Bg fault, (a) MAC, (b) SDC.

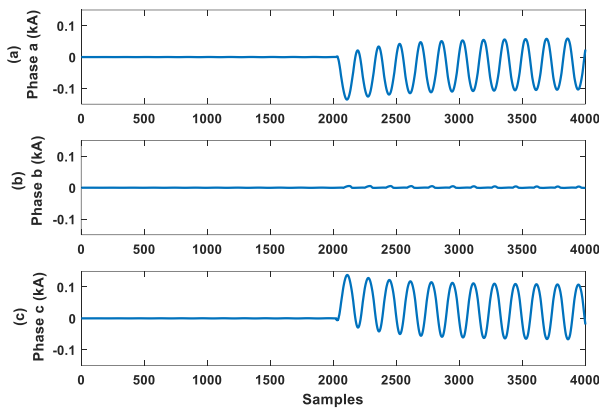


Fig. 5: Sampling data for a double-phase-to-ground fault, (a) Phase A, (b) Phase B, (c) Phase C.

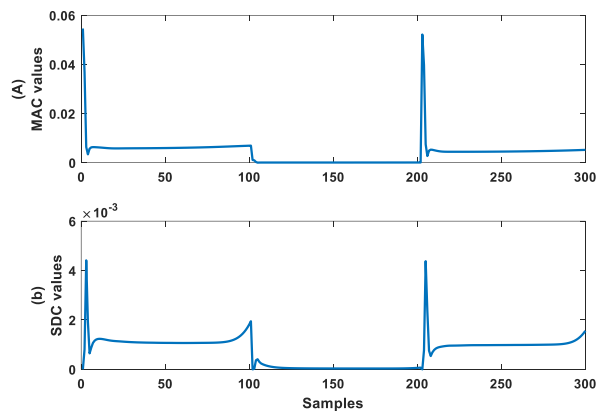


Fig. 6: ST outputs for the three phases for the ACg fault, (a) MAC, (b) SDC.

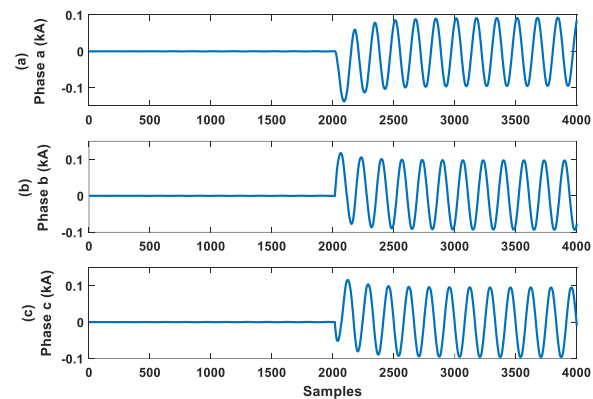


Fig. 7: Sampling data for a three-phase-to-ground fault, (a) Phase A, (b) Phase B, (c) Phase C.

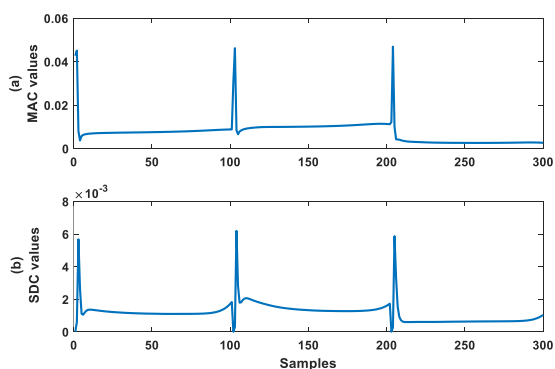


Fig. 8: ST outputs for the three phases for the ABC fault, (a) MAC, (b) SDC.

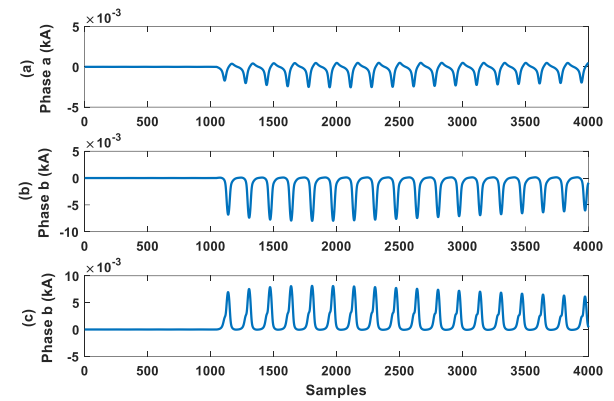


Fig. 9: Sampling data for an inrush current, (a) Phase A, (b) Phase B, (c) Phase C.

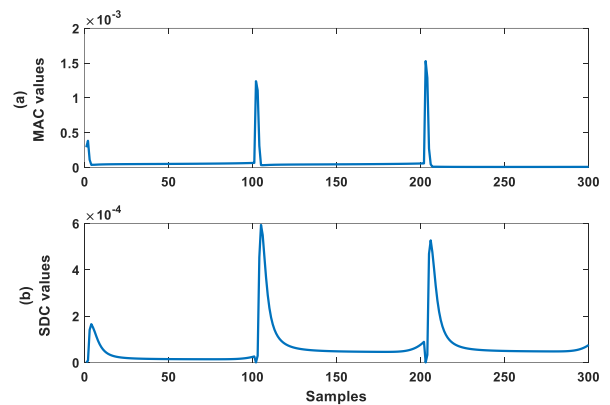


Fig. 10: ST outputs for the three phases for an inrush current, (a) MAC, (b) SDC.

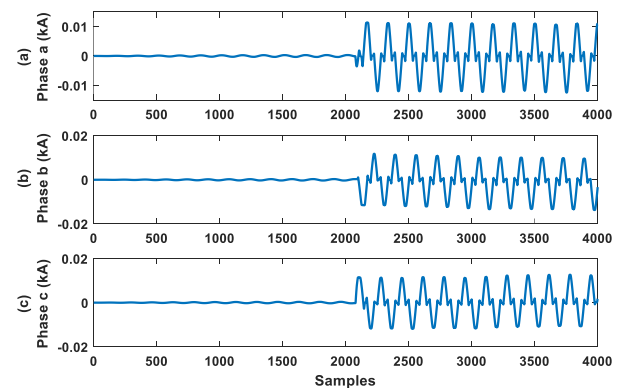


Fig. 11: Sampling data for an external ABCg fault, (a) Phase A, (b) Phase B, (c) Phase C.

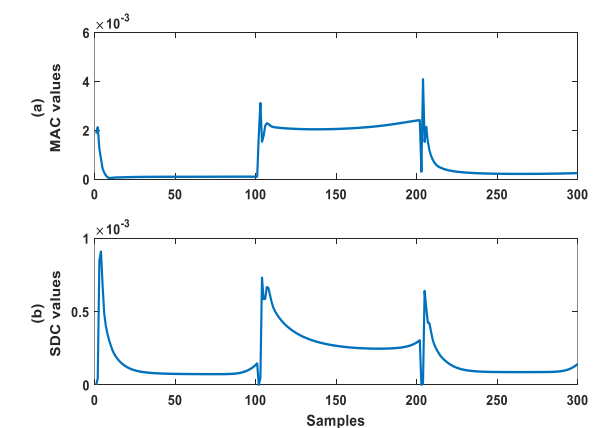


Fig. 12: ST outputs for the three phases for the three-phase external fault, (a) MAC, (b) SDC.

Fig. 11 shows the three-phase current signals for an external fault. Here, the fault impedance is 5 Ohms and the voltage angle of phase A is 120 degrees at the fault inception time.

Fig. 3 shows a single-phase-to-ground internal fault. As can be seen in Fig. 4, there is only one peak in its related MAC, and according to its related SDC, the area under this curve has a relatively higher value than the respective curve of the inrush current. Fig. 5 shows the sampling data of a double-phase-to-ground fault. Fig. 6 indicates that there are two peaks in the MAC of the double-phase-to-ground fault and the area under the SDC for this type of fault is significant. Fig. 7 shows the sampling data for an internal three-phase-to-ground fault. There are three peaks in its MAC and its SDC has still a significant value. According to Figs. 3 to 8, this is obvious that the number of peaks in MAC has a direct relationship with the number of faulted phases.

Fig. 10 shows that for the inrush current signal, there are three peaks in the related MAC, which is the first difference between the output curves of the magnetizing inrush currents and single- and double-phase internal faults. When a double-phase or a three-phase external fault occurs in a power system, transformer differential relay will detect an over-current. Fig. 11 shows the three-phase signals related to a three-phase external fault and its MAC and SDC are shown in Fig. 12. The internal fault has a random nature and its SDC is expected to have a significant value in all frequency samples. So, the area under the SDC for the internal fault is higher than that of the inrush current. In fact, having a significant value in all frequencies of the SDC related to an internal fault is because of the fault-generated high-frequency components. However, for high impedance internal faults, the area under the SDC has a relatively lower value compared to that of the low impedance faults. But, because of existing the high-frequency components, this parameter has still a relatively higher value than that of the inrush currents. As can be seen in Figs. 3-12, the number of peaks in the three-phase MAC and the area under the SDC are the key features to discriminate between the magnetizing inrush currents, internal faults and external faults. To discriminate between the grounded and ungrounded faults, the zero sequence of the three-phase signals should be calculated. This parameter can also make the whole method more precise.

To have a fast, accurate, and easy method, it is necessary to extract some numerical indices from the previous wave type features. Automatic decision-making by numerical parameters is much easier than decision-making by waveforms. So, in this paper, we extract three numerical indices, named C_1 , C_2 , and C_3 from SDC and MAC of each signal.

C_1 : This index represents the number of peaks in the main frequencies of the three phases in the three-phase MAC. If there is a single-phase-to-ground fault, then only one of the main frequencies has a significant value, so there is only one peak in the three-phase MAC and as a result, C_1 would be 1. If there is a double-phase fault, then two of the main frequencies have a significant value, so there are two peaks in its three-phase MAC and as a result, C_1 would be 2. A similar rule exists for a three-phase fault. In the case of having the magnetizing inrush current, all the three main frequencies have a significant value, so there are three peaks in the related

MAC and as a result, $C_1 = 3$ for the signal of magnetizing inrush current. For example, in Fig. 6, $C_1 = 2$ and in Fig. 10, $C_1 = 3$.

C_2 : This index is the area under the SDC of the signal. As can be seen in Figs. 6 and 10, the area under the SDC of the internal fault is greater than that for the inrush current. So, C_2 can be considered as a discriminative parameter.

C_3 : This index is defined to know if the signal is connected to the ground or not. This index is useful for the fault type identification. This is related to the content of the zero sequence of the input signal. To calculate this index, first, by the summation of the samples of the three phases, the zero-sequence current is calculated. Then, ST is applied to the zero-sequence current. C_3 is the maximum value in the MAC of the zero-sequence current. We know that for an ungrounded fault, the zero sequence of a three-phase input signal is nearly zero and for a grounded fault, this parameter has a significant value.

By analyzing a large number of magnetizing inrush, internal and external fault current signals, possible values for C_1 , C_2 , and C_3 are calculated. Table 1 shows the values of the indices for each fault type.

4.2. Signal Classification

Up to this step, values for each numerical feature are extracted. Now, it is needed to have an efficient classifier to classify the input signals. Fuzzy logic is a good decision-maker and can be used to classify signals according to the numerical features extracted from the input signal. We need a deterministic output as the magnetizing inrush, external fault, single-phase internal fault, double-phase internal fault, double-phase-to-ground internal fault, three-phase internal fault, and three-phase-to-ground internal fault. As a result, a Sugeno-type fuzzy system is required. Digits 1 to 7 represent the signal types mentioned above, respectively. Figs. 13 to 15 show the membership functions for the three variables. These variables are defined according to C_1 , C_2 , and C_3 .

Table 1: Possible values of indices for each signal type.

Disturbance type	C_1	C_2	C_3
Single-phase-to-ground fault	1	0.0032~0.0331	0.0042~0.0229
Double-phase-to-ground fault	2	0.0736~0.2288	0.0021~0.0124
Double-phase fault	2	0.0486~0.1934	4.18×10^{-8} ~ 8.5×10^{-7}
Three-phase-to-ground fault	3	0.2531~0.2626	2×10^{-6} ~ 9×10^{-5}
Three-phase fault	3	0.2018~0.2094	3.9×10^{-8} ~ 5.6×10^{-7}
External fault	3	0.0029~0.0045	3.87×10^{-12} ~ 14×10^{-11}

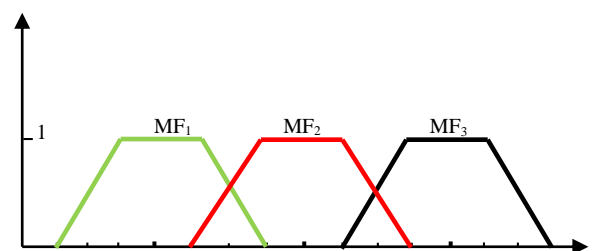


Fig. 13: Membership functions for the variable related to C_1 .

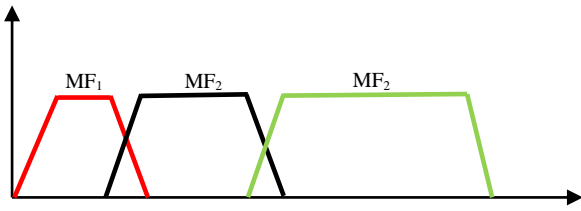


Fig. 14: Membership functions for the variable related to C₂.

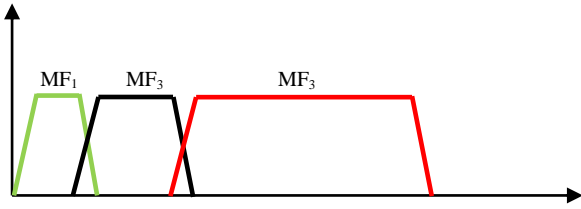


Fig. 15: Membership functions for the variable related to C₃.

Table 2: Values of membership functions for each variable.

Variable	MF ₁	MF ₂	MF ₃
First	0.25-0.75- 1.25-1.75	1.25-1.75-2.25- 2.75	2.25-2.75- 3.25-3.75
Second	0-0.0029- 0.0045-0.0046	0.0045-0.0046- 0.0321-0.0322	0.0313-0.0314- 0.263-0.27
Third	0-10 ⁻¹² -3 × 10 ^{- 12} -10 ⁻⁹	10 ⁻⁸ -3 × 10 ⁻⁸ -9 × 10 ⁻⁷ -10 ⁻⁶	10 ⁻⁶ -2 × 10 ⁻⁶ - 0.023-0.024

After defining the membership function, some rules should be defined for the fuzzy engine to make the decision-making process possible. Table 3 shows the set of rules used in this paper.

The values for each membership function must be defined according to the values of the numerical features extracted from the input signal to make it possible for the fuzzy system to classify the input signal correctly and accurately. Table 2 shows the proper value for each membership function.

4.3. Faulted Phase Selection

To find the faulted phases, the three-phase-based MAC is utilized in this paper. It is worth mentioning that ST is separately applied to the differential current signals of phases A, B, and C. Then, we put the extracted MACs in one matrix and name it the three-phase-based MAC. As stated before, there are three regions in the three-phase-based MAC. The first region is related to phase A (samples 1 to 100 in Fig. 4), the second one is related to phase B (samples 101 to 200 in Fig. 4), and the third one is related to phase C (samples 201 to 300 in Fig. 4). Having a peak at the beginning of each region shows that the respective phase has encountered a fault. For example, consider the MAC shown in Fig. 4. At the beginning of the second region, there is one peak in the mentioned MAC. The second region is related to phase B. Therefore, the fault is concluded to be a Bg one. Consider the MAC shown in Fig. 6. In this curve, there are two peaks at the beginning of the first and the third regions. The first region is related to phase A and the third one is related to phase C. Therefore, the faulted phases are concluded to be phases A and C. The flowchart of the proposed algorithm is depicted in Fig. 16.

5. SIMULATION AND RESULTS

A simulation study was done on a system comprising a typical 500 MVA with a 400/230-kV three-phase transformer

Table 3: Decision-making rules.

Rules	Membership function			Output	Result
	Variable	Variable	Variable		
	1	2	3		
Rule1	MF ₃	MF ₁	MF ₁	MF ₁	Inrush
Rule2	MF ₁	MF ₂	MF ₃	MF ₂	Single-phase fault
Rule3	MF ₂	MF ₃	MF ₂	MF ₃	Double-phase fault
Rule4	MF ₂	MF ₃	MF ₃	MF ₄	Double-phase-to-ground fault
Rule5	MF ₃	MF ₃	MF ₂	MF ₅	Three-phase fault
Rule6	MF ₃	MF ₃	MF ₃	MF ₆	Three-phase-to-ground fault
Rule7	MF ₂	MF ₂	--	MF ₇	External fault
Rule8	MF ₃	MF ₂	--	MF ₈	External fault

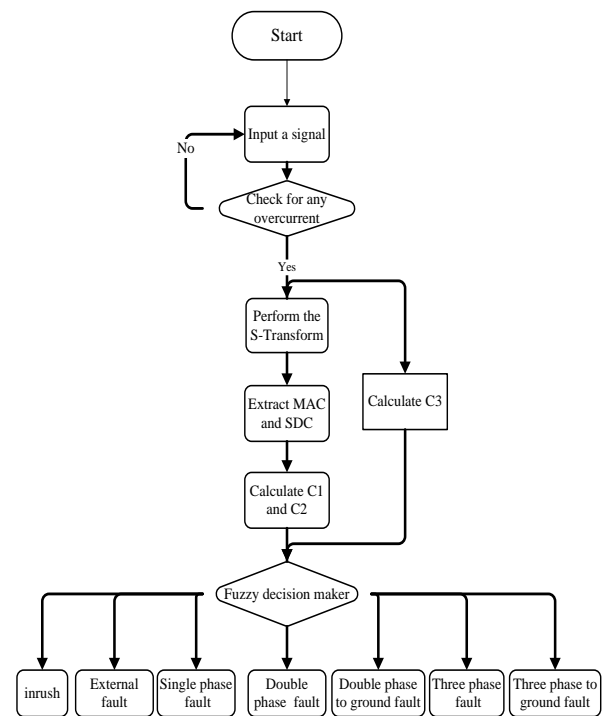


Fig. 16: The flowchart of the proposed method.

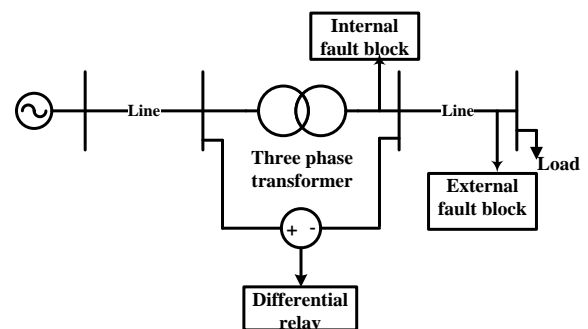


Fig. 17: A single-line diagram of the simulated power system.

that is modeled in PSCAD/EMTDC. To take the effect of long lines into consideration, the distributed model for lines is used in this paper. A single-line diagram of the simulated Y/ Δ transformer along with other network elements is shown in Fig. 17.

5.1. Testing the accuracy of the algorithm

To test the performance of the proposed algorithm, 100 signals for each disturbance type are first generated in PSCAD/EMTDC and are classified by the algorithm. To generate different internal faults, the fault type, the fault impedance and the fault inception angle are changed. The source impedance and the voltage angle at the instant of switching are changed to generate different inrush current signals. The results are shown in Table 4.

According to Table 4, it can be seen that this method has a high classification accuracy. The only errors that can be seen in Table 4 are the inrush current and the single-phase fault. There were four mistaken inrush current signals. The output for two of these mistaken signals was "2", which is the index related to the single-phase fault, and the output for two of them was "3", which is the index related to the double-phase fault. For the single-phase-to-ground set of signals, there is one mistaken signal that has the output of "1", which is the index related to the magnetizing inrush currents.

In this paper, faulted phase selection has a very simple algorithm, as described in Section 4.3. This simplicity leads to the high accuracy of this algorithm. This means that all the faulted phases are identified correctly.

5.2. Signal Type Classification

In this section, the process of the signal type classification is analyzed for some sample disturbances. Table 5 shows the related results.

For example, consider the BCg internal fault in Table 5. Here, C_1 is 2, which means that two of the phases have encountered a fault. This means that the signal is an internal or an external fault. The value of C_1 along with the values of C_2 and C_3 shows that there is a double-phase-to-ground internal fault.

5.3. Fault Type Classification and Faulted Phases Selection

To show the robustness of the fault type classification and faulted phases selection algorithm, different internal fault

Table 4: The first simulation results for the proposed algorithm.

Disturbance type	Index number	Classification accuracy
Single-phase-to-ground fault	2	99%
Double-phase fault	3	100%
Double-phase-to-ground fault	4	100%
Three-phase fault	5	100%
Three-phase-to-ground fault	6	100%
Inrush current	1	96%
External fault	7	100%

Table 5: The results for the signal type classification.

Applied disturbance	C_1	Index number	C_2	C_3	Fuzzy output	Result
Inrush	3	2	0.0034	2.4×10^{-11}	1	Inrush
Internal fault, Ag	1	3	0.0033	0.0085	2	Single-phase-to-ground fault
Internal fault, BCg	2	4	0.1278	0.0114	4	Double-phase-to-ground fault
Internal fault, ABC	3	5	0.2094	3.9×10^{-8}	5	Three-phase fault
External fault, AB	2	6	0.0059	--	7	External fault
External fault, ABCg	3	1	0.0142	--	7	External fault

Table 6: The results of the fault type classification.

Applied fault	C_1	C_2	C_3	Peak region	Fuzzy output	Result
Bg	1	0.0047	0.0143	2	2	Bg
ACg	2	0.0842	0.0118	1 and 3	4	ACg
AB	2	0.1896	4.3×10^{-8}	1 and 2	3	AB
ABg	2	0.228	0.0057	1 and 2	4	ABg
BC	2	0.1448	1.51×10^{-7}	2 and 3	3	BC
ABC	3	0.2018	5.57×10^{-7}	1, 2 and 3	5	ABC

types are generated and tested by the proposed algorithm. Table 6 presents some of the results.

For example, for the Bg fault in Table 6, the values of C_1 , C_2 , and C_3 show that there is an internal fault. The value of C_1 shows that only one of the phases has encountered a fault. The second region has a peak and therefore, the test signal is the result of a Bg fault.

5.4. Comparison With Other Algorithms

In [26], an algorithm based on the rate change of the phase angle of the differential current is presented. In [27], using a modified least square algorithm, the sinusoidal part of the differential current is produced, and then using the probabilistic distance measure algorithm, it is analyzed if the signal has resulted from an internal fault or an inrush current. The identification of the single-phase faults is considered in this reference. Another algorithm is presented in [28] to identify only single-phase internal faults. None of these references provide an algorithm for fault type classification and faulted phases selection. The identification of the external faults is not considered in these references either.

References [29] and [30] provide high-frequency-based algorithms for the transformer differential protection. Both fault type classification and external fault identification are not performed in these references.

The algorithm presented in [31] uses the convolutional neural network (CNN) for the transformer differential protection. This type of algorithm needs a large amount of data for the training process, which is a drawback of such protection algorithms. In this reference, different fault types

and external faults are considered in the simulation stage. But there is still no algorithm for fault type identification and faulted phases selection.

The proposed algorithm covers different aspects of the transformer differential protection. The discrimination between the internal faults and inrush currents, fault type classification and faulted phases selection, and the identification of external faults are all considered in the proposed algorithm. Besides, in some references such as [32-34], the existence of the low-order harmonic components affects the performance of the algorithms. The proposed algorithm covers the gap between the fundamental frequency-based algorithms and high-frequency-based algorithms. Low-order harmonic components such as the ones resulting from the CT saturation do not affect the performance of the proposed algorithm.

6. CONCLUSION

This paper presents a new algorithm to discriminate between the magnetizing inrush currents, external faults, and internal faults. The algorithm uses wave shapes of the three signal types. In the first step, some discriminative features are extracted from the MAC and SDC of the faulted signal using ST. In the second step, to classify the transformer signals according to the numerical indices, a fuzzy expert system is utilized. Converting the wave shape characteristics to the numerical features simplifies the classification process. Using fuzzy logic as a decision-maker, makes the algorithm more flexible and reliable. Finally, testing the proposed algorithm by means of the test signals generated by PSCAD/EMTDC software shows the effectiveness of the proposed method in the transformer differential protection.

CREDIT AUTHORSHIP CONTRIBUTION STATEMENT

Saeid Hasheminejad: Conceptualization, Data curation, Formal analysis, Funding acquisition, Investigation, Methodology, Project administration, Resources, Software, Supervision, Validation, Visualization, Roles/Writing - original draft, Writing - review & editing.

DECLARATION OF COMPETING INTEREST

The authors declare that they have no known competing financial interests or personal relationships that could have appeared to influence the work reported in this paper. The ethical issues; including plagiarism, informed consent, misconduct, data fabrication and/or falsification, double publication and/or submission, redundancy has been completely observed by the authors.

REFERENCES

- [1] H. Esponda, E. Vazquez, M. A. Andrade, and B. K. Johnson, "A setting-free differential protection for power transformers based on second central moment", *IEEE Transactions on Power Delivery*, vol. 34, no. 2, pp.750-759, 2019.
- [2] H. Dashti, and M. Sanaye-Pasand, "Power transformer protection using a multi-region adaptive differential relay", *IEEE Transactions on Power Delivery*, vol. 29, no. 2, pp. 777-785, 2014.
- [3] A. Ashrafian, M. Mirsalim, and M. A. S. Masoum, "Application of a recursive phasor estimation method for adaptive fault component based differential protection of power transformers", *IEEE Transactions on Industrial Informatics*, vol. 13, no. 3, pp. 1381-1392, 2017.
- [4] M. R. Tripathy, P. Maheshwari, and H. K. Verma, "Power transformer differential protection based on optimal probabilistic neural network", *IEEE Transactions on Power Delivery*, vol. 25, no. 1, pp. 102-112, 2010.
- [5] F. Peng, H. Gao, and Y. Liu, "Transformer sympathetic inrush characteristics and identification based on substation-area information", *IEEE Transactions on Power Delivery*, vol. 33, no. 1, pp. 218-228, 2018.
- [6] M. Tripathy, R. P. Maheshwari, and H. K. Verma, "Advances in transform protection: A review", *Electric Power Components and Systems*, vol. 33, no. 11, pp. 1203-1209, 2005.
- [7] A. G. Phadke, and J. S. Thorp, "A new computer-based flux-restrained current differential relay for power transformer protection", *IEEE Transactions on Power Apparatus and Systems*, vol. 102, no. 11, pp. 3624-3629, 1983.
- [8] T. Zheng, T. Huang, Y. Ma, Y. Z. Zhang, and L. Liu, "Histogram-based method to avoid mal-operation of transformer differential protection due to current-transformer saturation under external faults", *IEEE Transactions on Power Delivery*, vol. 33, no. 2, pp. 610-619, 2018.
- [9] M. C. Shin, C. W. Park, and J. H. Kim, "Fuzzy logic based relaying for large power transformer protection", *IEEE Transactions on Power Delivery*, vol. 18, no. 3, pp. 718-724, 2003.
- [10] S. K. Murugan, S. P. Simon, K. Sundareswaran, P. S. R. Nayak, and N. P. Padhy, "An empirical Fourier transform-based power transformer differential protection", *IEEE Transactions on Power Delivery*, vol. 32, no. 1, pp. 209-218, 2017.
- [11] P. B. Thote, M. B. Daigavane, P. M. Daigavane, and S. P. Gawande, "An intelligent hybrid approach using KNN-GA to enhance the performance of digital protection transformer scheme", *Canadian Journal of Electrical and Computer Engineering*, vol. 40, no. 3, pp. 151-161, 2017.
- [12] A. R. Moradi, E. Ebadian, M. Yazdani-Asrami, and M. Taghipour, "Artificial intelligence based techniques for distinguishing inrush current from faults in large power transformers", *International Review of Electrical Engineering*, vol. 6, no. 5, pp. 2198-2206, 2011.
- [13] R. P. Medeiros, and F. B. Costa, "A wavelet-based transformer differential protection with differential current transformer saturation and cross-country fault detection", *IEEE Transactions on Power Delivery*, vol. 33, no. 2, pp. 789-799, 2018.
- [14] R. P. Medeiros, and F. B. Costa, "A wavelet-based transformer differential protection: internal fault

- detection during inrush conditions", *IEEE Transactions on Power Delivery*, vol. 33, no. 6, pp. 2965-2977, 2018.
- [15] F. Zhao, and R. Yang, " Power Quality Disturbance Recognition Using S-transform", *IEEE Transaction on power delivery*, vol.25, no. 4, pp. 944-950, 2007.
- [16] A. Hooshyar, S. Afsharnia, M. Sanaye-Pasand, and B. M. Ebrahimi, "A new algorithm to identify magnetizing inrush conditions based on instantaneous frequency of differential power signal", *IEEE Transactions on Power Delivery*, vol. 25, no. 4, pp. 2223-2233, 2010.
- [17] D. Barbosa, U. C. Netto, D. V. Coury, and M. Oleskovicz, "Power transformer differential protection based on Clark's transform and fuzzy system", *IEEE Transactions on Power Delivery*, vol. 26, no. 2, pp. 1212-1220, 2011.
- [18] S. A. Saleh, and M. A. Rahman, "Testing of a Wavelet-Packet-Transform-Based Differential Protection for Resistance-Grounded Three-Phase Transformers", *IEEE Transactions on Industrial Applications*, vol. 46, no. 3, pp. 1109-1117, 2010.
- [19] S. A. Saleh, B. Scaplen, and M. A. Rahman, "A new implementation method of wavelet-pocket-transform differential protection for power transformers", *IEEE Transactions on Industrial Applications*, vol. 47, no. 2, pp. 1003-1012, 2011.
- [20] F. Naseri, Z. Kazemi, M. M. Arefi, and E. Farjah, "Fast discrimination of transformer magnetizing current from internal faults: An extended Kalman Filter-Based Approach", *IEEE Transactions on Power Delivery*, vol. 33, no. 1, pp. 110-118, 2018.
- [21] S. Hasheminejad, S. Esmaili, and S. Jazebi, "Power quality disturbance classification using S-Transform and hidden Markov model", *Electric Power Components and Systems*, vol. 40, no. 10, pp. 1160-1182, 2010.
- [22] H. W. Dommel, "Transformer models in the simulation of electromagnetic transients", *Proceedings of 5TH power system computing conference*, 1975, paper 3.1/4
- [23] D. Woodford, "Introduction to PSCAD/EMTDC V3", *Manitoba HVDC research center Inc*, 2000.
- [24] S. Jazebi, B. Vahidi, and S. H. Hosseinian, "A novel discriminative approach based on Hidden Markov Models and wavelet transform to transformer protection", *Journal of Simulation*, vol. 86, no. 2, pp. 93-107, 2010.
- [25] R. G. Stockwell, L. Mansinha, and R. P. Lowe, "Localization of the complex spectrum: The S-transform", *IEEE Transactions on signal processing*, vol. 44, no. 4, pp. 998-1001, 1996.
- [26] H. Samet, M. Shadaei, and M. Tajdinian, "Statistical discrimination index founded on rate of change of phase angle for immunization of transformer differential protection against inrush current", *Int. j. of Elect. power and ener. Syst.*, vol.13, no. 4, 107381, 2022.
- [27] M. Tajdinian, and H. Samet, "Application of probabilistic distance measures for inrush and internal fault currents discrimination in power transformer differential protection", *Elect. Power Syst. Res*, vol. 19, no. 3, 107012, 2021.
- [28] A. Moradi, and S. M. Madani, "Predictive formulas to improve transformer protection during inrush current using the proposed equivalent circuit", *IEEE trans. on power deliv*, vol. 35, no. 2, pp. 919-928, 2020.
- [29] L. D. Simoes, H. J. D. Costa, M. O. Aires, R. P. Medeiros, F. B. Costa, and A. S. Bretas, "A power transformer differential protection based on support vector machine and wavelet transform", *Elec. power syst. Res.*, vol. 19, no. 7, 107297, 2021.
- [30] M. N. O. Aires, R. P. Medeiros, K. M. Silva, J. J. Chavez, and M. Popov, "A wavelet-based restricted earth-fault power transformer differential protection", *Elect. Power syst. Res.*, vol. 19, no. 6, 107246, 2021.
- [31] S. Afrasiabi, M. Afrasiabi, B. Paarang, and M. Mohammadi, "Integration of accelerated deep neural network into power transformer differential protection", *IEEE trans. on indist. Inform.*, vol. 16, no. 2, pp. 865-876, 2020.
- [32] H. Weng, S. Wang, X. Lin, Z. Li, and J. Huang, " A novel criterion applicable to transformer differential protection based on waveform sinusoidal similarity identification", *Int. J. Electr. Power Energy Syst.*, vol. 10, no. 5, pp. 305-314, 2019.
- [33] L. Zhang, Q. Wu, and T. Ji, "Identification of inrush currents in power transformers based on high-order statistics", *Electr. Powe Syst. Res.*, vol. 14, no. 6, pp. 161-169, 2017.
- [34] F. Naseri, H. Samet, T. Ghanbari, and E. farjah, " Power transformer differential protection based on least square algorithm with extended kernel", *IET science, Measur. Techn.*, vol. 18, no. 8, pp. 1102-1110, 2019.

BIOGRAPHY



system protection.

Saeid Hasheminejad was born in Kerman, Iran in 1985. He received his B.Sc., M.Sc., and Ph.D. degrees in 2008, 2011, and 2016, respectively. He is currently an assistant professor at the Graduate University of Advanced Technology, Kerman, Iran. His research interests are in the areas of signal processing, power quality, and power

Copyrights

© 2022 Licensee Shahid Chamran University of Ahvaz, Ahvaz, Iran. This article is an open-access article distributed under the terms and conditions of the Creative Commons Attribution –NonCommercial4.0 International (CC BY-NC 4.0) License (<http://creativecommons.org/licenses/by-nc/4.0/>).





Iranian Association of
Electrical and Electronics
Engineers

Journal of Applied Research in Electrical Engineering

E-ISSN: 2783-2864

P-ISSN: 2717-414X

Homepage: <https://jaree.scu.ac.ir/>



Research Article

Investigating the Effects of Phosphorene Nanotubes (PNTs)-on-Gold Substrates on the Enhancements of the Sensitivity of SPR Biosensors

Amir Davami , Mohammad Hadi Shahrokh Abadi*

Electrical and Computer Engineering Faculty, Hakim Sabzevari University, Sabzevar 9617976487, Iran

* Corresponding Author: mhshahrokh@ieee.org

Abstract: Surface plasmon resonance (SPR) sensors have been widely considered for their sensitivity, accuracy, and appropriate response speed. This article simulates and analyzes the effects of phosphorene nanotubes (PNTs) layer with various diameters and rolling directions on the structure of SPR biosensor in the Lumerical software environment. The main structure is based on the structure of Kretschmann and the use of the BK₇ prism, a gold (Au) layer, and the end layer of phosphorene nanotubes. The proposed SPR biosensor reflectance curves are obtained, analyzed, and compared for various modes of refractive index $n = 1.33$ and 1.339 , resembling a neutral watery medium and a bacterial medium, respectively. The results show that the minimum reflection is achieved for 30 nm Au at an SPR resonance angle of $\theta = 71.59^\circ$ while by adding phosphorene nanotubes, it is observed that at a diameter of 10.08 Å and an armchair rolling direction, the configuration on the Au layer becomes favorable. The minimum reflectance of 0.199 is observed for the armchair phosphorene nanotubes (10.08Å) layer over 30 nm Au. The combination also provides a sensitivity of 152°/RIU for $\Delta n = 0.009$ with a high detection accuracy of 0.079. The results demonstrate that the layer of phosphorene nanotubes has a positive effect on SPR biosensors, and it can be used as a controlling factor in SPR biosensors.

Keywords: Biosensor, phosphorene nanotubes, reflectance, surface plasmon resonance, sensitivity.

Article history

Received 25 December 2021; Revised 01 February 2022; Accepted 04 February 2022; Published online 14 March 2022.

© 2022 Published by Shahid Chamran University of Ahvaz & Iranian Association of Electrical and Electronics Engineers (IAEEE)

How to cite this article

A. Davami, and M. H. Shahrokh Abadi, "Investigating the effects of phosphorene nanotubes (PNTs)-on-gold substrates on the enhancements of the sensitivity of SPR biosensors," *J. Appl. Res. Electr. Eng.*, vol. 1, no. 2, pp. 169-174, 2022.

DOI: 10.22055/jaree.2022.39570.1044



1. INTRODUCTION

Surface plasmon resonance (SPR) is a label-free detection method that has emerged over the past two decades as an appropriate and reliable platform in clinical analysis for biomolecular interactions. The technique can measure interactions in real-time with high sensitivity and without the need for labels. SPR sensors are one of several kinds of optical sensors that measure a variety of biological and chemical parameters according to the interaction between the sample environment and the sensor surface [1-2]. To excite surface plasma at the metal-dielectric interface, the electrons of the metal conduction band must be able to resonate with radiated light on the surface at a given wavelength [3]. There are common methods for exciting surface plasmons, including prism coupling and diffraction grating coupling [1, 4]. The prism coupling is introduced using two different structures, i.e., Krishmann and Otto [5].

In SPR-based biosensors, gold or silver is typically coated directly on the prism to separate the sensor medium and prism. Gold is used as one of the most appropriate materials because of its great resistance to oxidation and its high chemical stability.

However, the capacity of biomolecules to interact with gold is weak, thereby reducing the sensitivity of the sensor. To solve this problem, recent research on biosensor structure has used one or more layers of graphene because of its high surface-volume ratio, high electrical mobility, and stability of its atomic structure [3]. However, it does not act as a semiconductor due to the inadequate bandgap in its electronic structure [6]. This deficiency inhibits its use in many applications, including optoelectronics.

Transition metal dichalcogenides (TMDCs), another important member of the 2D material family, have also generated interest among scientists. Molybdenum disulfide (MoS₂), the most common TMDCs [7], has a perceptible band

gap, allowing the conversion of electrons into light photons and resulting in extraordinary on/off ratios. However, the MoS₂ sandwich structure the mobility of the charge carrier [8].

It seems that phosphorene can be a good alternative because it does not have any of the disadvantages of graphene and TMDCs. Black phosphorus (BP), one of the three main phosphorus allotropes, is the most thermodynamically stable relative to its red and white counterparts. An extraordinary property of black phosphorus is its high mobility [9-13], which is responsible for most of BP's unique electronic properties. Previous studies have shown that low-layer BP has great mobility, ranging from 600 cm²/V.s to 1000 cm²/V.s at room temperature [10-12, 14], which makes it possible to apply BP in electrode materials.

In addition, another remarkable property of BP is its direct and tunable bandwidth in single and multi-layer forms [10, 11], making BP an ideal semiconductor for potential applications in extraordinary light emission and effective photoelectric conversion. In addition, because of the low bandgap assigned to the significant excitation binding energy, p-type and n-type configurations can be set in BP to meet the broad range of demands in optoelectric devices, including tubular devices. BP's thin films have received scientific attention from all over the world. The puckered structure provides the BP with anisotropy in the plane, resulting in its thermal conductivity [19] and transportation anisotropy dependent on the single angle [15], particularly in the mobility of carriers [16, 17].

According to the specific properties of black phosphorus, the features of BP nanotubes have attracted more attention [18-20], such as carbon nanotubes. In comparison, research on BP tubes is limited. However, the urgent demand for tubular electronics highlights the importance of research on BP tubes, particularly for their electronic and optical properties. Due to the anisotropy of BP, the rolling direction of BP nanotubes is a decisive factor in their electrical properties.

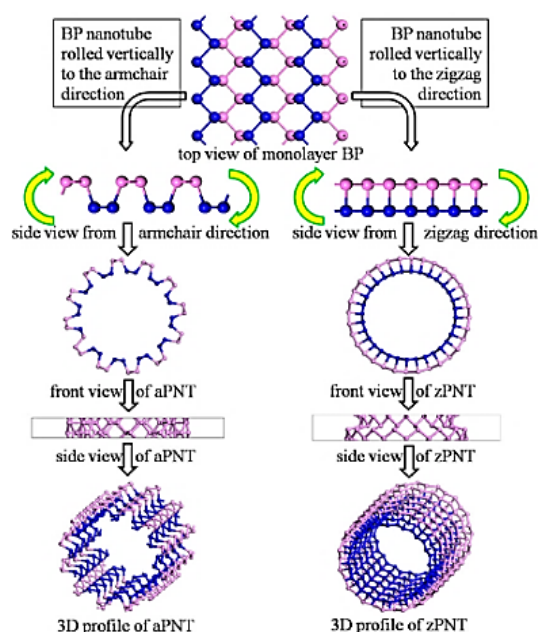


Fig. 1: A schematic diagram of the construction of BP nanotubes [21].

In addition, BP nanotubes' bandgap and optical properties can be modulated by their diameter. Therefore, we systematically investigated the properties of BP nanotubes with two different rolling directions and different radii. Similar to graphene, bulk black phosphorus is a stratified material with atomic layers superimposed by van der Waals interactions. Fig. 1 shows the structure of BP in various side views and a flow chart for the construction of PB nanotubes.

Based on the puckered structure of BP, BP nanotubes are separately rolled vertically to the zigzag or armchair direction to construct the nanotubes known as armchair phosphorene nanotubes (aPNTs) (Fig. 1) and zigzag phosphorene nanotubes (zPNTs). Based on BP's pleated structure, BP nanotubes are separately rolled vertically to the zigzag direction or armchair to construct the nanotubes accordingly [21].

In addition to the rolling direction factor, the curve radius was also taken into account. As a result, BP nanotubes were constructed with different radii of 5.2 Å, 7.3 Å, 10.06 Å, and 11.5 Å to analyze the effect of bending stress energy on electronic and optical properties. The radius values are consistent with the median circles of the models, and non-integer values have been chosen to ensure the integrity of the atomic periodicity of the puckered structure [21].

This paper proposes a phosphorene layer with different diameters and rolling directions on the top of an Au layer. The structure is formed as an SPR biosensor at 632 nm incident light, the sensitivity and resonance angle of the biosensor are studied, and the order of the layer is optimized for better resolution. The different structures are then simulated in the Lumerical environment, and changes in the refractive index are studied and compared.

2. THE PROPOSED SPR-BIOSENSOR STRUCTURE

2.1. Schematic of the Structure

In this paper, we use a four-layer Krishmann structure, including the prism, gold (Au) layer, phosphorene nanotubes, and the sampling environment, respectively. As shown in Fig. 2, the gold layer is placed on the prism without an intermediary, and the PNT layer is then placed between the Au layer and the sample medium. The physical properties of various simulated materials are presented in Table 1.

2.2. Theoretical Discussion of SPR-Biosensor

Resonance occurs when the tangential component of the incident light wave vector (k_{in}) is equal to the wave vector of the surface plasmons (k_{sp}). The incident light wave vector can increase as much as the surface plasmon wave vector and be excited at a special angle called the surface plasmon resonance angle at the metal-sample interface.

Table 1: Refractive index and thickness of different layers.

Layer	Refractive index	Thickness (or diameter) of PNTs
Prism [22]	1.515	-----
Au [22]	0.185+3.423i	30nm
aPNT(5.2Å) [21]	1.3+0.33i	0.52nm
aPNT(7.3Å)	1.25+0.41i	0.73nm
aPNT(10.08Å)	1.05+0.30i	1.00nm
aPNT(11.5Å)	1+0.22i	1.15nm
zPNT(7.3Å)	1.43+0.37i	0.73nm
zPNT(11.5Å)	1.40+0.22i	1.15nm

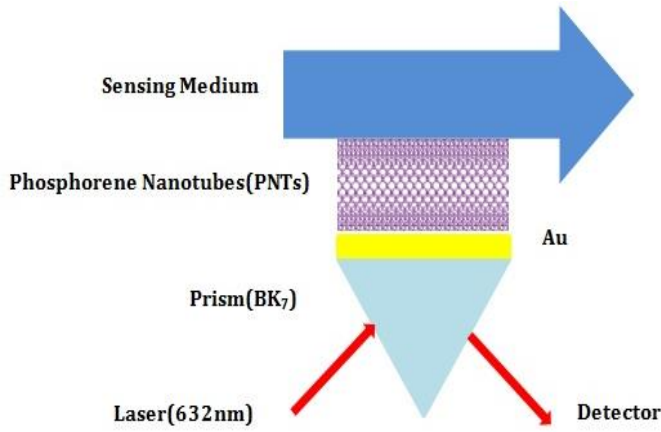


Fig. 2: Illustration of the SPR-biosensor structure.

The resonant angle can be computed by

$$k_{sp} = k_0 \sqrt{\frac{\epsilon_1 \epsilon_2}{\epsilon_1 + \epsilon_2}} \quad (1)$$

$$\theta_{SPR} = \sin^{-1} \left[\frac{1}{n_p} \sqrt{\frac{\epsilon_1 \epsilon_2}{\epsilon_1 + \epsilon_2}} \right] \quad (2)$$

in which ϵ_1 and ϵ_2 are the dielectric constant of the metal and the sensor environment, respectively, and n_p is the refractive index of the prism. Assuming resonance and energy transfer from photons to surface plasmons, the intensity of the reflected light is significantly reduced [23, 24]. In general, the characteristic of a reflective wave, including intensity, phase, and polarization under resonance conditions, is entirely dependent on the refractive index of the adjacent medium.

The important parameter in the surface plasmon resonance sensor that reflects the performance of this sensor is sensitivity (S), which indicates the rate of changes in sensor output to the changes in the measured characteristic. For example, in angular modulation, the ratio of the surface plasmon resonance angle variations to the changes in the refractive index of the sensor environment is expressed as

$$S = \frac{\Delta \theta_{SPR}}{\Delta n_s} \quad (3)$$

Detection accuracy (D.A) indicates the proximity of the measured characteristic to its true value and is calculated by

$$D.A = \frac{\Delta \theta_{SPR}}{FWHM} \quad (4)$$

Finally, the quality factor (Q) is obtained by [25]

$$Q = \frac{S}{FWHM} \quad (5)$$

3. RESULTS AND DISCUSSION

The article aims to study a new detection setup with the use of PNT layers on a thin layer of gold to enhance the light absorption capacity of the SPR biosensor and to further improve its sensitivity. The efficiency of the proposed configurations is verified in the Lumerical environment.

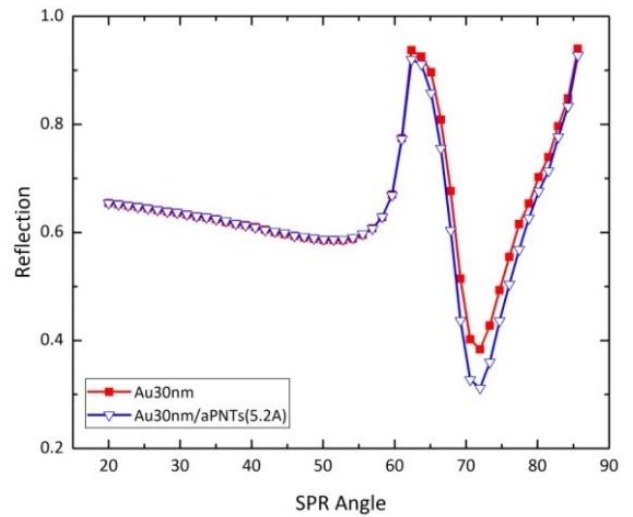


Fig. 3: The reflection spectra curves of the monolayer of Au and aPNTs/Au layers.

As shown in Fig. 3, we first examine the structure with the Au-PNTs, an armchair rolling direction (aPNTs) sensitive layer, and compare it with the results of the gold monolayer at the top of the prism.

The effect of reflected light is examined once in the presence of a gold layer and once again in the presence of aPNTs/Au. Due to the interaction between the incoming light and the surface plasmons of the gold layer, the reflected light will be of minimal intensity at a particular angle. The aim is to find this minimum angle in structures of different thicknesses. The lower the minimum reflection, the more favorable the result will be, indicating that the surface plasmon resonance occurs more strongly. In other words, the incoming light wave vector is perfectly coupled to the surface plasmon on the metal surface.

As can be seen in Fig. 3, the minimum reflectance (R_{min}) in the structure with the Au layer and the thickness of 30 nm is 0.383 and by adding an additional aPNTs layer on 30 nm Au, a ~19% reduction in R_{min} occurs in 0.311 and an approximate difference in SPR angle is $\Delta \theta \approx 0^\circ$. This configuration causes the minimum reflectance to increase dramatically, which is in good agreement with other reports.

By retaining the Au layer thickness at 30 nm, the impact of the additional layer of aPNTs on the minimum reflectance of the aPNTs/30Au configuration was also investigated and compared. As shown in Fig. 4, when the diameter of aPNTs layer grows, the lowest reflectance approaches 0.199 for aPNTs(10.08A)/30Au. Table 2 lists the minimum reflectance's corresponding to the angles of occurrence for the setup simulation at the different diameters of pants layer.

By considering zPNTs/30Au configuration as the optimized reflection spectra and to investigate the effect of zPNTs flakes on the reflection spectra, the diameter of zPNTs layer was increased to 7.3A and 11.5A flakes. Fig. 5 shows that the minimum reflectance does change significantly when the diameter of zPNTs flakes is increased, which has an impact on R_{min} . Details of the values to R_{min} and RA are listed in Table 3.

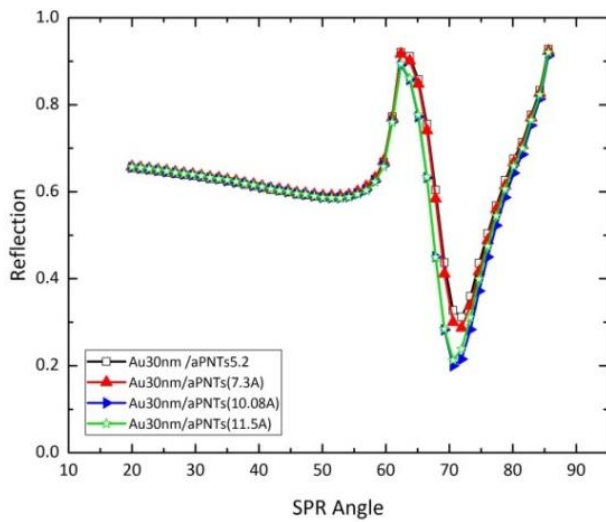


Fig. 4: The reflection spectra for different diameters of aPNTs layers in aPNTs/30Au.

Table 2: Resonance angle (θ°) and R_{min} values for different diameters of aPNTs layers in aPNTs/30Au configurations in $n = 1.33$ environment.

Diameter of aPNTs layer (Å)	Resonance angle (θ°)	Minimum reflectance (R_{min})
5.2	71.959	0.311
7.3	71.959	0.287
10.08	70.591	0.199
11.5	70.591	0.212

Table 3: Resonance angle (θ°) and R_{min} values for different diameters of zPNTs layers in zPNTs/30Au configurations in $n = 1.33$ environment.

Diameter of zPNTs layer (Å)	Resonance angle (θ°)	Minimum reflectance (R_{min})
7.3	71.959	0.309
11.5	71.959	0.295

Table 4: The sensitivity (S), detection accuracy (DA), and quality (Q) of the proposed aPNTs(10.08Å)/30Au SPR-biosensor versus work in for $n = 1.339$ medium.

SPR-Biosensor Configuration	aPNTs(10.08Å) /30Au	2L_G/30Au
FWHM	17.23	22.06
$\Delta\theta$ SPR	1.368	6.25
S ($^\circ$ /RIU)	152	89.29
DA	0.079	0.29
Q	8.82	4.26
Reference	This work	[26]

From the results in Figs. 4 and 5, we can see that the minimum reflectance happens at 0.199. This means that the combination of aPNTs(10.08Å)/30Au is the most optimal structure among the available configurations. By modifying the medium to $n = 1.339$, the sensor's sensitivity and the spectral response of the aPNTs (10.08Å)/30Au structure are investigated. Fig. 6 indicates the response of the spectral reflection to various environments. Sensitivity, S , can now be

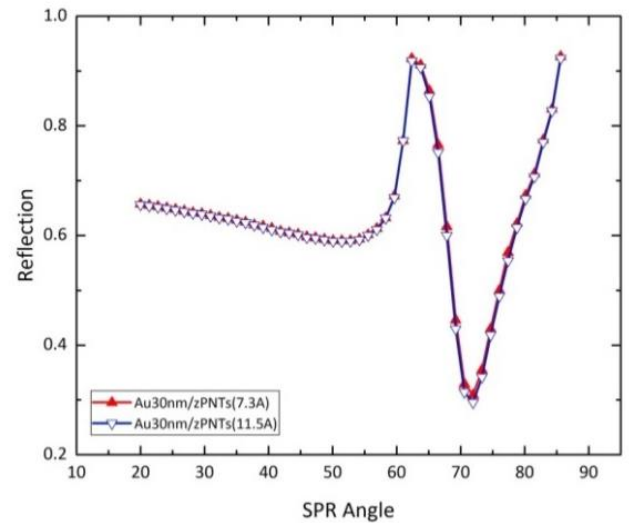


Fig. 5: The reflection spectra for different diameters of zPNTs layers in zPNTs/30Au.

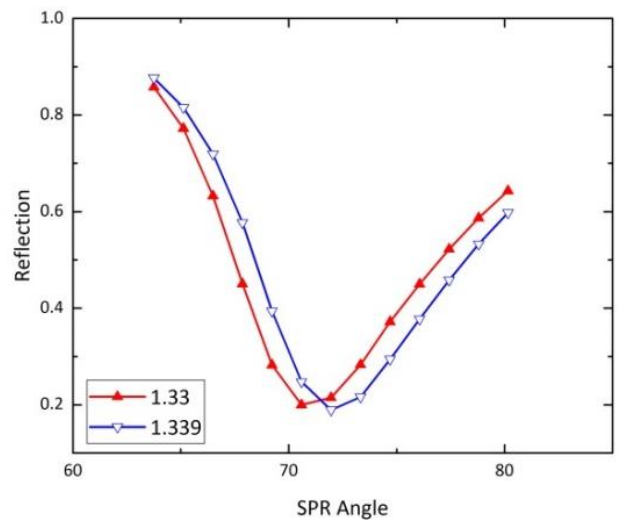


Fig. 6: The reflection spectra for aPNTs(10.08Å)/30Au configuration at watery ($n = 1.330$) and analyte ($n = 1.339$) representing.

determined using (4) and the details of Fig. 6 in response to $n = 1.330$ and $n = 1.339$.

Moreover, FWHM may be estimated at 17.23 based on the results. Equations (3-5) are used to determine sensitivity, detection accuracy, and quality, as listed in Table 5 based on the information in Fig. 5. The results of another investigation [26] into 2L_G/30Au are also presented for comparison.

4. CONCLUSION

This paper studied and introduced the effect of various PNTs/Au combinations and the diameter of their flakes on the spectral response of an SPR biosensor. In addition, the orders and diameters of the PNT layer and the medium were compared. We also examined the sensor's sensitivity and reflectivity to achieve the best configuration functionality. The results show that aPNTs (10.08Å) over 30nm Au have the highest sensitivity of 152° /RIU. The results also show that increasing the diameter of the layers in the outlet has a direct effect on the sensor's efficiency and enhances the sensor's performance.

CREDIT AUTHORSHIP CONTRIBUTION STATEMENT

Amir Davami: Conceptualization, Data curation, Formal analysis, Investigation, Software, Visualization, Roles/Writing - original draft, Writing - review & editing.
Mohammad Hadi Shahrokh Abadi: Conceptualization, Methodology, Project administration, Supervision, Validation, Visualization, Writing - review & editing.

DECLARATION OF COMPETING INTEREST

The authors declare that they have no known competing financial interests or personal relationships that could have appeared to influence the work reported in this paper. The ethical issues; including plagiarism, informed consent, misconduct, data fabrication and/or falsification, double publication and/or submission, redundancy has been completely observed by the authors.

REFERENCES

- [1] Li. Wu, H. S. Chu, W. S. Koh, and E. P. Li., "Highly sensitive graphene biosensors based on surface plasmon resonance," *Optics Express*, vol. 18, no. 14, pp. 14395-14400, 2010.
- [2] J. Homola, *Surface plasmon resonance based sensors*. Springer Science & Business Media, vol. 4, 2006.
- [3] K.V. Sreekanth, S. Zeng, K. Yong, and T. Yu, "Sensitivity enhanced biosensor using graphene-based one-dimensional photonic crystal," *Sensors and Actuators B: Chemical*, vol.182. pp. 424-428, 2013.
- [4] P. K. Maharana, and R. Jha, "Chalcogenide prism and graphene multilayer based surface plasmon resonance affinity biosensor for high performance," *Sensors and Actuators B: Chemical*, vol. 169, pp. 161-166, 2012.
- [5] A. Komlev, R. Dyukin, and E. Shutova, "The method of controlling the thickness of the deposited film on the basis of the surface plasmon resonance effect," *Journal of Physics: Conference Series*, 2017, IOP Publishing.
- [6] T. H. Wang, Y. Zhu, and Q. Jiang, "Bandgap opening of bilayer graphene by dual doping from organic molecule and substrate," *Journal of Physical Chemistry C*, vol. 117, no. 24, pp. 12873-12881, 2013.
- [7] K. S. Yong, D. M. Otalvaro, I. Duchemin, M. Saeys, and C. Joachim, "Calculation of the conductance of a finite atomic line of sulfur vacancies created on a molybdenum disulfide surface," *Physical Review B*, vol. 77, no. 20, 205429, 2008.
- [8] M. S. Fuhrer, and J. Hone, "Measurement of mobility in dual-gated MoS₂ transistors," *Nature nanotechnology*, vol. 8, no. 3, pp. 146-147, 2013.
- [9] S. I. Allec, and B. M. Wong, "Inconsistencies in the electronic properties of phosphorene nanotubes: new insights from large-scale DFT calculations," *Journal of Physical Chemistry Letters*, vol. 7, no. 21, pp. 4340-4345, 2013.
- [10] V. Sorkin, Y. Cai, Z. Ong, G. Zhang, and Y. W. Zhang, "Recent advances in the study of phosphorene and its nanostructures," *Critical Reviews in Solid State and Materials Sciences*, vol. 4, no. 2, pp. 1-82, 2017.
- [11] L. Lia, Y. Yu, and G. Ye, "Black phosphorus field-effect transistors," *Nature NanoTechnology*, vol. 9, no. 5, pp. 372-377. 2014.
- [12] W. Zhang, J. Yin, P. Zhang, and Y. Ding, "Strain/stress engineering on the mechanical and electronic properties of phosphorene nanosheets and nanotubes," *The Royal Society of Chemistry 2017 advances*, vol. 7, no. 81, pp. 51466-51474. 2017.
- [13] W. H. Chen, C. Yu, I. C. Chen, and H. C. Cheng, "Mechanical property assessment of black phosphorene nanotube using molecular dynamics simulation," *Computational Materials Science*, vol. 133, pp. 35-44, 2017.
- [14] Y. Deng et al., "Black phosphorus–monolayer MoS₂ van der Waals heterojunction p–n diode," *2014 American Chemical Society Nano*, vol. 8, no. 8, pp. 8292-8299. 2014.
- [15] C. Gomez et al. , "Isolation and characterization of few-layer black phosphorus," *2D Materials*, vol. 1, no. 2, 025001, 2014.
- [16] H. Liu, Y. Du, and Y. Deng, "Semiconducting black phosphorus: synthesis, transport properties and electronic applications," *Chemical Society Reviews*, vol. 44, no. 9, pp. 2732-2743, 2015.
- [17] P. Yasaei et al., "High-quality black phosphorus atomic layers by liquid-phase exfoliation,"*Advanced Materials*, vol. 27, no. 11, pp. 1887-1892, 2015.
- [18] S. Yu, H. Zhu, K. Eshun, A. Arab, A. Badwan, and Q. Li, "A computational study of the electronic properties of one-dimensional armchair phosphorene nanotubes," *Journal of Applied Physics*, vol. 118, no. 16, article 164306, 2015.
- [19] T. Hu, A. Hashmi, and J. Hong, "Geometry, electronic structures and optical properties of phosphorus nanotubes," *Journal of Applied Physics*, vol. 26, no. 41, 2015.
- [20] R. Ansari, A. Shahnazari, and S. Rouhi, "Density-functional-theory-based finite element model to study the mechanical properties of zigzag phosphorene nanotubes," *Physica E: Low-dimensional Systems and Nanostructures*, vol. 88, pp. 272-278, 2017.
- [21] Z. Xie , Z. Chen, N. Cheng , J. Wang ,and G. Zhu , "Tunable bandgap and optical properties of black phosphorene nanotubes," *Materials*, vol. 11, no. 2, article 304, 2018.
- [22] H. Vahed, and C. Nadri, "Sensitivity enhancement of SPR optical biosensor based on Graphene–MoS₂ structure with nanocomposite layer," *Optical Materials*, vol. 88, pp. 161-166, 2019.
- [23] H. Raether, *Surface plasmons on smooth and rough surfaces and on gratings*. Springer, vol. 118, pp. 4-39, 1988.
- [24] K. Choi, H. Kim, and Y. Lim, "Analytic design and visualization of multiple surface plasmon resonance excitation using angular spectrum decomposition for a

Gaussian input beam," *Optics Express*, vol. 13, no. 22, pp. 8866-8874, 2005.

- [25] X. Dai, Y. Liang, Y. Zhao, S. Gan, Y. Jia, and Y. Xiang, "Sensitivity enhancement of a surface plasmon resonance with tin selenide (SnSe) allotropes," *Sensors*, vol. 19, no. 1, article 173, 2019.
- [26] J. Maurya, Y. Prajapati, and R. Tripathi, "Effect of molybdenum disulfide layer on surface plasmon resonance biosensor for the detection of bacteria," *Silicon*, vol. 10, no. 2, pp. 245-256, 2018.

BIOGRAPHY



Amir Davami received his B.Sc. degree in electrical engineering from Islamic Azad University of Tabriz, Iran in 2011, his M.Sc. degree in Nanoelectronics Engineering from Tabriz University, Iran in 2014. Now, he is an Electrical Engineering Ph.D. student at Hakim Sabzevari University, Iran. His research interests are nanoelectronics, semiconductor technology, and optoelectronic devices.



Mohammad Hadi Shahrokh Abadi has received his B.Sc. in electronics engineering (1994) from the University of Semnan, Iran, and his M.Sc. (2007) and Ph.D. (2010) in Electronics Engineering from the University of Putra Malaysia (UPM). He joined the Department of Electrical and Electronics

Engineering, Hakim Sabzevari University, in 2012 as a full-time teacher and researcher in the area of semiconductor devices and materials. He is now Associate Professor at Hakim Sabzevari University, Iran. In 2020, he became a Senior Member of IEEE, where he has joined the organization since 2006. His research areas are not limited to but mainly include semiconductor materials characterization, bending electronics, MOX gas sensors, and biosensors. Currently, he is working on "Wide Band Gap Materials for Solar Cells", "Polymer-Based Solar Cell", "Electronic Biosensor for Detection of Pathogens", and "MOX Gas Sensor for Illicit Drug Detection".

Copyrights

© 2022 Licensee Shahid Chamran University of Ahvaz, Ahvaz, Iran. This article is an open-access article distributed under the terms and conditions of the Creative Commons Attribution –NonCommercial 4.0 International (CC BY-NC 4.0) License (<http://creativecommons.org/licenses/by-nc/4.0/>).



Shahid Chamran
University of AhvazIranian Association of
Electrical and Electronics
Engineers

Journal of Applied Research in Electrical Engineering

E-ISSN: 2783-2864

P-ISSN: 2717-414X

Homepage: <https://jaree.scu.ac.ir/>

Research Article

Designing of the Controller for Shipboard Microgrid Based on Linear Matrix Inequality

Farhad Amiri , Mohammad Hassan Moradi* 

Electrical Engineering Department, Faculty of Engineering, Bu-Ali Sina University, Hamedan 6516738695, Iran

* Corresponding Author: mh_moradi@yahoo.co.uk

Abstract: With the presence of distributed energy resources in microgrids, the problem of load-frequency control (LFC) becomes one of the most important concerns. Changes in the parameters of the microgrid components, as well as the disturbances forced on the grid, make it more difficult to design a suitable LFC. This paper discusses the design of a robust model predictive controller (RMPC) based on the linear matrix inequality as a secondary controller in LFC systems for controlling a microgrid on the shipboard. The main purpose of the proposed method is to improve the frequency stability of the microgrid in the presence of disturbances and the uncertainty of its parameters. The proposed controller is simulated and compared in several different scenarios considering the uncertainty of the microgrid parameters and the input disturbances. The main controllers are the fuzzy proportional-integral type 1 and 2, and multi-objective multi-purpose functions optimized with the MOFPI (MBBHA) and MOIT2FPI (MBHA) algorithms. The effectiveness of the proposed method in terms of increasing the response speed, reducing fluctuations, overcoming uncertainties of the parameters, and ensuring robustness to disturbances are discussed. The simulations are made in MATLAB software. The proposed method reduces the frequency oscillations caused by disturbances on the microgrid by 68% (68% improvement over other methods used in this field). Also, using this method, the damping speed of microgrid frequency fluctuations is increased by 53% (performance improvement).

Keywords: Microgrid on the shipboard, load-frequency control, linear matrix inequality, uncertainty.

Article history

Received 17 December 2021; Revised 27 February 2022; Accepted 02 March 2022; Published online 17 March 2022.

© 2022 Published by Shahid Chamran University of Ahvaz & Iranian Association of Electrical and Electronics Engineers (IAEEE)

How to cite this article

F. Amiri, and M. H. Moradi, "Designing of the controller for shipboard microgrid based on linear matrix inequality,"

J. Appl. Res. Electr. Eng., vol. 1, no. 2, pp. 175-185, 2022. DOI: 10.22055/jaree.2022.39484.1041



1. INTRODUCTION

The increasing need for electrical power has forced system operators to use more renewable energy resources. However, despite their many advantages in comparison with fossil-based resources, the energy resources increase the control complexity and pose many challenges to system stability and security [1, 2]. Renewable energy resources are often used as an alternative resource in modern power systems. Although increasing the penetration of these energy resources has many advantages, it poses new challenges, e.g., whether these resources can be operated beside the existing generation units properly [1, 2]. Two of the major challenges in distributed generation resources and energy storage resources are the regulation of the system voltage and frequency and if it is a suitable and proper control design both in network-connected and isolated mode.

The concept of the microgrid, which is a combination of renewable energy resources, storage devices, communication systems, loads, and controllers, was introduced in 1998. Microgrids are usually located on the distribution side and can be connected to or isolated from the upstream network. In a network-connected microgrid, it is responsible to inject real and reactive power into the system, while in the isolated mode, it is responsible for providing local loads and adjusting frequency and voltage characteristics in the nominal value. As a result, the role of automatic control is more fundamental in microgrids due to more generation and load disturbances. In the steady-state, microgrids are in equilibrium between production and consumption. If this equilibrium is lost, the frequency will deviate from its nominal value. If frequency deviations are not controlled, they can cause a lot of damage [1]. Frequency variations are very important in microgrids and

must always be in an acceptable bond. For example, if the load increases suddenly, the frequency will drop from the nominal value, which will lead to frequency instability if not controlled.

The primary-control loop is the first control loop that reacts to limit the frequency drop after unwanted events [2]. The primary-control loop limits the dropped frequency, but it is unable to return the frequency to its nominal value, and thus another control loop, called the frequency secondary control, is used [2]. The secondary-control loop is controlled by the load-frequency control (LFC). Different controllers are used in the second control loop. Due to the random and uncertain nature of wind, solar radiation, and sea waves, the power derived from renewable energy resources varies randomly. Random variations of generated power and load variations can cause load-generation imbalance and significant deviations in the microgrid frequency, especially in the isolated mode [2]. Among many factors that are important in the design of LFC, one of the most important challenges is the uncertainty in the parameters of the microgrid components. LFC approaches have already been used in research studies to eliminate the generation and frequency variations, return the frequency to the nominal value, and restore the power of the transmission line [2, 3]. Some researchers have specifically concentrated on microgrids [4-27].

Several controllers, such as typical PI [4-6], typical PID, PID based on the Ziegler-Nichols coefficient method [7], PID based on the genetic algorithm [8], PI based on PSO [9], biogeography-based PID [10], PI/PID based on quasi-oppositional harmony search algorithm (QOH) [11], fractional-order PID [12], fuzzy-PID based on fractional-order [13], PI based on fuzzy logic type 2 in combination with improved harmony search algorithm [14, 15], have been introduced for controlling load-frequency in microgrids. Also, H infinite control (H^∞) methods [16-18], fuzzy-based pso control [19], and human brain emotional learning (HBEL) [20] are some other approaches to controlling load-frequency in microgrids. In [21], the time delay effect of telecommunication systems on the load-frequency control in a multi-region system is investigated. In [22], the tertiary monitoring control strategy for controlling load-frequency in a multi-region microgrid system is introduced. In [23], fuzzy PID-based control is presented in a small three-zone system for LFC. In [24], the effect of transmission lines and super-capacitors on load-frequency control in a multi-region network is investigated. In [25], the effect of storage systems on LFC in a multi-region network is discussed. In [26], the load-frequency control is presented in a multi-region microgrid with the fuzzy PID control adjusted by the Nagai method. In [27], the load-frequency control is presented in a two-zone microgrid network with PID based on a social-spider optimizer (SSO). In [28], the load-frequency control of an isolated microgrid is investigated on the ship by a type-I and multi-objective fuzzy proportional controller, which is optimized with the online black hole algorithm.

In the proposed methods [4-27], the problem of uncertainty of system parameters (microgrid) has not been addressed for the load-frequency control loop of microgrids. The uncertainty of microgrid parameters jeopardizes the

performance of the load frequency control loop and may cause microgrid frequency instability. On the other hand, severe load disturbances and distributed energy resources are effective in the performance of this loop. When faced with severe disturbances, the loop may not be able to function properly, and the microgrid may experience frequency instability. Therefore, in the load-frequency control structure, it is necessary to have a robust controller that can attenuate disturbances on the islanded microgrid and is resistant to the uncertainty of the parameters in order to ensure the frequency stability of the microgrid.

This paper presents a control method (robust model predictive controller) for the load-frequency control loop. The robust model predictive controller is based on linear matrix inequality, and the proof of this method is based on the Lyapunov stability criterion. The proposed method can attenuate the disturbances on the microgrid on the shipboard and is very resistant to the uncertainty of the microgrid parameters. In other words, the proposed method is capable of maintaining the frequency stability of the microgrid under disturbance and parametric uncertainty. To prove the efficiency of the proposed method, several scenarios have been considered and compared with several methods used in this field.

The rest of this paper is organized as follows. Section 2 introduces the components and model of a microgrid on the slope of the shipboard. Section 3 introduces the proposed control method for microgrids based on linear matrix inequality. In Section 4, simulations are performed in several scenarios to prove the improvement of microgrid performance using the proposed controller. Finally, the conclusion is given in Section 5.

2. COMPONENTS AND MODEL OF A MICROGRID ON THE SHIPBOARD

2.1. The Model of Microgrid on the Shipboard

A microgrid on the shipboard based on LFC is depicted in Fig. 1. Microgrids on shipboards consist of photovoltaic (PV), a wind turbine (WT), a sea wave energy converter, a diesel generator (DG), a flywheel energy storage system (FESS), and a battery energy storage system (BESS). The photovoltaic, wind turbine, and wave energy converters are the main sources of load supply, but due to their power variations, the diesel generator acts as a backup power source to respond to load variations. BESS and FESS consume the surplus power and compensate for the load in the short term [23-28]. The dynamical model of each microgrid resource on the shipboard is discussed below. A microgrid on the ship is depicted in Fig 2, which represents an islanded microgrid on the ship, which includes energy resources such as wind turbines, photovoltaic, sea wave energy converters, diesel generators, and energy storage devices such as batteries and flywheels.

2.2. Wind Turbine (WT):

The wind turbine is a component that is used to convert wind energy into mechanical and electrical energy. The wind turbine power (P_{WT}) is calculated by (1) [7-9]. The dynamic model of the wind turbine is considered the first-order transform function, which is defined as (2).

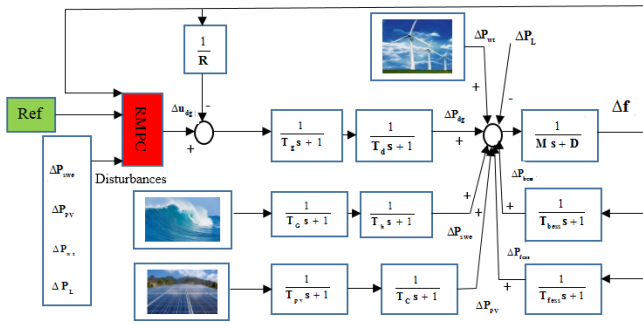


Fig. 1: A schematic of microgrids on shipboards based on the LFC.

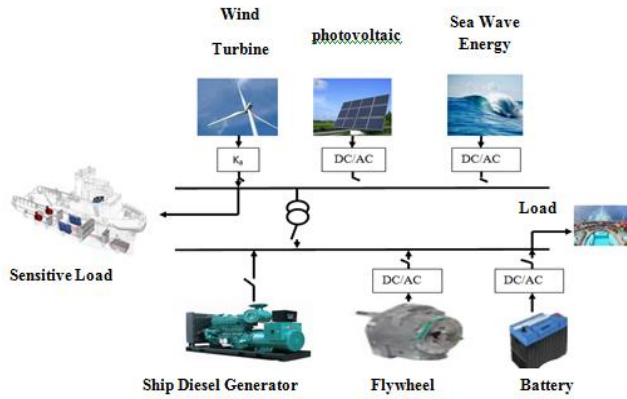


Fig. 2: A schematic of microgrids on shipboards.

$$P_{WT} = \frac{1}{2} C_p(\beta, \lambda) \rho A V_w^3 \quad (1)$$

$$G_{WT} = \frac{k_{WT}}{T_{WT}s + 1} \quad (2)$$

In (1), ρ is the air density, A is the surface swept by the blades, V_w is the wind speed, and $C_p(\beta, \lambda)$ is the turbine performance factor that depends on the environmental conditions and how the turbine is made. In (2), T_{WT}, k_{WT} are the wind turbine gain and time constant, respectively [7, 9].

2.3. Photovoltaic (Solar Cell)

The photovoltaic converts solar energy into electrical energy [4-5]. Solar power is dependent on temperature and radiation. The dynamical model of the solar cell with the inverter model is represented by (3) and (4) [4-5]. The inverter and photovoltaic model are considered a first-order transform function. In (3), T_c is the time constant of the inverter related to the photovoltaic, and in (4), and T_{pv} is the time constant of the photovoltaic.

$$G_c = \frac{1}{T_c s + 1} \quad (3)$$

$$G_{pv} = \frac{1}{T_{pv} s + 1} \quad (4)$$

2.4. Sea Wave Energy (SWE)

The energy of sea waves is considered a distributed energy resource. The conversion of sea waves into energy is carried out by wave energy converter (WEC). In this study, the energy of sea waves is considered a renewable energy resource. Also, the transform function of the wave converter for shipboards is considered a first-order time delay [28].

2.5. Diesel Generator Model (DG)

The block diagram of a diesel generator and governor is shown in Fig. 3, which includes the droop control loop R. A first-order time delay for the valve drive system and diesel engine with the time constants T_g and T_d are shown, respectively. Δu_{dg} is the load-frequency control signal and ΔF is the frequency deviation. ΔX_g is the valve position [6].

2.6. Battery Energy Storage Model (BESS)

The battery stores electrical energy in the form of chemical mechanism and DC voltage. It requires a charger and an inverter to generate AC current and voltages. In this paper, an oxidation battery is used due to its features, including higher capacity, quicker mechanism, and discharge during the operation. The battery model and the inverter connected to the microgrid are represented as a first-order time delay in (5). T_{bess} is the battery time constant [12].

$$\frac{1}{T_{bess}s + 1} \quad (5)$$

2.7. Flywheel Energy Storage System (FESS)

In the flywheel, the energy is stored as kinetic energy. Equation (6) represents the kinetic energy [12, 28]. In (6), I is the inertia of the flywheel and W is the angular velocity (rad/sec). The dynamic model of the flywheel is represented as the first-order transform function in (7). T_{fess} is the time constant of the flywheel [12, 28].

$$k_E = \frac{1}{2} I W^2 \quad (6)$$

$$G_{fess} = \frac{1}{T_{fess}s + 1} \quad (7)$$

2.8. Model of the Rotoring Mass on the Shipboard

To keep the microgrid on the shipboard in a stable and balanced situation, frequency deviation occurs with power changes. In practice, however, there is a time delay between the system power deviation and frequency deviation. The rotor-mass model of microgrids on shipboards is shown in (8). In (8), M is the inertia constant and D is the damping constant [7, 28]

$$G = \frac{1}{Ms + D} \quad (8)$$

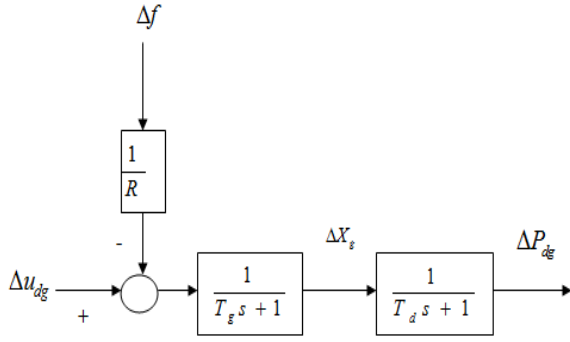


Fig. 3: The dynamic model of diesel generators.

2.9. The Load Dynamic Model

This paper presents two different types of shiploads, which are equivalent to asynchronous motors and the resistive load with respect to 350 HP and 400 kW, separately. The variations of the shiploads are also considered. The variations of the shipload in this paper only include the variations of the resistive loads. The dynamic model of the variations of the resistive loads is shown in Fig. 4. The standard deviation is multiplied by the random output fluctuations derived from the white noise block in MATLAB/SIMULINK to simulate the real-time random power fluctuations on the load profile [28, 29].

3. DESIGNING A PROPOSED CONTROL METHOD FOR MICROGRID BASED ON LINEAR MATRIX INEQUALITY

3.1. Dynamic Model of Microgrid on the Shipboard

First, according to Fig. 1, linear equations at the operating point of the microgrid on the ship are introduced as (9)-(13).

$$\dot{\Delta X}_g = \frac{\Delta u_{dg}}{T_g} - \frac{\Delta f}{RT_g} - \frac{\Delta X_g}{T_g} \quad (9)$$

$$\dot{\Delta P}_{dg} = \frac{\Delta X_g}{T_d} - \frac{\Delta P_{dg}}{T_d} \quad (10)$$

$$\dot{\Delta P}_{fess} = \frac{\Delta f}{T_{fess}} - \frac{\Delta P_{fess}}{T_{fess}} \quad (11)$$

$$\dot{\Delta P}_{bess} = \frac{\Delta f}{T_{bess}} - \frac{\Delta P_{bess}}{T_{bess}} \quad (12)$$

$$\dot{\Delta f} = \frac{-D \times \Delta f}{M} - \frac{\Delta P_L}{M} + \frac{\Delta P_{swe}}{M} + \frac{\Delta P_{bess}}{M} + \frac{\Delta P_{pv}}{M} + \frac{\Delta P_{wt}}{M} + \frac{\Delta P_{dg}}{M} + \frac{\Delta P_{fess}}{M} \quad (13)$$

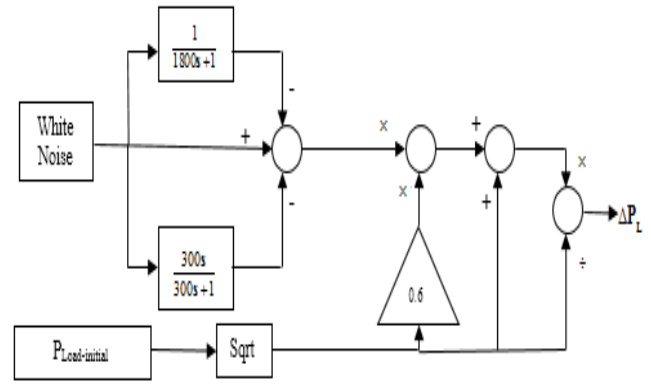


Fig. 4: The dynamic model of the variations of the resistive loads

In (9)-(13), ΔP_{fess} is the flywheel power, ΔP_{bess} is the battery power, ΔP_L is the Load variation, ΔP_{swe} is the power taken from sea waves, ΔP_{pv} is the photovoltaic power, ΔP_{wt} is the wind turbine power, R is the dropped factor, Δu_{dg} is the signal sent to the generator, ΔX_g is the output generator changes, and ΔP_{dg} is the diesel generator changes. The state equations are represented as (14). Based on (14), the equations of the microgrid states on the ship are obtained as (15) and (16).

$$\begin{aligned} \dot{X} &= A X + B U + D W \\ Y &= C X \end{aligned} \quad (14)$$

in which X is the vector of state variables for the model predictive control, A is the model predictive control state space, matrix U is the model predictive control output vector, B is the model predictive control coefficients matrix, W is the disturbance vector (uncontrolled input) of model predictive control, and D is the disturbance coefficient matrix.

$$\begin{bmatrix} \dot{\Delta X}_g \\ \dot{\Delta P}_{dg} \\ \dot{\Delta P}_{fess} \\ \dot{\Delta P}_{bess} \\ \dot{\Delta f} \\ 0 \end{bmatrix} = \begin{bmatrix} -\frac{1}{T_g} & 0 & 0 & 0 & -\frac{1}{R \times T_g} \\ \frac{1}{T_d} & -\frac{1}{T_d} & 0 & 0 & 0 \\ 0 & 0 & \frac{-1}{T_{fess}} & 0 & \frac{1}{T_{fess}} \\ 0 & 0 & 0 & \frac{-1}{T_{bess}} & \frac{1}{T_{bess}} \\ 0 & \frac{1}{M} & \frac{1}{M} & \frac{1}{M} & \frac{-D}{M} \end{bmatrix} \begin{bmatrix} \Delta X_g \\ \Delta P_{dg} \\ \Delta P_{fess} \\ \Delta P_{bess} \\ \Delta f \end{bmatrix} + \begin{bmatrix} \frac{1}{T_g} \\ 0 \\ 0 \\ 0 \\ 0 \end{bmatrix} \begin{bmatrix} \Delta u_{dg} \end{bmatrix} \quad (15)$$

$$\begin{bmatrix} 0 \\ 0 \\ 0 \\ 0 \\ \frac{1}{M} \end{bmatrix} + \begin{bmatrix} \Delta P_{wt} + \Delta P_{swe} + \Delta P_{pv} - \Delta P_L \end{bmatrix}$$

$$y = \begin{bmatrix} \Delta X_g \\ \Delta P_{dg} \\ \Delta P_{fess} \\ \Delta P_{bess} \\ \Delta f \end{bmatrix} \quad (16)$$

3.2. Model Predictive Control (MPC)

In the model predictive control, the control signal is obtained by minimizing a cost function. The control signal values in the control horizon are determined so that the system outputs follow the specified reference path in the future and on a given horizon. For this purpose, the cost function, which is generally considered the square of the deviation of the controlled variables from the desired values, is minimized [29-35]. The structure of the model predictive control is depicted in Fig. 5.

3.3. Converting the Model Predictive Control to the Robust Model Predictive Control

Firstly, the state space of a microgrid on the shipboard obtained from (15) and (16) is introduced in the discrete form as (17). The objective function of the model predictive control is defined as (18). In (18), $J(k)$ is the cost function at time k , N_2 is the upper prediction horizon, Q_1 is the weighting coefficient, R is the weight factor, and $u(k+i)$ is the control signal.

First, uncertainty is introduced in the prediction model control for which multi-dimensional uncertainty is implemented as (19). $A(k), B(k)$ are the dynamical time-varying matrices. In a convex set Ω , there are all possibilities for $A(k), B(k)$ which is expressed in (20). As a result, the objective function of the model predictive control is expressed as (21). The purpose of the robust model predictive control problem is to find the coefficient F in (22) in such a way that on a certain horizon, a huge number of cost functions in (21) is minimized. By obtaining a control signal F and implementing it in the process, the output is re-measured and the optimization problem is solved again. To apply the minimization problem to the maximization of uncertainty problems, an upper bound is defined in (18) as the Lyapunov function (23). The Lyapunov function is defined as in (24). Given (23) and (24), if a matrix P is found in such a way that it is greater than the cost function, for all situations the uncertainty is taken into account in the matrix P . The stability condition of the Lyapunov function is $V(k+1) - V(k) < 0$ and $P > 0$. Considering (25), if the left-hand side of (25) is summed up from j - and from the left $-V(x(k))$, it will be $i = 0 - \infty$ from the right. Finally, it leads to (26), and eventually, the upper bound of the cost function is found. Therefore, (26) is transformed into a squared Lyapunov function and implicitly implies the uncertainties of the system. (27) is obtained by defining an upper bound for (26). The modified (28) of (27) has the constraints to solve the robust prediction control problem.

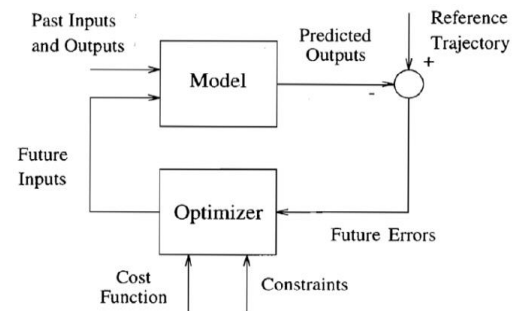


Fig. 5: The structure of the model predictive control.

To solve the problem, the constraint in (28) is represented as (29) using linear matrix inequality and Schur complement. The stability condition of the Lyapunov function is also introduced as (30) in which L is the number of vertices in the multi-dimensional model. The constraints on the input of the system are formed as (31) that is transformed into (32) using matrix inequalities. The constraints on the output of the system are formed as (33) that is transformed into (34) using matrix inequalities.

$$\begin{aligned} x(k+1) &= Ax(k) + Bu(k) \\ y(k) &= Cx(k) \end{aligned} \quad (17)$$

$$\min j(k) \quad (18)$$

$$u(k+i), i = 1, 2, \dots, N_2$$

$$j(k) = \sum_0^{N_2} (x(k+i)^T Q_1 x(k+i) + u(k+i)^T Ru(k+i))$$

$$[A(k) \ B(k)] \in \Omega \quad (19)$$

$$\Omega = Co\{[A_1, B_1], [A_2, B_2], \dots, [A_L, B_L]\} \quad (20)$$

$$\min_{u(k+i), i = 1, 2, \dots, N_2} \max_{[A(k+i), B(k+i)] \in \Omega} j_\infty(k) \quad (21)$$

$$u(k+i) = Fx(k+i) \quad (22)$$

$$j_\infty < V(x(k)) \quad (23)$$

$$V(x(k)) = x^T(k)Px(k) \quad (24)$$

$$\begin{aligned} V(x(k+i+1|k)) - V(x(k+i|k)) &< \\ -(x(k+i|k)^T Q_1 x(k+i|k) + u(k+i|k)^T Ru(k+i|k)) \end{aligned} \quad (25)$$

$$\min_{u(k+i), i = 1, \dots, N_2} V(x(k)) \quad (26)$$

$$\min_{x^T(k)Px(k)} \eta \quad (27)$$

$$\min_{\gamma, Q, Y} \gamma \quad (28)$$

$$\begin{bmatrix} 1 & x^T(k) \\ x(k) & Q \end{bmatrix} \geq 0 \tag{29}$$

$$\begin{bmatrix} Q & QA_j^T + Y^T B_j^T & QQ_j^{\frac{1}{2}} & Y^T R^{\frac{1}{2}} \\ A_j Q + B_j Y & Q & 0 & 0 \\ Q_j^{\frac{1}{2}} Q & 0 & \eta I & 0 \\ R^{\frac{1}{2}} Y & 0 & 0 & \eta I \end{bmatrix} \geq 0 \quad j=1,2,\dots,L \tag{30}$$

$$\|u(k+i|k)\|_2 \leq u_{\max} \tag{31}$$

$$\begin{bmatrix} u_{\max}^2 I & Y \\ Y^T & Q \end{bmatrix} \geq 0 \tag{32}$$

$$\|y(k+i|k)\|_2 \leq y_{\max} \tag{33}$$

$$\begin{bmatrix} Q & (A_j Q + B_j Y)^T C^T \\ C(A_j Q + B_j Y)^T C^T & Q \end{bmatrix} \geq 0 \quad j=1,2,\dots,L \tag{34}$$

3.4. Designing a Robust Model Predictive Control System for the Problem

- 1) Form the continuous state-space system
- 2) Convert the continuous state space to a discrete state space using the Euler approximation method
- 3) Minimize (28) by considering the constraints (29), (30), (32), and (34).
- 4) Calculate the control signal and apply it to the system

The flowchart of the method proposed for solving the problem is shown in Fig. 6. The proof of the above equations is given in [31-36].

4. SIMULATION

4.1. Parameters Related to the Microgrid on the Shipboard

The parameters of a microgrid on the ship are provided in Table 1.

4.2. Scenarios

In the first scenario, the load disturbances in a microgrid are considered without any regard to the power generated from distributed energy resources. In the second scenario, disturbances of the distributed energy resources are considered and finally, in the third scenario, load disturbances with given uncertainty of the parameters are considered.

Scenario (1): In this scenario, the changes in the distributed energy resources are not considered, and only load disturbances are considered. The load disturbances have been applied to the microgrid according to Fig. 7. In Fig. 8, the frequency response of the microgrid is in terms of load disturbances. The maximum frequency deviation using

the proposed method is 0.005 Hz. The maximum frequency deviation using a multi-objective fuzzy proportional-integral controller type 2 optimized by the black hole algorithm is 0.027 Hz. The maximum frequency deviation using a multi-objective proportional-integral controller optimized with the black hole algorithm is 0.033 Hz. As can be seen in the simulation results, the proposed RMPC in comparison with the multi-objective proportional-integral controller optimized with the black hole algorithm [28] and multi-objective fuzzy proportional-integral controller type 2 optimized by the black hole algorithm [28] has a better response speed and lower fluctuation and is more robust to load disturbances.

Scenario (2): In this scenario, changes in distributed energy resources are considered while load disturbances aren't. Disturbances of distributed energy resources (wind turbine, photovoltaic, sea wave) have been applied to the microgrid according to Fig. 9. Fig. 10 depicts the frequency response of the microgrid in terms of disturbances. The maximum frequency deviation using the proposed method is 0.13 Hz. The maximum frequency deviation using the multi-objective fuzzy proportional-integral controller type 2 optimized by the black hole algorithm is 0.97 Hz. The maximum frequency deviation using the multi-objective proportional-integral controller optimized with the black hole algorithm is 0.73 Hz. As can be seen in the simulation results, the proposed RMPC controller in comparison with the multi-objective proportional-integral controller optimized with a black hole algorithm [28] and multi-objective fuzzy-proportional integral controller type 2 optimized with the black hole algorithm [28] has a better response speed and lower fluctuation and is more robust to distributed energy resources disturbances.

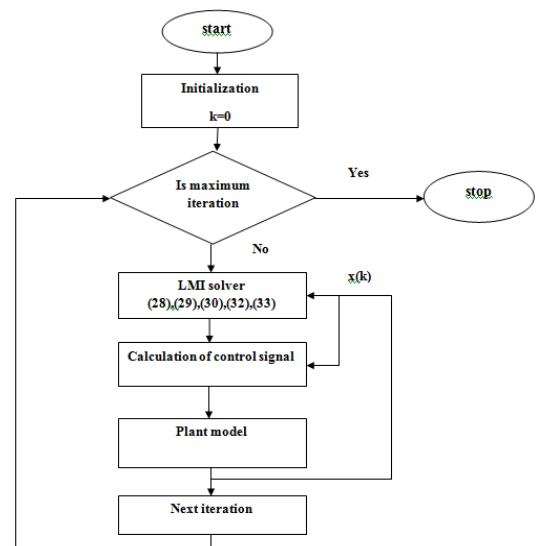


Fig. 6: The flowchart of the proposed method.

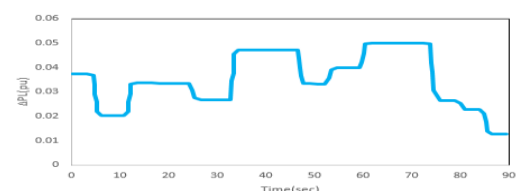


Fig. 7: The load disturbances.

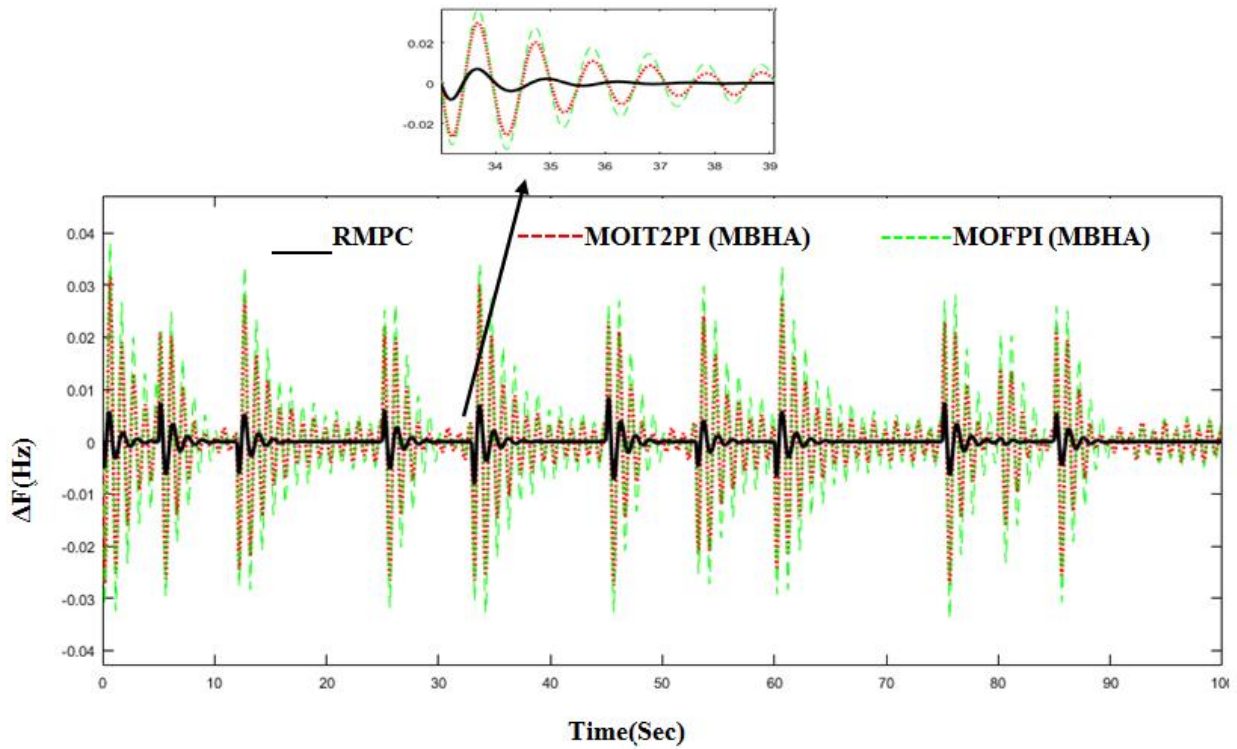


Fig. 8: The frequency response of the microgrid.

Table 1: The parameters of the microgrid on the shipboard.

Parameter	Value	Parameter	Value
T_g	2s	T_{fess}	0.1s
T_d	1s	T_{bess}	0.1s
R	3(pu Mw/second)	T_c	0.5s
T_G	0.5s	T_{pv}	4s
T_h	4s	C_p	0.195
D	0.012(pu/Hz)	ρ_A	1.225Km/m ³
$T(\text{mpc})$	0.1		

Scenario (3): In this scenario, changes in distributed energy resources are not considered and only load disturbances are considered with the uncertainty in parameters. Table 2 shows the changes in the parameters related to the microgrid. The load disturbances have been applied to the microgrid according to Fig. 7, taking into account the uncertainty of the parameters. The frequency response of the microgrid in terms of load disturbances is depicted in Fig. 11. The maximum frequency deviation using the proposed method is 0.006 Hz. The maximum frequency deviation using the multi-objective fuzzy proportional-integral controller type 2 optimized by the black hole algorithm is 0.034 Hz. The maximum frequency deviation using the multi-objective proportional-integral controller optimized with the black hole algorithm is 0.042 Hz. As can be seen in the simulation results, the proposed RMPC controller in comparison with the multi-objective proportional-integral controller optimized with the black hole algorithm [28] and multi-objective fuzzy-proportional-integral controller type 2 optimized with the black hole algorithm [28] has a better response speed and lower fluctuation and is more robust to parameter uncertainties.

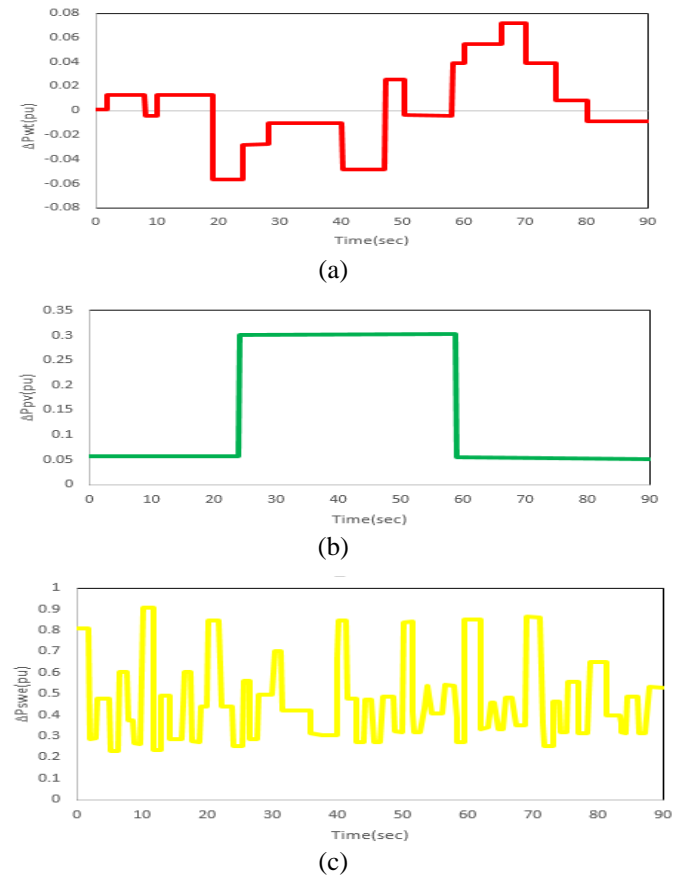


Fig. 9: Disturbances of (a) the wind turbine, (b) photovoltaic, and (c) sea wave.

Scenario (4): In this scenario, changes in distributed energy resources and load disturbances are considered. Fig. 12 shows the changes in distributed generation sources.

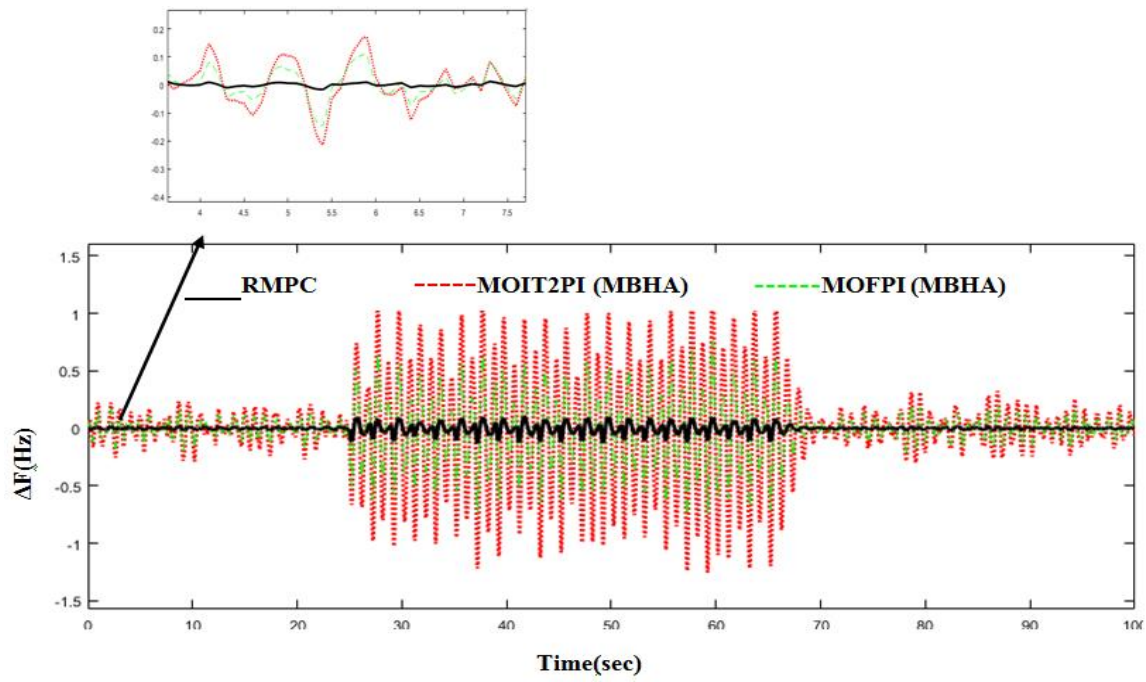


Fig. 10: The frequency response of the microgrid.

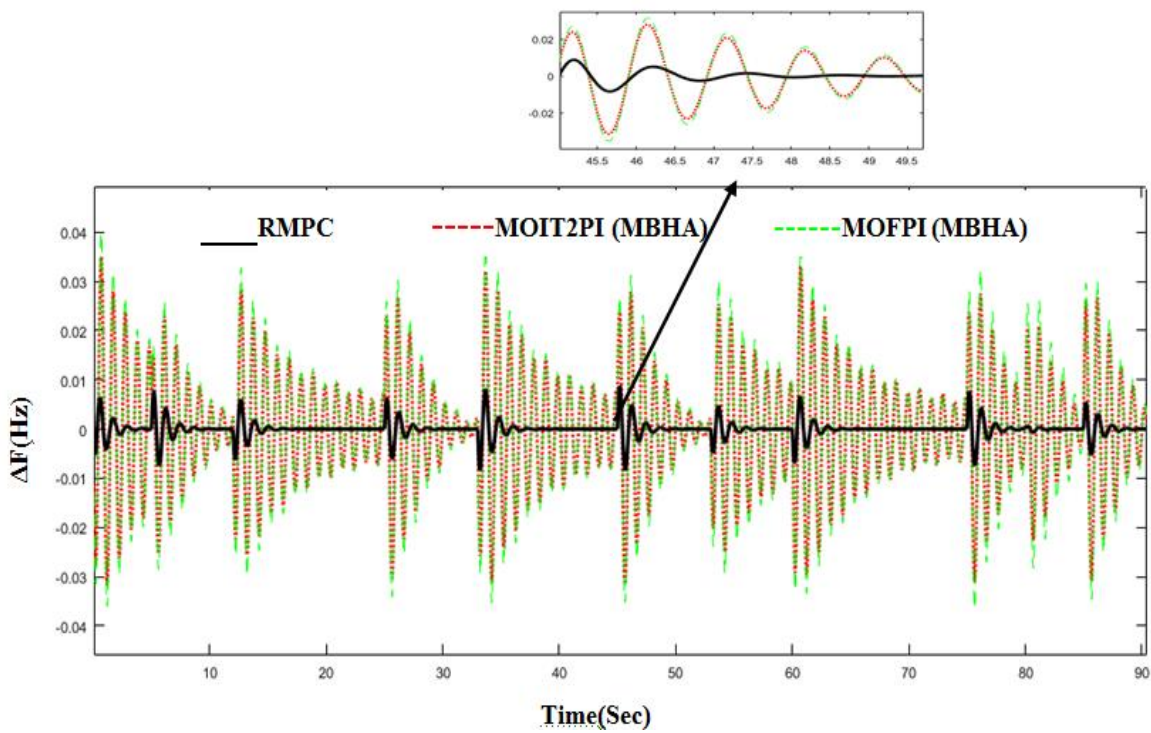


Fig. 11: The frequency response of the microgrid.

Table 2: The changes in the microgrid parameters.

Parameter	Range
R	+25%
D	-15%
M	+45%
T_e	-35%
T_g	+15%
$T_{r_{ess}}$	-15%
$T_{b_{ess}}$	+25%

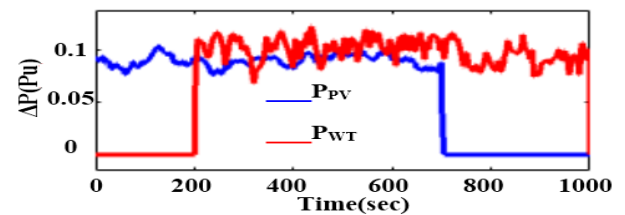


Fig. 12: The changes in distributed generation sources.

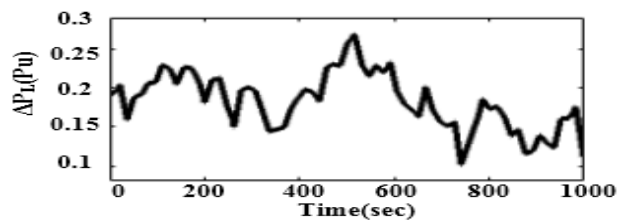


Fig. 13: Load changes applied to the islanded microgrid.

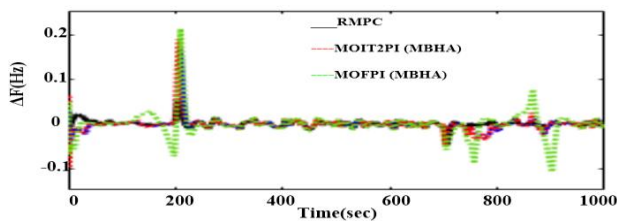


Fig. 14: The frequency response of the microgrid.

Fig. 13 shows the load changes applied to the islanded microgrid. Fig. 14 shows the microgrid frequency response to changes in distributed generation and load sources. The maximum frequency deviation using the proposed method is 0.05 Hz. The maximum frequency deviation using the multi-objective fuzzy proportional-integral controller type 2 optimized by the black hole algorithm is 0.17 Hz. The maximum frequency deviation using the multi-objective proportional-integral controller optimized with the black hole algorithm is 0.21 Hz.

5. CONCLUSION

The issue of frequency stability in microgrids is important. One of the most important components for improving frequency stability is the load-frequency control loop. The load-frequency control loop is used to improve the microgrid frequency stability and return the frequency to the nominal value after a fault. In this paper, a control method (predictive controller of a robust model based on linear matrix inequality) is designed in the load-frequency control structure. According to the results, the frequency fluctuations due to load disturbances have been reduced by 80% using the proposed method (compared to other methods proposed in this field). Frequency fluctuations caused by load disturbances and uncertainty of system parameters have been reduced by 82% using the proposed method compared to the other methods proposed in this field. Frequency fluctuations induced by disturbances of distributed energy resources have been reduced by 82% using the proposed method versus the other methods proposed in this field. According to these results, the proposed method is very robust to disturbances and uncertainty of microgrid parameters and improves the microgrid frequency stability on the shipboard.

CREDIT AUTHORSHIP CONTRIBUTION STATEMENT

Farhad Amiri: Conceptualization, Data curation, Formal analysis, Methodology, Resources, Software, Roles/Writing - original draft, Writing - review & editing.
Mohammad Hassan Moradi: Supervision, Validation.

DECLARATION OF COMPETING INTEREST

The authors declare that they have no known competing financial interests or personal relationships that could have appeared to influence the work reported in this paper. The ethical issues, including plagiarism, informed consent, misconduct, data fabrication and/or falsification, double publication and/or submission, and redundancy, have been completely observed by the authors.

REFERENCES

- [1] F. Amiri, and A. Hatami, "A model predictive control method for load-frequency control in islanded microgrids," *Computational Intelligence in Electrical Engineering*, vol. 8, no. 1, pp. 9-24, 2017.
- [2] F. Amiri, and M. H. Moradi, "Coordinated control of LFC and SMES in the power system using a new robust controller," *Iranian Journal of Electrical and Electronic Engineering*, vol. 17, no. 4, pp. 1912-1912, 2021.
- [3] F. Amiri, and M. H. Moradi, "Designing a fractional order PID controller for a two-area micro-grid under uncertainty of parameters," *Iranian Journal of Energy*, vol. 20, no. 4, pp. 49-78, 2018.
- [4] F. Amiri, and A. Hatami, "Nonlinear Load frequency control of isolated microgrid using fractional order PID based on hybrid craziness-based particle swarm optimization and pattern search," *Journal of Iranian Association of Electrical and Electronics Engineers*, vol. 17, no. 2, pp. 135-148, 2020.
- [5] D. K. Lal, A. K. Barisal, and M. Tripathy, "Load frequency control of multi area interconnected microgrid power system using grasshopper optimization algorithm optimized fuzzy PID controller," in *2018 Recent Advances on Engineering, Technology and Computational Sciences (RAETCS)*, 2018, pp. 1-6.
- [6] Y. Yang, C. Li, J. Xu, F. Blaabjerg, and T. Dragičević, "Virtual inertia control strategy for improving damping performance of DC microgrid with negative feedback effect," in *IEEE Journal of Emerging and Selected Topics in Power Electronics*, vol. 9, no. 2, pp. 1241-1257, April 2021.
- [7] F. Amiri, and M. H. Moradi, "A new control strategy for controlling isolated microgrid," *The Journal of Energy: Engineering & Management*, vol. 10, no. 4, pp. 60-73, 2021.
- [8] D. C. Das, A. Roy, and N. Sinha, "GA based frequency controller for solar thermal diesel-wind hybrid energy generation/energy storage system," *International Journal of Electrical Power & Energy Systems*, vol. 43, no. 1, pp. 262-79, 2012.
- [9] D. C. Das, A. K. Roy, and N. Sinha, "PSO based frequency controller for wind-solar-diesel hybrid energy generation/energy storage system," in *2011 International Conference on Energy, Automation and Signal*, Bhubaneswar, Odisha, 2011, pp. 1-6.
- [10] R. H. Kumar, and S. Ushakumari, "Biogeography-based Tuning of PID controllers for load frequency

- control in microgrid," in *2014 International Conference on Circuit, Power and Computing Technologies [ICCPCT], Nagercoil*, 2014, pp. 797-802.
- [11] G. Shankar, and V. Mukherjee, "Load frequency control of an autonomous hybrid power system by quasi-oppositional harmony search algorithm," *International Journal of Electrical Power & Energy Systems*, vol. 78, pp. 715–734, 2016.
- [12] M. Shahbazi, and F. Amiri, "Designing a neuro-fuzzy controller with CRPSO and RLSE algorithms to control voltage and frequency in an isolated microgrid," *2019 International Power System Conference (PSC)*, 2019, pp. 588-594.
- [13] I. Pan, and S. Das, "Fractional order fuzzy control of hybrid power system with renewable generation using chaotic PSO," *The International Society of Automation*, vol. 62, pp. 19-29, 2016.
- [14] M. H. Khooban, T. Niknam, F. Blaabjerg, P. Davari, and T. Dragicevic, "A robust adaptive load frequency control for micro-grids," *The International Society of Automation*, vol. 65, pp. 220-229, 2016.
- [15] M.H. Khooban, T. Niknam, F. Blaabjerg, P. Davari, and T. Dragicevic, "A new load frequency control strategy for micro-grids with considering electrical vehicles," *Electric Power Systems Research*, vol. 143, pp. 585-598, 2017.
- [16] V. P. Singh, S. R. Mohanty, N. Kishor, and P. K. Ray, "Robust H-infinity load frequency control in hybrid distributed generation system," *International Journal of Electrical Power & Energy Systems*, vol. 46, pp. 294-305, 2013.
- [17] H. Bevrani, M. R. Feizi, and S. Ataee, "Robust frequency control in an islanded microgrid: H-infinity and μ -synthesis approaches," *IEEE Transactions on Smart Grid*, vol. 7, no. 2, pp. 706-717, March 2016.
- [18] S. M. Azizi, and S. A. Khajehoddin, "Robust load frequency control in islanded microgrid systems using μ -synthesis and D-K iteration," *2016 Annual IEEE Systems Conference (SysCon)*, Orlando, 2016, pp. 1-8.
- [19] H. Bevrani, F. Habibi, P. Babahajyani, M. Watanabe, and Y. Mitani, "Intelligent frequency control in an ac microgrid: online pso-based fuzzy tuning approach," *IEEE Transactions on Smart Grid*, vol. 3, no. 4, pp. 1935-1944, 2012.
- [20] M. Khalghani, M. Khooban, M. Moghaddam, N. Vafamand, and M. Goodarzi, "A self-tuning load frequency control strategy for microgrids: Human brain emotional learning," *International Journal of Electrical Power & Energy Systems*, vol. 75, pp. 311-319, 2016.
- [21] V. P. Singh, N. Kishor, and S. Paulson, "Communication time delay estimation for load frequency control in two-area power system," *Ad Hoc Networks*, vol. 41, pp. 69-85, 2016.
- [22] F. Tedesco, and A. Casavola, "Fault-tolerant distributed load/frequency coordination strategies for multi-area power microgrids," *International Federation of Automatic Control –Papers OnLine*, vol. 48, no. 21, pp. 54-59, 2015.
- [23] R. Fan, J. Zhao, B. Pan, N. Chen, T. Wang, and H. Ma, "Automatic generation control of three-area small hydro system based on fuzzy PID control," in *2014 International Conference on Power System Technology*, Chengdu, 2014, pp. 2522-2528.
- [24] P. Ray, S. Mohanty, and N. Kishor, "2010. Small-signal analysis of autonomous hybrid distributed generation systems in presence of ultracapacitor and tie-line operation," *Journal of Electrical Engineering*, vol. 61, no. 4, pp. 205-214, 2010.
- [25] G. Messinis et al., "A multi-microgrid laboratory infrastructure for smart grid applications," *MedPower 2014*, Athens, 2014. pp. 1-6.
- [26] D. I. Makrygiorgou and A. T. Alexandridis, "Nonlinear modeling, control and stability analysis of a hybrid ac/dc distributed generation system," in *2017 25th Mediterranean Conference on Control and Automation (MED)*, 2017, pp. 768-773.
- [27] H. M. Hasanien, and A. A. El-Fergany, "Salp swarm algorithm-based optimal load frequency control of hybrid renewable power systems with communication delay and excitation cross-coupling effect," *Electric Power Systems Research*, vol. 176, 105938, 2019.
- [28] M. H. Khooban, T. Dragicevic, F. Blaabjerg, and M. Delimar, "Shipboard microgrids: A novel approach to load frequency control," *IEEE Transactions on Sustainable Energy*, vol. 9, no. 2, pp. 843-852, 2018.
- [29] G. Magdy, G. Shabib, A. A. Elbaset, and Y. Mitani, "Renewable power systems dynamic security using a new coordination of frequency control strategy based on virtual synchronous generator and digital frequency protection," *International Journal of Electrical Power & Energy Systems*, vol. 109, pp. 351-368, 2019.
- [30] F. Amiri, and M. Moradi, "Microgrid on the ship: load Frequency- control of the microgrid, taking into account the Sea Wave energy by the optimized model predictive controller," *Journal of Renewable and New Energy*, vol. 8, no. 1, pp. 78-90, 2021.
- [31] F. Amiri, and M. Moradi, "Designing a new robust control for virtual inertia control in the microgrid with regard to virtual damping," *Journal of Electrical and Computer Engineering Innovations (JECEI)*, vol. 8, no. 1, pp. 53-70, 2020.
- [32] M. H. Moradi, and F. Amiri, "Virtual inertia control in islanded microgrid by using robust model predictive control (RMPC) with considering the time delay," *Soft Computing*, vol. 25, no. 8, pp. 6653-6663, 2021.
- [33] F. Amiri, and M. H. Moradi, "Angular speed control in a hybrid stepper motor using linear matrix inequality," *Computational Intelligence in Electrical Engineering*, vol. 12, no. 3, pp. 33-50, 2020.
- [34] F. Amiri, and M. H. Moradi, "Designing a new robust control method for AC servo motor," *Journal of Nonlinear Systems in Electrical Engineering*, vol. 7, no. 1 pp. 55-80, 2020.

- [35] M. H. Moradi, and F. Amiri, "Load frequency control in a two area microgrid by optimized model predictive controller," *Journal of Iranian Association of Electrical and Electronics Engineers*, vol. 19, no. 1, 2021.
- [36] F. Amiri, and S. Afshar, "Load frequency control via adaptive fuzzy PID controller in an isolated microgrid," in *2017 International Power System Conference (PSC)*. 2017.

BIOGRAPHY



Farhad Amiri was born in Ilam, Iran. He received his M.Sc. degree in Electrical Engineering from Bu-Ali Sina University in 2017. He is currently working toward his Ph.D. degree in Electrical Engineering at Bu-Ali Sina University. His research interests include dynamic and

transient operation of power systems, control, microgrids, and renewable energy.



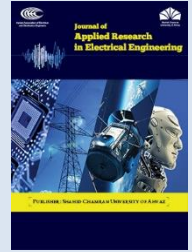
Mohammad Hassan Moradi was born in Nowshahr, Mazandaran, Iran. He obtained his B.Sc., M.Sc. and Ph.D. from the Sharif University of Technology, Tarbiat Modares University, and Strathclyde University in Glasgow, Scotland in 1991, 1993, and 2002, respectively. His research

interests include new and green energy, microgrid modeling and control, DG location and sizing in power systems, photovoltaic systems and power electronics, combined heat and power plant, power quality, supervisory control, and fuzzy control.

Copyrights

© 2022 Licensee Shahid Chamran University of Ahvaz, Ahvaz, Iran. This article is an open-access article distributed under the terms and conditions of the Creative Commons Attribution –NonCommercial 4.0 International (CC BY-NC 4.0) License (<http://creativecommons.org/licenses/by-nc/4.0/>).





Research Article

Energy Management in Distribution Systems Considering Consumer Behavior and Internet of Things

Moaiad Mohseni ^{1,*}, Mahmood Joorabian ², and Afshin Lashkar Ara ³

¹ Khuzestan Regional Electric Company, Ahvaz 61365-1373, Iran

² Department of Electrical Engineering, Faculty of Engineering, Shahid Chamran University of Ahvaz, Ahvaz 61357-85311, Iran

³ Department of Electrical Engineering, Dezful Branch, Islamic Azad University, Dezful 646616-45169, Iran

*Corresponding Author: moaiadmohsenii@gmail.com

Abstract: Internet of Things (IoT)-based energy management systems (EMSs) are considered a new technology in which consumers can manage their electricity payments according to their preferences, such as reducing costs or increasing satisfaction. Each consumer has its own program for communicating with a central control unit. In addition, the central control unit that is responsible for energy pricing can access consumer information and network performance status through the IoT infrastructure. Therefore, technical analysis can be performed using big data to determine the optimal price in order to make a compromise between the buyer and the goals of the distribution system operators. This paper presents a model to accurately assess the impact of pricing on the behavior of IoT-based energy systems. Then, according to the load specifications of each item and the technical limitations of the distribution network, the best time to use pricing is determined. The results show that the higher the price variance, the more discomfort the consumer and the lower the daily payment. Therefore, in this paper, the main goal of energy management is to minimize the total weight of the costs paid and their discomfort level. The paper could facilitate further penetration of IoT-based EMSs into smart grids. The study was performed on an IEEE standard 33-bus network. Optimization was implemented using YALMIP and MOSEK toolboxes. Therefore, it can be concluded that IoT technology allows consumers to enjoy the benefits of the network and makes optimal consumption management possible.

Keywords: Internet of things, distribution networks, energy management, smart grids, consumer discomfort.

Article history

Received 15 October 2021; Revised 26 February 2022; Accepted 27 February 2022; Published online 4 April 2022.

© 2022 Published by Shahid Chamran University of Ahvaz & Iranian Association of Electrical and Electronics Engineers (IAEEE)

How to cite this article

M. Mohseni, M. Joorabian, and A Lashkar Ara, "Energy management in distribution systems considering consumer behavior and internet of things," *J. Appl. Res. Electr. Eng.*, vol. 1, no. 2, pp. 186-196, 2022.

DOI: 10.22055/jaree.2022.38871.1037



Symbol	NOMENCLATURE Description
Variables	
C_t^{DG}	Generation price of DG
$C_t^{DG,wholesale}$	Wholesale rate of DG generation
C_t^{TOU}	Retail rate with their term of use
C_{nl}^{TOU}	Term of use rate of the no-load
C_{ml}^{TOU}	Term of use rate of the mid-load
C_{pl}^{TOU}	Term of use rate of the peak-load
$C_t^{TOU,wholesale}$	Wholesale rate market with a term of use
$C_{min}^{TOU,wholesale}$	Min wholesale rate market with a term of use

$C_{max}^{TOU,wholesale}$	Max wholesale rate market with a term of use
C_{min}^{TOU}	Min retail sell rate market with a term of use
C_{max}^{TOU}	Max retail sell rate market with a term of use
\underline{C}	The minimum amount of rate market with a term of use
\overline{C}	The maximum amount of rate market with a term of use
E_t^S	The energy level of the storage system
$\underline{E}_t^S, \overline{E}_t^S$	The min/max energy level of the storage system

$E_{t_{ini}}^S, E_{t_{final}}^S$	Initial/final mode of charging the storage system
MUT^L	Minimum loading time
$N(\varepsilon_1^i)$	Number of consumers with the ε_1^i coefficient
p_n^{base}	The node basis electricity of n
p_t^{DG}	Retail electricity purchase from DG
$p_{t,wholesale}^{DG}$	Wholesale electricity purchase from DG
$\underline{p}_t^{DG}, \overline{p}_t^{DG}$	Min/max range of DG
p_t^{Grid}	Electricity purchase of the net
$p_{i,t}^{Grid}$	Electricity purchase of the net by consumer i
$\underline{p}_t^{Grid}, \overline{p}_t^{Grid}$	Min/max range of the net power
$p_{tUpGrid}$	Electricity purchase of the upstream net
p_t^L	Electric power of load
\tilde{p}_t^L	Ideal electric power of load
\hat{p}_t^L	Nominal electric power of load
p_t^S	Electric storage charging
$\underline{p}_t^S, \overline{p}_t^S$	Min/max electric storage charging
$t, \Delta t$	Time distance and its duration
t_{ini}, t_{final}	Initial and final time
$t_{operation}^L$	Operating time for each load
t_{des}^L	Desired time to start the time flexible load
γ_t^L	Discomfort rate of the load
ξ_t^L	Changing load situation
τ_t^L	Binary for turn on/turn off situation of the load
σ_{TOU}^2	Rate amount with a term of use

$\sigma_{TOU,desired}^2$	Desired rate amount with a term of use
h_{nl}	No load factor
h_{md}	Medium load factor
h_{peak}	Peak load factor
Parameters	
$p_{\gamma}^{new}(\chi)$	New Possibility related to the χ
\mathcal{T}	Collection of time parts
δ_t^L	A hypothetical vector that shows the effect of time delay on time flexible loads
$\varepsilon_1, \varepsilon_2$	Coefficients Weighting of the consumer cost
ε_1^i	Weight Coefficient of the i th consumer cost
$\Omega^{Bus}, \Omega^{DG}, \Omega^{Line}$	Collection of DGs , lines , nodes
$\Omega^{TFL}, \Omega^{PFL}, \Omega^{NFL}$	Collection of time flex, power flex, and non-flex loads
$\Omega^{Load}, \Omega^{customers}$	Collection of loads, consumers
$\Omega^{storage}$	Collection of batteries
d_{KL}	Kullback Leibler distance
$f_{customer}$	The fitness function of consumer
$f_{discomfort}$	Discomfort cost
$f_{Payment}$	Electricity payment cost
L_t^{Total}	Total load; considering normal consumer behavior
PD_t^{total}	The total power demand of the net
PD_n^t	Node load of n
p_{Total}^{base}	The general basis power of the net
$Pr(\varepsilon_1^i)$	Possibility related to the ε_1^i
$Pr(\chi)$	Possibility related to the χ

1. INTRODUCTION

The Internet of Things (IoT) has transformed traditional energy management systems into responsive embedded systems that reflect consumer preferences in their energy supply process [1]. The concept of IoT is somehow simple while its practical implementation requires several infrastructures such as communication systems, instruments, sensors, actuators, control, and protection systems [2-3]. Bilateral communication of costumers with smart grid operators will have several technical and economic benefits for various components of the system including consumers, distribution system operators, and central control units (e.g., government entities) [4]. The IoT technology is a technology similar to smartphone architectures but it is more complex since data is shared among several sensors and actuator interfaces simultaneously. Each home utility can share its data via the Internet and contribute to distribution system management with or without the presence of smart meters. IoT application in smart homes has been reviewed in [5] in view of technical challenges in the communication protocol and interoperability. The potential of the US electricity grid for the implementation of the IoT system has been investigated in [6]. A review of smart cities operating with IoT has been presented in [7]. Several merits of IoT-based systems have been investigated in [8]. Distribution operation cost minimization, loss minimization, encouragement of renewable energy resource utilization, end-user payment minimization, and customer satisfaction improvement have been enumerated as the main economic benefits of IoT development [9]. Moreover, some technical benefits such as load profile flattening, peak shaving, loss minimization, and

voltage deviation optimization can be achieved by this technology. Here, we concentrate on how these benefits can be achieved by properly modeling IoT-based energy management systems (EMSs). An IoT-based framework has been introduced in [10] for the integration of energy storage and renewable energy resources in distribution systems. An autonomous energy management cost reduction solution has been proposed in [11] using the home energy management system (HEMS). IoT has found its way into smart grids, especially in distribution systems. Demand-side management can be more efficient in the presence of IoT. IoT-based EMSs can have bidirectional communication with smart grids and decide according to their preferences, time-of-use pricing, and flexible devices. Therefore, customers would consume electricity more interactively [12].

The future of IoT does not seem to be unforeseen. Various legal projects are running recently to practically implement IoT in smart grids. A smart IoT-based substation has been designed by the cooperation of Siemens and Glitre Energi Nett (a Norwegian distribution system operator (DSO)) as a pilot project to improve reliability through earlier fault and risk detection, continuous monitoring, cloud-based operating system, and maintaining cybersecurity [13]. CyberSANE is another innovative dynamic security system for continuous learning of cyber attacks of IoT-based environments with a budget of over six million EUR. Several capabilities of these systems are threat prevention and detection, security exploitation, risk information analysis, and protection [14]. A comprehensive centralized structure for microgrid operations, including active and reactive power sources, is presented in this paper. In this method, distributed generation (DGs), energy storage systems (ESS), response

demand program (DR), load change scheme, changeable capacitor banks, and plug-in hybrid electric vehicles are considered simultaneously [15]. This paper deals with the optimal energy management and performance of network microgrids by considering different types of portable units such as fuel cells and microturbines and inseparable units such as wind turbines and solar units. To change the role of vehicle-only consumption to an active role with the potential for profitability, vehicle network (V2G) technology is presented in [16].

In recent years, with the rapid development of the battery energy storage industry, its technology has demonstrated the features and processes of large-scale integration and distributed multi-objective applications. As a grid-level application, EMS, a real-time battery energy storage system, was deployed in instrument control centers as an important component of grid management. Based on the analysis of the development status of a BESS. This paper introduced practical scenarios such as reducing output power fluctuations, agreeing with the output plan on the side of renewable energy production, regulating the frequency of the power grid, and optimizing the current flow in power transmission [17]. This paper provides presentation, deployment, and validation of an IoT-based SEMS strategy and its related benefits to overcome challenges of energy management on the consumer side. The presented SEMS incorporates various communication interfaces and protocols to integrate with any software-based smart solution [18]. A two-layer in-depth secured management architecture has been proposed in [19] for the optimal operation of energy Internet in hybrid microgrids. In the cyber layer of the proposed architecture, a two-level intrusion detection system is proposed to detect various cyber-attacks (i.e., Sybil attacks, spoofing attacks, false data injection attacks) on wireless-based advanced metering infrastructures [19].

In previous research, demand response has been used to manage the energy of distribution networks. So far, the analysis of the issue of energy management with IoT has not been considered. Also, most studies have not considered the issue of changing consumer behavior as an essential parameter in energy management. Distribution energy resources are modeled based on the traffic flow of computer network principles. This paper quantitatively analyzes an IoT-based EMS in a distribution system. A practical and straightforward framework is presented to facilitate the control of this system. This framework considers the benefits of both customers and DSOs simultaneously. Several analyses are presented to show the effect of time of use (ToU) variance and customer satisfaction factor on either economic (e.g., total payment and discomfort cost of customers) or technical parameters (such as peak load, average load, and load factors). The results show that this framework can provide more benefits from the IoT infrastructure of smart grids.

The innovations of the paper are as follows:

1. Performing an EMS in the presence of the IoT
2. Using the Kohlberg convergence distance to show the difference between the general consumer distribution function and the normal distribution function
3. Considering the effect of changes in consumer behavior on energy management in the presence of IoT

4. Considering the effect of consumer discomfort on energy management in the presence of IoT

The rest of the paper is organized as follows. Section 2 describes the model of the problem and the governing relationships that will be extracted. Section 3 presents the simulation data and its results. Section 4 provides some conclusions.

2. MODEL DESCRIPTION

The case study is a radial distribution network that has several residential loads connected via IoT technology. Each home in the network has a renewable energy resource (photovoltaic, in this paper), an energy storage unit, nonflexible load, time flexible load, and power flexible one. Each consumer has his/her preference to select the weight of payment and discomfort. The IoT-based EMS receives the day ahead of the ToU tariff from the central control unit, schedules all flexible or nonflexible loads according to user preferences, and sends this information to the central unit for more analysis. Then, the aggregated load is calculated by the central control unit and sent to the power system operators to be used for distribution system studies. The operators use this information for optimal power flow (according to its benefits) and extract any technical or economic violations and communicate the results to the central unit. Again, the price is adjusted by the central unit to provide the optimal solution. It is assumed that the DSO is just concerned about peak load level. No optimal power flow or security constraints are considered for the power system operator. Just load level is selected as a limitation for simplicity. So, at first, the IoT-based EMS model is presented.

The mathematical model of the problem optimization is fully described here. The control system type is a combination of decentralized and centralized control. The home energy management department is managed locally based on its interests and the information transmitted to it from the central server. The necessary analyses are performed on it, and the results are sent back to the central server. Based on the information received by the central server, a decision is made on changing or not changing the price of electricity based on the interests of the central server, these changes are sent to the home energy management units, the results are sent intermittently until the best decision is made, and the information is provided on the web and sent to the consumer program so that they can consume electricity accordingly. IoT offers a structure for communicating and managing different parts of the distribution system. There are many benefits to using IoT for consumers, DSO, and the power market. Decisions can be made based on the limitations, benefits, information received from the Internet of Things Central Unit, and new information sent to each unit. Data analysis is then performed in the center to gather the final optimization decision. Fig. 1 shows the structure of IoT. In this structure, consumers, DSOs, and the power market connect to the center through communications.

Electricity consumers take the time-based tariff price from the center and return the load profile to the center (power purchased from the grid) for extensive data analysis. The electricity procured from the upstream network gets even to

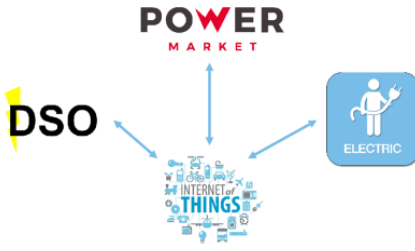


Fig. 1: The schematic of the proposed IoT-based infrastructure.

the center. Then, to achieve the optimal time consumption and wholesale tariff, the amount of power purchased from the wholesale and consumer markets is sent to the electricity market. These prices are then sent to the center. This process is repeated until the best price is reached.

2.1. MILP MODEL OF CONSUMERS BEHAVIOR

The HEMS finds information about the home's electrical equipment and the number of typical desires. It optimizes domestic electricity consumption based on the electricity received from the central server. In general, loads of a home can be divided into three categories: nonflexible loads (NFLs), time flexible loads (TFLs), and power flexible loads (PFLs). NFLs are unchangeable and are operated at the desired time and with a specific power. TFLs can shift time, and the consumer can change the operating time according to his/her interests. The third category is flexible loads with a specific working time but can be increased or decreased depending on the conditions. It is also assumed that each home is equipped with renewable resources and storage. The use of renewable resources is also included in the cost. The user can choose to supply a few percent of his energy from renewable sources and a few percent from upstream network electricity depending on the cost of using renewable products or the price of electricity. In this study, the purpose of EMS is to minimize the weight of the costs paid and the amount of their discomfort. Therefore, the objective function of EMS will be equal to

$$f_{customer} = \varepsilon_1 f_{payment} + \varepsilon_2 f_{discomfort} \quad (1)$$

in which the first term is related to the costs paid by consumers, which includes two costs: (a) the cost of electricity purchased from the network and the cost of electricity provided by DG, which is calculated by (4). The second term is also related to the cost of consumer welfare or discomfort, which is due to the difference between the electricity consumed and the desired consumption pattern being predetermined according to (5). There is a predetermined pattern of electricity consumption. If electricity consumption conforms to this pattern, there will be no discomfort. Otherwise, a cost of discomfort will be added to the objective function. The ε_1 and ε_2 weighting coefficients indicate the consumer's desire to pay or discomfort. According to (2), the sum of these coefficients must be equal to 1 and have positive values where ε_1 and ε_2 are constant coefficients selected as:

$$\begin{aligned} \varepsilon_1 + \varepsilon_2 &= 1 \\ \varepsilon_1, \varepsilon_2 &\geq 0 \end{aligned} \quad (2)$$

The selection of these coefficients is entirely on the consumer's basis, and based on their selection, the analysis and studies are performed for domestic energy management. Therefore, each consumer has complete control over the choice of their interests. It should be noted that the vector of domestic energy management decision variables is equal to :

$$X=[P_t^L, \tau^L, \dots, P_t^S, E_t^S, \dots, P_t^{DG}],$$

$$L \in \Omega^{Load}, DG \in \Omega^{DG}, S \in \Omega^{Strg}, t \in T \quad (3)$$

which includes the power of each load, their time delay, the power of energy storage, the management of DG sources, and the energy level of the storage. All variables in this program are real numbers. Equation (1) can be rewritten as (4) and (5). In (4), $f_{payment}$ consists of two terms. The first term shows the amount paid by consumers to the upstream network, and the second term shows the amount paid by consumers to DG. In (5), $f_{discomfort}$ also consists of two terms; the first term shows the degree of discomfort with PFLs, and the second term shows the degree of discomfort with TFLs. In the first term, when the power consumption is equal to the desired power of the network, there will be no discomfort. Still, if the power consumption is more than the desired power, discomfort is caused by PFLs, which are multiplied by the price of electricity. In the second term, fines are imposed for TFLs. This penalty is considered when the consumption of these loads is more than the allowable limit. Otherwise, there will be no discomfort.

$$f_{payment} = \sum_{t \in T} (C_t^{TOU} P_t^{Grid} + C_t^{DG} P_t^{DG}) \quad (4)$$

$$f_{discomfort} = \sum_{t \in T} \sum_{L \in \Omega^{PFL}} \gamma_t^L (P_t^L - \tilde{P}_t^L) + \sum_{t \in T} \sum_{L \in \Omega^{TFL}} \gamma_t^L \delta_t^L \tau_t^L \quad (5)$$

In (6), δ_t^L is a hypothetical vector that shows the effect of time delay on TFLs and is expressed as follows:

$$\delta_t^L = \begin{cases} 0 & t \leq t_{des}^L \\ t - t_{des}^L & t > t_{des}^L \end{cases} \quad (6)$$

Also, τ_t^L is a fixed fine for any kind of load, γ_t^L is the price of electricity, and \tilde{P}_t^L is the shape of the desired load for each PFL. It can be determined as follows as per the consumers' desire:

$$\tilde{P}_t^L = \begin{cases} \tilde{P}_t^L & t \in t_{operational}^L \\ 0 & t \notin t_{operational}^L \end{cases} \quad (7)$$

Equation (7) states that ideal PFLs must operate at rated power at the allowable period distance and be OFF at other times. Assuming (1) to (7), the priorities of the consumer objective function can be called linear. Also, the electricity consumption of PFLs is a continuous variable, and the execution time of TFLs are binary variables. Domestic energy management should be done so that the boundary conditions of the problem are observed. To achieve an acceptable method, which is listed below, various boundary constraints shall be met.

$$\sum_{L \in \Omega} P_t^L + \sum_{S \in \Omega} P_t^S = \sum_{DG \in \Omega} P_t^{DG} + P_t^{Grid} \quad (8)$$

$$\sum_{L \in \Omega^{Load}} P_t^L = \sum_{L \in \Omega^{PFL}} P_t^L + \sum_{L \in \Omega^{TFL}} P_t^L + \sum_{L \in \Omega^{NFL}} P_t^L \quad (9)$$

$$0 \leq P_t^L \leq \bar{P}_t^L, \quad \forall L \in \Omega^{PFL}, t \in T \quad (10)$$

$$P_t^L = \tau_t^L \bar{P}_t^L, \quad \forall L \in \Omega^{TFL}, t \in T \quad (11)$$

$$P_t^L = \bar{P}_t^L, \quad \forall L \in \Omega^{NFL}, t \in T \quad (12)$$

$$E_{t+1}^S = E_t^S + P_t^S \Delta t, \quad \forall S \in \Omega^{Strg}, t \in T \quad (13)$$

$$P_{-t}^S \leq P_t^S \leq P_t^{-S}, \quad \forall S \in \Omega^{Strg}, t \in T \quad (14)$$

$$E_{-t}^S \leq E_t^S \leq E_t^{-S}, \quad \forall S \in \Omega^{Strg}, t \in T \quad (15)$$

$$E_{t_{final}}^S = E_{t_{ini}}^S, t_{final}, t_{ini} \in T, \quad \forall S \in \Omega^{Strg} \quad (16)$$

$$P_{-t}^{DG} \leq P_t^{DG} \leq P_t^{-DG}, \quad \forall DG \in \Omega^{Strg}, t \in T \quad (17)$$

$$P_{-t}^{Grid} \leq P_t^{Grid} \leq P_t^{-Grid}, \quad t \in T \quad (18)$$

$$\tau_t^L \in \{0,1\}, \quad \forall L \in \Omega^{TFL}, t \in T \quad (19)$$

$$\xi_t^L = \tau_t^L - \tau_{t-1}^L, \quad \forall L \in \Omega^{TFL}, t \in T \quad (20)$$

$$\tau_{ti}^L \geq \xi_t^L, \quad \forall L \in \Omega^{TFL}, t \in [t, t + MUT^L - 1] \quad (21)$$

Equation (8) shows the total power distributed generation and electricity procurement from the network, which should be equal to the power consumption of the load and the charging power of the energy storage. Equation (9) shows that the sum of three load types equals the total network load. PFLs turn on and off at certain times that cannot be changed, and only their rated power in this range can change between zero (off) to their ideal level. According to Equation (10), other types of loads are flexible so that their on and off times can be moved, but no change can be made in the value, and only the entire ideal customer curve can be shifted in the time domain only according to (11). Given that neither time nor consumer power can be changed and shifted in nonflexible loads, the power and energy level of energy storage devices should always be within their minimum and maximum range according to (14) and (15). Also, the relationship between charging power and storage energy level is determined by (13). The battery energy level at the beginning and end of the study period should also be calculated by (16). The power level harvested from each of the DGs should be in a range from minimum (usually zero) to maximum (available renewable power), and the electricity purchase from the upstream network must be within the minimum and full capacity according to (17) and (18). Equation (19) shows the constraints of a binary variable. Equations (20) and (21) mean that when a TFL is on, that is $\xi_t^L \geq 1$, they cannot be turned off in the time interval $[t, t + MUT^L - 1]$ due to $\tau_t^L \geq \xi_t^L \geq 1$ constraints. Upon receipt of ToU price data from the center, each consumer proceeds to plan the load according to their interest. Customers can choose the weight of ε_1 to show their demands between reducing electricity payment and

discomfort costs. Also, energy storage provides the option to preserve energy at charge and discharge energy at higher price distances. NFLs can overstep their defined values acceptably. Still, TFLs can vary their operative time, and PFLs can regulate their electrical power at work to provide favorable cost and discomfort. After planning, the total net hourly consumption information of each consumer is sent to the center to be utilized in data analysis [12].

2.2. IMPACT of Price Tariff at Time of Use on Consumer Behavior

First, the role of pricing tariffs in various parameters of a smart home is evaluated. It is assumed that the price of electricity follows the tariff of consumption time, and the hours of the day are divided into three parts: no-load, medium load, and high load as shown in Table 1.

To investigate the effect of price variations on the subject, different scenarios have been considered. In these scenarios, it is assumed that the average consumption time tariff is equal to the unit value of a per unit (PU) to create a competitive environment between renewable products and the electricity distribution network. If the average price of electricity tariff is higher than a renewable generation, the consumer will have an intense desire for DG, and if the average price of this tariff is less than DG, the consumer will prefer to consume all its consumption from the supply network. Therefore, to balance, it is assumed that the average tariff is equal to the price of DG, i.e., PU. But, to model price variations, a parameter called the standard deviation of price standard had been used. The typical (consumer) reaction to price changes is essential. Undoubtedly, changing the price variance can affect consumer behavior. Therefore, a model for determining the consumption hour tariff based on the standard deviation and the average tariff is formed as follows, the purpose of which is to find the tariff related to each hour of the day and night. The times of no-load, medium load, and peak load are pretty clear. The mean and standard deviation of the price is also considered a particular input parameter of the problem, the allowable limits of which are based on Table 1. The price of electricity is related to the periods of no-load, medium load, and peak load as to be unknown. Therefore, the equation system is formed as follows:

$$h_{nl} C_{nl}^{TOU} + h_{md} C_{md}^{TOU} + h_{Peak} C_{Peak}^{TOU} = T\mu \quad (22)$$

$$h_{nl} (C_{nl}^{TOU} - \mu)^2 + h_{md} (C_{md}^{TOU} - \mu)^2 + h_{Peak} (C_{Peak}^{TOU} - \mu)^2 = T\sigma^2 \quad (23)$$

$$C_{nl}^{TOU} \leq C_{md}^{TOU} \geq C_{Peak}^{TOU} \quad (24)$$

$$\underline{C} \leq C_{nl}^{TOU} \geq \bar{C} \quad (25)$$

$$\underline{C} \leq C_{md}^{TOU} \geq \bar{C} \quad (26)$$

$$\underline{C} \leq C_{Peak}^{TOU} \geq \bar{C} \quad (27)$$

To better understand the answers to the problem, a drawing method has been used to display the answers. Equation (23) represents an ellipse in three-dimensional space. Equation (22) corresponds to a plane in space, and Equations (24) to (27) also represent the ranges that divide space by a similar plane into two parts. The answer to the problem is obtained by sharing the answers of all these

Table 1: Network electricity consumption hours [12].

	No load	Mid load	Peak load
Time	11pm-7am(8 hr)	7am-19pm(12hr)	19pm-2pm(4hr)
Price	0-3pu	0-3pu	0-3pu

subspaces according to Fig. 3. There are various ways to solve this problem where it can be converted into a conical optimization form and solved using MOSEK and YALMIP toolboxes. The standard form of optimization is as follows:

$$Min \ abs(\sum_i hi(xi - \mu)^2 / T \sigma^2) \tag{28}$$

$$\sum_i hixi = T\mu \tag{29}$$

$$x_{i-1} \leq x_i \leq x_{i+1} \tag{30}$$

$$\underline{x} \leq x_i \leq \bar{x} \tag{31}$$

In (28) and (31), the values of μ , σ^2 , T , hi , \bar{x} and \underline{x} represent the average price, price variance, period of study, length of the period such as price, upper and lower acceptable price, which is all known data of the problem coming, respectively.

2.3. Data Solving for Load Collecting

By calculating the load of each consumer, data solving is executed in the center to compute the total load profile in the distribution network. To further simplify computations, the load profiles of all distribution systems are obtained only by adding the information of each consumer (according to (32)). Then, the load accumulated on all buses is distributed according to the load of the nominal basis of each bus (according to (33) and (34)). It is as follows:

$$PD_t^{Total} = \sum_{i \in \Omega_{customers}} P_{i,t}^{Grid}(\epsilon_1, C_t^{TOU}) \tag{32}$$

$$PD_n^t = \frac{P_n^{base}}{P_{Total}^{base}} PD_t^{Total} \tag{33}$$

$$P_{Total}^{base} = \sum_{n \in \Omega_{bus}} P_n^{base} \tag{34}$$

where $P_{i,t}^{Grid}$ refers to the electricity purchased by the consumer i from the net. In this paper, to show the relationship of $P_{i,t}^{Grid}$ between the effect of two parameters ϵ_1 and C_t^{TOU} without considering the total losses, several valuable curves have been extracted. Also, a probability distribution function has been evaluated to select all consumers with the parameter ϵ_1 . Therefore, Equation (35) is:

$$L_t^{Total} = \sum_{\epsilon_1^i} N(\epsilon_1^i) Pr(\epsilon_1^i) P_{i,t}^{Grid}(\epsilon_1^i, C_t^{TOU}) \tag{35}$$

Considering the law of probability for each density function as follows:

$$\sum_{\epsilon_1^i} Pr(\epsilon_1^i) = 1 \tag{36}$$

The paper aims to achieve the whole distribution system's load profile for each price by the standard normal probability density function and accordingly evaluate the impact of the distribution function changes. The parameter KL is applied as a convergence to display the interval by the

probability distribution function to $Pr(\chi)$, which is as follows:

$$d_{KL} = \sum_{\chi} (Pr(\chi) \log \frac{Pr(\chi)}{Pr^{new}(\chi)}) \tag{37}$$

Thus, the different effects of the normal distribution function can be shown for each parameter. The outcome displays that a more significant distance from the standard normal distribution function will cause more maximum and minimum peaks in the load profile curve [12].

2.4. Market Preferences

Electricity market decisions are usually adjusted according to ToU prices to maximize total profile supply. The profile of the distribution system is obtained from the difference between the cost of supplying electrical energy from the upstream network and the income from the sale of electricity to consumers and is expressed as follows:

$$max \ benefit = \sum_{t \in T} (C_{t,wholesale}^{TOU} P_t^{UPGRID} - C_t^{TOU} PD_t^{TOTAL}) \tag{38}$$

Some of the boundary constraints should be considered to support the competition between DGs.

1. The average price should be equivalent to the average price (DG) units (according to (39) and (40)).
2. The prices should be within their prescribed range (according to (41) and (42)).
3. Price variance can be selective to show the effect of price changes on consumer behavior (according to (43) and (44)).

$$\sum_{t \in T} C_t^{TOU} = \sum_{t \in T} C_t^{DG} \tag{39}$$

$$\sum_{t \in T} C_{t,wholesale}^{TOU} = \sum_{t \in T} C_{t,wholesale}^{DG} \tag{40}$$

$$C_{min}^{TOU} \leq C_t^{TOU} \leq C_{max}^{TOU} \tag{41}$$

$$C_{min}^{TOU,wholesale} \leq C_t^{TOU,wholesale} \leq C_{max}^{TOU,wholesale} \tag{42}$$

$$Var(\sum_{t \in T} C_t^{TOU}) = \sigma_{TOU,desired}^2 \tag{43}$$

$$Var(\sum_{t \in T} C_t^{TOU,wholesale}) = \sigma_{TOU,wholesale,desired}^2 \tag{44}$$

The flowchart of the proposed method is shown in Fig.2 .

3. SIMULATION RESULTS

In this section, the EMS of a home is examined. Then, the role of network consumers in the load profile of each home and their purchased electricity is reviewed. Then, assuming that the network consumers criterion follows the normal distribution function, the network load profile is obtained. It, then, looks at how electricity pricing can affect grid load profiles and electricity costs. Finally, network load profiles are displayed in different pricing. Assuming that the load profile distribution in the network buses follows a uniform function, the load of each network bus is obtained. This paper includes a standard 33 bus network (IEEE) with 2000 consumers with the same features as classified in Table 2. Every consumer uses a 1kW/3 kWh battery, and also, a 2kW ceiling photovoltaic system is provided for each consumer.

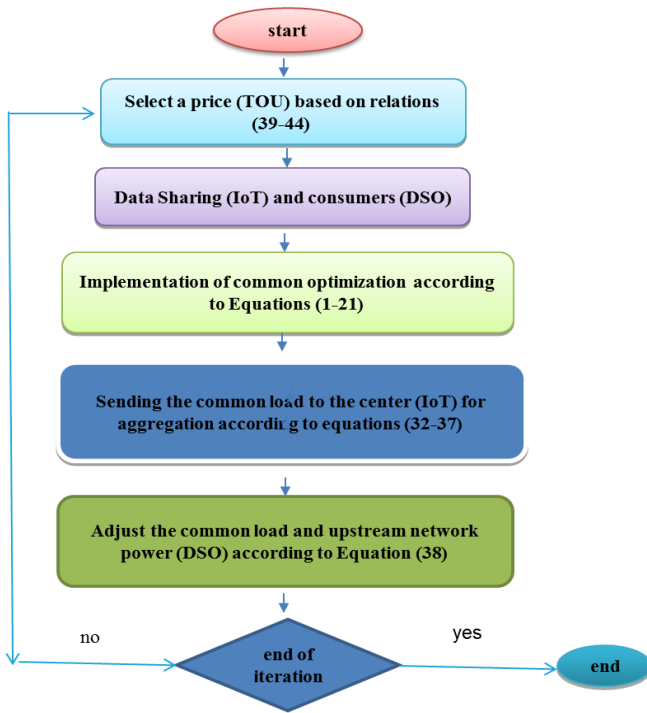


Fig. 2: The flowchart of the proposed method.

Table 2: Consumer load data [12].

Type	Name	Time (h)	kW	γ_i^c (\$/kWh)
Time Flex	Wash-machine	2hr working duration	0.7	1
Power Flex	Light	11-17	0-0.8	0.8
	Air conditioner	Full time	0-1.4	1.4
Non Flex	Kettle	8-9,17-18, 20-21	0.3	0
	Toaster	8-9	0.2	0
	Refrigerator	Full time	0.2	0

Table 3: Technical and economic data of the net [12].

Item	Value	Item	Value
DG unit location	Bus 6, 7, 13, 18, 28, 33	$c_{t,min}^{TOU}$	0 pu
DG unit capacity	500, 1200, 1350, 1350, 1200, 500kW	$c_{t,max}^{TOU}$	3 pu
DG power factor	1, 0.8, 0.9, 0.9, 0.8, 1	No Load interval	0-7
Voltage Limits	0.95-1.05 pu	Mid interval	7-19
$c_{t,wholesale}^{DG}$, c_t^{DG}	1 pu	Peak interval	19-24

The studied intervals are 24 hours. The difference between consumers is based only on their benefit factors. Some technical and economic data of the distribution network are presented in Table 3.

Energy storage is a 1kW/3-kWh battery charged or discharged without wasting energy. The cost of TFL and PFLS is considered 0.001 per unit per hour and 1 per unit per

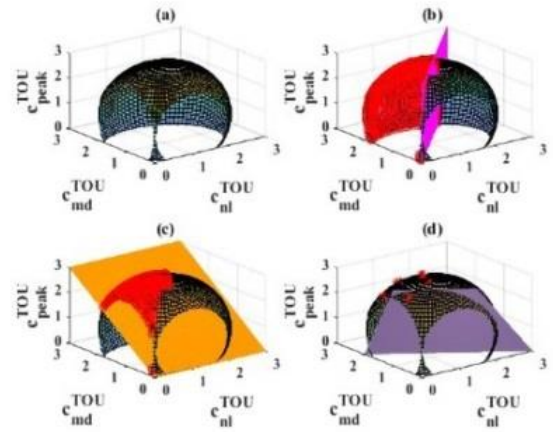


Fig. 3: Procedure for finding the solution space of TOU tariffs for $\sigma^2 = 1$, (a) Solution of (23), and (25)-(27), (b) Adding constraint $c_{nl}^{TOU} \leq c_{md}^{TOU}$, (c) Adding constraint $c_{md}^{TOU} \leq c_{peak}^{TOU}$, and (d) Adding constraint (23).

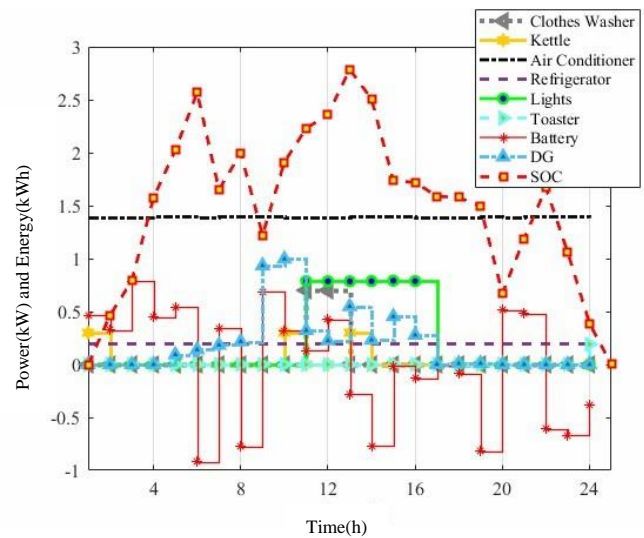


Fig. 4: Energy management system results for $\sigma^2 = 1$ and $\epsilon = 0$.

kilowatt-hour, respectively. The results of IoT-based EMS optimization are displayed in Fig. 4. This indicates a situation where the customer tends to minimize his/her discomfort regardless of the cost. Therefore, PFLs at their maximum rating and TFLs are launched precisely at the desired time and without delay.

3.1. Impact of ϵ_1 and σ_{TOU}^2 on Network Technical Parameters

In Table 4, the total payment is obtained simultaneously with the changes in ϵ_1 , σ_{TOU}^2 . Table 5 shows that market benefit is obtained from the difference between retail and wholesale prices. Table 6 shows that considering several cases, with increasing standard deviation, the cost of payment decreases, and discomfort, peak load, and average load increase. Table 7 shows that with increasing consumer weight ϵ_1 , the cost of payment decreases and discomfort increases, as well as peak load and average load decrease.

3.2. Data Analysis to Calculate the Total Network Load

To show the effect of approximate error, several standard normal distribution functions have been considered to investigate the mutual satisfaction behavior. Fig. 5 shows that

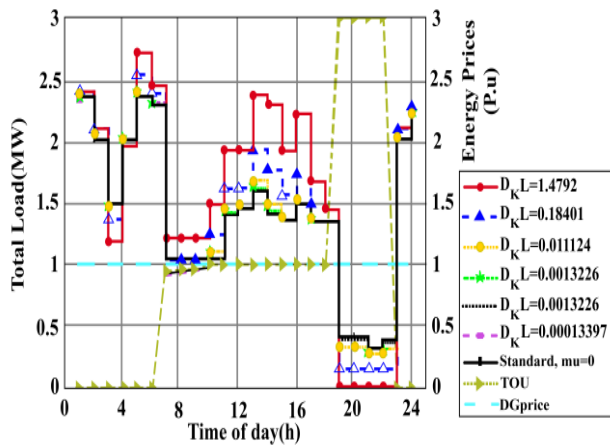


Fig. 5: The whole load in various standard probability density functions (pdf) of ϵ_1 .

Table 4: Impact of changes of ϵ_1 and σ_{TOU}^2 on the total cost.

$\frac{\epsilon_1}{\sigma_{TOU}^2}$	0	0.1	0.2	0.3	0.4	0.5
0	45.1201	44.1113	42.0398	39.3618	35.7096	30.8990
0.1	45.1904	43.3885	40.7477	37.9936	34.1628	29.2118
0.2	45.1392	41.7038	39.9498	36.7433	32.7051	28.7185
0.3	44.9410	41.0773	38.3843	35.0943	31.1537	25.7690
0.4	44.5359	39.5955	37.2538	33.7937	29.8272	24.6544
0.5	44.3943	38.2162	35.6013	31.6939	27.5399	21.3524
0.6	45.0616	37.5760	33.3571	30.1942	25.6445	18.9922
0.7	46.2372	35.1883	32.5725	28.7632	23.1035	15.4657
0.8	42.3949	34.8915	31.0184	27.3300	21.5086	13.1245
0.9	44.8860	33.8534	31.0236	26.0376	19.7878	12.5736
1	42.0014	31.9110	28.4341	25.1953	17.3905	10.2588

Table 5: Results of different pricing methods using electricity market decisions.

σ_{TOU}^2 wholesale	σ_{TOU}^2 retail	Total cost (p.u)	Total income (p.u)	Benefit (p.u)	PDG%
0	1	22.019	28.508	6.489	20.47
0.1	1	13.676	25.572	11.896	19.37
0.2	1	11.931	25.633	13.702	25.95
0.3	1	13.993	26.807	12.814	17.41
0.4	1	11.761	27.035	15.273	24.47
0	0.5	14.476	28.508	14.032	41.62
0.1	0.5	11.883	25.572	13.689	33.56
0.2	0.5	11.828	25.633	13.805	33.72
0.3	0.5	12.435	26.807	14.371	31.80
0.4	0.5	12.435	27.035	14.599	31.80
0	0	21.022	28.508	7.486	26.26
0.1	0	18.513	25.572	7.059	30.20
0.2	0	20.717	25.633	4.916	21.90
0.3	0	20.472	26.807	6.335	26.06
0.4	0	20.537	27.035	6.498	25.82

Table 6: Impact of electricity price variations on technical and economic parameters of consumers.

ϵ_1	Cost	Discomfort	Peak load	Mid load
0	45.1201	0.0174	3.0317	1.7164
0.1	44.1113	0.0873	3.7532	1.7481
0.2	42.0398	0.4483	2.4608	1.5929
0.3	39.3618	1.3417	2.4699	1.5098
0.4	35.7096	3.3390	2.5572	1.2913
0.5	30.8990	7.3074	1.9115	1.0849
0.6	24.3335	15.3327	1.6400	0.8631
0.7	14.2211	34.3327	1.5844	0.4125
0.8	9.1808	47.4616	1.7644	0.2308
0.9	9.1333	47.4851	1.0729	0.2125
1	9.2647	47.214	1.4466	0.1943

Table 7: The results of changing consumers' interests in their behavior.

Item	Standard deviation	Cost	Discomfort	Peak load	Mid load
1	0	30.6999	7.4912	2.3842	1.0600
2	0.1	29.0947	7.7809	2.5964	0.9612
3	0.1	29.2460	7.6795	2.3985	0.9652
4	0.1	29.4847	7.5922	2.7519	1.1822
5	0.1	29.6018	7.5130	2.5932	1.2818
6	0.2	27.2362	8.1549	2.8855	0.9538
7	0.2	27.5776	7.9302	2.8807	0.9624
8	0.2	28.0290	7.7758	2.4379	1.0540
9	0.2	28.2538	7.6124	2.5905	1.2853
10	0.3	25.1129	8.6651	2.9706	0.9461
11	0.3	25.6328	8.3360	2.4153	0.9582
12	0.3	26.3439	8.0758	2.7296	1.1461
13	0.3	26.6610	7.8343	2.3017	1.2888
14	0.4	22.8845	9.1535	2.6606	0.9437
15	0.4	23.4480	8.8475	3.0342	0.9548
16	0.4	24.4065	8.8457	2.8479	1.1158
17	0.4	24.8286	8.1785	2.9332	1.2923
18	0.5	20.4807	9.6939	2.7226	0.9437
19	0.5	20.7654	9.6061	2.8821	0.9468
20	0.5	21.1511	9.4810	3.0985	0.9512
21	0.5	22.2355	9.0356	2.5160	1.1022
22	0.5	22.7540	8.6448	2.8317	1.2958
23	0.5	22.9575	8.5538	2.6165	1.3003

the load profile can be plotted using different normal distribution functions with a constant mean of 0.5 and variable variance $\sigma^2 = 0.2, 0.4, 0.6, 0.8, 1$ (according to (37)).

Here, the distance from the normal distribution function (KI) for each distribution function is equal to (0.0001, 0.0013, 0.0111, 0.1840, 1.4792). Therefore, the total network load under these distribution functions is shown in Fig. 5.

It is evident from Fig. 5 that the distance (KI) causes more deviation of the load profile from its mean value than the normal distribution function and will also cause peaks (MIN, MAX) in the load profile curve. Therefore, the standard normal distribution function assumed for consumer behavior

was considered a clear idea of problem-solving and the high cost of network operation as a pessimistic idea.

3.3. Comparison Based on the Total Cost

To evaluate the IoT method with other methods, four types of load profiles named LS1, LS2, LS3, and LS4 are first considered, and their required data such as residential load profiles and their desired schedule are extracted from reference [11]. According to reference [11], the number of household appliances ($M = 10$) in different time slots ($N = 8$) have been considered. Therefore, each time slot represents 3 hours of continuous work of each piece of equipment to obtain $(8 * 3)$ 24 hours a day. The details of different load scenarios and their demand are given in [11].

The 24-hour loads including four load profiles LS1, LS2, LS3, and LS4 are equal to 63kW, 57kW, 44.5kW, 44.5kW, respectively. To analyze performance, the total cost of consumption per day is calculated by demand response (DR), DijCosMin Algorithm (PRDSol), Low Complexity Algorithm (LCSol), Optimum Solution (OPTSol), and Pmanuscript Swarm Optimization (PSO). Table 8 shows the results of this comparison. To clarify the subject, these results are plotted in Fig. 6. According to Fig. 6, it is clear that the total cost of IoT analysis is much lower than other algorithms. Therefore, according to this comparison, it can be concluded that the IoT method reduces the total cost of consumption per day and night.

3.4. Comparison Based on the Time Response

IoT time response is compared with existing algorithms, and its results are given in Table 9. According to Table 9, the time response of the IoT method is 0.047 seconds, which is the lowest time compared to the time response of other algorithms. In practical applications, time response parameters include communication time, the distance between the central system and home appliances, Internet speed, etc.

3.5. Comparison Based on the Peak Load Demand

To test the capability of the IoT method in managing peak load demand and reducing the peak to average load ratio, a case study of peak load demand has been performed by considering IoT and other existing algorithms for LS1. To clarify the issue, the IoT method is compared with different existing algorithms to reduce the peak load demand for LS1. The results are shown in Fig. 7. In general, the cost of electricity consumption increases during peak hours and decreases during off-peak hours. Therefore, peak demand can be reduced by shifting the load from a high-cost time slot (peak load hours) to a low-cost time slot (non-peak load hours). In Fig. 7, cost-based time slots are arranged in ascending order. The highest cost time slot is related to T6, and the lowest cost time slot is associated with T7. According to Fig. 7, it can be seen that the amount of IoT loading in the time slot T6 is low and increases for subsequent time slots. Also, the highest demand for IoT is in the time slot T7. Therefore, the effect of the IoT method in reducing peak load demand and reducing the peak to average load ratio compared to other algorithms is very clear.

Table 8: A comparison based on the total cost.

Cost (Pu)						
LS	IoT	DR	LCsol	OPTsol	PRDSol	Pso
LS1	29.7	36	33.5	30.4	32.8	32.7
LS2	29.4	36.5	30.8	27.2	28.7	31.8
LS3	23.1	29.7	26.9	24.2	25.5	26.3
LS4	24.5	30.1	26.7	25.3	26.8	28.7

Table 9: A comparison based on time response.

Type of method	Simulation time (s)
IoT	0.047
DR	0.534
LCsol	0483
OPTsol	8.599
PRDSol	179
Pso	18.58

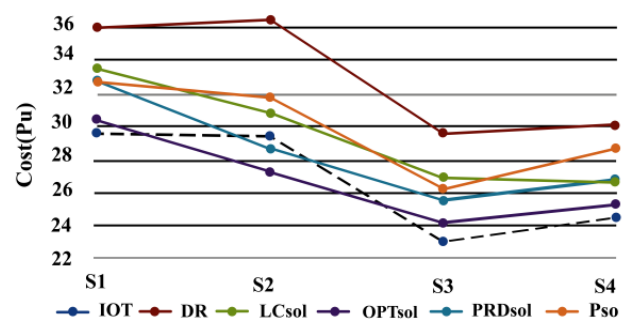


Fig. 6: A comparison based on the total cost.

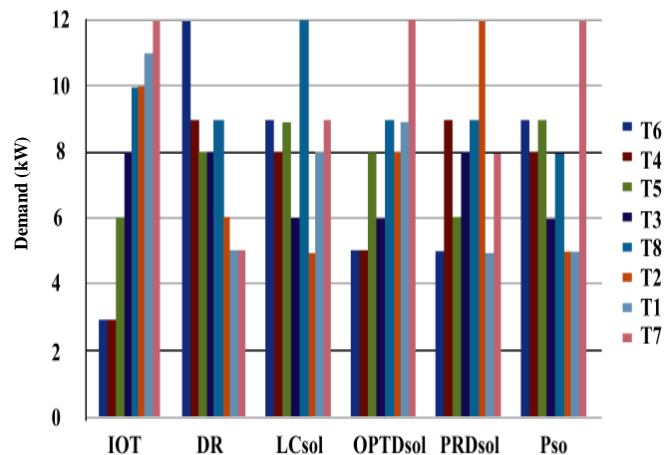


Fig. 7: A comparison based on peak load reduction.

4. CONCLUSION

This paper presents a conceptual and straightforward framework for energy-efficient management in IoT-based distribution systems, including IoT-based residences, power system operators, and central control units. End-user preferences are considered according to the definition of customer satisfaction factor. In addition, the central unit changes the usage time of prices to trade between the DSO and consumers. Several detailed analyzes have been performed to ascertain the impact of energy pricing and customer preferences

on technical parameters, e.g., the load index of distribution systems and economic indicators such as daily payment or the cost of discomfort to end-users. This data provides a good framework for the central unit to manage the IoT-based system efficiently. As such, both the benefits of the DSO and consumer expectations are met. Distribution network energy management by comparing changes in IoT-based consumer behavior has been compared with previous works regarding cost, time response, and peak load demand. The results show that the IoT method will reduce the total cost and lower the system response time and ultimately reduce the peak load demand.

CREDIT AUTHORSHIP CONTRIBUTION STATEMENT

Moaïad Mohseni: Conceptualization, Data curation, Formal analysis, Funding acquisition, Investigation, Methodology, Project administration, Resources, Software, Supervision, Validation, Visualization, Roles/Writing - original draft, Writing - review & editing. **Mahmood Joorabian:** Data curation, Investigation, Software, Visualization, Writing - review & editing. **Afshin Lashkar Ara:** Investigation, Project administration, Visualization.

DECLARATION OF COMPETING INTEREST

The authors declare that they have no known competing financial interests or personal relationships that could have appeared to influence the work reported in this paper. The ethical issues; including plagiarism, informed consent, misconduct, data fabrication and/or falsification, double publication and/or submission, redundancy has been completely observed by the authors.

REFERENCES

- [1] B. Guneet, G. K. Venayagamoorthy, R. Singh, R. R. Brooks, and K. C. Wang, "Review of internet of things (IoT) in electric power and energy systems," *IEEE Internet of Things Journal*, vol. 5, no. 2, pp. 847-870, April 2018.
- [2] B. N. Silva, M. Khan, and K. Han, "Internet of things: A comprehensive review of enabling technologies, architecture, and challenges," *IETE Technical Review*, vol. 35, no. 2, pp. 205-220, 2018.
- [3] M. Aazam, S. Zeadally, and K. A. Harras, "Deploying fog computing in industrial internet of things and industry 4.0," *IEEE Transactions on Industrial Informatics*, vol. 14, no. 10, pp. 4674-4682, 2018.
- [4] S. S. Reka, and T. Dragicevic, "Future effectual role of energy delivery: A comprehensive review of internet of things and smart grid", *Renewable and Sustainable Energy Reviews*, vol. 91, pp. 90-108, 2018.
- [5] S. Biljana, L. Risteska, and K. V. Trivodaliev, "A review of internet of things for smart home: challenges and solutions," *Journal of Cleaner Generation*, vol. 140, no. 3, pp. 1454-1464, 2017.
- [6] B. Collier, and E. Steven, "The emerging enernet: Convergence of the smart grid with the internet of things." *IEEE Industry Applications Magazine*, vol. 23, no. 2, pp. 12-16, 2017.
- [7] S. Talari, M. Shafie-Khah, P. Siano, V. Loia, A. Tommasetti, and J. P. Catalão, "A review of smart cities based on the internet of things concept", *Energies*, vol. 10, no. 4, 421, 2017.
- [8] Q. Yang, "Internet of things application in smart grid: A brief overview of challenges, opportunities, and future trends in smart power distribution systems", *Academic Press*, pp. 267-283, 2019.
- [9] A. Zareifar, H. Zartabi, and Z. Ouraei, "Internet of things benefits on smart grid," in *27th Iranian Conference on Electrical Engineering (ICEE)*, 2019, pp. 725-730.
- [10] G. Xu, W. Yu, D. Griffith, N. Golmie, and P. Moulema, "Toward integrating distributed energy resources and storage devices in smart grid", *IEEE Internet of Things Journal*, vol. 4, no. 1, pp. 192-204, 2017.
- [11] A. Basit, G. A. S. Sidhu, A. Mahmood, and F. Gao, "Efficient and autonomous energy management techniques for the future smart homes," *IEEE Transactions on Smart Grid*, vol. 8, no. 2, pp. 917-926, 2017.
- [12] M. Mohseni, M. Joorabian, A. Lashkar Ara, "Distribution system reconfiguration in presence of Internet of Things," *IET Generation, Transmission and Distribution*, vol. 15, no. 3, 2020.
- [13] Siemens. (April 1, 2022). *Siemens to build digital substation with grid IoT applications for Glitre Energi Nett* [Online]. Available: <https://press.siemens.com/global/en/pressrelease/siemens-build-digital-substation-grid-iot-applications-glitre-energi-nett>.
- [14] CyberSANE. (April 1, 2022). *Cybersane Project* [Online]. Available: <https://www.cybersane-project.eu/project/>.
- [15] R. Ashrafi, and S. Soleymani, "An energy management system based on economic and environmental aspects for microgrids incorporating active and reactive power sources and demand response programs," *International Journal of Industrial Electronics, Control and Optimization*, vol. 3, no. 3, pp. 259-273, 2020.
- [16] M. Vosoogh, M. Rashidinejad, and A. Abdollahi, "Efficient networked microgrid management considering plug-in electric vehicles and storage units," *International Journal of Industrial Electronics Control and Optimization*, vol. 4, no. 2, pp. 245-255, 2019.
- [17] X. Li and S. Wang, "Energy management and operational control methods for grid battery energy storage systems," *CSEE Journal of Power and Energy Systems*, vol. 7, no. 5, pp. 1026-1040, 2021.
- [18] M. U. Saleem, M. R. Usman, and M. Shakir, "Design, implementation, and deployment of an IoT based smart energy management system," *IEEE Access*, vol. 9, pp. 59649-59664, 2021.
- [19] M. Mohammadi, A. Kavousi-Fard, M. Dabbaghjamesh, A. Farughian, and A. Khosravi, "Effective management of energy internet in renewable

hybrid microgrids: a secured data driven resilient architecture," *IEEE Transactions on Industrial Informatics*, vol. 18, no. 3, pp. 1896-1904, 2022.

BIOGRAPHY



Moaiad Mohseni was born in Kuwait. He received his B.SC Degree in Electrical Engineering, Kazeroon Branch, Islamic Azad University, Kazeroon, Iran in 2001, and his M.Sc. and Ph.D. degrees in Electrical Engineering from Dezful Branch, Islamic Azad University, Dezful, Iran in 2011 and 2021, respectively. His research interests include the power market and smart grid and renewable energy systems.



Mahmood Joorabian received his B.E.E Degree from the University of New Haven, CT, USA, M.Sc. degree in Electrical Power Engineering from Rensselaer Polytechnic Institute, NY, USA and his Ph.D. degree in Electrical Engineering from the University of Bath, Bath, UK in 1983, 1985, and 1996, respectively. He is a Professor of Electrical Engineering Dap

at Shahid Chamran University. His main research interests are smart grids and power system studies.



Afshin Lashkar Ara received his B.Sc degree in electrical engineering from the Islamic Azad University, Dezful Branch, Dezful, Iran in 1995, his M.Sc degree from the University of Mazandaran, Babol, Iran in 2001, and his Ph.D. degree from the Iran University of Science and Technology (IUST), Tehran, Iran in 2011. Currently, he is an associate professor at Dezful Branch, Islamic Azad University. His research interests include power systems studies, FACTS controllers, and smart grids.

Copyrights

© 2022 Licensee Shahid Chamran University of Ahvaz, Ahvaz, Iran. This article is an open-access article distributed under the terms and conditions of the Creative Commons Attribution –NonCommercial4.0 International (CC BY-NC 4.0) License (<http://creativecommons.org/licenses/by-nc/4.0/>).





Iranian Association of
Electrical and Electronics
Engineers

Journal of Applied Research in Electrical Engineering

E-ISSN: 2783-2864

P-ISSN: 2717-414X

Homepage: <https://jaree.scu.ac.ir/>



Research Article

Design of a Tuneable Low-Power Band-Stop Filter for the Elimination of 50-Hz Power-Line Noise

Amirreza Solaymanpour , and Shahbaz Reyhani* 

Department of Electrical Engineering, University of Guilan, Persian Gulf Highway, Rasht 41996-13776, Iran

* Corresponding Author: shahbaz@guilan.ac.ir

Abstract: The electrocardiogram is affected by various noises among which one of the most important ones is 50-Hz power-line noise. On the other hand, it is necessary to use a battery in portable devices, so it is necessary to use low-power consumption circuits. Therefore, one of the challenges ahead when designing this type of device is the use of energy-saving filters that can integrate devices and attenuate unwanted signals properly. This paper presents a low-power tuneable sixth-order band-stop filter that does not need off-chip capacitors. The filter structure is based on operational transconductance amplifiers and integrated capacitors. Also, it is possible to change the central attenuation frequency of the proposed filter using the bias voltage of the transconductance amplifiers. The proposed band-stop filter is designed and simulated in 180-nm CMOS technology at the transistor level. The simulation results show that the proposed filter can attenuate unwanted signals at 50 Hz by 102 dB while the maximum capacitance used in the filter is 54 pF. The power consumption of the proposed band-stop filter is 13.1 nW at a supply voltage of 1.8 V.

Keywords: Electrocardiogram, low-power filter, band-stop filter, notch filter, power-line noise.

Article history

Received 23 December 2021; Revised 04 March 2022; Accepted 11 March 2022; Published online 9 April 2022.

© 2022 Published by Shahid Chamran University of Ahvaz & Iranian Association of Electrical and Electronics Engineers (IAEEE)

How to cite this article

A. Solaymanpour, and S. Reyhani, "Design of a tuneable low-power band-stop filter for the elimination of 50-Hz power-line noise," *J. Appl. Res. Electr. Eng.*, vol. 1, no. 2, pp. 197-202, 2022. DOI: 10.22055/jaree.2022.39545.1042



1. INTRODUCTION

The electrocardiogram is one of the most common devices in medical applications to measure electrical signals related to heart patients [1]. Portable electrocardiogram devices enable physicians to measure and remotely control patient conditions, which is essential given the advancement of technology and the conditions of some patients [1-3].

One of the factors that can disrupt the operation of the electrocardiogram device is a variety of noises among which one of the most important ones is power-line noise that occurs at a frequency of 50 or 60 Hz. This unwanted signal interferes with the original signal and makes the process of measuring and diagnosing patients' problems difficult [4-6].

Band-stop or notch filters, which are analog and suitable for real-time processing, are used to eliminate power-line noise. Unlike digital filters and adaptive filters, analog filters do not require high-speed processors [2-8].

Various structures of analog filters have been used to eliminate power-line noise [8]. Due to the high sensitivity of electrocardiogram devices, the circuits used in these devices must have high accuracy, low power, proper attenuation of

noise, and also the ability to integrate. Therefore, the band-stop filter used in electrocardiogram devices must also have these specifications [1-3].

Portable electrocardiogram devices are no exception to this rule. In some studies, the use of circuits with high power consumption and the use of resistors and capacitors with high values in the filter do not make it possible to integrate these circuits [9-13].

This article presents a tuneable band-stop filter that can attenuate the annoying 50-Hz signal of the power line by 102 dB. The proposed filter outperforms other filters owing to its very low power consumption (nano-watts), good attenuation, simple structure, small capacitor, and no resistor.

2. THE STRUCTURE OF THE SECOND-ORDER OTA-C BAND-STOP FILTER

The proposed band-stop or notch filter uses three stages of second-order band-stop filters. The second-order notch filter uses only operational transconductance amplifiers (OTA) and capacitors and is based on the OTA-C structure. Fig. 1 shows the second-order OTA-C band-stop filter circuit.

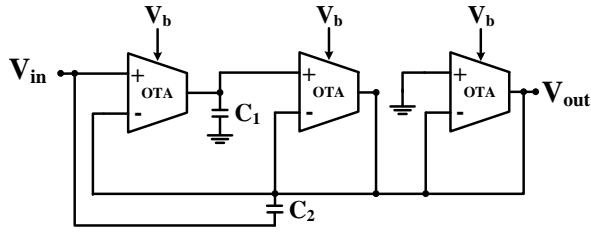


Fig. 1: The second-order band-stop filter, used in the proposed filter.

The second OTA-C notch filter uses three transconductance amplifiers. The proposed filter transfer function is shown in (1).

$$TF = \frac{S^2 C_1 C_2 + g_{m1} g_{m2}}{S^2 C_1 C_2 + S g_{m2} C_1 + g_{m1} g_{m2}} \quad (1)$$

where C_1 and C_2 are the capacitors used in the circuit, and g_{m1} , g_{m2} , and g_{m3} are the first, second, and third transconductance amplifiers in the band-stop filter. The cut-off frequency (ω_0) and the quality factor (Q) of the filter are obtained by (2) and (3).

$$\omega_0 = \sqrt{\frac{g_{m1} g_{m2}}{C_1 C_2}} \quad (2)$$

$$Q = \left(\frac{\sqrt{g_{m1} g_{m2}}}{g_{m3}} \right) \sqrt{\frac{C_2}{C_1}} \quad (3)$$

By changing the transconductance of the amplifiers according to (2), the cut-off frequency of the filter can be changed, which is possible by changing the amount of bias voltage (V_b) in the amplifier, which is described in the next section.

Although the proposed band-stop filter is used to attenuate 50-Hz noise by changing the bias voltage between 0.12 and 0.2 V, the central frequency of the filter can be changed approximately between 4 and 100 Hz for $C_1=16\text{pF}$ and $C_2=2\text{pF}$. Table 1 compares the calculated and simulated values of the transconductance for different central frequencies of the filter. The bias voltages of the OTAs in the proposed filter are the same. The higher bias voltages increase the central frequency of the filter, but since the amplifier exits from the sub-threshold region, the attenuation of the filter decreases and its power consumption also increases. Table 2 compares the calculated transconductance and quality factor with the simulated ones for central frequency of 50 Hz.

Fig. 2 shows the frequency response of the proposed second-order notch filter.

2.1. The Operational Transconductance Amplifier

The transconductance amplifier circuit used in the proposed filter stages shown in Fig. 3.

The proposed differential amplifier has a gain of 90 dB, a bandwidth of 5.7 MHz, a phase margin of 69°, and a common-mode rejection ratio (CMRR) of 110 dB. The inputs of this amplifier are PMOS type, which is not sensitive to flicker and offset noise. The gain and phase characteristics of the proposed transconductance amplifier are shown in Fig. 4.

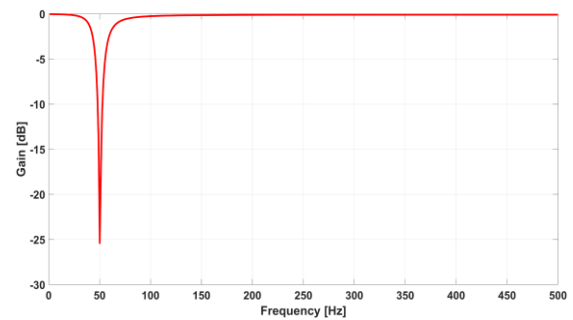
By changing the bias voltage (V_b), the amount of transconductance (g_m) will change.

Table 1: The comparison of calculated g_m with simulated values. The calculated g_m is obtained using existing central frequency for $C_1=16\text{pF}$ and $C_2=2\text{pF}$.

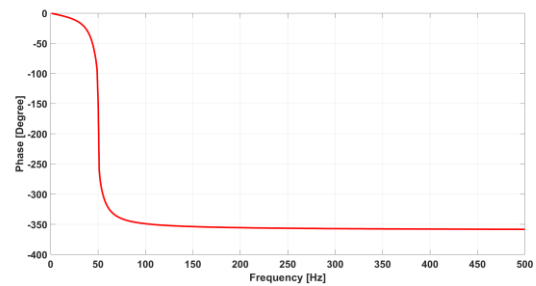
V_{bias} (V)	f_0 (Hz)	g_m (calc.) (nS)	g_m (simu.) (nS)
0.125	4.1	0.146	0.346
0.13	8.07	0.287	0.434
0.14	21.47	0.763	0.670
0.15	29.6	1.05	0.922
0.16	39.17	1.39	1.28
0.17	50.93	1.81	1.78
0.18	65.46	2.33	2.47
0.19	83.56	2.97	3.40
0.20	105.68	3.76	4.66

Table 2: The comparison of calculated parameters of the second-order 50-Hz notch filter with the simulated values.

Parameters for central frequency of 50 Hz	Filter Specification	
	Calculation	Simulation
g_m	1.78nS	1.81nS
Q	2.82	3.19



(a)



(b)

Fig. 2: The frequency response of the proposed second-order band-stop filter including (a) gain, and (b) phase.

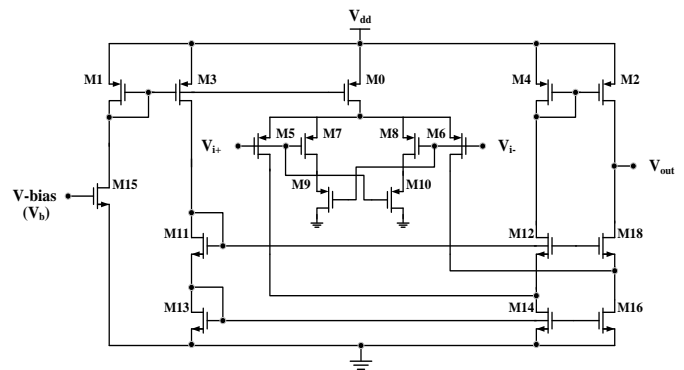


Fig. 3: The proposed transconductance amplifier circuit.

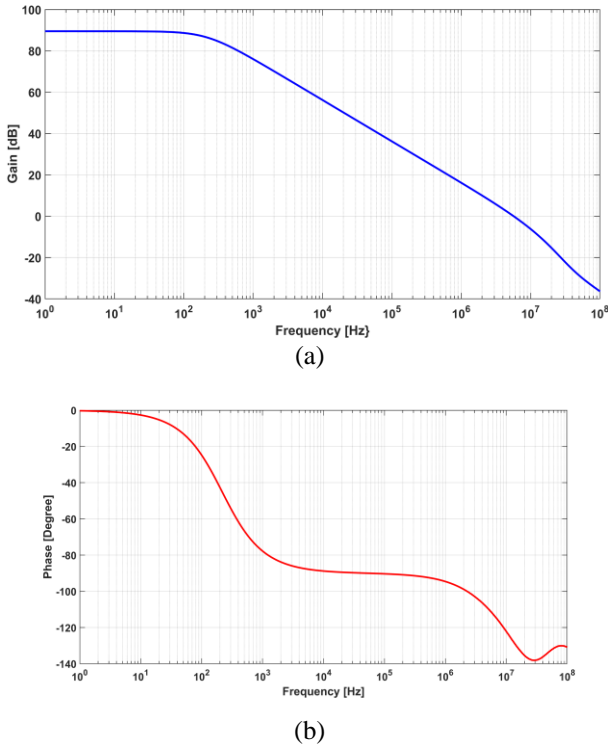


Fig. 4: The frequency response of the proposed operational transconductance amplifier for $V_b=0.9V$ including (a) gain and (b) phase.

The OTA is designed by the following procedure. 1) The current of each branch is determined from the slew rate requirements. 2) The transconductance of the input transistors is determined from the GBW.

$$g_m = 2\pi \times GBW \times C_L \quad (4)$$

3) The size of the input transistors is obtained by

$$\left(\frac{W}{L}\right) = \frac{(g_m)^2}{2\mu C_{ox} \times I_D} \quad (5)$$

4) For other transistors, V_{DSAT} is at least 50-200mV. When V_{DSAT} is determined, the size of each transistor is set using

$$\left(\frac{W}{L}\right) = \frac{2I_D}{\mu C_{ox} \times V_{DSAT}^2} \quad (6)$$

Based on the above-mentioned designing procedure, the single-stage OTA is designed. Then, the W/L of transistors are obtained using a sizing procedure (based on the trade-off method) performed by a simulation tool in CMOS 180nm technology. Table 3 shows the design results of the proposed OTA.

The power consumption of the proposed OTA with a bias voltage of 0.9V and a power supply of 1.8V is 69 μW . To use this OTA in the proposed filter, the bias voltage must be reduced to 0.17V, which will reach a power consumption of 1.4 nW. In this case, the dc gain will be equal to 25 dB.

3. THE PROPOSED LOW-POWER TUNEABLE BAND-STOP FILTER STRUCTURE

The proposed structure of the sixth-order low-power tuneable band-stop filter is shown in Fig. 5.

Table 3. The parameters of transistors in the proposed OTA

Transistor	W (μm)	L (μm)	I_D (μA)	g_m (μS)	V_{DSAT} (mV)
M ₀	28	0.18	9.6	82	120
M ₁	28	0.18	10	213	57
M ₃	28	0.18	10	210	60
M ₂ -M ₄	28	0.18	4.3	98	50
M ₅ -M ₆	14	0.18	3.3	72	52
M ₇ -M ₈	14	0.18	1.5	31	51
M ₉ -M ₁₀	14	0.18	1.5	33	47
M ₁₁	10	2	10	148	128
M ₁₂ -M ₁₈	2.5	2	4.3	53	159
M ₁₃	10	2	10	147	126
M ₁₄ -M ₁₆	7.5	2	7.7	112	126
M ₁₅	0.61	2	10	40	440

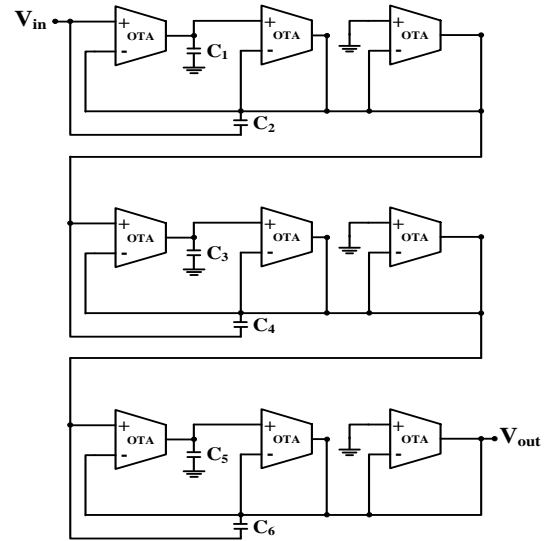


Fig. 5: The structure of the proposed sixth-order band-stop filter.

In each stage, there are three transconductance amplifiers that can be tuned by changing the bias voltage. For a central frequency of 50 Hz, the values of the capacitors used are $C_1=C_3=C_5=16pF$ and $C_2=C_4=C_6=2pF$, and the bias voltage is $V_b=170mV$.

4. SIMULATION RESULTS

The proposed filter was designed and simulated in 180 nm technology at the transistor level. The frequency response of the filter is shown in Fig. 6.

As can be seen, the proposed filter attenuates the 50-Hz signal by 102 dB. This filter is tuneable and the central attenuation frequency can be changed by adjusting the g_m values of the transconductance amplifiers.

Fig. 7 shows the frequency response of the proposed filter output for schematic and post-layout simulation. Due to the tuneable nature of the filter, the central frequency in the post-layout circuit can be shifted by changing the input bias voltage, which will eliminate the negative effect of parasitic components on the filter performance.

This feature also makes the proposed filter compatible to eliminate the power-line noise in some countries with a frequency of 60 Hz. Also, the low power consumption of 13.1 nW and integrability can be considered the advantages of the proposed filter.

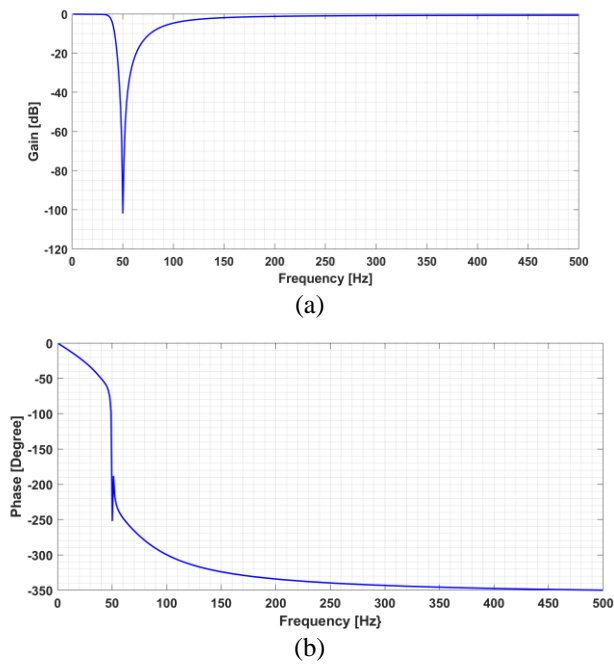


Fig. 6: The frequency response of the proposed sixth-order band-stop filter including (a) gain, and (b) phase.

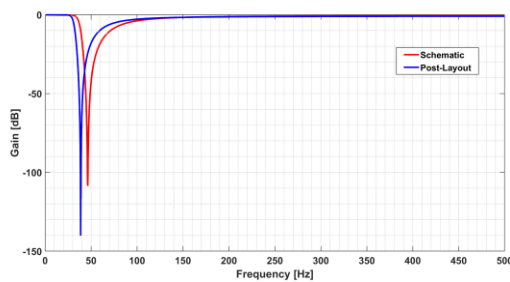


Fig. 7: The frequency response for schematic and post-layout simulation of the proposed sixth-order band-stop filter.

The effect of the capacitance deviation on the central frequency of the proposed sixth-order band-stop filter is investigated using Monte Carlo analysis. As shown in Fig. 8, the error created in the central frequency of the filter is not significant for 2% deviation in the capacitance of the capacitors. Also, separate simulations were performed for different corners. Their frequency responses are shown in Fig. 9. Considering the capability of the proposed filter, the central frequency of the band-stop filter can be set to the desired frequency by changing the input bias voltage.

The layout of the proposed sixth-order band-stop filter is shown in Fig. 10. The dimensions of the layout are $459\ \mu\text{m}$ by $303\ \mu\text{m}$.

The proposed filter is compared with the previously reported works. As shown in Table 4, this filter is superior to the reported filters in terms of low power consumption, low capacitance, high attenuation rate, and lack of resistance.

5. CONCLUSION

The tuneable sixth-order band-stop filter to eliminate power-line noise for use in portable electrocardiograms is designed and simulated in 180 nm CMOS technology. The

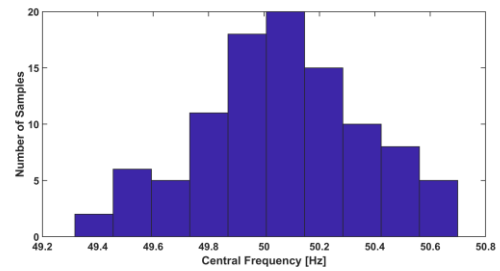


Fig. 8: The histogram of Monte Carlo analysis on the proposed filter.

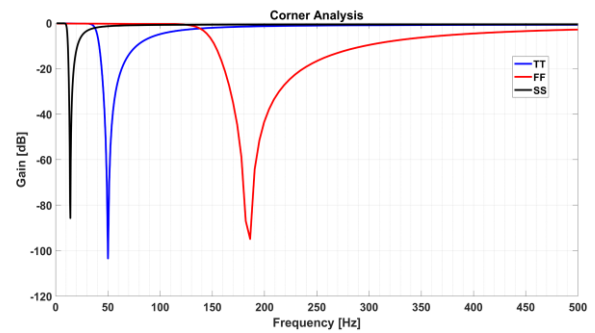


Fig. 9: The frequency response of the proposed filter for different corner simulations.

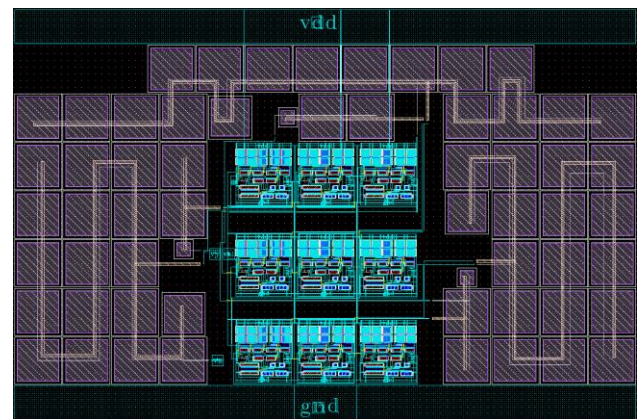


Fig. 10: The layout of the proposed sixth-order band-stop filter.

proposed filter is based on the OTA-C structure, in which the central frequency of the filter is tuned by adjusting the bias voltage. The tunability of the proposed filter makes it possible to be used in eliminating power-line noise with a frequency of 50 or 60 Hz. The power consumption of the proposed filter is 13.1 nW. The total capacitance in the sixth-order band-stop filter is 54 pF, which makes it possible to integrate the proposed filter. As such, no off-chip capacitors will be needed.

CREDIT AUTHORSHIP CONTRIBUTION STATEMENT

Amirreza Solaymanpour: Formal analysis, Resources, Software, Roles/Writing - original draft. **Shahbaz Reyhani:** Methodology, Supervision, Validation, Writing - review & editing.

Table 4: The comparison of the proposed filter with the reported works.

	This article	[12]	[14]	[15]
Technology (nm)	180	180	250	90
Amplifier type	Folded Cascade OTA	Gm-C	Cascaded	OTA-C
Voltage (V)	1.8	0.5	±0.8	±0.6
Number of amplifiers	9	10	9	16
Cut-off frequency (Hz)	50	50	50	50
Attenuation (dB)	-102	-75	-43	-44
Capacitive capacity (nF)	0.054	0.1	0.032	0.02688
Power consumption (μW)	0.0131	280	25	0.0145

DECLARATION OF COMPETING INTEREST

The authors declare that they have no known competing financial interests or personal relationships that could have appeared to influence the work reported in this paper. The ethical issues; including plagiarism, informed consent, misconduct, data fabrication and/or falsification, double publication and/or submission, redundancy has been completely observed by the authors.

REFERENCES

- [1] S. L. Tripathi, K. B. Prakash, V. E. Balas, S. K. Mohapatra, and J. Nayak, *Electronic devices, circuits, and systems for biomedical applications: Challenges and intelligent approach*. San Diego, CA: Academic Press, 2021.
- [2] D. Bansal, *Real-time data acquisition in human physiology: Real-time acquisition, processing, and interpretation-A MATLAB-based approach*. San Diego, CA: Academic Press, 2021.
- [3] D. J. Hemanth, D. Gupta, and V. E. Balas, *Intelligent Data Analysis for Biomedical Applications: Challenges and Solutions*. San Diego, CA: Academic Press, 2019.
- [4] J. P. Vale Madeiro, P. C. Cortez, J. M. Da Silva Monteiro Filho, and A. R. Alencar Brayner, *Developments and applications for ECG signal processing: Modeling, segmentation, and pattern recognition*. San Diego, CA: Academic Press, 2018.
- [5] L. Tan, and J. Jiang, *Digital Signal Processing: Fundamentals and Applications*, 3rd ed. San Diego, CA: Academic Press, 2018.
- [6] H. Li, J. Zhang, and L. Wang, "A fully integrated continuous-time 50-Hz notch filter with center frequency tunability," in *2011 Annual International Conference of the IEEE Engineering in Medicine and Biology Society*, 2011, vol. 2011, pp. 3558–3562.
- [7] A. R. Verma, and Y. Singh, "Adaptive tuneable notch filter for ECG signal enhancement," *Procedia Computer Science*, vol. 57, pp. 332–337, 2015.
- [8] E. V. Zaitsev, "Elimination on power line interference from ECG signal using combined bidirectional narrow-band notch filter," *Biophysics (Oxf.)*, vol. 60, no. 4, pp. 656–658, 2015.
- [9] S. K. Paul, C. K. Choubey, and G. Tiwari, "Low power analog comb filter for biomedical applications," *Analog Integrated Circuits Signal Process*, vol. 97, no. 2, pp. 371–386, 2018.
- [10] M. De Matteis, F. Fary, E. A. Vallicelli, and A. Baschirotto, "A 28 nm CMOS 100 MHz 67 dB-dynamic-range 968 μW flipped-source-follower analog filter," *Journal of low power electronics and applications*, vol. 11, no. 2, pp. 15, 2021.
- [11] R. K. Ranjan, C. K. Choubey, B. C. Nagar, and S. K. Paul, "Comb filter for elimination of unwanted power line interference in biomedical signal," *Journal of Circuits, Systems and Computers*, vol. 25, no. 06, pp. 1650052, 2016.
- [12] C. Yehoshuva, R. Rakhi, D. Anto, and S. Kaurati, "0.5 V, ultra low power multi standard Gm-C filter for biomedical applications," in *2016 IEEE International Conference on Recent Trends in Electronics, Information & Communication Technology (RTEICT)*, 2016.
- [13] A. K. Luhach, D. Singh, P.-A. Hsiung, K. B. G. Hawari, P. Lingras, and P. K. Singh, Eds., in *Advanced informatics for computing research: Second international conference, ICAICR 2018, Shimla, India, July 14-15, 2018*.
- [14] S. A. Mahmoud, A. Bamakhramah, and S. A. Al-Tunaiji, "Six order cascaded power line notch filter for ECG detection systems with noise shaping," *Circuits Systems Signal Process.*, vol. 33, no. 8, pp. 2385–2400, 2014.
- [15] M. S. Diab and S. A. Mahmoud, "14.5nW; 30 dB analog front-end in 90-nm technology for biopotential signal detection," in *2020 43rd International Conference on Telecommunications and Signal Processing (TSP)*, 2020, pp. 681-6840.

BIOGRAPHY



Amirreza Solaymanpour was born in 1995. He received his B.Sc. degree in Electronic Engineering from Shomal University of Amol, Iran in 2018. He is currently a graduate student in electronic engineering-integrated circuits at the University of Guilan, Rasht, Iran. His field of interest is the design of analog integrated circuits.



Shahbaz Reyhani was born in 1969. He received his B.Sc., M.Sc., and Ph.D. degrees in Electronic Engineering from the University of Guilan, Shiraz University, and Shahid Beheshti University, respectively, in Iran. Dr. Reyhani is an Assistant Professor with the Department of Electrical Engineering, University of Guilan, Rasht,

Iran. His research interests include low-power integrated circuits, data converters, digital systems, and neural networks.

Copyrights

© 2022 Licensee Shahid Chamran University of Ahvaz, Ahvaz, Iran. This article is an open-access article distributed under the terms and conditions of the Creative Commons Attribution–NonCommercial 4.0 International (CC BY-NC 4.0) License (<http://creativecommons.org/licenses/by-nc/4.0/>).



Shahid Chamran
University of AhvazIranian Association of
Electrical and Electronics
Engineers

Journal of Applied Research in Electrical Engineering

E-ISSN: 2783-2864

P-ISSN: 2717-414X

Homepage: <https://jaree.scu.ac.ir/>

Research Article

Novel 2-D BWA-MEM FPGA Accelerator for Short-Read Mapping of the Whole Human Genome

Mahdi Taheri , and Ali Mahani* 

Reliable and Smart Systems Lab (RSS), Shahid Bahonar University of Kerman, Kerman 7616913439, Iran

*Corresponding Author: amahani@uk.ac.ir

Abstract: The mapping of DNA subsequences to a known reference genome, referred to as “short-read mapping”, is essential for next-generation sequencing. Hundreds of millions of short reads need to be aligned to a tremendously long reference sequence, making short-read mapping very time-consuming. Day by day progress in Next-Generation Sequencing (NGS) is enabling the generation of DNA sequence data at ever faster rates and lower cost, which means a dramatic increase in the amounts of data being sequenced. Nowadays, sequencing of nearly 20 billion reads (short DNA fragments) costs about 1000 dollars per human genome, and sequencers can generate 6 Terabases of data in less than two days. This article considers the seed extension kernel of the Burrows-Wheeler Alignment (BWA) genomic mapping algorithm for accelerating with FPGA devices. We propose an FPGA-based accelerated implementation for the seed extension kernel. The Smith-Waterman algorithm is used during the seed extension to find the optimum alignment between two sequences. The state-of-the-art architectures use 1D-systolic arrays to fill a similarity matrix. Based on the best score out of all match combinations, mismatches and gaps are computed. The cells on the same anti-diagonal are calculated in parallel in these architectures. We propose a novel 2-dimensional architecture. Our new modified algorithm is based on two editing and calculating phases. In each step of the calculation, some errors may occur in which all the cells on the same row and same column are computed in parallel, which significantly speeds up the process. Needless to say, these probable errors will be omitted before the next step of the calculation begins. Our simulation results show that the proposed architecture can work with up to 312 MHz frequency in Synopsys Design-Compiler for 180-nm CMOS technology and be up to 570x and 1.4x faster than the software execution and 1D-systolic arrays, respectively.

Keywords: Bioinformatics, FPGA, smith-waterman.

Article history

Received 20 December 2020; Revised 27 March 2021; Accepted 15 August 2021; Published online 11 April 2022.

© 2022 Published by Shahid Chamran University of Ahvaz & Iranian Association of Electrical and Electronics Engineers (IAEEE)

How to cite this article

M. Taheri, and A. Mahani, "Novel 2-D BWA-MEM FPGA accelerator for short-read mapping of the whole human genome," *J. Appl. Res. Electr. Eng.*, vol. 1, no. 2, pp. 203-210, 2022. DOI: [10.22055/jaree.2021.36116.1015](https://doi.org/10.22055/jaree.2021.36116.1015)



1. INTRODUCTION

As a result of advances in next generation sequencing (NGS) techniques, the amount of genomic data is accumulating extremely rapidly [1]. Some projects will grow on an order of 1018 bytes per year by the next decade [2, 3]. Naturally, data of such scales impose a significant processing load in many aspects of bioinformatics. The new NGS techniques reduce the cost of generating a whole human genome, which, in return, further increases the amount of data [4]. Typically, NGS techniques produce millions of short reads, usually less than 200 bases in length [5]. In many cases, the short reads must be aligned to a

reference sequence to obtain useful information about the sequenced molecule [6]. There are several different alignment algorithms to choose from, among which dynamic programming solutions, such as Bowtie [7], Burrows-Wheeler Alignment (BWA) [8], and SOAP2 [9], are shown to provide a better trade-off between the accuracy and speed. The most well-known, the BWA-MEM algorithm, which is popular for its high accuracy, is considered in this article as the target for FPGA acceleration.

The BWA-MEM algorithm, introduced in [10], manages superior alignment to a number of its contemporaries, but at the cost of a higher computational load. The three main operations in the BWA-MEM

algorithm are (1) generating the super-maximal exact matches (SMEMs), (2) extending the seeds, and (3) generating the final outputs. The three kernels that perform these operations are listed in Table 1 along with their main bottlenecks [11]. As shown in Table 1, the step with the most severe computational bound is the seed extension kernel, which accounts for almost 33% of the execution time. A similarity matrix is dynamically filled during the seed extension operation. To compute the value of the cell (i, j) in the similarity matrix, the values of the following cells are required: (1) the west cell at $(i, j-1)$, (2) the north cell at $(i-1, j)$, and (3) the north-west cell at $(i-1, j-1)$. State-of-the-art architectures aimed at accelerating this problem use 1D-systolic arrays to fill the similarity matrix [8]. Specifically, for such computations, 1D-systolic arrays use a 1-dimensional array of n processing elements (PEs) where n is the number of cells on the main diagonal [11]. Note that increasing the number of PEs in such an architecture does not reduce execution time.

This article proposes a novel FPGA-based architecture to speed up the process of filling the similarity matrix, the bottleneck of the seed extension kernel. To the best of our knowledge, this is the first 2-dimensional architecture that, unlike 1D-systolic arrays, achieves higher throughput by increasing the number of PEs. The proposed architecture can compute the cells on the same row and on the same column in parallel as opposed to existing architectures that can only compute the cells on the same anti-diagonal in parallel. Novel PEs are proposed that compute cells in two phases: (1) the calculation phase that roughly approximates the cells and (2) the error compensation phase that fixes the potentially introduced errors during the first phase. The two phases are described in detail in Section 3.

The rest of the paper is organized as follows. Section 2 provides general information on the BWA-MEM algorithm and related work. The mathematical description of the proposed architecture, the PE designs, and the final hardware implementation are discussed in Section 3. Section 4 evaluates the proposed architecture. Finally, Section 5 concludes the article.

2. BACKGROUND

This section describes the BWA-MEM algorithm and related previous works dedicated to its acceleration. DNA sequences are chains comprised of the four nucleotide monomers (A, C, G, T). Alternative permutations of these nucleotides typically encode alternate biochemical functions and products within the DNA. A 2-bit representation is used in our implementation for each of these four nucleotides. Although even simple organisms possess contiguous DNA exceeding a million nucleotides in length, DNA measurements (i.e. the products of sequencing machines) rarely produce sequences this long due to a combination of technical limits at present. In fact, it is common for leading sequencers to produce outputs, ‘reads’, on an order of 100 nucleotides in length, obtained from unknown regions of the native DNA originally fed into the sequencer.

As a result, pairwise local alignment, searching for similarities between a new read (the query) and anticipated DNA pattern (reference genome), is one of the first steps in bioinformatics algorithms [12]. The main workload of the

Table 1: Profiling the BWA-MEM algorithm [11].

Kernel	Execution time (%)	Bound
SMEM generation	56%	Memory
Seed extension	32%	Computational
Output generation	9%	Memory
Other	3%	I/O

BWA-MEM algorithm is aligning millions of short DNA reads against a reference genome (usually the human genome) [13]. The authors introduced a new low-power and high-speed bioinformatic engine, a hardware-accelerated base caller, for mobile sequencing applications [14]. There are also several other works providing a generalized methodology and insights for efficient implementation of the DNA sequencing algorithms [15–19].

Several techniques have been proposed to accelerate the Smith-Waterman inexact alignment algorithm. However, the seed extension step of this algorithm makes it inherently a slow design. Authors have provided a new 2-D technique regarding the Smith-Waterman inexact alignment algorithm in which they have used fix numbers for the match, mismatch, and gap penalty [20]. An FPNI structure is proposed in [21] that uses race logic and CMOS-gate representation and leads to compromising results in the case of flexible input read length and omitting unnecessary latency. This is a new re-configuration sequencing method for difference of read lengths that may take place as input data in which crucial drawbacks impact DNA sequencing methods. A hardware acceleration of the BWA-MEM genomics short read mapping for longer read length is implemented in [22]. This design is based on an architecture previously proposed in [11] where an FPGA-based 1D-systolic array is used to accelerate the BWA-MEM genomics mapping algorithm. The main idea is to insert some exit points between the PEs of the 1D-systolic array to avoid unnecessary calculations for shorter reads. By doing so, shorter reads do not have to go through all of the PEs and can exit the array once they get to the first exit point.

3. PROPOSED ARCHITECTURE

This section describes the methodology proposed for filling the similarity matrix and introduces the new architecture for implementing the seed extension kernel of the BWA-MEM algorithm.

Unlike the 1D-systolic array-based architectures, we propose a 2-dimensional architecture in which two different strings of PEs are assigned to all of the cells in the same rows and on the same columns. By doing so, the Smith-Waterman algorithm can be executed faster compared to the 1D-systolic array-based architectures. Although the proposed architecture is more resource-hungry than 1D-systolic arrays, it runs significantly faster. Note that the 1D-systolic arrays cannot operate faster even with more PEs. Each PE computes the values of its assigned cells (fills the similarity matrix) in two phases that, in total, take three clock cycles. During the first phase, the calculation phase, the value of each cell is roughly approximated by the corresponding PEs. Then, the $Error_{flag}$ signal is asserted and the second phase, i.e. the error editing phase, starts. The main advantage of our structure is that the rows and columns calculation of the

similarity matrix are performed independently. In some rare cases, the parallel calculations lead to approximation in the obtained scores. So, the editing phase (second phase) is needed to correct the approximated scores of the first phase.

Fig. 1 shows how PEs are assigned to cells in the similarity matrix in the proposed method and in the previously reported 1D-systolic array-based architectures. The cells with the same numbers in Fig. 1a are computed simultaneously and the cells with the same colors in Fig. 1b can be computed in parallel in the proposed architecture. It can be clearly seen in Fig. 1 that the similarity matrix can be filled in fewer steps by using the proposed architecture (three versus five).

Note that the 1D-systolic array needs only three PEs to fill the similarity matrix, while the proposed architecture uses five PEs. However, the main advantage of the proposed architecture is that more PEs are processed in parallel, thereby speeding up the process. Taking advantage of our two-phase architecture lets us better exploit the parallelism available in the process. The timing diagram of the proposed architecture is given in Fig. 2. As shown in this figure, when the first phase – the calculation phase – is completed, the PE may or may not perform the second phase. The error signal *Errorflag* is updated after the end of the calculation phase and, if it is set, then the 2nd phase (the editing phase) needs to be performed.

The two phases of the proposed architecture and the details of its hardware implementation are thoroughly explained below.

3.1. Calculation Phase

During the calculation phase, an approximation of each cell is calculated. Depending on the position of the cell in the similarity matrix, this approximation follows different rules, as described below.

3.1.1. Cells on the main diagonal

For the cells on the main diagonal, we use the exact PE functionality, as given by:

$$DP(i, i) = \text{MAX} \begin{cases} DP_{(i-1, i-1)} + T_{(Match, Miss-Match)} \\ DP_{(i-1, i)} + T_{(GAP)} \\ DP_{(i, i-1)} + T_{(GAP)} \\ 0 \end{cases} \quad (1)$$

where DP denotes the similarity matrix, $T_{(Match, Miss-Match)}$ is the assigned score for when a match or a mismatch occurs (usually +2 for a match and a -1 for a mismatch [11]), and $T_{(Gap)}$ is the gap penalty.

As shown, (1) accounts for all contributions neighboring cells (i, i) on the main diagonal and is thus ‘exact’. However, since the adjacent cells, i.e., west, north, and north-west, have approximate values (see immediately following sub-section), the output of this equation would likely be an erroneous value.

3.1.2. Other cells

As implied above, the elements that are not placed on the main diagonal use only two of the three adjacent cells. Note that this approximation is a property of the underlying algorithm and not a specific hardware-related design choice. For the main diagonal of the cells below, we use the values of the west and the north-west cells as given by (2).

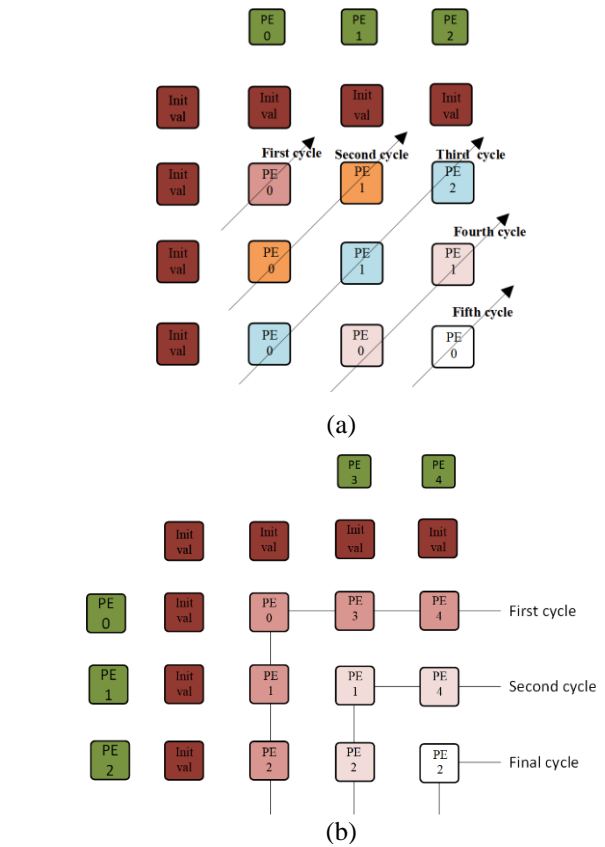


Fig. 1: The PE assignment in (a) 1D-Systolic array-based architecture and (b) the proposed design.

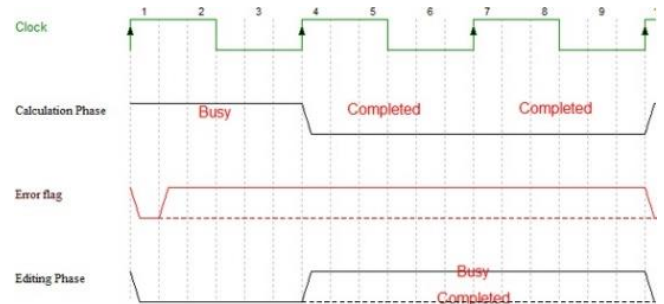


Fig. 2: Timing diagram of the proposed 2-dimensional architecture. The editing phase might or might not be required depending on the value of the *Errorflag* signal.

$$DP(i, j) = \text{MAX} \begin{cases} DP_{(i-1, j-1)} + T_{(Match, Miss-Match)} \\ DP_{(i, j-1)} + T_{(GAP)} \\ 0 \end{cases} \quad (2)$$

$$DP(i, j) = \text{MAX} \begin{cases} DP_{(i-1, j-1)} + T_{(Match, Miss-Match)} \\ DP_{(i, j-1)} + T_{(GAP)} \\ 0 \end{cases}$$

For the cells on the top of the main diagonal, on the other hand, we use the values of the north and the north-west cells as given by:

$$DP(i, j) = \text{MAX} \begin{cases} DP_{(i-1, j-1)} + T_{(Match, Miss-Match)} \\ DP_{(i-1, j)} + T_{(GAP)} \\ 0 \end{cases} \quad (3)$$

Fig. 3 provides a graphical description of the three above-mentioned equations to make the proposed architecture clearer. As shown in Fig. 3, the cells on the main diagonal ((1, 1) and (2, 2)) use the values of the three

adjacent cells. The cell below the main diagonal, i.e. (2, 1) uses the values of the west and the north-west adjacent cells. Finally, the cell on the top of the main diagonal, i.e., (1, 2) uses the values of the north and the north-west adjacent cells. Note that according to (1), (2), and (3), two types of PEs are required in the proposed architecture. The horizontal PEs are used to calculate the values of the cells on the same row, from the first column to the column on which the cell on the main diagonal is located, and the vertical PEs calculate the values of the cells on the same column, from the first row to the row just below the row on which the cell on the main diagonal is located. Note that the horizontal PEs are distinct from the vertical PEs as they use the values of different neighbors to calculate their outputs during the first phase. Unlike the existing architectures, including 1D-systolic arrays, the distinction between the horizontal and vertical PEs in this work allows us to perform the calculations independently and in parallel. Thus, the proposed architecture is notably faster than the existing designs, as will be discussed later in the simulation results section, Section IV. With the given approximations in (1), (2), and (3), cells would most likely have erroneous values. Thus, a second phase is required i.e., the editing phase to compensate for the introduced errors.

3.2. Editing Phase

Similar to the calculation phase, the editing phase is also done differently for the cells on the main diagonal and the other cells.

3.2.1. Cells on the main diagonal

For the cells on the main diagonal, our calculation phase was performed based on (1). Consider Fig. 3 where a subset of the similarity matrix is shown. The cells (0, 0), (1, 1), and (2, 2) are explained here, and calculations for other cells on the main diagonal would be just like the cell (2, 2).

Cell (0, 0): The value of this cell is calculated according to (1) by using PE11, see Fig. 3, during the calculation phase. Since (1) is the exact equation and the three cells that are used to calculate the value of the cell (0, 0) have all exact values (i.e. the initial values), there is no calculation error. Hence, the editing phase is not performed for the cell (0,0).

Cell (1, 1): The value of the cell (1, 1) is calculated based on the values of the cells (1, 0) and (0, 1), which are computed according to (2) and (3), respectively, and the value of the cell (0, 0). There is no error in the value of the cell (0, 0) and, therefore, to edit the value of the cell (1,1), we only need to edit the values of the cells (1,0) and (0,1).

The value of the cell (1, 0) is initially computed by ignoring the value of the cell (0, 0). Hence, the first step in editing this cell would be figuring out if (0, 0) was effective in the value of the cell (1, 0), which can be checked with the following condition: $DP_{(0,0)} + T_{(gap)} > DP_{(1,0)}$. If this condition is met, it means that an error has occurred in the calculation of the value of the cell (1, 0) and, therefore, the $Error_{flag}$ of $PE_{(12)}$ is set. Similarly, the cell (0, 1) should be checked for possible errors that happen in some seldom cases. Finally, the value of the cell (1, 1) is recomputed based on (1) to avoid any possible error if at least one of the two $Error_{flag}$ signals for the two corresponding PEs is set.

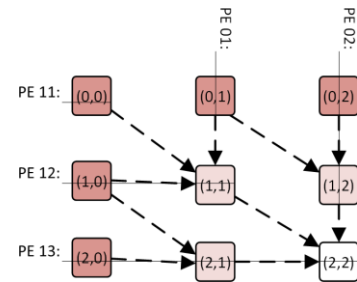


Fig. 3: The graphical description of the PEs' functionality during the calculation phase.

Cell (2, 2): The value of the cell (2, 2) is calculated based on the values of the cells (1, 1), (2, 1), and (1, 2). The details for this error correction are provided in Algorithm 1. The editing phase for the cell (1, 1) is already explained and the cells (2, 1) and (1, 2) have similar error editing calculations. Thus, only the calculation for the cell (2, 1) is explained here.

Cell (2, 1) might have an erroneous value caused by the values of the cells (1, 0) and (2, 0) and more importantly, by

Algorithm 1: Editing phase for the cells that are located on the main diagonal.

```

1: Editing by using horizontal PEs
2: if  $Error_{flag}(PE_{12}) = 1$  then
3:   if  $DP_{(1,0)} + T_{(gap)} > DP_{(2,0)}$  then
4:      $DP_{(2,0)} \leftarrow DP_{(1,0)} + T_{(gap)}$ 
5:      $DP_{(2,1)} = MAX \begin{cases} DP_{(1,0)} + T_{(Match, Miss-match)} \\ DP_{(2,0)} + T_{(gap)} \\ 0 \end{cases}$ 
6:      $Error_{flag}(PE_{12}) \leftarrow 0$ 
7:   else
8:      $Error_{flag}(PE_{12}) \leftarrow 0$ 
9:   end if
10:  if  $DP_{(1,1)} + T_{(gap)} > DP_{(2,1)}$  then
11:     $DP_{(2,1)} \leftarrow DP_{(1,1)} + T_{(gap)}$ 
12:     $Error_{flag}(PE_{13}) \leftarrow 1$ 
13:  else
14:     $Error_{flag}(PE_{13}) \leftarrow 0$ 
15:  end if
16:  ▷ Editing by using vertical PEs
17:  if  $Error_{flag}(PE_{01}) = 1$  then
18:    if  $DP_{(0,1)} + T_{(gap)} > DP_{(0,2)}$  then
19:       $DP_{(0,2)} \leftarrow DP_{(0,1)} + T_{(gap)}$ 
20:       $DP_{(1,2)} = MAX \begin{cases} DP_{(0,1)} + T_{(Match, Miss-match)} \\ DP_{(0,2)} + T_{(gap)} \\ 0 \end{cases}$ 
21:       $Error_{flag}(PE_{01}) \leftarrow 0$ 
22:    else
23:       $Error_{flag}(PE_{01}) \leftarrow 0$ 
24:    end if
25:    if  $DP_{(1,1)} + T_{(gap)} > DP_{(1,2)}$  then
26:       $DP_{(1,2)} \leftarrow DP_{(1,1)} + T_{(gap)}$ 
27:       $Error_{flag}(PE_{02}) \leftarrow 1$ 
28:    else
29:       $Error_{flag}(PE_{02}) \leftarrow 0$ 
30:    end if
31:     $DP_{(2,2)} = MAX \begin{cases} DP_{(1,1)} + T_{(Match, Miss-match)} \\ DP_{(2,1)} + T_{(gap)} \\ DP_{(1,2)} + T_{(gap)} \end{cases}$ 

```

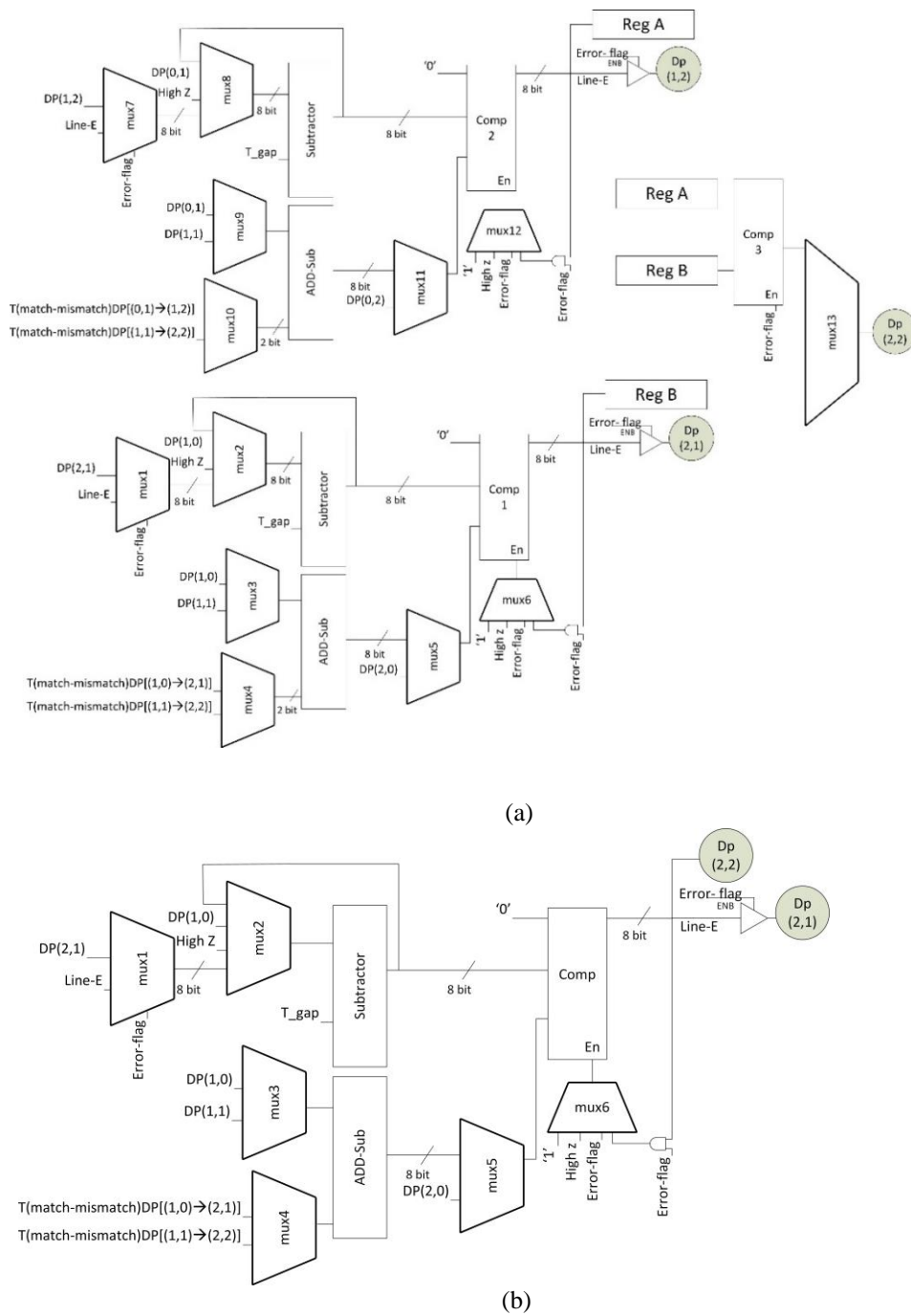


Fig. 4: The data path architecture of the proposed method: (a) horizontal PE and (b) vertical PE.

ignoring the value of the cell (1,1). Error editing for the cell (1, 0) is already explained, so the cell (2, 0) and the effects of ignoring the value of the cell (1, 1) need to be elaborated. According to Algorithm 1, the value of the cell (2, 0) is corrected by considering the gap penalty at the cell (1, 0) and the effect of ignoring the cell (1, 1) is addressed by reflecting the gap penalty at the cell (1, 1). Note that the entire calculation and edition phase are completed within three clock cycles and, therefore, a 3x3 subset as shown in Fig. 3 is large enough to explain the entire calculation. In fact, for larger matrices, the errors for the cells that are located further away will be completely edited within the three clock cycles and, therefore, we do not need to consider them in our calculations.

3.2.2. Other cells

Editing the values of the cells that are not located on the main diagonal is simpler than that of those on the main diagonal and can be easily concluded from Algorithm 1.

3.3. Hardware Implementation

This section describes the hardware implementation of the proposed horizontal and vertical PEs and describes how they calculate the roughly approximated values for each cell and also the error editing phase. Fig. 5 shows a simplified block diagram of the proposed architecture. As shown in this figure, the control unit manages the control signals on the data path. Additionally, the query and reference symbols should be stored in shared memory and the score arrays will be sent to the local memory for the editing and calculation phases.

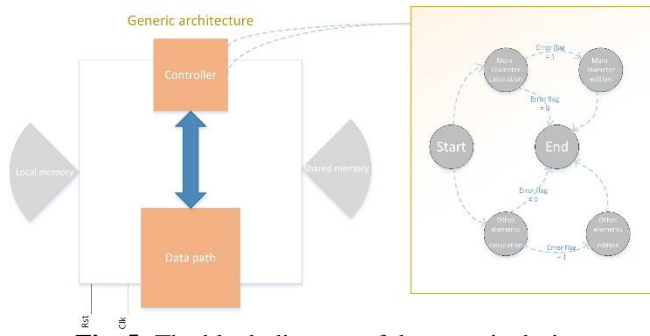


Fig. 5: The block diagram of the generic design.

Other than the control unit, an important part of the hardware implementation is the design of PEs. As mentioned earlier, two types of PEs are used in the proposed architecture i.e., vertical PEs and horizontal PEs. The detailed hardware implementation of these PEs is described below.

3.3.1. Vertical PE

A vertical PE does not compute the cells on the main diagonal and, therefore, implements simpler equations. Hence, they are less complex and, of course, have faster designs than the horizontal PEs. Fig. 4b shows the functionality of the proposed architecture

3.3.2. Horizontal PE

Unlike vertical PEs, horizontal PEs are further used to compute the cells on the main diagonal. Hence, they are more complex and, consequently, have slower designs. The hardware

4. SIMULATION RESULTS

This section is further divided into two sections. The first section provides the FPGA and ASIC implementation results of the proposed architecture, while the second section analyzes the performance of the proposed architecture in terms of the total execution time.

4.1. Synthesis Results

The proposed architecture is implemented in VHDL hardware description language and synthesized on (1) FPGA and (2) using an ASIC implementation.

Table 2 reports the resource utilization of the horizontal and vertical PEs when implemented on Virtex-7 and Spartan-7 FPGAs. Moreover, both designs are implemented by using Synopsys Design Compiler for 180-nm CMOS technology, and the results are provided in Table 3.

Our simulation results, specifically the results in Table 2, show that the proposed architecture can operate at 360Mhz on Virtex 6. Note that this is the worst-case scenario, i.e., all of the cells have erroneous values and the error editing phase needs to be performed for all of them.

4.2. Performance

In this section, we analyze the worst-case execution time of the proposed architecture. Given that each PE requires three clock cycles to accomplish its computations, the total execution time T_{total} for an $(N + 1) \times (N + 1)$ similarity matrix (a seed with the length of N) can be calculated as:

$$T_{total} = N \times 3 \times \frac{1}{clk_{horizontal}} \quad (4)$$

where $clk_{horizontal}$ is the maximum clock frequency of the horizontal PEs, i.e., the slowest part of the proposed architecture. Note that in an $(N + 1) \times (N + 1)$ similarity matrix with a seed length of N , the first row and the first column of the matrix are initial values, which are calculated by the SMEM kernel. We need three clock ticks for each PE in the worst case, and all of the matrix elements will be calculated in N cycles of the calculation, which is shown in Fig. 1.

Compared to the state-of-the-art 1D-systolic array-based architecture that computes an $N \times N$ matrix in $2N-1$ clock cycles, the proposed architecture is faster as it only requires $N-1$ clock cycles. We compare our architecture performance with the original algorithm in terms of execution time on Intel(R) Core(TM) i7-4702 MQ CPU. The BWA-MEM 0.7.11 is used and run over the free NCBI dataset [23]. Since we are interested in comparing the execution time of the seed extension kernel, we only used the output of the SMEM kernel as the input to the proposed design. Note that the speedup in Table 4 is the average speedup over 1000 randomly selected inputs from the dataset. The comparison results are provided in Table 4 and Fig. 6. Fig. 6a provides a comparison of the execution time of our proposed method and 1-D systolic architecture based on different seed lengths. As indicated from this figure, our execution time decreases asymptotically with the growth of seed length, and our acceleration pace is fixed for longer seed lengths. This speed-up ratio is illustrated in Fig. 6b.

Area overhead of both 1D-Systolic arrays and our approach is enlightened herein. Based on [11], implementation results considering a 131×131 array on Xilinx Virtex-6 LX760 FPGA show 4% of total FPGA resources, while our approach utilizes almost 13.5% of Xilinx Virtex-6 LX760 FPGA resources that is about 3.3x more area overhead than the 1D-systolic. This increase in area overhead is due to the addition of the editing phase, which lets us for the first time eliminate data dependency in calculating the Smith-Waterman matrix in a 2D manner (Fig. 1). However, the area is not usually a bottleneck in the implementation of the BWA-MEM algorithm on FPGA, and the execution time is a more important concern. The main contribution of our work lies in the fact that we have eliminated the data dependency to devise a new 2D approach to speeding up the seed extension kernel. It is

Table 2: Result of FPGA implementation.

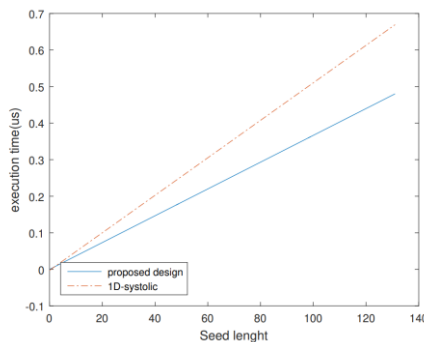
FPGA	PE	LUT			FF			IO		BUFG		Freq. (MHz)
		Usage	Utilization	Available	Usage	Utilization	Available	Usage	Utilization	Usage	Utilization	
xc7s50csga324-2	Vertical	89	0.2%	32600	18	0.03%	65200	72	32%	1	3.13%	189
xc7s50csga324-2	Horizontal	205	0.7%	32600	39	0.05%	65200	123	57.7%	1	3.13%	185
xc7v58tffg1157-3	Vertical	89	0.02%	364200	18	0.01%	728400	72	11.8%	1	3.13%	363
xc7v58tffg1157-3	Horizontal	205	0.05%	364200	39	0.01%	728400	123	20.4%	1	3.13%	360

Table 3: The ASIC design of the proposed architecture.

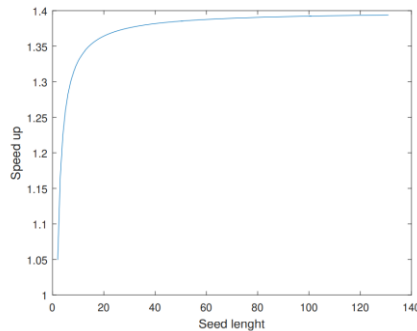
PE Leakage Type	Vertical	Horizontal
Critical path delay (ns)	3.2	3.22
Cell area (nm ²)	10245.31	21584.18
Number of nets	446	830
Levels of logic	14	18
Dynamic power (nW)	2.23	4.4
Power (nW)	366.7	747.3

Table 4: Execution time comparison of CPU vs. the proposed architecture (us).

Matrix dimension	i7-4702	Proposed architecture	FPGA Utilization	Speedup
10 × 10	8.956	0.0366	0.95%	245 ×
25 × 25	43.178	0.091	2.45%	474 ×
50 × 50	105.24	0.183	4.95%	576 ×
100 × 100	198.35	0.366	9.95%	542 ×
131 × 131	244.21	0.48	13.5%	509 ×



(a)



(b)

Fig. 6: The proposed architecture with operating Freq. 360 MHz vs. 1-D systolic arrays with operating Freq. 380 MHz (on the same platform Xilinx Vertix 6), (a) Execution time, and (b) Speedup.

obvious that our proposed architecture can benefit from more parallelism for computing different seeds in parallel, and we will not face the lack of FPGA resources.

5. DISCUSSION

The proposed architecture can be implemented on a Virtex 6 FPGA device with a typical 131 × 131 matrix dimension and a minimum of 19 base-pairs seed length from a read containing 150 base-pairs, while using less than 15% of the FPGA available resources. This indicates that the

proposed architecture can benefit from more parallelism for computing different seeds in parallel. Our simulation results show up to 570x and 1.4x acceleration and speedup in comparison to software execution and the 1D-systolic arrays, respectively in case of the 131 × 131 matrix dimension on Virtex 6 FPGA.

6. CONCLUSION

We have proposed a newly developed algorithm of the seed extension kernel for the well-known BWA-MEM sequence alignment algorithm. This novel 2-dimensional, high-throughput seed extension kernel is implemented on FPGA. We achieved up to 570x speedup with 360MHz operating frequency in comparison to the Intel(R) Core(TM) i7-4702 MQ CPU. Also, we achieved up to 1.4x speedup in comparison to the 1D-systolic arrays implemented on the same hardware as our architecture. Our simulation results show that the proposed architecture can work with up to 312 MHz frequency in Synopsys Design-Compiler for 180-nm CMOS technology. By introducing the calculation and error editing phase, we notably reduced the number of required clock cycles for filling an $N \times N$ similarity matrix. In fact, the state-of-art 1D-systolic array-based architectures fill the $N \times N$ similarity matrix in $2N-1$ cycles, while our proposed architecture only takes $N-1$ cycles to fill the same matrix.

CREDIT AUTHORSHIP CONTRIBUTION STATEMENT

Mahdi Taheri: Conceptualization, Formal analysis, Methodology, Resources, Roles/Writing - original draft, Writing - review & editing. **Ali Mahani:** Formal analysis, Project administration, Software, Writing - review & editing.

DECLARATION OF COMPETING INTEREST

The authors declare that they have no known competing financial interests or personal relationships that could have appeared to influence the work reported in this paper. The ethical issues, including plagiarism, informed consent, misconduct, data fabrication and/or falsification, double publication and/or submission, and redundancy, have been completely observed by the authors.

REFERENCES

- [1] H. Jung, C. Winefield, A. Bombarely, P. Prentis, and P. Waterhouse, "Tools and strategies for long-read sequencing and De novo assembly of plant genomes," *Trends in plant science*, vol. 24, no. 8, pp. 700 -724, 2019.
- [2] C. Pham-Quoc, B. Kieu-Do, and T.N. Thinh, "A high-performance FPGA-based BWA-MEM DNA sequence alignment," *Concurrency and Computation: Practice and Experience*, vol. 33, no. 18, pp. 5328, 2019.
- [3] Li. Wu et al., "FPGA accelerated INDEL realignment in the cloud," in *2019 IEEE International Symposium on High Performance Computer Architecture (HPCA)*, 2019, pp. 277–290.
- [4] C. Pham-Quoc, B. Kieu-Do, and T. Ngoc Thinh, "An FPGA-based seed extension IP core for BWA-MEM DNA alignment," in *2018 International Conference on Advanced Computing and Applications*, 2018, pp. 1–6.

- [5] S. Canzar, and S. Salzberg, "Short read mapping: an algorithmic tour," *Proceedings of the IEEE*, vol. 105, no.3, pp. 436-458, 2015.
- [6] D. Fujiki et al., "Genax: a genome sequencing accelerator," in *45th Annual International Symposium on Computer Architecture*, 2018, pp. 69–82.
- [7] B. Langmead, C. Trapnell, M. Pop, and S. Salzberg, "Ultrafast and memory-efficient alignment of short DNA sequences to the human genome," *Genome biology*, vol. 10, no. 3, 2009.
- [8] H. Li and R. Durbin, "Fast and accurate short read alignment with burrows-wheeler transform," *bioinformatics*, vol. 25, no. 14, pp. 1754–1760, 2009.
- [9] R. Li et al., "SOAP2: an improved ultrafast tool for short read alignment," *Bioinformatics*, vol. 25, no. 15, pp. 1966–1967, 2009.
- [10] H. Li, "Aligning sequence reads, clone sequences and assembly contigs with BWA-MEM," *ArXiv Preprint ArXiv*, vol. 1303, pp. 3997, 2013.
- [11] E. J. Houtgast, V. M. Sima, K. Bertels, and Z. Al-Ars, "An FPGA-based systolic array to accelerate the BWA-MEM genomic mapping algorithm," in *2015 International Conference on Embedded Computer Systems: Architectures, Modeling, and Simulation (SAMOS)*, 2015, pp. 221–227.
- [12] J. Cohen, "Bioinformatics an introduction for computer scientists," *Association for Computing Machinery Computing Surveys*, vol. 36, no. 2, pp. 122–158, 2004.
- [13] H. Cao et al., "A short-read multiplex sequencing method for reliable, cost-effective and high-throughput genotyping in large-scale studies," *Human Mutation*, vol. 34, no. 12, pp. 1715–1720, 2013.
- [14] K. Hammad, Z. Wu, E. Ghafar-Zadeh, and S. Magierowski, "A scalable hardware accelerator for mobile dna sequencing," *IEEE Transactions on Very Large Scale Integration (VLSI) Systems*, vol. 29, no. 2, pp. 273–286, 2021.
- [15] M. Taheri, and A. Mahani, "Development and hardware acceleration of a novel 2-D BWA-MEN DNA sequencing alignment algorithm," *1st Conference on Applied Research in Electrical Engineering (AREE)*, 2021.
- [16] T. J. Ham et al., "Genesis: A hardware acceleration frame- work for genomic data analysis," in *2020 ACM/IEEE 47th Annual International Symposium on Computer Architecture (ISCA)*, 2020, pp. 254–267.
- [17] Y. L. Chen, B. Y. Chang, C. H. Yang, and T. D. Chiueh, "A high-throughput FPGA accelerator for short-read mapping of the whole human genome," *IEEE Transactions on Parallel and Distributed Systems*, vol. 32, pp. 6, pp. 1465–1478, 2021.
- [18] Y. T. Chen, J. Cong, Z. Fang, Ji. Lei, and P. Wei, "When spark meets FPGA: A case study for next-generation DNA sequencing acceleration," in *8th USENIX Workshop on Hot Topics in Cloud Computing (HotCloud 16)*, June 2016.
- [19] P. Faes et al., "Scalable hardware accelerator for comparing DNA and protein sequences," in *Proceedings of the 1st International Conference on Scalable Information Systems*, 2006, pp. 33–es.
- [20] M. Taheri, S. Ansari, S. Magierowski, and A. Mahani, "Hardware acceleration of burrows-wheeler aligner algorithm with maximal exact matches seed extension kernel," *IET Circuits, Devices and Systems*, vol. 15, no. 3, pp. 1–10, 2020.
- [21] M. Taheri, H. Zandevakili, and A. Mahani, "A high-performance memristor-based smith-waterman DNA sequence alignment using FPNI structure," *Iranian Association of Electrical and Electronics Engineers (IAEEE)*, vol. 1, no. 1, pp. 59-68, 2020.
- [22] E. J. Houtgast, V. M. Sima, K. Bertels, and Z. Al-Ars, "Hardware acceleration of BWA-MEN genomic short read mapping for longer read lengths," *Computational Biology and Chemistry*, vol. 75, pp. 54–64, 2018.
- [23] D. Wheeler et al., "Database resources of the national center for biotechnology information," *Nucleic Acids Research*, vol. 35, no. suppl_1, pp. D5–D12, 2006.

BIOGRAPHY



Mahdi Taheri received his B.Sc. degree in Electronic Engineering from the Khaje Nasir University of Technology (KNTU), Tehran, Iran in 2017 and his M.Sc. degree in Electronic Engineering from Shahid Bahonar University, Kerman, Iran in 2020. Since then, he was with the RSS Lab at Shahid Bahonar University for 1 year, and now, he is studying for his Ph.D. at the Tallinn University of Technology (TalTech). His research interests focus on hardware assessment and reliability of neural networks, fault- tolerant design, and FPGA-based accelerators.

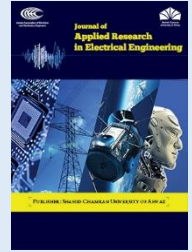


Ali Mahani received his B.Sc. degree in Electronic Engineering from Shahid Bahonar University, Kerman, Iran in 2001 and his M.Sc. and Ph.D. degrees both in Electronic Engineering from the Iran University of Science and Technology, Tehran, Iran in 2003 and 2009, respectively. Since then, he has been with the Electrical Engineering Department of Shahid Bahonar University where he is currently an associate professor. His research interests focus on fault-tolerant design, FPGA-based accelerators, approximate digital circuits, stochastic computing, and networked systems.

Copyrights

© 2022 Licensee Shahid Chamran University of Ahvaz, Ahvaz, Iran. This article is an open-access article distributed under the terms and conditions of the Creative Commons Attribution –NonCommercial 4.0 International (CC BY-NC 4.0) License (<http://creativecommons.org/licenses/by-nc/4.0/>).





Research Article

A Fourth-order MASH DDSM for Accurate Fractional Frequency Synthesizers

Seyed Ali Sadatnoori*

Department of Electrical Engineering, Shoushtar Branch, Islamic Azad University, Shoushtar 64517-41117, Iran

*Corresponding Author: a.sadatnoori@iau-shoushtar.ac.ir

Abstract: The output of a Digital Delta-Sigma Modulator (DDSM) is always a periodic signal and the input is constant. A hybrid DDSM is a premiere to its conventional counterpart for having a potential speed, by the choice of its smaller bus. This paper offers an implementation for multi-stage noise shaping (MASH) DDSMs that includes four modulators named hybrid DDSM-1, DDSM-2, DDSM-3, and DDSM-4. Also, it introduces a new solution, where the desired ratio in fractional frequency synthesizers is formed by combining four different modulus. The first stage modulator is a programmable modulus EFM1 and has a modulus M_1 that is not a power of 2. The second, third, and fourth stage modulators are modified MASH 1-1, multi-modulus MASH 1-1-1, and the efficiently dithered MASH 1-1-1-1 modulator that have conventional modulus $M_2, M_3,$ and $M_4,$ respectively. The M_1 modulus is optimally selected to synthesize the new structure of the desired frequencies. Design results confirm the suppositional predictions. In addition, the results of the circuit implementation proposed method offer a 17% reduction in hardware complexity.

Keywords: Fractional frequency synthesizers, digital delta sigma modulator, dither, low complexity, hybrid modulators.

Article history

Received 13 December 2021; Revised 3 March 2022; Accepted 4 March 2022; Published online 13 April 2022.

© 2022 Published by Shahid Chamran University of Ahvaz & Iranian Association of Electrical and Electronics Engineers (IAEEE)

How to cite this article

S. A. Sadatnoori, "A fourth-order MASH DDSM for accurate fractional frequency synthesizers," J. Appl. Res. Electr. Eng., vol. 1, no. 2, pp. 211-220, 2022. DOI: 10.22055/jaree.2022.39450.1040



1. INTRODUCTION

In a $\Delta\Sigma$ fractional-N frequency synthesizer, the multiple modulus divider is modulated by the output sequence of a digital sigma-delta modulator. Fractional-N frequency synthesis provides agile switching in narrow channel spacing systems and alleviates Phase-Locked Loop (PLL) design constraints for phase noise and reference spur. The PLL-based frequency synthesis technique is extensively employed in electronic measurement instruments, wireless communications, and class D amplifiers. The inherent problem of the fractional-N frequency synthesizer is that the periodic operation of the dual modulus divider produces fractional tones. Modern frequency synthesizers for portable applications use an indirect method known as a PLL (Fig. 1). These synthesizers consist of a Phase Detector (PD), a Loop Filter (LPF), a Voltage Controlled Oscillator (VCO), and a Multi Modulus Controller (MMC). The PC compares its two input signals phases and generates a measure of their phase error. A Low Pass Filter (LPF) must filter the phase error. The LPF takes out the DC part of the phase error. The loop is locked if the phase error is constant over time. In this synthesizer, the average output frequency is defined by:

$$f_{VCO} = \left(N_0 + \frac{N_1}{M_1}\right) \cdot f_{PD} \tag{1}$$

where f_{PD} is the input frequency at the input to the phase detector and $N_0, N_1,$ and M_1 are integer divider number, the input of DDSM, and modulus quantizer, respectively. Usually, the modulus M is a multiple of two.

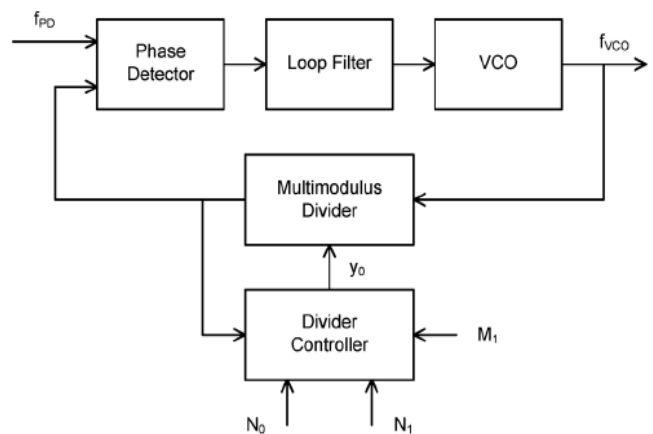


Fig. 1: Block diagram of a PLL-based fractional-N frequency synthesizer.

Input frequency multiples are synthesized by frequency synthesizers and produce higher reference frequencies and have higher frequency resolution. Since the phase detector frequency is higher than the frequency resolution in fractional-N frequency synthesizer, the loop bandwidth of the PLL is not limited by the frequency resolution. Fractional-N frequency synthesis is not useful in practical applications unless the fractional spurs are suppressed [1].

The sequence length of the output cycle is determined by the input, initial states, and DDSM architecture. There exist two classes of techniques to maximize cycle lengths in DDSMs: stochastic and deterministic. The application of additive least significant bit (LSB) dithering [2-5] is the most common stochastic technique. It can be presented at different points of the DDSM architecture to separate alternative cycles. A high-resolution digital MASH modulator can be employed to diminish the spur tone magnitude. As demonstrated by Kozak and Kale [6], the DDSM does not show large spurs with the constant input and the odd initial state of the first stage. In [7], a digital sigma delta modulator of separate lines is designed by pipeline method and its power spectral density is plotted. This method increases the speed of the modulator and reduces the hardware consumption. In [8], a ring-oscillator (RO)-based low-jitter digital fractional-N frequency synthesizer is presented. In [9, 10], the authors presented deterministic modifications to the DDSM architecture (an additional output feedback path and prime modulus) that maximize the cycle length of the error signal. Nevertheless, to have a maximal period by the modified MASH modulators, every EFM needs an extra M bit adder. Wang *et al.* [11] recommended a method for avoiding the development of spurs by substituting the sigma-delta modulator for a new type of digital quantizer and a charge pump offset incorporated with a sampled loop filter. In [12-14], a solution is presented based on mixed-radix algebra, where the required ratio is formed by combining two and three different modulus. Using error masking methodology, this modulator can decrease the hardware consumption and increase the accuracy of the fractional frequency synthesizer. In [15-17], a novel method is proposed for applying periodic dither to a DDSM to obtain minimized spurious tones. The effects of adding the pseudorandom dither signal in different stages within the proposed multi-stage noise shaping (MASH) modulator are expressed in a set of equations. In [18], the design of a new architecture of Continuous-Time (CT) MASH 2-2 (multi-stage noise shaping modulators) full feedforward Sigma Delta ($\Sigma\Delta$) modulator is presented. In [19], it is shown that applying a linear feedback shift register (LFSR) dither to a digital delta-sigma modulator (DDSM) cannot always increase its fundamental period.

Gonzalez-Diaz *et al.* [20] proposed a technique for the dithered MASH 1-1-1 DDSM. In their structure, a dither signal is injected simultaneously at the inputs of the second and third stages of a MASH 1-1-1 DDSM. These authors suggest that an m-bit LFSR dither generator is particularly "efficient" to eliminate fractional tones. In the present work, we introduce hybrid DDSM 1-2-3-4 modulator architecture. In this method, the First Order Error Feedback Modulator (EFM1) in the first stage has a variable programmable modulus M_1 that is not a power of 2. The modulators in the second, third and four stages (M_2 , M_3 , and M_4 , respectively)

are the power of 2. This method uses separate line technology [21, 22].

In [23], the modulator was presented for the third time. In addition, the proposed modulator simulation at the transistor level has been investigated and performed. Noise level simulations and power consumption of transistors for different levels of transistors are also provided. In this paper, the structure of each stage of the modulator is designed to reduce the noise level of the output. In this paper, a 4th order modulator with a multi-stage structure is presented.

The remainder of this paper is structured as follows: Section 2 describes the MASH modulators and summarizes background. Section 3 represents the 1-2-3-4 modulator. Word length optimization is analyzed in Section 4. Section 5 illustrates the simulation results. Finally, conclusions are made in Section 6.

2. BACKGROUND

The initial block diagram of a multi-tier MASH modulator is made from a digital storage. The warehousing model is shown in Fig. 2. In this form, the input of the storage is the digital word $x[n]$ with a length of n_0 bits. In decimal frequency synthesizers, the input is constant and sets the desired fraction value of $\frac{x}{2^{n_0}}$. The string stability of the error $e[n]$ is delayed by one unit of time. The delay string $s[n]$ is summed with the input signal $x[n]$. Whenever the warehouse keeper is overloaded, the transport bit $c[n]$ becomes one. The average time of the output string has a number of zeros and ones, which is equal to the average time of the input. Fig. 2b shows the digital storage model. The output string $y[n]$ corresponds to the output digit $c[n]$. If the signal $v[n]$, which is equal to the sum of the signals $x[n]$, $s[n]$, is greater than or equal to $M = 2^{n_0}$, it overflows and $y[n] = 1$. Otherwise, it is zero. So mathematically we have:

$$c[n] = y[n] = Q(v[n]) = \begin{cases} 0, & v[n] < M \\ 1, & v[n] \geq M \end{cases} \quad (2)$$

The difference between $v[n]$ and $My[n]$ is fed to the input through the register, if $y[n] = 0$ then $e[n] = v[n]$ and if $y[n] = 1$ then $e[n] = v[n] - M$. Hence, we have:

$$e[n] = v[n] \bmod M \quad (3)$$

This structure is called EFM, because the error signal $s[n]$ is fed back to the storage input. Fig. 3 shows the block diagram of the digital Sigma Delta MASH modulator of the 1st order, which consists of a cascading connection of EFM1_N bit blocks and a noise cancelling network. In this negative structure, the quantization error of each stage is entered to the next stage and the output of each stage is entered into the noise removal network, which will eliminate the quantization error of the middle stages. The output of the 1st order MASH modulator in the z domain is expressed by the following equation.

$$Y(z) = \frac{1}{2^N} \cdot X(z) + \frac{1}{2^N} (1 - z^{-1})^l \cdot E_l(z) \quad (4)$$

The structure of the HK-EFM1 (Hosseini and Kennedy EFM) used in the HK-MASH (Hosseini and Kennedy MASH) is illustrated in Fig. 4. There is just one difference between this structure and the classical EFM1 in Fig. 2; i.e.,

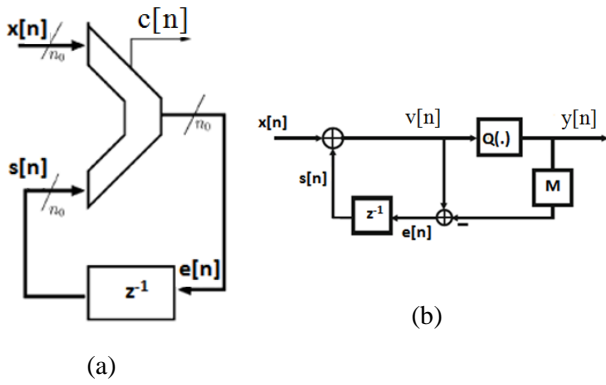


Fig. 2: (a) The digital storage used in the MASH structure, and (b) Its model

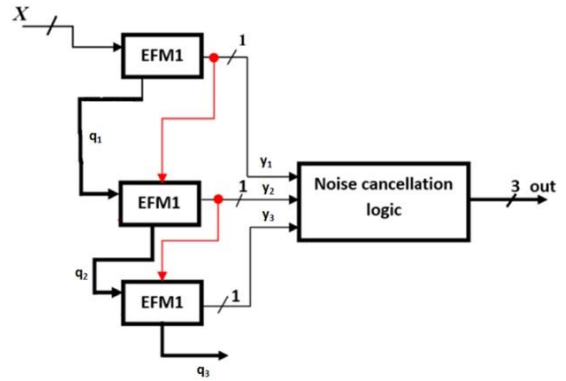


Fig. 5: Block diagram of the modified MASH 1-1-1 proposed in Sond and Park [24].

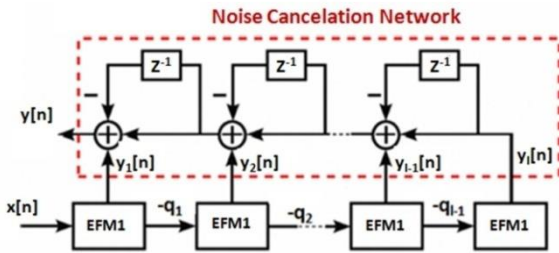


Fig. 3: Block diagram of an l^{th} order MASH DDSM incorporating a cascade of EFM1s [1].

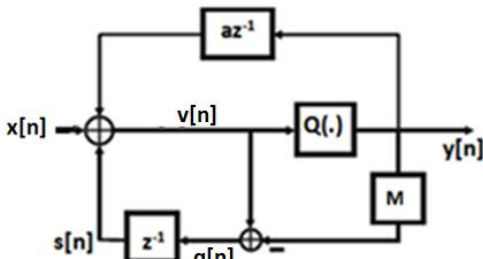


Fig. 4: The modified EFM1 used in HK-MASH [9].

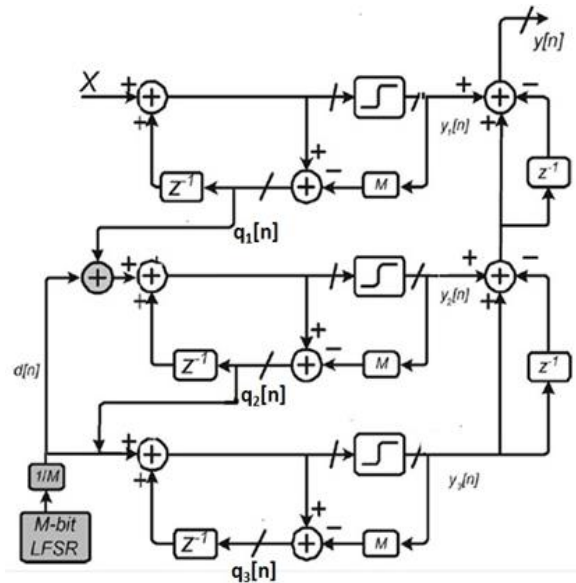


Fig. 6: Solution proposed by Gonzalez-Diaz et al. [20] for efficiently dithering a MASH 1-1-1.

the existence of the feedback block az^{-1} . Here, a is a selected small integer to make $(M-a)$ the maximum prime number below M . The cycle length of it is $(M-a)^l = (2^N - a)^l$, where l is the order of the modulator. Song and Park [24] proposed the modified MASH 1-1-1, as shown in Fig. 5. The modified MASH structure cascades several first-order digital accumulators like the traditional MASH structure but has a supernumerary feedforward connection between two adjoining categories and increases the sequence period of quantization error. The sequence period in the l^{th} MASH DDSM structure is $N_1 \cdot M^{l-1}$, where N_1 is the period of the first stage, and l is the order of the MASH modulator.

Gonzalez-Diaz *et al.* [20] added LSB dither to the second and third stages of a MASH 1-1-1, as shown in Fig. 6. Thus, the output spectrum appears to approach the ideal spectrum.

Le and Chen [25] presents a self-adaptive Sigma-Delta modulator, which offers opportunity to simplify the process of tuning parameters and further improve the noise performance. This paper presents a 5th order Sigma-Delta modulator to obtain higher SNR. Specifically, an additional 3rd order digital loop integrator is inserted between the AFE and the quantizer, which increases overall loop order to

produce much higher SNR for Sigma-Delta modulator and the parameters of the 3rd order digital loop integrator are optimized by swarm intelligent algorithm.

Mazzaro and Kennedy [26] presents a Fractional-N Charge Pump (CP) PLL with a Multi-stage noise Shaping (MASH) 1-1-1 divider controller to exhibit pairs of spurious tones called “horn spurs”. The phenomenon has been confirmed in measurements on a commercial wideband synthesizer.

Mai and Kennedy [27] describes a detailed analysis of the cause of wandering spur patterns in a MASH 1-1-1 DDSM-based fractional-N frequency synthesizer, supported by experimental measurements.

As shown in Fig. 1, this classical MASH 1-1-1 can be used in the fractional frequency synthesizer. In this synthesizer architecture, both f_{out} and f_{ref} are integer multiples of f_s , where $f_s = \frac{f_{ref}}{M}$ is the channel spacing. If modulus M is a power of 2, then only integer multiples f_{ref} of divided by a power of 2 can be synthesized.

The Global System for Mobile communication (GSM) system is a time and frequency division system in which a carrier frequency and a time slot number characterize each physical channel. GSM system frequencies include two bands at 900 MHz and 1800 MHz commonly referred to as the GSM-900 and DCS-1800 systems, respectively. For the primary band in the GSM-900 system, 124 radio carriers have been defined and assigned in two sub-bands of 25 MHz, each in the 890–915 MHz and 935–960 MHz ranges with the channel widths of 200 kHz.

Thus, in GSM 450, the problem of synthesizing is considered an output frequency of 0.45 GHz from a 13 MHz reference clock. In this example, $f_{ref} = 13 \text{ MHz}$, $f_s = 200 \text{ KHz}$, $f_{out} = 0.45 \text{ GHz}$ yielding, $N_0 = 34$, and $N_1 = 20648881$, $M = 2^{25}$. In conventional MASH 1-1-1 based fractional frequency synthesizers having $M = 2^{25}$, the required division number can be approximated as follows:

$$f_{out} = \left(34 + \frac{20648881}{2^{25}}\right) \cdot f_{ref} = 0.449999999999 \text{ GHz} \quad (5)$$

Hence, a frequency offset is approximately 89.408 Hz.

The approximation noise can be reduced using a larger value of modulus M . Also, it correlates with increasing the word length of the modulator, hardware complexity, and power consumption.

3. THE PROPOSED METHOD

In this section, we introduce a novel structure for the dithered MASH DDSM 1-2-3-4 that produces a long sequence period.

This paper attempts to reduce the hardware and power consumption of the fourth-order Digital Sigma-Delta Modulator and improve the noise level. Therefore, a fourth-order sigma-delta modulator with a high bit numbers broken down into several smaller sigma-delta modulators with fewer bits. Then, the input of the fourth-order modulator is divided into four segments so that each part of it is subdivided into first, second, third, and fourth-order modulators. We call this modulator, which consists of 4 sub-sections, a hybrid modulator.

The hybrid modulator architecture is shown in Fig. 7. In this architecture, instead of a single classical power-of-two modulus sigma-delta modulator in the fractional-N frequency synthesizer, we can use four modulators. The first stage modulator is a Variable Modulus EFM1 (VM-EFM1) and has a programmable modulus M_1 that is not a power of 2.

The second modulator in the hybrid structure is modified MASH 1-1, which has conventional modulo M_2 . The cycle length in modified MASH 1-1 structure is M_2^2 , where M_2 is the quantizer modulus in the classical DDSM.

The third modulator in the hybrid structure is multi-modulus MASH 1-1-1, which has conventional modulo M_3 . The small positive integer a in the i^{th} stage of HK EFM1 is denoted as a_i . This value will be assumed different for each stage. The values of a_i are selected such that to make $\{M - a_1, M - a_2, \dots, M - a_l\}$ co-prime numbers to maximize the period. A few values of a_i are given in Table 1.

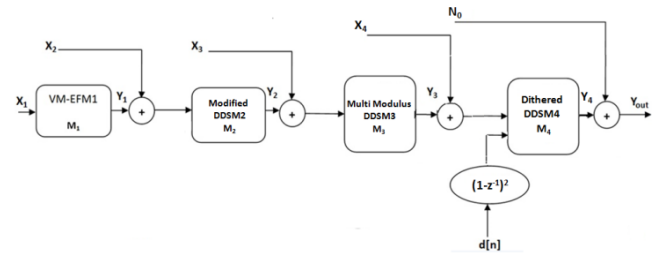


Fig. 7: Block diagram of the hybrid modulator DDSM 1-2-3-4 used in fractional frequency synthesizer.

Table 1: Some values of a_i in HK-MASH 1-1-1.

Word length (N)	a_1	a_2	a_3
4, 6, 9, 10, 12	3	0	1
3, 5, 7	1	0	3
8	5	0	1
11	9	0	1

It is of note that to make the period independent of the input, $M - a_1$ is set as a prime number.

If the greatest common divisor of any two numbers is 1, they are co-prime numbers. A prime number is a natural number that is divisible only by itself and 1.

The fourth modulator in the hybrid proposed structure is dithered MASH 1-1-1-1, which a periodic LFSR dither input with a period N_d added to the third and fourth stages of MASH 1-1-1-1. Fig. 8 presents an implementation of the second-order dither hybrid modulator.

The output frequency (f_{out}) in the fractional frequency synthesizer is determined by:

$$f_{out} = \left(N_0 + \frac{X_4 + \frac{X_3 + \frac{X_2 + \frac{X_1}{M_1}}{M_2}}{M_3}}{M_4}\right) \cdot f_{ref} \quad (6)$$

In this case, the z-transforms y_1 , y_2 , y_3 , y_4 , and y_{out} are shown by:

$$Y_{out}(z) = N_0 + Y_4(z) \quad (7)$$

$$Y_4(z) = STF_4(z)(X_4 + Y_3(z)) + NTF_4(z)Q_4(z) \quad (8)$$

$$Y_3(z) = STF_3(z)(X_3 + Y_2(z)) + NTF_3(z)Q_3(z) \quad (9)$$

$$Y_2(z) = STF_2(z)(X_2 + Y_1(z)) + NTF_2(z)Q_2(z) \quad (10)$$

$$Y_1(z) = STF_1(z) \cdot X_1 + NTF_1(z)Q_1(z) \quad (11)$$

where STF_1 , STF_2 , STF_3 , STF_4 , NTF_1 , NTF_2 , NTF_3 , and NTF_4 are the signal and error transfer functions of first, second, third and fourth stage modulators, respectively, and $Q_1(z)$, $Q_2(z)$, $Q_3(z)$, and $Q_4(z)$ are the quantization error signals introduced by the first, second, third, and fourth sigma-delta modulators, respectively. X_1 , X_2 , X_3 , and X_4 are the integer inputs of the VM-EFM1, modified MASH 1-1, multi-modulus MASH 1-1-1, and second-order dithered MASH 1-1-1-1 in the hybrid architecture, respectively. Hence, the final output y_{out} can be attained by:

$$Y_{out}(z) = N_0 + STF_4(z) \cdot X_4 + STF_4(z) \cdot STF_3(z) \cdot X_3 + STF_4(z) \cdot STF_3(z) \cdot STF_2(z) \cdot X_2 + STF_4(z) \cdot STF_3(z) \cdot STF_2(z) \cdot STF_1(z) \cdot X_1 + NTF_4(z)Q_4(z) + STF_4(z) \cdot NTF_3(z) \cdot Q_3(z) + STF_4(z) \cdot STF_3(z) \cdot NTF_2(z) \cdot Q_2(z) + STF_4(z) \cdot STF_3(z) \cdot STF_2(z) \cdot NTF_1(z) \cdot Q_1(z) \quad (12)$$

where,

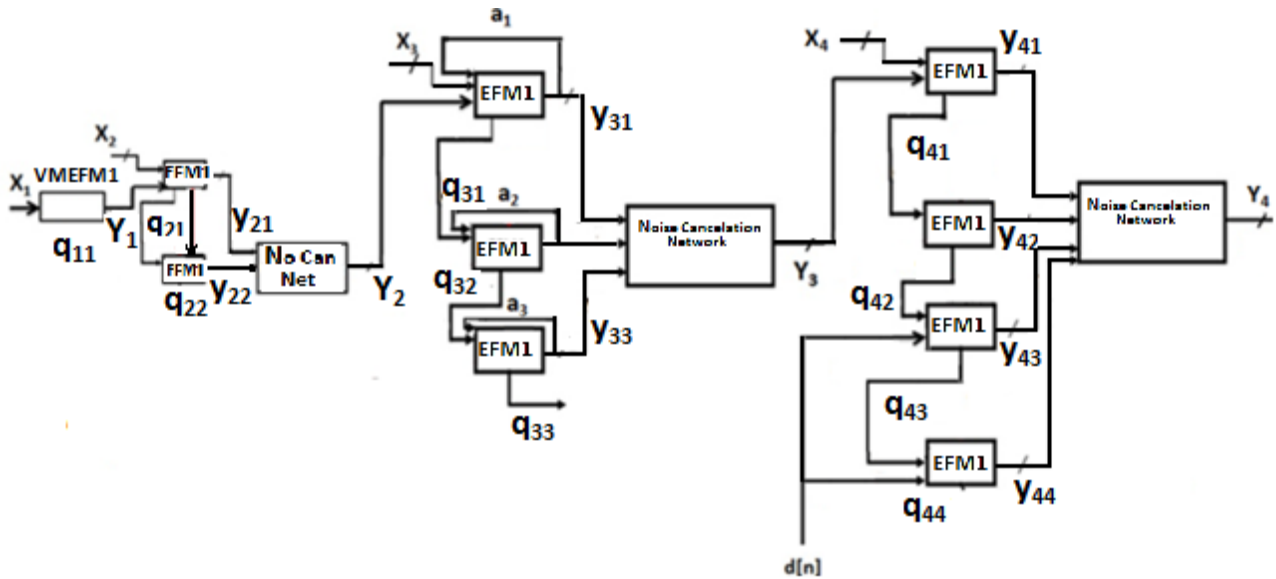


Fig. 8: Implementation of the second order dither hybrid DDSM 1-2-3-4 modulator.

$$STF_4(z) = \frac{1}{M_4}, STF_3(z) = \frac{1}{M_3}, STF_2(z) = \frac{1}{M_2}, STF_1(z) = \frac{1}{M_1}, NTF_4(z) = (1 - z^{-1})^4, NTF_3(z) = (1 - z^{-1})^3, NTF_2(z) = (1 - z^{-1})^2, \text{ and } NTF_1(z) = (1 - z^{-1}).$$

4. THE DESIGN APPROACH

The DDSM quantization error power is distributed over a few tones that are specified by the period, leading to a tone spacing of $df[k] = \frac{f_s}{N}$, where f_s is the sampling frequency and N is the period. When the sequence length and, consequently, the number of tones is large, the Power Spectral Density (PSD) approaches the classical white noise approximation. It is noteworthy that all quantization error terms can be considered as independent additive white sources. The PSD of Y_2, Y_3 , and Y_4 in the second-order LSB LFSR dither signal in the DDSM2, the multi-modulus DDSM3, and dithered DDSM4 are defined by:

$$P_2(\Omega[k]) = \frac{1}{12} (|1 - z^{-1}|^4)_{z=e^{j\Omega}} = \frac{1}{12} \left(2 \sin\left(\frac{\Omega}{2}\right) \right)^4 \tag{13}$$

$$P_3(\Omega[k]) = \frac{1}{12} (|1 - z^{-1}|^6)_{z=e^{j\Omega}} = \frac{1}{12} \left(2 \sin\left(\frac{\Omega}{2}\right) \right)^6 \tag{14}$$

$$\Omega[k] = \frac{2\pi}{N} \cdot k, \quad k = 0, 1, \dots, \frac{N}{2} \tag{15}$$

$$P_4(\Omega[k]) = \frac{1}{12} (|1 - z^{-1}|^8)_{z=e^{j\Omega}} + \frac{1}{12} \frac{1}{M_4^2} (|1 - z^{-1}|^4)_{z=e^{j\Omega}} \tag{16}$$

where Ω is the angular frequency of the oscillation and P is the density of the power spectrum. Also, at the output of the proposed hybrid modulator, since P_2 and P_3 are second-order

and third-order shaped, respectively, while P_4 is fourth-order shaped, if the level of the lowest frequency tone in P_2 and P_3 is below that of P_4 , the overall power of P_2 and P_3 should always be below the P_4 envelope. This can be expressed as:

$$P_2 < P_4, f = \frac{f_s \cdot k}{N_2}, k = 1, 2, \dots, \frac{N_2}{2} \tag{17}$$

$$P_3 < P_4, f = \frac{f_s \cdot k}{N_3}, k = 1, 2, \dots, \frac{N_3}{2} \tag{18}$$

Note that for a DDSM with an output period of N , the lowest frequency tone is at $\frac{f_s}{N}$. Therefore, since the periods for modified DDSM2 and multi-modulus DDSM3 are approximately M_2^2 and $(M_3 - \alpha)^3$, respectively, the lowest frequency tones in the power spectra are at $\frac{f_s}{M_2^2}$ and $\frac{f_s}{(M_3 - \alpha)^3}$.

Thus, at low frequencies:

$$|1 - z^{-1}|^2 = \left| 1 - e^{-\frac{j2\pi f}{f_s}} \right|^2 = \left| 2 \sin\left(\frac{\pi f}{f_s}\right) \right|^2 \cdot \sin^2\left(\frac{\pi f}{f_s}\right) \approx \frac{\pi f}{f_s} \text{ for } f \ll f_s \tag{19}$$

We can approximate P_2, P_3 , and P_4 at low frequencies by:

$$P_2 = \frac{1}{12} \left(\frac{1}{M_3 \cdot M_4} \right)^2 2^4 \cdot \left(\frac{\pi f}{f_s} \right)^4 \tag{20}$$

$$P_3 = \frac{1}{12} \frac{1}{M_4^2} 2^6 \cdot \left(\frac{\pi f}{f_s} \right)^6 \tag{21}$$

$$P_4 = \frac{1}{12} 2^8 \cdot \left(\frac{\pi f}{f_s} \right)^8 + \frac{1}{12} \frac{1}{M_4^2} 2^4 \cdot \left(\frac{\pi f}{f_s} \right)^4 \tag{22}$$

Substituting (20)-(22) into the constraints (17) and (18), we have:

$$\frac{1}{12} 2^8 \cdot \left(\frac{\pi f}{f_s} \right)^8 + \frac{1}{12} \frac{1}{M_4^2} 2^4 \cdot \left(\frac{\pi f}{f_s} \right)^4 \approx \frac{1}{12} 2^8 \left(\frac{\pi f}{f_s} \right)^8 \tag{23}$$

$$\left(\frac{1}{M_3 \cdot M_4}\right)^2 \cdot 2^4 \cdot \left(\frac{\pi f}{f_s}\right)^4 < 2^8 \cdot \left(\frac{\pi f}{f_s}\right)^8, f = \frac{f_s}{M_2^2} \quad (24)$$

$$2^6 \cdot \frac{1}{M_4^2} \left(\frac{\pi f}{f_s}\right)^6 < 2^8 \cdot \left(\frac{\pi f}{f_s}\right)^8, f = \frac{f_s}{(M_3 - \alpha)^3} \quad (25)$$

Therefore:

$$\left(\frac{1}{M_4}\right)^2 < \frac{2^2 \cdot \pi^2}{M_3^6} \quad (26)$$

$$\begin{aligned} M_3^3 < 2\pi \cdot M_4 \rightarrow 2^{3n_3} < 2\pi \cdot 2^{n_4} \rightarrow 3n_3 \\ < \log_2(2\pi) + n_4 \rightarrow n_3 \\ < \frac{2.65 + n_4}{3} \end{aligned} \quad (27)$$

$$\left(\frac{1}{M_3 \cdot M_4}\right)^2 < \frac{2^4 \cdot \pi^4}{M_2^4} \quad (28)$$

$$M_2 < \frac{\sqrt{M_3 \cdot M_4}}{2\pi} \quad (29)$$

In the VM-EFM1 accumulator, the output Y_l will be periodic with a cycle length between two and M_1 . In the worst case, the quantization noise power of VM-EFM1 is spread over (M_1-1) tones. The power in the lowest tone, after passing through MASH 1-1, multi-modulus MASH 1-1-1, and dithered MASH 1-1-1-1, is obtained by:

$$\begin{aligned} P_{tone} &= \left(\frac{1}{M_1 \cdot M_2 \cdot M_3 \cdot M_4}\right)^2 \\ &= STF_1^2 \cdot STF_2^2 \cdot STF_3^2 \cdot STF_4^2 \end{aligned} \quad (30)$$

Consequently, to mask the worst-case tone from VM-EFM1 at the output of dithered DDSM 1-1-1-1, it is required that:

$$\Omega_1[1] = \frac{2\pi}{M_1}, k = 1, N_1 = M_1 \quad (31)$$

$$P_4(\Omega_1[1]) \geq N_f \cdot P_{tone} \quad (32)$$

where N_f is FFT length, which presents the frequencies at which the PSD is estimated.

Substituting (22) and (30) into the constraint (32), we obtain:

$$\begin{aligned} N_f \left(\frac{1}{M_1 \cdot M_2 \cdot M_3 \cdot M_4}\right)^2 &\leq \frac{1}{12} \left(\frac{2\pi}{M_1}\right)^8 \rightarrow M_1 \\ &\leq \sqrt[6]{\frac{(2\pi)^8 \cdot M_2^2 \cdot M_3^2 \cdot M_4^2}{12N_f}} \end{aligned} \quad (33)$$

5. DESIGN EXAMPLE

5.1. Simulation Results

Given three design parameters of the reference frequency f_{ref} , the channel spacing f_s , and the output frequency f_{out} , we need to determine nine integers of $N_0, X_1, X_2, X_3, X_4, M_1, M_2, M_3$, and M_4 . First, M_4 is obtained and then M_1, M_2 , and M_3 are calculated.

Selecting the variable modulus EFM1, we compute:

$$p_1 = \gcd(f_{ref}, f_{out}, f_s) \quad (34)$$

$$p_2 = \frac{f_{pc}}{p_1} \quad (35)$$

where $\gcd(a, b, c)$ denotes the greatest common divisor of a , b , and c . Then, the modulus M_1 is calculated as follows:

$$M_1 = \frac{p_2}{\gcd(p_1, p_2)} \quad (36)$$

M_2 and M_3 can be obtained from and (29) and (27), respectively.

Next, the inputs N_0, X_1, X_2, X_3 , and X_4 can be determined.

$$I_1 = \frac{f_{out}}{f_{ref}} \quad (37)$$

The integer division number is obtained as:

$$N_0 = \text{floor}(I_1) \quad (38)$$

where $\text{floor}(x)$ returns the largest integer less than x .

$$I_4 = M_4 \cdot (I_1 - N_0) \quad (39)$$

The input of dithered MASH 1-1-1-1 modulator is determined as:

$$X_4 = \text{floor}(I_4) \quad (40)$$

The input of multi-modulus MASH 1-1-1 modulator is determined as:

$$I_3 = M_3 \cdot (I_4 - X_4) \quad (41)$$

$$X_3 = \text{floor}(I_3) \quad (42)$$

The input of modified MASH 1-1 modulator is calculated as:

$$I_2 = M_2 \cdot (I_3 - X_3) \quad (43)$$

$$X_2 = \text{floor}(I_2) \quad (44)$$

The input integer number of VM-EFM1 is obtained by choosing:

$$X_1 = M_1 \cdot (I_2 - X_2) \quad (45)$$

In GSM 450, consider the problem of synthesizing an output frequency of 0.45 GHz from a 13 MHz reference clock. In this example, $f_{ref} = 13\text{MHz}$, $f_s = 200\text{KHz}$, $f_{out} = 0.45\text{GHz}$ yielding, $N_0 = 34$, $X_4 = 630$, $X_3 = 2$, $X_2 = 7$, $X_1 = 5$, $M_1 = 13$, $M_2 = 2^4$, $M_3 = 2^4$, and $M_4 = 2^{10}$. In contrast, in the classical MASH 1-1-1-1, no approximation is implicated in the hybrid modulator. In particular,

$$f_{out} = \left(34 + \frac{630 + \frac{2 + \frac{7+5}{13}}{2^4}}{2^{10}}\right) \cdot f_{ref} = 0.4500\text{GHz} \quad (46)$$

In order to compare classical and hybrid modulators, we demonstrate simulation results. The initial states of the first stage registers are set to odd values to avoid short cycles. The simulated output power spectrum of the classical 25-bit MASH 1-1-1-1 DDSM is shown in Fig. 9. The simulated output PSD of the hybrid DDSM 1-2-3-4 is illustrated in Fig. 10. As expected, the hybrid DDSM 1-2-3-4 achieves an almost identical PSD compared to the traditional 25-bit MASH 1-1-1-1.

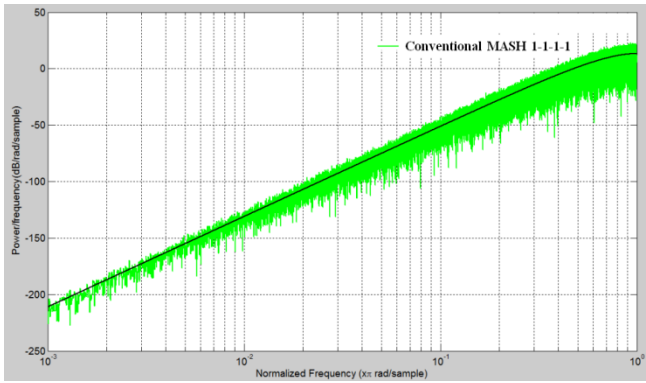


Fig. 9: Simulated PSD at the output of a second-order dithered classical MASH 1-1-1-1 DDSM; the input is 20648881, $M = 2^{25}$. The solid black curve shows the PSD of the fourth-order shaped quantization noise of MASH 1-1-1-1 with second-order shaped additive LSB dither.

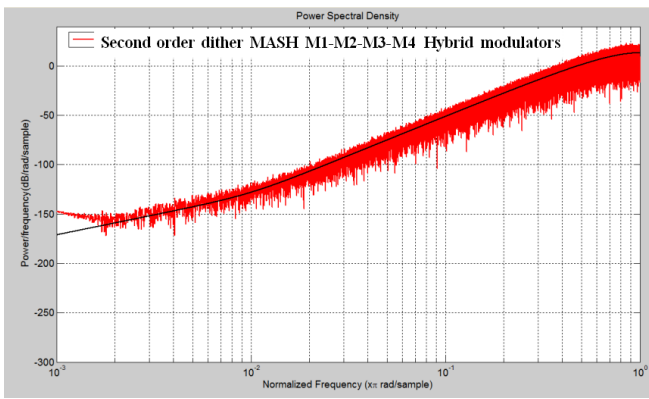


Fig. 10: Simulated PSD at the output of a second-order dithered hybrid DDSM 1-2-3-4; the inputs are $X_4 = 630, X_3 = 2, X_2 = 7, X_1 = 5$, the modulus are $M_1 = 13, M_2 = 2^4, M_3 = 2^4, M_4 = 2^{10}$. The FFT length is $N_f = 2^{18}$. The solid curves assume shaped white quantization noise including second-order shaped additive LSB dither.

5.2 Hardware Complexity

The first stage of the hybrid modulator consists of an accumulator with variable module $M_1 = 13$, which is not a multiple of 2 and has the input of $X_1 = 1$. The digital implementation of this feedback modulator with the variable module is shown in Fig. 11. The signal is X_1 input and M_1 modulo. The modulator consists of a subtractor, a multiplexer, and a NOT gate. This modulator is more complex than the fixed multiplier 2 modulators, which include the adder and the register [16].

The output of VM-EFM1 can be represented as:

$$y = \begin{cases} 0, & v < M_1 \\ 1, & v \geq M_1 \end{cases} \quad (47)$$

The error feedback signal in this modulator can be obtained as follows:

$$e[n] = v - M_1 \cdot y \quad (48)$$

In case $v[n]$ is greater than M_1 , the sign bit of subtractor is 0, the output signal $y[n]$ will be 1, and the selection input

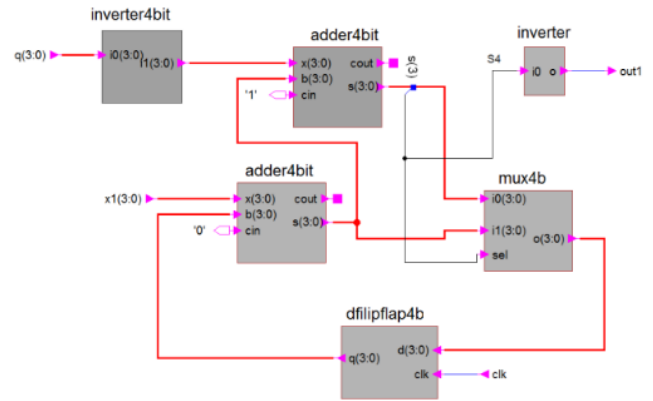


Fig. 11: Digital implementation of a First-Order VMFEM.

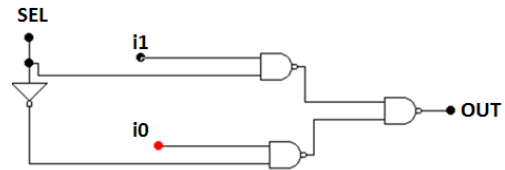


Fig. 12: The 2×1 multiplexer circuit.

of MUX is 0. Therefore, $e = v - M_1$. On the other hand, when $v[n]$ is smaller than M_1 , the sign bit of subtractor is 1, $y[n]$ will be 0, and $e = v$.

Each 4-bit adder is made with a 1-2-1 Carry Skip Adder (CSA) structure. The 2×1 multiplexer circuit is shown in Fig. 12. This circuit has three NAND gates and one inverter. A 2-complement performance of the noise cancellation network needs 6 flip-flops and 18 full adders. Thus, the number of flip-flops and full-adders required to implement a conventional N-bit MASH 1-1-1-1 DDSM can be written as:

$$n_{FF} = 4N + 6, n_{FA} = 4N + 15 \quad (49)$$

Consequently, the total Hardware Consumption (HC) of the traditional N-bit MASH 1-1-1-1 DDSM is given by:

$$HC_{conv} = 8N + 21 \quad (50)$$

The number of flip-flops and full-adders required to implement the proposed hybrid DDSM 1-2-3-4 is given by:

$$n_{FF} = 4n_4 + 3n_3 + 2n_2 + n_1 + 10 \quad (51)$$

$$n_{FA} = 4n_4 + 4n_3 + 3n_2 + n_1 + 25 \quad (52)$$

Hence, the total hardware consumption of the proposed hybrid DDSM 1-2-3-4 is given by:

$$HC_{Hy} = 8n_4 + 7n_3 + 5n_2 + 2n_1 + 35 \quad (53)$$

The Relative Hardware Consumption (RHC) of our hybrid DDSM 1-2-3-4 designed compared with the traditional DDSM4 is:

$$RHC\% = \frac{8n_4 + 7n_3 + 5n_2 + 2n_1 + 35}{8N + 21} \%100 \quad (54)$$

The RHC is demonstrated as the number of Look-Up Tables (LUTs), number of Flip-Flops (FFs), and the Total-Equivalent-Gate (TEG) count. In the example of Fig. 9 and Fig. 10, RHC is 83% from below for large N , suggesting that a hardware saving of at least 17% can be expected for typical values of N .

Table 2: Hardware reduction comparison.

FF & LUC	Area	Type	Ref.
98	2250 μm^2	MASH 1-1-1-1 (23 bit)	[13]
105	2050 μm^2	DDSM 4 (23 bit)	[22]
92	2150	MASH 2-2 (23 bit)	[23]
90	2100 μm^2	DDSM 4 (23 bit)	[24]
82	1750 μm^2	The DDSM 1-2-3-4 (4-4-4-10 bit)	Proposed method

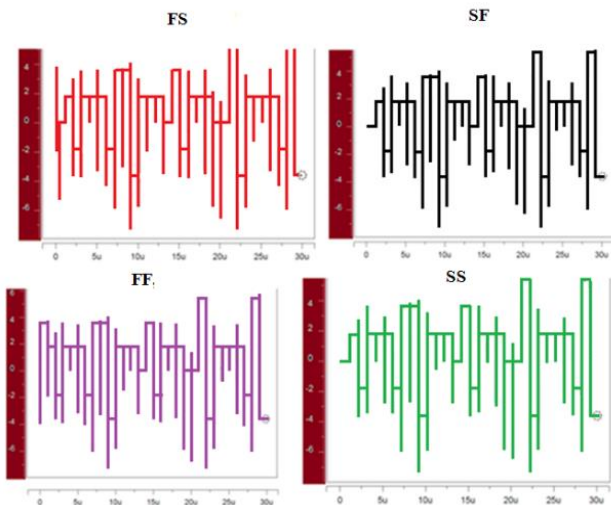


Fig. 13: The waveforms of the sigma delta modulator proposed by the 0.18 μm CMOS. The inputs are $X_1 = 5$, $X_2 = 7$, $X_3 = 2$, $X_4 = 630$ and $M_1 = 13$, $M_2 = 16$, $M_3 = 16$, $M_4 = 2$ and $f_s = 1$ MHz.

These results are based on the map report from the Xilinx ISE program. In terms of overall complexity, the 4-4-4-10 bit 1-2-3-4 hybrid DDSM4 requires 17% less hardware than the conventional 25-bit MASH 1-1-1-1 DDSM and has the marginally better spectral performance.

The synthesized hardware specifications for conventional and hybrid architectures are summarized in Table 2. It is notable that the proposed circuit requires 22% of the area as the conventional solution.

The results of Monte Carlo analysis are shown in Table 3. In this table, the power dissipation of transistors in the proposed method is compared for different models of transistors. In Fig. 13, the waveform of the modulator time domain is plotted after simulating different transistor models. The figure illustrates the Temperature effects and Mismatches of transistor simulation. Fig. 14 presents the Monte Carlo simulation results of temperature, noise, and delay variations.

6. CONCLUSION

This paper presents a novel method for digital delta sigma modulators (DDSMs) that can be used for precision frequency synthesizers. The hybrid DDSM 1-2-3-4 has four

Table 3: Comparison of power dissipation hybrid modulator structure. The proposed modulator is 4-4-4-10 bit with different transistor models n, p.

Types of transistors in proposed hybrid modulator	Power dissipation (nW)
TT	14.06
FF	75.36
FS	71.09
SF	16.75
SS	80.12

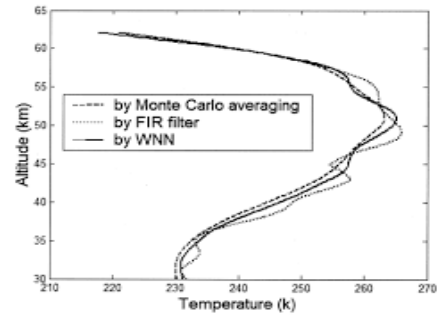


Fig. 14: The Monte Carlo design analyzing.

stages and the inputs of these stages are fixed numbers. The first stage of this modulator is programmable EFM1 and the module is not power of two. The second stage is a second-order modulator whose modulus of power of 2. The third stage is a third-order modulator with different modules and the fourth stage is a fourth-order modulator with a dither signal. Optimal input signals are applied to each modulator to provide error masking. In this method, the input with high word length is divided into several optimal and smaller parts and each input is applied to a modulator. Therefore, because smaller inputs are applied to third- and fourth-order modulators, the hardware consumption is reduced by 17% and improves power consumption. It also simulates corner effects.

CREDIT AUTHORSHIP CONTRIBUTION STATEMENT

Seyed Ali Sadatnoori: Conceptualization, Funding acquisition, Investigation, Software, Writing - review & editing.

DECLARATION OF COMPETING INTEREST

The author declares that they have no known competing financial interests or personal relationships that could have appeared to influence the work reported in this paper. The ethical issues; including plagiarism, informed consent, misconduct, data fabrication and/or falsification, double publication and/or submission, redundancy has been completely observed by the authors.

REFERENCES

- [1] K. Hosseini, and M. P. Kennedy, *Minimizing spurious tones in digital delta – sigma modulator*. Springer, New York, 2011.
- [2] S. Pamarti, J. Welz, and I. Galton, "Statistics of the quantization noise in 1-bit dithered single-quantizer digital delta–sigma modulators," *IEEE Trans. Circuits Syst. I: Regular Papers*, vol. 54, no. 3, pp. 492–503, 2007.

- [3] S. Pamarti, and I. Galton, "LSB dithering in MASH delta-sigma D/A converters," *IEEE Trans. Circuits Systems I: Regular Papers*, vol. 54, no. 4, pp. 779–790, 2007.
- [4] M. P. Kennedy, H. Mo, and B. Fitzgibbon, "Spurious tones in digital delta-sigma modulators resulting from pseudorandom dither," *Journal of the Franklin Institute*, vol.352, no. 8, pp. 3325-3344, 2015.
- [5] M. P. Kennedy, B. Fitzgibbon, and K. Dobmeier, "Spurious tones in digital delta sigma modulators with pseudorandom dither," in *2013 IEEE International Symposium on Circuits and Systems (ISCAS)*, 2013, pp. 2747-2750.
- [6] M. Kozak, and I. Kale Rigorous, "Analysis of delta-sigma modulators for fractional-N PLL frequency synthesis," *IEEE Transactions on Circuits and Systems I: Regular Papers*, vol. 51, no. 6, pp. 1148-1162, 2004.
- [7] L. Jahan Panah, S. A. Sadatnoori, and I. Chaharmahali, "Design of a digital sigma delta modulator with separate pipeline lines for fractional frequency synthesizers," *Majlesi Journal of Telecommunication devices*, vol. 10, no. 4, pp. 159-163, 2021.
- [8] A. Elmallah, J. Zhu, A. Khashaba, K. Megawer, and A. Elkholy, "A 3.2-GHz 405 fs_{rms} Jitter –237.2 dB FoM_{JIT} Ring-Based Fractional-N Synthesizer," *IEEE Journal of Solid-State Circuits*, vol. 57, no. 3, pp. 698-708, 2022.
- [9] K. Hosseini, and M. P. Kennedy, "Architectures for maximum sequence length digital delta-sigma modulators," *IEEE Transactions on Circuits and Systems II: Express Briefs*, vol. 55 no. 10, pp. 1104–1108, 2008.
- [10] K. Hosseini, and M. P. Kennedy, "Mathematical analysis of a prime modulus quantizer MASH digital delta-sigma modulator," *IEEE Transactions on Circuits and Systems II: Express Briefs*, vol.54, no. 12, pp. 1105–1109, 2007.
- [11] K. J. Wang, A. Swaminathan, and I. Galton, "Spurious tone suppression techniques applied to a wide-bandwidth 2.4 GHz fractional-NPLL," *IEEE Journal on Solid-State Circuits*, vol. 43, no. 12, pp. 2787–2797, 2008.
- [12] M. P. Kennedy, H. Mo, B. Fitzgibbon, A. Harney, H. Shanan, and M. Keaveney, "0.3–4.3 GHz Frequency-accurate fractional- frequency Synthesizer with integrated VCO and nested mixed-radix digital-modulator-based divider controller," *IEEE Journal of Solid-State Circuits*, vol. 49, no. 7, pp. 1595-1605, 2014.
- [13] S. A. Sadatnoori, E. Farshidi, and S. A. Sadughi, "A Novel architecture of pseudorandom dithered MASH digital delta-sigma modulator with lower spur," *Journal of Circuits, Systems and Computers*, vol. 25, no. 7, article 02181266, 2016.
- [14] S. A. Sadatnoori, E. Farshidi, and S. A. Sadughi, "A Novel structure of dithered nested digital delta sigma modulator with low-complexity low-spur for fractional frequency synthesizers," *Compel - The International Journal for Computation and Mathematics in Electrical and Electronic Engineering*, vol. 35, no. 1, pp. 157-171, 2016.
- [15] H. Mo, and M. P. Kennedy, "Masked dithering of MASH digital delta-sigma modulators with constant inputs using multiple linear feedback shift registers," *IEEE Transactions on Circuits and Systems I: Regular Papers*, vol. 64, no. 6, pp. 1390-1399, 2017.
- [16] Y. Zhang, R. Wunderlich, and S. Heinen, "A low-complexity low-spurs digital architecture for wideband PLL applications," *Microelectronics Journal*, vol. 45, no. 7, pp. 842–847, 2014.
- [17] L. Bertulesi, D. Cherniak, M. Mercandelli, C. Samori, A. Lacaíta, and S. Levantino, "Novel feed-forward technique for digital bang-bang PLL to achieve fast lock and low phase noise," *IEEE Transactions on Circuits and Systems I: Regular Papers*, pp. 1-13, 2022.
- [18] Y. Liao, X. Fan, and Z. Hua, "Influence of LFSR dither on the periods of a MASH digital delta-sigma Modulator," *IEEE Transactions on Circuits and Systems II: Express Briefs*, vol. 66, no. 1, pp. 66-70, 2019.
- [19] M. Borkowski, and J. Kostamovaara, "Variable modulus delta-sigma modulation in fractional-N frequency synthesis," *Electronics Letters*, vol. 43, no. 25, pp. 1399-1400, 2007.
- [20] V. R. Gonzalez-Diaz, and M. A. Garcia-Andrade, G. E. Flores-Verdad, F. Maloberti, "Efficient dithering in MASH sigma-delta modulators for fractional frequency synthesizers," *IEEE Transactions on Circuits and Systems I: Regular Papers*, vol. 57, no. 9, pp. 2394–2403, 2010.
- [21] Z. Ye, and M. P. Kennedy, "Hardware reduction in digital delta-sigma modulators via error masking—Part I: MASH DDSM," *IEEE Transactions on Circuits and Systems I: Regular Papers*, vol. 56, no. 4, pp. 714–726 2009.
- [22] Z. Ye, and M. P. Kennedy, "Hardware reduction in digital delta-sigma modulators via error masking—Part II: SQ-DDSM," *IEEE Transactions on Circuits and Systems II - Express Briefs*, vol. 56, no. 2, pp. 112–116, 2009.
- [23] Y. Zhang, R. Wunderlich, and S. Heinen, "A low-complexity low-spurs digital architecture for wideband PLL applications," *Microelectronics Journal*, vol. 45, no. 7, pp. 842–847, 2014.
- [24] J. Song and I. C. Park, "Spur-free MASH delta-sigma modulation," *IEEE Transactions on Circuits and Systems I: Regular Papers*, vol. 57, no. 9, pp. 2426–2437, 2010.
- [25] L. Le, and G. Chen, "Designing and optimizing of sigma-delta modulator using PSO algorithm," in *IEEE International Conference of Safety Produce Informatization (IICSPI)*, 2019, pp. 642-644.
- [26] V. Mazzaro and M. P. Kennedy, "Mitigation of horn spurs in a MASH-based fractional-N CP-PLL," *IEEE Transactions on Circuits and Systems II: Express Briefs*, vol. 67, no. 5, pp. 821-825, 2020.

- [27] D. Mai, and M. P. Kennedy, "Analysis of wandering spur patterns in a fractional- N frequency synthesizer with a MASH-based divider controller," *IEEE Transactions on Circuits and Systems I: Regular Papers*, vol. 67, no. 3, pp. 729-742, 2020.

BIOGRAPHY



Seyed Ali Sadatnoori received his BSc degree in Electrical Engineering from the Islamic Azad University of Dezful Branch and MSc degree in Electrical Engineering from the central Tehran branch Islamic Azad University, respectively, in 2001 and 2006. He received the PhD degree in

Electrical Engineering from the Tehran science and research branch Islamic Azad University in 2016. He is also an Assistant Professor of Shoushtar Branch Islamic Azad University. His current research interests include mobile ad hoc networks, wireless networks, transmitter and receiver circuits, analog to digital modulator, integrated circuits, and neural network.

Copyright

© 2022 Licensee Shahid Chamran University of Ahvaz, Ahvaz, Iran. This article is an open-access article distributed under the terms and conditions of the Creative Commons Attribution –NonCommercial4.0 International (CC BY-NC 4.0) License (<http://creativecommons.org/licenses/by-nc/4.0/>).



RTWSM: Real-Time Ad Hoc Wireless Sensor System Monitoring of Local Air Particle Pollution Reza Ghanavati, Yousef Seifi Kavian, and Abdolnabi Kosarian	112
Reactive Power Coordination Between Solid Oxide Fuel Cell and Battery for Microgrid Frequency Control Saeed Aminzadeh, Mehrdad Tarafdar Hagh, and Heresh Seyedi	121
On the Cramer-Rao Lower Bound Based Analysis of Direct Position Determination and DOA Position Finding for Co-Channel Emitter Localization Ali Eshkevari, and Seyed Mohammad Sajad Sadough	131
Influence of Gas Insulated Switchgear Configuration Components on UHF PD Signals Reza Rostaminia, Mehdi Vakilian, and Keyvan Firuzi	139
Optimal Switch Placement in Radial Distribution Networks to Reduce Energy Loss and Improve Network Security in Khuzestan Province Conditions Ali Rouhipour, Elaheh Mashhour, and Mohsen Saniei	149
A New Approach for the Transformer Differential Protection Based on S-Transform and Fuzzy Expert System Saeid Hasheminejad	159
Investigating the Effects of Phosphorene Nanotubes (PNTs)-on-Gold Substrates on the Enhancements of the Sensitivity of SPR Biosensors Amir Davami, and Mohammad Hadi Shahrokh Abadi	169
Designing of the Controller for Shipboard Microgrid Based on Linear Matrix Inequality Farhad Amiri, and Mohammad Hassan Moradi	175
Energy Management in Distribution Systems Considering Consumer Behavior and Internet of Things Moaiad Mohseni, Mahmood Joorabian, and Afshin Lashkarara	186
Design of Tunable Low-Power Band-Stop Filter for Elimination of 50 Hz Power-Line Noise Amirreza Solaymanpour, and Shahbaz Reyhani	197
A Novel 2-D BWA-MEM FPGA Accelerator for Short-Read Mapping of the Whole Human Genome Mahdi Taheri, and Ali Mahani	203
A Fourth-order MASH DDSM for Accurate Fractional Frequency Synthesizers Seyed Ali Sadatnoori	211

